

Welcome Message from the Congress Chairman

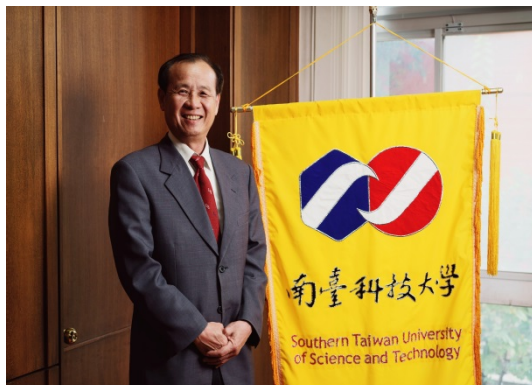
Dear attendees of the 18th ISAT Conference,

It is my great pleasure to welcome you to the 18th International Symposium on Advanced Technology (ISAT). This year the Southern Taiwan University of Science and Technology (STUST) is honored to host the conference. Especially, on behalf of the STUST I would like to extend a warm welcome to all delegates to join us to celebrate the 50th school anniversary celebration.

The ISAT 2019 holds 7 oral sessions, 2 poster sessions, as well as two keynote speakers presented by professors in Japan and Philippines. The selected 87 papers cover a variety of timely topics, out of which 48 papers are organized into 7 oral sessions and 39 papers that are presented in a poster session.

Also, I would like to thank all the authors for making a great effort of sharing their innovative minds and the latest research results to all the participants for your loyal support. I wish to express my sincere gratitude to the organizing committees, invited keynote speakers, and reviewers.

And finally, I wish to thank each participant for making this conference successful. Thank you for attending the ISAT 2019, this is an important conference for the partnership universities. I hope you have an enjoyable with your participation, the oral and poster sessions, networking with colleagues and friends, and the city tour activity at the ISAT 2019 conference in Tainan, Taiwan.



Yours sincerely

Deng-Maw Lu

The President of Southern Taiwan University of Science and Technology

The 18th international symposium on advanced technology (ISAT-18)
organization committee

Symposium Chairperson

Prof. Deng-Maw Lu

*President of Southern Taiwan University
of Science and Technology*

Co-Chairperson

Prof. Mitsunobu Sato

President of Kogakuin University

Prof. Fernando C. Sanchez, Jr.

*Chancellor of University of Philipines
Los Banos*

Prof. Doan Quang Vinh

*Rector of Danang University of
Technology*

Vice-Chairperson

Prof. Min-Tsai Lai

*Vice President of Southern Taiwan
University of Science and Technology*

Prof. Imamura Yasutada

Vice President of Kogakuin University

Prof. Serlie B. Jamias

*Vice Chancellor of University of
Philipines Los Banos*

Prof. Le Thi Kim Oanh

*Vice Rector of Danang University of
Technology*

Organization Committee

Chair Prof. Chih-Liang Chu

*Southern Taiwan University of Science
and Technology*

Co-chair Prof. Chao-Tang Yu

*Southern Taiwan University of Science
and Technology*

Member Prof. Wei-Wen Hu

*Southern Taiwan University of Science
and Technology*

Prof. Chien-Min Cheng

*Southern Taiwan University of Science
and Technology*

Prof. Chun-Hung Yang

*Southern Taiwan University of Science
and Technology*

Dr. Liang-Bi Chen *Southern Taiwan University of Science
and Technology*

Prof. Imamura Yasutada *Kogakuin University*

Prof. Le Thi Kim Oanh *Danang University of Technology*

Prof. Arnold R. Elepano *University of Philipines Los Banos*

Technical Program Committee

Chair **Prof. Chao-Tang Yu** *Southern Taiwan
University of Science and
Technology*

Co-chair **Prof. Wei-Wen Hu** *Southern Taiwan
University of Science and
Technology*

Member **Dr. Nguyen Hoang Mai** *Danang University of
Technology*

MSc. Nguyễn Quang Trung *Danang University of
Technology*

MSc. Nguyễn Thị Thảo Nguyễn *Danang University of
Technology*

MSc. Lê Thị Huỳnh Anh *Danang University of
Technology*

MSc. Trương Ngọc Sơn *Danang University of
Technology*

MSc. Nguyễn Hồng Nguyễn *Danang University of
Technology*

Dr. Arnold R. Elepano *University of Philipines
Los Banos*

Dr. Myra G. Borines *University of Philipines
Los Banos*

Dr. Alfredo Jr. Fortu *Romblon State University*

Dr. Reynold Caoili *Mariano Marcos State
University*

Prof. Kazuhiro Suga *Kogakuin University*

Prof. Yongchol Shin *Kogakuin University*

Prof. Masato Morita *Kogakuin University*

Prof. Masaki Tamura *Kogakuin University*

Prof. Takashi Saika *Kogakuin University*

Prof. Hidenori Fukuda *Kogakuin University*

	Prof. Toshiyuki Ozaki	<i>Kogakuin University</i>
Secretariat		
Chair	Prof. Wei-Wen Hu	<i>Southern Taiwan University of Science and Technology</i>
Co-chair	Prof. Chun-Hung Yang	<i>Southern Taiwan University of Science and Technology</i>
Member	Dr. Liang-Bi Chen	<i>Southern Taiwan University of Science and Technology</i>

■ Introduction to the symposium

The 18th international symposium on advanced technology (ISAT-18) organized by the Southern Taiwan University of Science and Technology (STUST) have been set for December 12-14, 2019. The STUST cordially invite you to attend the symposium and participate in its scientific and social programs. The theme of the ISAT-18 will be intelligent engineering technology. Presentations will consist of three categories, several keynote lectures, oral presentations, and poster presentations. The STUST hope all registrants will present a paper, but acceptance of papers will be at the discretion of the committee. The official language of the symposium will be English. In the following pages, you will find details concerning the symposium. We are looking forward to meeting you in Tainan, Taiwan.

■ Scope of the symposium

2019 International Symposium on Advanced Technology Engineering Innovation for Sustainable Future (ISAT-18) will be held at the Southern Taiwan University of Science and Technology (STUST), Tainan City, Taiwan from December 12 to 14, 2019. The scientific program will include oral and poster sessions.

Main theme of ISAT-18: Intelligent Engineering Technology

Topics of ISAT-18 include, but not limited to:

1. Intelligent Manufacture and Robot
2. Information and Communications Technology (ICT)
3. Internet of Things (IoT) and Smart Systems
4. Polymer Composite Materials
5. Biomedical Engineering and Biochemistry
6. Advanced Functional Materials
7. Education and Human Science
8. Architecture and Civil Engineering
9. Energy and Transportation
10. Artificial Intelligence (AI)

■ Conference Venue

2019 ISAT will be held in the Building L at the Southern Taiwan University of Science and Technology (STUST), No. 1, Nan-Tai Street, Yung Kang Dist., Tainan City 710, Taiwan.

■ Important Dates

- Abstract Submission Deadline: November 1, 2019
- Paper Acceptance Notification: November 08, 2019
- Camera-Ready Paper Submission: November 18, 2019
- Registration Deadline: November 22, 2019
- Conference Dates: December 12-14, 2019

2019-ISAT Symposium Program

December 12 (Thur.)

18:30~21:00	Welcome Reception (Lixin Grand Hotel)
-------------	---

December 13 (Fri.)

09:00-09:30	Registration (L008-Lobby)
-------------	-------------------------------------

09:30-10:20	Keynote Speaker 1 Prof. Yasutada Imamura Vice President of Kogakuin University, Japan. (L008)
-------------	---

10:20-10:40	Coffee Break (L008-Lobby)
-------------	-------------------------------------

10:40-11:30	Keynote Speaker 2 Prof. Arnold R. Elepaño Dean of University of the Philippines Los Baños, Philippines. (L008)
-------------	--

11:30~12:00	Opening ceremony Opening remark: Prof. Deng-Maw Lu, Chairman of Congress (L008)
-------------	--

12:00-13:30	Lunch (L007、L003、L001)
-------------	----------------------------------

13:30-15:15	Session I : Artificial Intelligence (L008)	Session II : IoT (L007)	Session III : Biomedical Engineering (L003)	Session IV: Architecture and Manufacture engineering (L001)	Poster Session (I) (L008-Lobby) 14:30-15:30
-------------	---	----------------------------	--	--	---

15:15-15:35	Coffee Break L008-Lobby
-------------	-----------------------------------

15:35-17:15	Session V : Energy and Transportation (L008)	Session VI : Electrical Engineering and Materials (L007)	Session VII : Materials (L003)		Poster Session (II) (L008-Lobby) 15:30-16:30
-------------	---	---	-----------------------------------	--	--

17:30-18:00	Closing Ceremony Closing remark: Prof. Min-Tsai Lai The Vice President for Academic Affairs of Southern Taiwan University of Science and Technology, Taiwan (L008)
-------------	---

18:30-21:30	Banquet (6th Dorm Student Cafeteria)
-------------	--

December 14 (Sat.)

9:00-12:00	City tour (Anping Tree House/old street)
------------	---

Oral Presentation		
Session I : Artificial Intelligence		
L008, 13:30-15:15		
Paper no.	Paper title	Authors
OS-I-1 13:30-13:45	A Visual Image Generation Method Using Generative Adversarial Networks	Yu Tajima, Qiu Chen
OS-I-2 13:45-14:00	Adversarial Knowledge Distillation Algorithm for a Compact Generator	Hideki Tsunashima, Hirokatsu Kataoka, Junji Yamato, Shigeo Morishima, Qiu Chen
OS-I-3 14:00-14:15	Single Image Dehazing Algorithm Based on Unet and ResNet-liked Structure	Li Ma, Qiu Chen
OS-I-4 14:15-14:30	An Advanced Generative Adversarial Networks Using Divided Z-vector	Taisei Hoshi, Hideki Tsunashima, Qiu Chen
OS-I-5 14:30-14:45	Taste Estimation Method from Food Images Based on deep learning	Akinobu Yoshioka, Qiu Chen
OS-I-6 14:45-15:00	Keyword Extraction Based on TF-IDF for TED Talks	Shu-Chen Cheng, Guo-Zhi Gu
OS-I-7 15:00-15:15	A Numerical Study on Intravascular Pressure Estimation with Convolutional Neural Network	Hikaru Kobayashi

Oral Presentation		
Session II : IoT		
L007, 13:30-15:15		
Paper no.	Paper title	Authors
OS-II-1 13:30-13:45	Threshold Setting Method considering General calls with Waiting Queue under Emergency Trunk Reservation Control	Kenta Kawai, Katsunori Yamaoka, and Ken-ichi Baba
OS-II-2 13:45-14:00	Black Holes and Beyond, the Taylor Switch Method for Image Filtering	Timothy Ryan Taylor, Chun-Tang Chao, and Juing-Shian Chiou
OS-II-3 14:00-14:15	The Anomaly Diagnosis Mechanism for Service Function Chaining Integrity in NFV Environments	Jia-Shing Shih, Sheng-Tzong Cheng, Chong-Yi Zhu, and Yu-Ming Chen
OS-II-4 14:15-14:30	A Bus Notifying System – A Proof of Concept	Chia-Nian Shyi, Jiun-Yu Tu, Jia-Xiang Zhao, Guo-Shun Hong, and Cong-Xun Yan
OS-II-5	Surface acoustic wave sensor for outdoor pollution	Yu-Jen Hsiao

14:30-14:45	air sensing	
OS-II-6 14:45-15:00	Power and Energy Optimization Strategies of a Wireless Sensor Network (WSN) for 2D Spatio Temporal Temperature Profiling in Marine Environments	Diogenes Armando D. Pascua and Michael Lochinvar S. Abundo
OS-II-7 15:00-15:15	A software defined radio design flow for FSK modulation and demodulation and its implementation using GNU radio	Yun-Tai Hsueh

Oral Presentation

Session III : Biomedical Engineering

L003, 13:30-15:15

Paper no.	Paper title	Authors
OS-III-1 13:30-13:45	Drying Kinetics and Anticoagulant Activity of Microwave-vacuum, Dehumidified-air and Freeze-dried African Night Crawler (<i>Eudrilus eugeniae</i> Kinberg)	Alfredo F. Fortu Jr, Ernesto P. Lozada, Engelbert K. Peralta, Kevin F. Yaptenco, and Delfin C. Suministrado
OS-III-2 13:45-14:00	Involvement of NTH α (IV) in formation of basement membrane-like structures around the endothelial cell network in a novel in vitro angiogenesis model	Yongchol Shin, Akane Moriya, Yuta Tohnishi, Takafumi Watanabe and Yasutada Imamura
OS-III-3 14:00-14:15	Tooth Segmentations from CBCT based on Image Processing with Tooth Smoothness and based on Deep Learning	Kazuhiro Suga, Akira Shinohara
OS-III-4 14:15-14:30	Development of trehalose bioconversion process in <i>Bacillus subtilis</i>	Xin-Ru Jiang, Yi-Fen Lin, and Po Ting Chen
OS-III-5 14:30-14:45	Development of imaging method of biological sample by TOF-SIMS	Kazuya Tamura
OS-III-6 14:45-15:00	Electro-Spray Dialysis for TOF-SIMS analysis of aerosol	T. Murata, S. Karasawa, M. Masato, and T. Sakamoto

Oral Presentation Session IV: Architecture and Manufacture engineering L001, 13:30-15:15		
Paper no.	Paper title	Authors
OS-IV-1 13:30-13:45	Practical functional performance of interior finishing wall using plastering material	Tomoko Kanemaki, Masaki Tamura, Yuto Nakamura
OS-IV-2 13:45-14:00	Study on improving residence and durability of concrete block construction in south east asia by using palm oil waste fiber.	Erika Futami and Masaki Tamura
OS-IV-3 14:00-14:15	Estimation of Long-Period Ground Motions Containing Permanent Displacement in the Near-Fault Region for 1999 Kocaeli Earthquake	Takumi Kiryu, Toshiaki Hisada, and Shinya Tanaka
OS-IV-4 14:15-14:30	Material characteristic evaluation for plastering restoration of Japanese style architecture in Taiwan	Misako Hanza
OS-IV-5 14:30-14:45	Collapse Prevention of a Lath and Plaster of Ceiling: Seismic Retrofitting of the Main Building of the Former Ibaraki Prefectural Tsuchiura First High School	Guanhan Jiang, Masaki Tamura, Osamu Goto and Naohiro Kobayashi
OS-IV-6 14:45-15:00	Design a Robot to Inspect Faults on the High Voltage Power Lines	Nguyen Hoang Mai
OS-IV-7 15:00-15:15	Design of 3 DoF Statically Balanced Articulated Manipulator Based on a New Gravity Balancer	Hong-Nguyen Nguyen

Oral Presentation**Session V : Energy and Transportation****L008, 15:35 ~ 17:15**

Paper no.	Paper title	Authors
OS-V-1 15:35-15:50	Evaluation of a locally-fabricated small-scale pyrolyzer for bio-oil and bio-char production of seaweeds (<i>Sargassum</i> sp.) from Roxas City, Capiz, Philippines	Romel A. Arrobang, Rossana Marie C. Amongo, Delfin C. Suministrado, Marisa J. Sobremisana
OS-V-2 15:50-16:05	Investigation of Optimum Geometry for Synthetic Jet Fan	Ryoichi Moriyama, Takeru Shinohara, Koichi Nishibe, Hiroshi Ohue, and Kotaro Sato
OS-V-3 16:05-16:15	[Li-doped C6 S8] cells for long-cycle-life Li-S batteries	Yusuke Ushioda, Kohei Inaba, Keitaro Takahashi, Yuki Ishino, Kazuki Machida, Hibiki Miyauchi, Tatsuya Kawamura, Masayoshi Watanabe, Shiro Seki,
OS-V-4 16:15-16:30	Development of sensitive ionization method for Sr isotopes imaging by R-SNMS	T. Yoshida, Y. Ohmori, Y. Miyashita, Y. Zhao, M. Morita, T. Sakamoto, K. Kato, V. Sonnenschein, H. Tomita, T. Kawai, T. Okumura, Y. Satou, M. Miyabe and I. Wakaida
OS-V-5 16:30-16:45	Study on Swirling Flow Produced by Annular Guide Vanes	Kotaro Yamanaka, Ryota Kobayashi, Koichi Nishibe, and Kotaro Sato
OS-V-6 16:45-17:00	Consideration of large capacity high voltage direct current transmission from photovoltaics in the desert area	Ryo Tabei
OS-V-7 17:00-17:15	Investigation of soundness evaluation method of electrode interface structure of all-solid-state battery using electrochemical simulation	Shodai Ban, Ayato Sakamoto, Kazuhiro Suga

Oral Presentation Session VI : Electrical Engineering and Materials L007, 15:35 ~ 17:15		
Paper no.	Paper title	Authors
OS-VI-1 15:35-15:50	Genetic algorithm and fuzzy multi-objective programming for optimizing maintenance policies of offshore wind systems	THI HUYNH ANH LE, THI KIM OANH LE
OS-VI-2 15:50-16:05	Relationship between aerodynamic characteristics of soccer balls and their panels	Yuki Sakamoto
OS-VI-3 16:05-16:15	Numerical Study on Fundamental Flow Characteristics of Excited Jets	Chisato Ichihara, Daiki Yamaguchi, Ryota Kobayashi, Koichi Nishibe, and Kotaro Sato
OS-VI-4 16:15-16:30	Dissociated ammonia as a sustainable energy source	Takashi Saika
OS-VI-5 16:30-16:45	Birefringent PET Transducers for Non-contact Liquid Concentration Measurements by Heterodyne Metrology	Ruey-Ching Twu*, Kai-Hsuan Li, and Bo-Lin Lin
OS-VI-6 16:45-17:00	Reinforcement of Epoxy Thermoset Composite Using Epoxidized Kraft Lignin from Sugarcane Bagasse	Rayman T. Almag, Myra G. Borines, Ronniel D. Manalo, Jerico Z. Alcantara and Jovita L. Movillon
OS-VI-7 17:00-17:15	Super-Hydrophilic Interface - Zwitterionic Structure Design for Multiple Application	Ying-Nien Chou

Oral Presentation
Session VII : Materials
L003, 15:35 ~ 17:15

Paper no.	Paper title	Authors
OS-VII-1 15:35-15:50	Optimization of Performance of a Sweet Sorghum Threshing Cylinder	Reynold M. Caoili, Delfin C. Suministrado, Rossana Marie C. Amongo, Arsenio N. Resurreccion, and Engelbert K. Peralta
OS-VII-2 15:50-16:05	Investigation on Deformation Behavior of Photomask Protective Film	Yu Ching Lee
OS-VII-3 16:05-16:15	Optical characteristics of high-In-incorporated GaInN MQWs grown by RF-MBE	Ryosuke Yoshida, Yusuke Nakajima, Hiroki Hirukawa, Soichiro Ohno, Tomohiro Yamaguchi, Takeyoshi Onuma, Tohru Honda
OS-VII-4 16:15-16:30	Preparation of cellulose nanocrystals and microfibrillated cellulose from bakong (Hanguana malayana (Jack) Merr.)	Glenn Christian P. Acaso, Veronica P. Migo, and Ramon A. Razal
OS-VII-5 16:30-16:45	Development of various techniques for aerosol analysis by TOF-SIMS	Masato Morita, Ryota Koiwai, Toru Murata, Tetsuo Sakamoto
OS-VII-6 16:45-17:00	Photoluminescence Au NDs — PNIPAM Hybrid Microspheres: Synthesis and Application as Hg ²⁺ Sensor	Wei-Yu Chen
OS-VII-7 17:00-17:15	Determination of Water Vapor Transmission Rate Using Nitrogen Encapsulated Calcium Sensor	Ching-Ming Hsu, Wen-Tuan Wu, Geng-Wei Zhou, and Yei-Hang Tsai

Poster Presentation

Poster Session (I), L008-Lobby, 14:30-15:30

Paper no.	Paper title	Authors
P-I-1	A Study of Japanese-text Compression and Punctuation Prediction with Natural Language Processing	Ryota Tominaga, and Hideoshi Saito
P-I-2	Root shape prediction from crown shape using machine learning	Yustaro iso
P- I-3	A Study of Modified Belief Propagation Decoding for Polar Codes	Naoya Takahashi , and Hideoshi Saito
P- I-4	Development of a Smart Device for V2X Driving Assistance	Zhao Li and Koyo Katsura,
P- I-5	Control of Multiple, Linked Air Conditioning Devices Using Deep Reinforcement Learning that Considers Both Power Saving and Comfort	Naotoshi Okuyama and Koyo Katsura
P- I-6	Applying IoT Technology in An Intelligent Guiding System for Blind People	Jiun-Yu Tu, Chia-Nian Shyi
P- I-7	Development of an Agricultural Automatic Spraying IoT System with Utilizing the Bluetooth Mesh Networking	Jeng-Han Li, Wei-Che Ho, Wei-Ting Wu, Ming-Jie Cheng, Yin-Fong Wang
P- I-8	Activation of chitinolytic activity of mouse acidic chitinase by sodium chloride	Shiori Takebe, Eri Tabata, Fumitaka Oyama l
P- I-9	The Strategy of Exopolysaccharide Production by Lactic Acid Bacteria	Yu-Xuan Zheng, Tux-Han Lin, Wei-Cheng Wang, Chia-Yu Lin, Po-Ting Chen
P- I-10	Examination of Cupulolithiasis Treatment Method by Using Vibration Response of Cupula to Detach Otoconial Mass	Kiyomasa Miura, Hirotoishi Hishida, and Koji Otsuka
P- I-11	Enhancement of the tumor cell migration on fibronectin by the metalloproteinase from <i>Ovophis okinavensis</i> snake venom	Yuna Saito, Yongchol Shin, and Yasutada Imamura
P- I-12	Inhibitory activity of sekothrixide on a drug efflux via P-glycoprotein	Ryoki Haruyama, Yongchol Shin, Yasutada Imamura
P- I-13	Analysis of the Factors Affecting the Implementation of Construction Quality Reports in Building Project through Case study of Danang City in Vietnam	Trung Quang Nguyen, Oanh Thi Kim Le, Chau Quynh Truong, and Pham Nguyen Ngan Hanh

P- I-14	Factors influencing the equipment cost estimation in the beginning stage building projects: case in Vietnam	Nguyen Thi Thao Nguyen, Oanh Thi Kim Le, Tuyet Phuoc Anh Mai
P- I-15	Developing the model for multiple-criteria decision-making for stakeholders in construction projects towards sustainable development	Ngoc Son Truong, Anh Duc Pham, and Le Thi Kim Oanh
P- I-16	Experiment on a Mass Change and Shrinkage of Concrete due to Carbonation	Masaru Oyama, Masaki Tamura, Michihiko Abe
P- I-17	An Embedded Real-time Monocular SLAM System Utilizing a Dynamically Reconfigurable Processor	Koki Kawashima and Koyo Katsura
P- I-18	Design and Achievement of a small Automatic Mapping Vehicle with a LiDAR Scanning Method	Sheng-He Wang, Yong-Qi Zhang, Kai-Cheng Hu Xu, and Chia-Pang Wei
P- I-19	The Study of Optical Phenomenon of a Rectangular Integrating Rod with a LED by Kaleidoscope Imaging Modelling and Experiment	Min-Yu Tsai, Zun-Xiong Ke, Jeng-Fneg Lin, and Chih-Chieh Kang
P- I-20	Applied to the intelligent ring pressure sensing system	Da-Hue Lee, Chia-Huang Lin, and Pi-Zhi Wang

Poster Session (II), L008-Lobby 15:30-16:30		
P-II-1	Use deep learning for polycrystalline solar panel defect detection	You-Teh Lin, Keh-Moh Lin, Harshad Dandage, Horng-Horng Lin
P-II-2	Control of Flow Instability in Axial-flow Fan with Upstream Obstacle Using Cross-partition Plate	Takeru Shinohara, Ryoichi Moriyama, Risa Yoshie, Koichi Nishibe, Hiroshi Ohue, and Kotaro Sato
P-II-3	Influence of Number of Partition Plates on Performance of Axial-flow Fan with Upstream Obstacle	Risa Yoshie, Takeru Shinohara, Ryouichi Moriyama, Koichi Nishibe, Hiroshi Ohue, Kotaro Sato
P-II-4	Numerical Investigation on Unsteady Characteristics of Vortex Tube	Shunsuke Kawamura, Ryoichi Moriyama, Takeru Shinohara, Koichi Nishibe, and Hiroshi Ohue
P-II-5	Study on improvement of water absorption effect in sipe of studless tire	Hiroto Uchiyama
P-II-6	Development of non-deteriorating lithium-sulfur battery	Kazuki Machida, Yusuke Ushioda, Tatsuya Kawamura, Hibiki Miyauchi, Kohei Inaba, Yuki Ishino, Keitaro Takahashi, Masayoshi Watanabe, and Shiro Seki
P-II-7	Design of Integrated Converter with Energy Multi-directional Transmissions for Photovoltaic Source Applications	Tsung-His Li, Yu-Hsiang Chen, and Te-Chun Hung
P-II-8	Development of the Residual Ammonia Removing System in Hydrogen Generation from Ammonia	Kana Hatori
P-II-9	Optical Characterization under Different Annealing Temperature by Sputter System Grow Ga ₂ O ₃ Film	Hon Kuan and Sheng-Hsiung Chang
P-II-10	GaAs-Based p-i-n Band-Pass Near-Infrared Photodetector Grown by Metal-Organic Chemical Vapor Deposition	Y. X. Xu, C. K. Wang, and Y. Z. Chiou
P-II-11	GaN-based Solar Devices featuring Mn-related	Kuan-Ting Chen, Feng-Wu Lin,

	Intermediate Band Absorption	Po-Cheng Chen, Jinn-Kong Sheu, and Ming-Lun Lee
P-II-12	LED miniaturization for monolithic μ -LED using ICP etching	Shoma Takeda, Tomohiro Yanaguchi, Takeyoshi Onuma, and Tohru Honda
P-II-13	Structural characterization of epitaxial GaInN films by X-ray diffraction	Hiroki Hirukawa, Ryosuke Yoshida, Tomohiro Yamaguchi, Takeyoshi Onuma, and Tohru Honda
P-II-14	Ultraviolet-Visible Absorption and Photocatalytic Properties of TiO ₂ Thin Film on Titanium Substrate via Ultrasonic Mechanical Coating Process	Jian-Yu Chen, Chin-Fu Chen, Chang-Ning Huang
P-II-15	Wettability of Sodium Halide Solutions on Hydrophobic Surfaces	Ibuki Shibagaki, Naoya Yoshida, Toshinori Okura
P-II-16	Microstructural analysis using TEM in GaInN film grown by RF-MBE	S. Ohno, H. Hirukawa, R. Yoshida, T. Yamaguchi, T. Kiguchi, H. Hashimoto, T. Onuma, T. Honda
P-II-17	Nano-micelles incorporated with quantum dots for anti-cancer drug therapy	Yiu-Juan Lin, Kun-Bau Huang, Yu-Chun Wu, Pragya Rani, Hong-Ru Lin
P-II-18	Proposal of sulfolane-based gel polymer electrolyte for Li-S batteries	Hibiki Miyauchi, Keitaro Takahashi, Yuki Ishino, Kohei Inaba, Yusuke Ushioda, Tatsuya Kawamura, Kazuki Machida, and Shiro Seki
P-II-19	Proposal and evaluation of physicochemical property for sodium conductive new solid electrolyte	Yuji Yokomaku, Koji Hiraoka, Masaki Kato, Kohei Inaba, Hibiki Miyauchi, Shiro Seki

Keynote Lecture

1. Collagen and NTH (non-triple helical collagen polypeptide)

Fibril forming collagens are produced by cells in the form of procollagens. The water-soluble molecules are exported to the outside of cells where they are processed to collagens. In the extracellular space, collagens form insoluble molecular aggregates which become solid-phase tissues. There is a graded structure model of tissues that focuses on collagen aggregates. The model is originally proposed by Adachi and Hayashi (1). There are thinner collagen fibrils just beneath the basement membrane. They are fused each other and gradually becoming thicker, resulting in a structure called connective tissue. The way to control diameter of collagen fibrils is thought to be differences in collagen composition. The basement membrane is formed mainly with type IV collagen which tends to form a two-dimensional meshwork structure. Collagen fibrils are made of fibril-forming collagens, mainly with type I collagen and partially with collagens of type III and type V. The ratio of type V collagen is higher at the vicinity of basement membrane. In the thick fibrils, type I collagen is predominant with less ratio of type II and/or V collagen. This idea is based on reconstitution experiments with purified collagens using each type alone or mixture of various types. Immuno-histochemical experiments also support the idea.

Prof. Imamura Yasutada



Vice President of Kogakuin University, Tokyo, Japan.

Prof. Dr. Imamura is the vice president of Kogakuin University of Technology & Engineering (KUTE-Tokyo) in charge of graduate school from 2018 and a full professor at the Department of Chemistry and Life Science, School of Advanced Engineering. He received his PhD in Science from the University of Tokyo, Japan, in 1989. From 1987 to 2005, he was an assistant professor in the department of chemistry, College of Arts and Sciences, The Tokyo University. From 2006 to 2007, he was an associate professor and from 2008 to 2014, a full professor in the Faculty of Engineering, KUTE-Tokyo. Since 2015, he has been a full professor in the School of Advanced Engineering.

Dr. Imamura's research interests center on biology related to collagen and include the biochemical analyses of extracellular matrix and the tissue regeneration using collagen materials and cells. He has published more than 50 original papers in international journals.

2. Title

Abstract

Prof. Arnold R. Elepaño



**Dean of College of Engineering and
Agro-Industrial Technology, University of the
Philippines Los Baños, Philippines.**

Oral Session

A Visual Image Generation Method Using Generative Adversarial Networks

Yu Tajima, Qiu Chen

Major of Electrical Engineering and Electronics, Kogakuin University, Japan
E-mail: cm19033@ns.kogakuin.ac.jp, chen@cc.kogakuin.ac.jp

Abstract

Designs such as posters of various products and movies are closely related to the need of attracting customers. In order to help designer's work to have stronger visual effects, we propose in this paper an image generation method using Generative Adversarial Networks (GANs). Specifically, a characteristic scene is firstly extracted from the video, and then filtered to determine the aesthetics of the image, and the object of interest in the image is enlarged and the brightness is adjusted. The aesthetics of the generated images are then numerically expressed and evaluated by MemNet, a deep learning algorithm that determines the "Memorability" of the images.

1. Introduction

Designs such as posters of various products and movies are greatly related to purchase motivation and attracting customers. In order to support the design with stronger visual effect, we propose in this paper an image generation method which is capable of attracting users by using Generative Adversarial Networks (GANs), one of the main image generation methods.

2. Proposed Method

The flowchart of the proposed method is shown as Fig. 1 below. Firstly, the characteristic scene (Key frame) is extracted from the input video sequence, and then filtered to determine the aesthetics of the image, and objects of interest in the image are enlarged and the brightness is adjusted. The aesthetics of the generated images are then numerically expressed and evaluated by MemNet, a deep learning algorithm that determines the "Memorability" of the images.

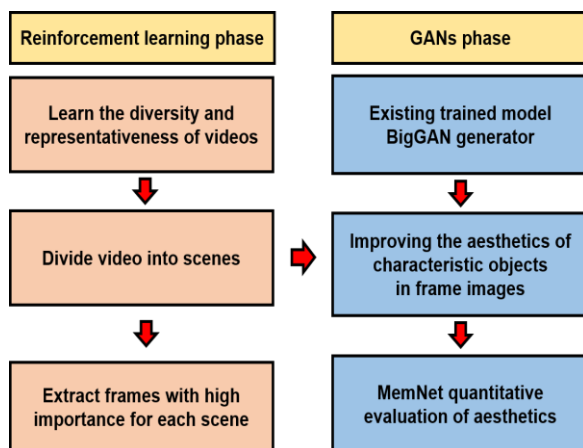


Fig. 1. Flow chart of the proposed method.

2.1. Deep Summarization Network

Reinforcement learning that gives video summaries diversity and representativeness as rewards. KTS^[1] (Segment video with Kernel Temporal Segmentation)

is used as a method for video summarization. An example of characteristic scene extraction is shown below as Fig.2.

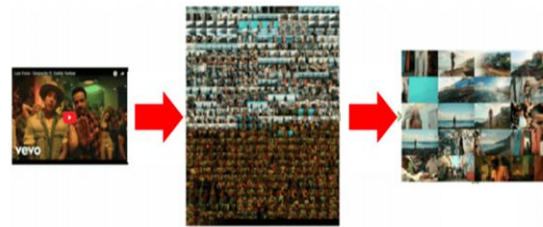


Fig. 2. The left is the original video, and the central are the frame images obtained by dividing the video sequence every 2 seconds, and the right are 20 images obtained by extracting characteristic scenes from the frame images.

2.2. GANalyze

By learning and optimizing what image operations are easy to memorize, you can change any image so that it is easy for humans to memorize. An image that is easy to remember can be "larger object, brighter image, rounded shape". It is made possible by creating a specific operation and learning the tendency. BigGAN^[2], an already learned model, is used as a generator, and MemNet, a type of CNN that can evaluate the ease of memory, is introduced as a score evaluator.^[3] An example of a GANalyze generated image and its score is shown in Fig.3.

2.3. BigGAN

BigGAN is proposed by DeepMind in 2018. It has succeeded in learning class-conditional image generation on a record-high scale using extremely complex data sets such as ImageNet. Fig. 4 is an example of the generated image.

3. Experimental Results

A characteristic scene is extracted from a video showing a 22-second zoo gorilla to enhance the aesthetics of the frame image. Fig.5 shows one

aesthetic score in the frame image.

4. Conclusion

In this paper, we have proposed a hostile generation network, which is suitable for visual image generation. As our future work, the accuracy of extracting characteristic scenes is less than 60% as F score. It is necessary to improve the accuracy of extracting more characteristic scenes. And, we will compare the aesthetics and the ease of memory between movie posters and music videos and the generation method of this study. Compare with other evaluation methods other than MemNet. Also, the generator used in GAN is changed to VQ-VAE2 and Progressive GAN for comparison.

- [1] K. Zhou, Y. Qiao, and T. Xiang, Deep Reinforcement Learning for Unsupervised Video Summarization with Diversity-Representativeness Reward, in *Proc. AAAI* (2018).
- [2] A. Brock, J. Donahue, K. Simonyan, Large Scale GAN Training for High Fidelity Natural Image Synthesis, in *Proc. ICLR* (2019).
- [3] L. Goetschalckx, A. Andonian, A. Oliva, and P. Isola, GANalyze: Toward Visual Definitions of Cognitive Image Properties, arXiv:1906.10112v1 (2019).

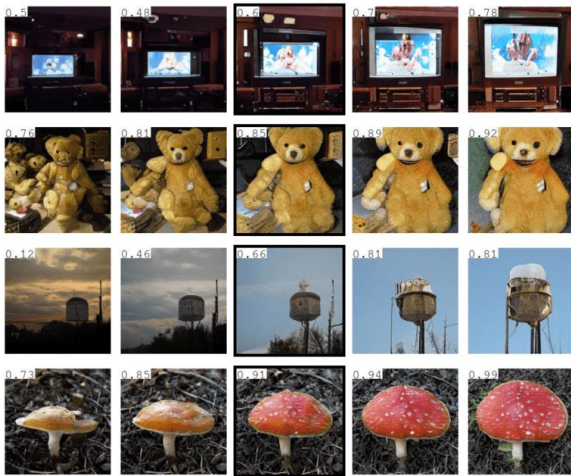


Fig. 3. An example of the aesthetic score of each image. The upper left value of each image is an aesthetic score (maximum is 1).



Fig. 4. Example of images generated from BigGAN

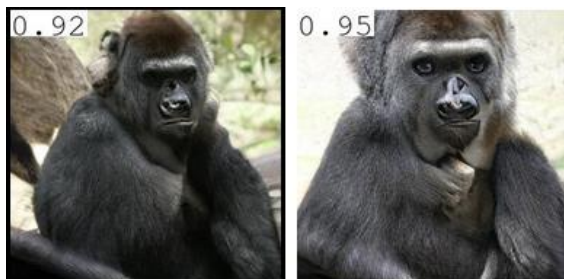


Fig. 5. The aesthetic score of each frame image. The value in the upper left of each frame image is the esthetic score to 1 as the maximum.

References:

Adversarial Knowledge Distillation Algorithm for a Compact Generator

Hideki Tsunashima^{1,2)}, Hirokatsu Kataoka²⁾, Junji Yamato³⁾, Shigeo Morishima⁴⁾, Qiu Chen¹⁾

¹⁾ Major of Electrical Engineering and Electronics, Kogakuin University, Japan
E-mail: cm18026@ns.kogakuin.ac.jp, chen@cc.kogakuin.ac.jp

²⁾ National Institute of Advanced Industrial Science and Technology, Japan
E-mail: hideki.tsunashima@aist.go.jp, hirokatsu.kataoka@aist.go.jp

³⁾ Major of Informatics, Kogakuin University, Japan
E-mail: yamato@cc.kogakuin.ac.jp

⁴⁾ Waseda Research Institute for Science and Engineering, Waseda University, Japan
E-mail: shigeo@waseda.jp

Abstract

The model size and training time of Generative Adversarial Nets (GANs) continue to increase (e.g. PGGAN takes two weeks with a single Tesla V100). To solve the above problems, we propose in this paper a novel method named Adversarial Knowledge Distillation (AKD) for GANs to reduce the amount of computation. AKD accomplishes the reduction of computation by adding adversarial training in which the knowledge-distillation-oriented discriminator judges a teacher or a student. There are no restrictions on network architecture of the teacher and student. Experimental results demonstrate that AKD is independent on the scale of datasets and network architectures by evaluating two network architectures on publicly available dataset, CIFAR-10.

1 Introduction

The generative models, including Generative Adversarial Nets (GANs) are active and flourishing in many research fields. According to recent studies, the generative model have realized the generation of high-fidelity image [1]. However, in contrast to performance improvements, the size matter is occurring in a limited computing resource.

In this paper, we propose the Adversarial Knowledge Distillation (AKD) for efficient generative model in terms of #model-layer (also parameters) and multiplication-addition (i.e. processing speed). Our proposed method can obtain approximate data distribution by reducing the model size and computational cost. Our AKD consists of KD discriminator to distillate a student generator from a teacher generator. The mechanism of AKD is contained in generative model, so can compress the student model and generates images close to the trained teacher model.

2 Method

In this section, we describe our training strategy for generative models with proposed AKD. Our proposed method named AKD enables to reduce the computational cost and model architecture (as well as parameters). Note that since we do not employ any discriminators in inference phase, the model size of discriminators based on distillation-D and normal-discriminator (in the following normal-D) is not considered. Normal-D affects the distribution in student generator so as to approximate the distribution

in the input dataset. Moreover, by using the distillation-D, it is expected that similar images will be output between generators in the teacher and student. Therefore, the student generator can approximate the distribution from the input dataset more similar to vanilla and MSE-based generators in terms of baseline and related methods by utilizing a teacher's support.

3 Experiments

In this section, we indicate AKD is effective in CIFAR-10 dataset and two architectures.

First, we qualitatively confirm the ability that AKD can approach a student generator to a teacher generator with 2D gaussian toy dataset.

In Fig. 2 at 2D Ring, the connections of the modes of the distribution acquired by the student are less in comparison with the ones of the vanilla model.

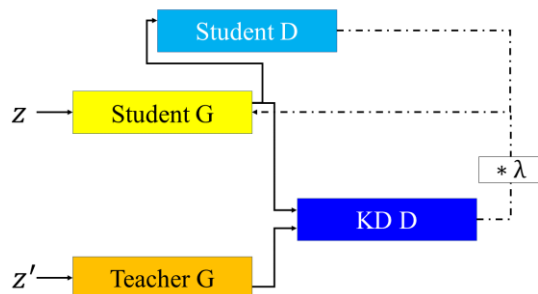


Fig. 1. Our proposed method named Adversarial Knowledge Distillation (AKD).

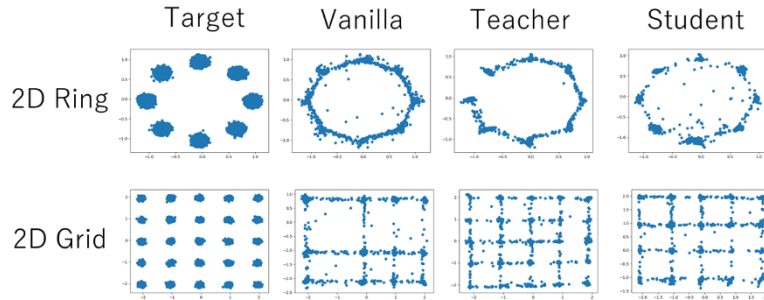


Fig. 2. We list well-known toy problems, 2D Ring and 2D Grid datasets. The results of ground truth (Target), baseline model with 3 layers MLP (Vanilla), teacher model with 4 layers MLP (Teacher) and our student model with AKD (Student).



Fig. 3. Qualitative evaluation on CIFAR-10. The results of teacher model with SNGAN (Teacher), baseline model with DCGAN (Vanilla), and our student model with AKD (Student). Images of AKD are more distinguishable than images of the Vanilla.

Table 1. In KD for generative model on CIFAR-10 dataset. We show qualitative comparisons among AKD-implemented methods and vanilla. The bold characters indicate the best results in compared methods, which is better if the score is similar to teacher model with SNGAN.

Methods	# layers	# params	# mult-add	IS \uparrow	FID \downarrow
Teacher (SNGAN)	8	4.1M	793M	8.49(\pm 0.13)	16.50
DCGAN vanilla	5	2.6M	229M	6.86(\pm 0.07)	31.58
DCGAN-AKD (ours)	5	2.6M	229M	7.05 (\pm 0.07)	29.52
MLP vanilla	4	2.2M	2.2M	4.66(\pm 0.02)	61.30
MLP-AKD (ours)	4	2.2M	2.2M	5.14 (\pm 0.05)	53.73

Note that although the generated points in the student model show less connections between modes than those of the teacher model, it still generates irrelevant points when compared to the real distribution. Therefore, the student model is not superior to the teacher model. Next, in 2D Grid the student acquires the distribution which doesn't miss modes in comparison to the vanilla. This result is intuitive because the student is trained with the assistance of the teacher which doesn't miss modes.

We evaluate AKD on CIFAR-10. The teacher employs SNGAN which has ResNet-8. The student employs 5 layers DCGAN and 4 layers MLP. Quantitative results were indicated in Tab. 1. In Tab. 1, AKD is effective in CIFAR-10 because AKD can improve inception score and FID of vanilla models. In Fig. 2, we indicate output images of the teacher, the vanilla models and the students. AKD is also effective perceptually because outputs images of the student are more distinguishable than the vanilla models.

4 Conclusion

We have proposed in this paper a novel method of computational cost and parameter reduction, called Adversarial Knowledge Distillation (AKD). Experimental results show that AKD is effective for CIFAR-10 dataset and several model architectures, which alleviates the trade-off between the reduction of computation and parameters, and the score of generative models. In addition, a student trained with AKD can generate more perceptually fidelity images than a vanilla model trained from scratch. In the future work, we plan to apply AKD to other generative models, domain adaptation tasks and high resolution datasets.

Reference

- [1] A. Brock, J. Donahue, and K. Simonyan, Largescale GAN training for high fidelity natural image synthesis, in *Proc. Int'l Conf. on Learning Representations* (2019).

Single Image Dehazing Algorithm Based on Unet and ResNet-like Structure

Li Ma¹⁾, Qiu Chen²⁾

1) 2) Major of Electrical Engineering and Electronics, Kogakuin University, Japan
E-mail: 1) cm18035@ns.kogakuin.ac.jp, 2) chen@cc.kogakuin.ac.jp

Abstract

Single image dehazing refers to removing the haze component in a blurred image without reference to other images. In this paper, we propose a trainable Unet-based method with ResNet-like structure (URN), which has skip connections between the encoder and part ResNet-like decoder. We adopt a pretrained VGG network as the encoder to exploit deep features. The experimental results show the effectiveness of group normalization for small mini-batch training, demonstrating that our proposed method can produce better dehazed output than physical-based method and other more complex neural networks.

1. Introduction

Images taken in the wild are often degraded by small dust particles or liquid droplets in the air, which deflect light. Image dehazing aims to recover the clear image from the hazy image, helping to reduce the impact of image degradation. In recent years, Convolutional Neural Networks (CNNs) has been frequently used to estimate components in the atmospheric scattering model for image dehazing [3][4].

The main contribution of this work is to design a novel trainable Unet-based method with ResNet-like structure (URN) for single image dehazing. This network adopts encoder-decoder architecture, in which we use pretrained VGG [5] as our encoder and a ResNet-like structure as decoder. We add the skip connection with group normalization between the encoder and decoder, and train the decoder with *logcosh loss* and *perceptual loss* [6]. Our method does not depend on the atmospheric scattering model and only exploits the deep network architecture and pre-trained models.

2. Related works

Because Unet [7] combines the encoder-decoder architecture with skip-connection between them, It shows better ability to solve localization and segmentation with few training datasets. This structure is used as the backbone in photo style Stylization [8] and image dehazing [9]. ResNet structure [10][12] has more layers, and shows better accuracy than VGG [5]. In case of small batch size, group norm [11] has lower classification error compared with batch norm.

3. Model

We are inspired by the Unet, which is used for biomedical image segmentation. In this section, we show our asymmetric Unet-like architecture, which uses pretrained VGG16 model as the encoder and more complex trainable ResNet-like CNN as the decoder. Moreover, we use skip connection with

group-norm between encoder and decoder blocks with the same output size (Fig.1).

Our total loss (4) is defined by combining *log-cosh loss* (1) and *perceptual loss* [6](2):

$$Loss_l = \frac{1}{N} \sum_{i=1}^N \log(\cosh(x_i)) \quad (1)$$

$$Loss_p = \sum_{j=1}^3 \frac{1}{C_j H_j W_j} \|\phi_j(j) - \phi_j(J)\|_2^2 \quad (2)$$

$$Loss_{total} = loss_l + \lambda Loss_p \quad (3)$$

Where x_i in (1) denote the differences between hazed images and ground truths. ϕ_j , $j = 1, 2, 3$, denote the Conv1_2, Conv2_2 and Conv3_3 in pretrained VGG16 network in (2), which uses same structure in encoder. And in (3), λ is a parameter for adjusting the relative weights of those two loss components.

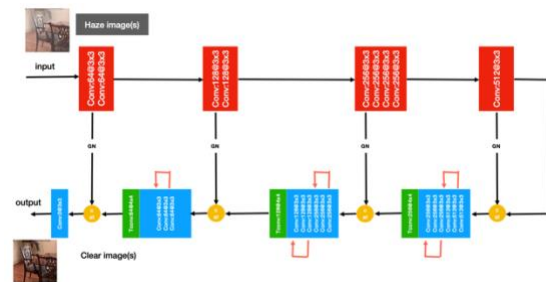


Fig.1. Architecture of URN, where the red block is the encoder part with convs and maxpool, while green blocks and blue blocks are the components of Decoder whom are transposeconvs and convs, respectively.

4. Experiments and Results

Since it is impractical to collect a large number of real-world hazy images and their haze-free counterparts, we adopt a large synthetic dataset,

named RESIDE [13], to train and test the proposed URN. RESIDE contains synthetic hazy images in both indoor and outdoor scenarios. The Indoor Training Set (ITS) of RESIDE contains a total of 13990 hazy indoor images, generated from 1399 clear images. For testing, the Synthetic Objective Testing Set (SOTS) is adopted, which consists of 500 indoor hazy images and 500 outdoor ones. We set 100 training epoch and $\lambda = 0.04$ same with [14]. Moreover, we use the dataset from [13] to get the result of utilizing trained model on real-world images (Fig.2). Table 1 shows the quantitative comparison on the SOTS in terms of average PSNR and SSIM values.

Table 1. PSNR and SSIM results on SOTS

Method	Indoor	
	PSNR	SSIM
DCP	16.61 _[14]	0.8546 _[14]
Dehaze_release	22.96	0.8224
AOD-Net	19.62	0.8374
MSCNN _[15]	17.57	0.8102
GridDehazeNet	32.16 _[14]	0.9836 _[14]
Ours	23.52	0.8914

5. Conclusion

We have proposed an end-to-end CNN, named URN, and demonstrated its performance for single image dehazing. Our network can be seen as an improvement of [9]. During our training, we find our model has a tendency to become overfitting within 100 epochs of avoiding the use of early stopping. Our work demonstrates that asymmetric encoder-decoder architecture, one with more complex decoder, has limited effect in improving dehaze task.



Fig. 2. dehazed images and primitive hazy images shown in the 1st and 2nd line, respectively.

References:

- [1] K. M. He, J. Sun, and X. Tang, Single image haze removal using dark channel prior, *IEEE TPAMI*, **33**(12), 2341-2353 (2011).
- [2] C. Chen, M. N Do, and J. Wang, Robust image and video dehazing with visual artifact suppression via gradient residual minimization, in *Proc. ECCV*, 576-591 (2016).
- [3] B. Cai, X. M. Xu, K. Jia, C. M. Qing, and D. C. Tao, Dehaznet: An end-to-end system for single image haze removal, *IEEE TIP*, **25**(11), 5187-5198 (2016).
- [4] W. Q. Ren, S. Liu, H. Zhang, J. S. Pan, X. C. Cao, and M. H. Yang, Single image dehazing via multi-scale convolutional neural networks, in *Proc. ECCV*, 154-169 (2016).
- [5] K. Simonyan, A. Zisserman, Very deep convolutional networks for large-scale image recognition, in *Proc. ICLR* (2015).
- [6] J. Johnson, A. Alahi, L. Fei-Fei, Perceptual losses for real-time style transfer and super-resolution, *arXiv: 1603.08155v1 [cs.CV]* (2016).
- [7] O. Ronneberger, P. Fischer, T. Brox, U-Net: convolutional networks for biomedical image segmentation. *arXiv:1505.04597v1* (2015).
- [8] Y. J. Li, M. Y. Liu, X. T. Li, M. H. Yang, J. Kautz. A closed-form solution to photorealistic image stylization. *arXiv: 1802.06474v5* (2018).
- [9] Z. Xu, X. T. Yang, X. Li, X. S. Sun. The effectiveness of instance normalization: a strong baseline for single image dehazing. *arXiv: 1805.03305v1* (2018).
- [10] K. M. He, X. Y. Zhang, S. Q. Ren, J. Sun, Deep residual learning for image recognition. *arXiv:1512.03385v1* (2015).
- [11] Y. X. Wu, K. Mi. Group normalization, *arXiv:1803.08494v3* (2018).
- [12] C. Szegedy, S. Ioffe, V. Vanhoucke, Inception-v4, Inception-ResNet and the impact of residual connections on learning. *arXiv: 1602.0761v2* (2016).
- [13] R. Fattal, Dehazing using color-lines, *ACM Transactions on Graphics*, **34**(1), 13 (2014).
- [14] X. H. Liu, Y. R. Ma, Z. H. Shi, J. Chen, GridDehazeNet: attention-based multi-scale network for image dehazing. *arXiv:1908.03245* (2019).
- [15] W. Ren, et al., Single image dehazing via multi-scale convolutional neural networks, in *Proc. ECCV*, 154-169 (2016).

An Advanced Generative Adversarial Networks Using Divided Z-vector

Taisei Hoshi, Hideki Tsunashima, Qiu Chen

Major of Electrical Engineering and Electronics, Kogakuin University, Japan
E-mail: cm18033@ns.kogakuin.ac.jp, cm18026@ns.kogakuin.ac.jp, chen@cc.kogakuin.ac.jp

Abstract

In our previous work, we have proposed an improved conditional GANs using divided z-vector (DzGAN), which is possible to control the intersection of generated image classes and reduce the computational amount. However, the flexibility to other datasets and network architectures is still a challenge. In this paper, we propose an advanced model of DzGAN, in which Residual Block and Spectral normalization are introduced to improve the quality of generated images. Moreover, we improve the adversarial loss by using hinge loss. The Advanced DzGAN is evaluated by the Inception Score on the Cifar 10 datasets, and experimental results demonstrate its better quality of generated images.

1. Introduction

Generative Adversarial Nets (GAN) [1] is one of the most novel approach for training generative models, which has achieved considerable success in generating real-valued data. Conditional Generative Adversarial Nets (cDCGAN) [2] is proposed as an extended model of Deep Convolutional Generative Adversarial Nets, which can carry out the conditioning by feeding some extra information into both the discriminator and the generator as additional input layer. The cDCGAN can generate desired images in accordance with the label by adding a label to input images in the discriminator and a z-vector in the generator. We propose DzGAN [3] as a model that improves the computational cost and inception score of cDCGAN. However, only the Mnist data set is used in the experiment, which is not convincing enough. In addition, DzGAN can be added to other network architectures to generate images desired by users, which has not been demonstrated yet.

In this paper, we perform experiments using DzGAN with additional datasets as well as an advanced model of DzGAN, in which a dataset of 32 x 32 Cifar 10 is added. The advanced DzGAN network architecture has been changed from infoGAN [4] to Spectral Normalization Generative Adversarial Networks (SNGAN) [5].

2. Proposed Method

Our main goal is to improve the flexibility of datasets and networks and the overall visual quality. Firstly, We first describe the adversarial loss of DzGAN and then discuss the improvement of the network architecture. Finally, the datasets is described.

GAN is composed of two kinds of adversarial models. Discriminator discriminates between a true image and a fake image generated by the generator. Generator tries to generating image to trick discriminator. In the Equation (1) when the discriminator is trained, $D(x)$ is minimized to raise discrimination and $D(G(z))$ is also minimized to fathom a fake image. Accordingly, a prior term is

minimized and a posterior term is maximized. When the generator is trained, $D(G(z))$ is maximized to want to mistake a fake image for a true image. Accordingly, a posterior term is minimized.

$$\min_G \max_D V(D, G) = \mathbf{E}_{x \sim P_{data}(x)} [\log D(x)] + \mathbf{E}_{z \sim P_z(z)} \left[\log \left(1 - D(G(z)) \right) \right] \quad (1)$$

cDCGAN is novel method that the generator can generate images desired by the user in accordance with label by feeding label into the generator and the discriminator input. In the equation (2) a point of difference from GAN is that cDCGAN employs conditional probability using label. Hence, cDCGAN can generate image desired by the user in accordance with label. But, when cDCGAN is trained, it must use black and white images as label. Accordingly, it increases computation amount.

$$\min_G \max_D V(D, G) = \mathbf{E}_{x \sim P_{data}(x)} [\log D(x|y)] + \mathbf{E}_{z \sim P_z(z)} \left[\log \left(1 - D(G(z|y)) \right) \right] \quad (2)$$

DzGAN generates images desired by the user in accordance with label by divided z-vector and feeding on one-hot vector as the label. In the equation (3) a part of log of a prior term of normal GAN objective is added conditional entropy $E(x|y)$ and a part of log of a posterior term is added conditional entropy $E(G(z_i)|y)$. “i” is a number of divided z-vector. In a prior term when the discriminator discriminates a true image, conditional probability $E(x|y)$ is loss which uses softmax cross entropy in 10 class values. In the case of a posterior term, conditional probability $E(G(z_i)|y)$ is loss which uses softmax cross entropy in several class values. DzGAN is trained to minimize these losses.

$$\min_{G,E} \max_D V(D, G, E) = \mathbf{E}_{x \sim P_{data}(x)} [\log D(x) \cdot E(x|y)] + \mathbf{E}_{z_i \sim P_{z_i}(z_i)} \left[\log \left\{ \left(1 - D(G(z_i)) \right) \cdot E(G(z_i)|y) \right\} \right] \quad (3)$$

The purpose of the experiment is to investigate whether DzGAN can generate images desired by users according to labels even in datasets other than mnist and can change to a high-performance network architecture. The network architecture uses the existing network architecture to verify the effectiveness of divided z-vector. SNGAN is used because the network structure is more complicated than InfoGAN and the generated image is clearer. Finally, Indicates the image that the user wants according to the label generated by advanced DzGAN using Cifar 10 and Mnist datasets.

3. Experimental Results

In this section, First, advanced DzGAN experiments are carried out in addition to the previous DzGAN experiments. Next, an experiment of image generation is carried out by increasing cifar10 datasets and conditioning DzGAN and Advanced DzGAN.

We train DzGAN used Mnist and Cifar10 dataset with label of one-hot vector. The last convolution layer of the discriminator is used for classification(e.g. In MNIST class numbers are 10). These 10-dim vectors(class numbers) are transform to $E(x|y)$ in the equation 3 by computing softmax cross entropy between 10-dim vectors and label “y”.

The generator generates hand written image of size of 32x32. prior “z” used input is 100-dim noises in accordance with gaussian distribution. Prior “z” (z range is -1~1) is divided to $z_1 \sim z_{10}$ (i.e. -1~-0.8, -0.8~-0.6, ..., 0.8~1) in MNIST dataset. Standard deviation of individual prior “ z_i ” is 0.1 because advanced DzGAN can’t generate image well in the case of that standard deviation is 0.1/2 and 0.1/3.

Table 1 shows comparative results of Inception Score (IS) among advanced DzGAN, DzGAN and cDCGAN using the Mnist, and the settings for cifar 10 are the same.

Table 1. Different model Inception Score(IS) using the Mnist dataset.

Model	IS in 32 images	IS in 320 images
Advanced DzGAN	2.6636448	2.7632058
DzGAN	2.5650206	2.6022177
cDCGAN	2.1210151	2.2031755

We experiment both 32 and 320 images of MNIST. Higher IS means good performance under IS criterion. IS of advanced DzGAN is constantly high in both 32 and 320 images of MINST, showing superior than DzGAN and cDCGAN.

Table 2 indicates comparative results of Inception Score (IS) between advanced DzGAN and DzGAN using the Cifar10.

Table 2. Different model inception score using the Cifar10 dataset.

Model	IS in 5000 images
Advanced DzGAN	5.0302824
DzGAN	5.263964

Fig. 1 shows the Mnist images generated by advanced DzGAN and desired by the user in accordance with the label. Those images (0~9) are generated in accordance with prior $z_1 \sim z_{10}$.

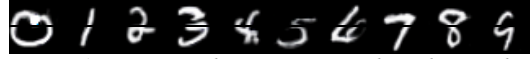


Fig. 1. Generated Mnist images by advanced DzGAN.

Fig. 2 shows the Cifar10 images generated by advanced DzGAN and desired by the user in accordance with the label. Those images (0~9) are generated in accordance with prior $z_1 \sim z_{10}$.



Fig. 2. Generated Cifar10 images by advanced DzGAN.

4. Conclusion

This paper demonstrates that DzGAN can learn from different network architectures and datasets.

Compared with previous approaches, IS value has been improved about 0.10 in 32 MNIST images and about 0.16 in 320 images. In the case of cifar 10, about 0.23 in 5000 images of MNIST has been decreased.

DzGAN is trained without changing previous architecture because we only divide z-vector and calculate softmax cross entropy between discriminated class and the label “y”.

References:

- [1] I. Goodfellow, et al., Generative adversarial nets, In *Proc. NIPS* (2014).
- [2] Q. Zhang, and Y. Liu, Improving brain computer interface performance by data augmentation with conditional deep convolutional generative adversarial networks, *arXiv:1806.07108v1* (2018).
- [3] H. Tsunashima, T. Hoshi, Q. Chen, DzGAN: Improved conditional generative adversarial nets using divided z-vector, In *Proc. ICCB* (2018).
- [4] T. Salimans et al., Improved techniques for training GANs, In *Proc. NIPS* (2016).
- [5] T. Miyato, T. Kataoka, M. Koyama, and Y. Yoshida, Spectral normalization for generative adversarial networks, In *Proc. ICLR* (2018).

Taste Estimation Method from Food Images Based on Deep Learning

Akinobu Yoshioka, Qiu Chen

Major of Electrical Engineering and Electronics, Kogakuin University, Japan
E-mail: cm19049@.kogakuin.ac.jp, chen@cc.kogakuin.ac.jp

Abstract

Since you cannot infer the taste of a dish just from the image of the food, it is difficult to find the food having your favorite taste from a large number of images. In this paper, we propose a method for estimating the taste of food images using deep learning, which combines a food image classifier that estimates cooking recipes from cooking images and a taste classifier that predicts tastes from cooking recipes. In addition, by estimating a recipe using a food image discriminator, it is considered that the taste estimation corresponding to the ingredients used in the same food can be performed. The taste discriminator uses word2vec to learn cooking recipes, by which the food names are associated with the tastes.

1. Introduction

In recent years, a large number of cooking images have been posted on SNS, etc., indicating that cooking is familiar to people in their lives.

However, it is difficult to find your favorite dish from a large number of images, because the taste of a food cannot be just guessed from the images of food. The purpose of this research is to develop a system to predict the taste of food from food images.

2. Proposed Method

In this research, we develop a system that can predict the taste of dishes from input cooking images. The dish name is inferred from the dish image by using a dish image discriminator, and then the taste is determined according to the dish name.

The taste of dish is estimated from the dish image, but it is impossible to estimate the taste corresponding to the dish of the same name with different ingredients.

In this study, we estimate the recipe and ingredients from the image of the dish. This paper proposes a method to estimate the taste corresponding to the ingredients contained in the dish of the same name.

Inverse Cooking [1] is used as the cooking recipe discriminator. The taste discriminator uses natural language processing word2vec [2], and builds a system by associating tastes with ingredients contained in the recipe. Figure 1 shows the flowchart of our taste estimation system.

2.1 Inverse Cooking

Inverse Cooking is a method of generate recipe from cooking image developed by A. Salvador et al [1].

Researches on traditional cooking images are related to the category classification of cooking. There is also research to guess the recipe, but it uses the similarity score of the image, and the model does not have generalization ability. In this research, a model for generating recipes is proposed, which makes it possible to accurately estimate ingredients

and recipes. This method is able to show superiority to each of the search approach and the result that made the human answer.

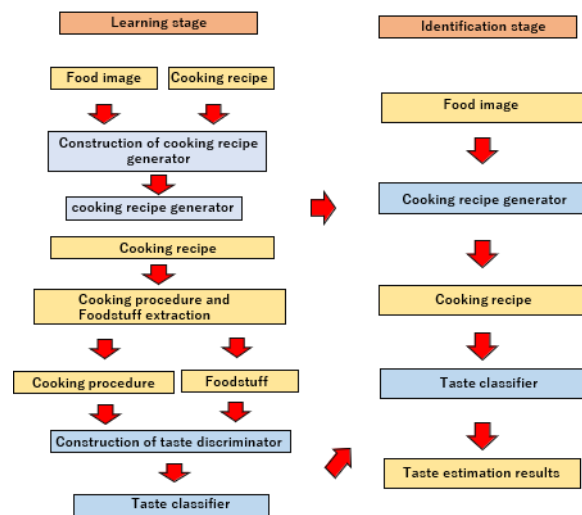


Fig. 1. Flowchart of proposed method.

2.2 word2vec

Word2vec is a method of vectorizing natural language using a neural network developed by T. Mikolov et al. [2]. The skip-gram model used in this experiment can obtain a word vector by estimating the output probability of words appearing around a sentence containing a word.

2.3 Evaluation method for taste estimation

The taste discriminator generates the word vectors of these five tastes and recipes and determines the cosine similarity of the word vectors of the recipes and flavors.

For the five tastes, we select sweet, sour, bitter, savory, and spicy of the taste sensed by stimulation or pain sensation such as capsaicin, because receptors exist in human taste buds.

3. Experimental Results

The Recipe1M data set is used as a data set for cooking images and cooking recipes. Inverse cooking [1] is used for the cooking recipe identifier, as well as Word2vec [2] for the taste discriminator. The parameters of word2vec are set to skip-gram model, with a window size of 10, mincount of 10, and vector dimension of 150.

When only the name of the dish is used as the taste identifier, the degree of cosine similarity between the dish and the taste is calculated, and the relationship between the dish name and the taste can be obtained. Table 1 shows cosine similarity of food name and taste obtained only using the food name.

Table 1. Cosine similarity of food name and taste obtained using only the food name.

Taste/food name	yogurt	stew	chocolate
spicy	0.0000	0.2302	0.0000
sweet	0.2472	0.0000	0.0000
sour	0.4246	0.0000	0.0000
bitter	0.0000	0.0000	0.0000
savory	0.0000	0.2619	0.0000

Input a dish name and output the cosine similarity of the taste associated with the dish, but because we only use one word corresponding to one taste for experiments, the cosine similarity between the dish name and the taste becomes very low. For example, the word “chocolate” has a high cosine similarity with “semisweet” and “bittersweet”, but “sweet” and “bitter” have a cosine similarity of 0, so it is output when there is no related taste.

The taste can also be estimated by setting a threshold for the obtained cosine similarity. For example, if a taste with a cosine similarity of 0.1000 or more is considered to be a taste of cooking, an estimation result can be obtained that "yogurt" contains sweetness and sourness.

4. Conclusion

In this paper, we have proposed a method to estimate the taste from food images using deep learning.

The cosine similarity is adopted to show the relationship between the dish name and the taste of the dish, which uses the word vector obtained by outputting the dish name from the dish image and letting word2vec learn the cooking recipe. By setting a threshold value for this cosine similarity, we can estimate the taste contained in a dish that exceeds the threshold value.

As a future issue, it is necessary to set appropriate cosine similarity thresholds to obtain results of taste estimation. It is also necessary to confirm the accuracy of the estimation results.

In this research, we use the word vector generated by word2vec as a vectorization technique of natural language for experiments, but it is also necessary to carry out an experiment using vectorization technique

of natural language. In addition, because there is only one word corresponding to one taste by increasing words corresponding to one taste, the cosine similarity of the taste output becomes 0 in spite of high cosine similarity between the taste and the close taste, which is a problem that needs to be solved.

References:

- [1] A. Salvador, M. Drozdal, X. Giro-i-Nieto, A. Romero, Inverse Cooking: Recipe Generation From Food Images, in Proc. *The IEEE Conference on Computer Vision and Pattern Recognition*, 10453–10462 (2019).
- [2] T. Milkov, K. Chen, G. Corrado, J. Dean, Efficient Estimation of Word Representations in Vector Space, *ICLR*, (2013).

Keyword Extraction Based on TF-IDF for TED Talks

Shu-Chen Cheng¹⁾, Guo-Zhi Gu²⁾

¹⁾ Department of Computer Science and Information Engineering, Southern Taiwan University of Science and Technology, Tainan, Taiwan
E-mail: kittyc@stust.edu.tw

²⁾ Department of Computer Science and Information Engineering, Southern Taiwan University of Science and Technology, Tainan, Taiwan
E-mail: ma7g0108@stust.edu.tw

Abstract

This is the era of information explosion. There is a lot of information on the Internet. People more and more used the Internet to self-learning, but they don't understand the field when they see the first time. So, people got the result of the keyword search was left unsatisfied. Therefore, this study constructs a system for articles classification, keyword extraction based on TF-IDF for content of TED talks. The system distinguish articles through the dictionary which one belongs to computer science. When the article classified as computer science, keywords will add to the dictionary. This system allow to continuously expand the keywords in the computer science category.

Keyword: TF-IDF, Data Mining, Keyword Extraction

INTRODUCTION

After the information revolution, the world came into the era of information explosion. More and more information is flooding the Internet. People learn new skills and knowledge through the Internet. However, people don't understand the field, so the results after the search are insufficient to satisfy the user. The system uses the established dictionary for the computer science category to retrieve a large amount of TED talks through web crawler. Then, the article will process by article classification and keyword extraction through artificial intelligence and keywords are obtained through TF-IDF to expand the existing dictionary.

METHOD

The system run a large number of searches in TED through web crawler with the existing dictionary. After collecting data, the data processed by remove stop words, word segmentation, and TF-IDF. Then, the system filter keywords with low TF-IDF. All keywords put TF-IDF in ascending order to select each of the article more important keywords. Then the system comparison important keywords to the dictionary, if there are most keywords in the dictionary, the system can confirm that the article belongs to the computer science category. At last, the system will add keywords into the dictionary if not exist in the dictionary.

$$TF-IDF(T_i, D_j) = TF(T_i, D_j) \times IDF(T_i) \quad (1)$$

$TF-IDF(T_i, D_j)$ = the weight of the calculation.
 T_i (=keyword) in the file. D_j (=the file in which the word is located).

$TF(T_i, D_j)$ = the frequency at which T_i appears in D_j .

$IDF(T_i) = \log\left(\frac{|D|}{|DF(T_i)|}\right)$ $|D|$ = the number of all files in the training set $DF(T_i)$ = the number of files containing T_i .

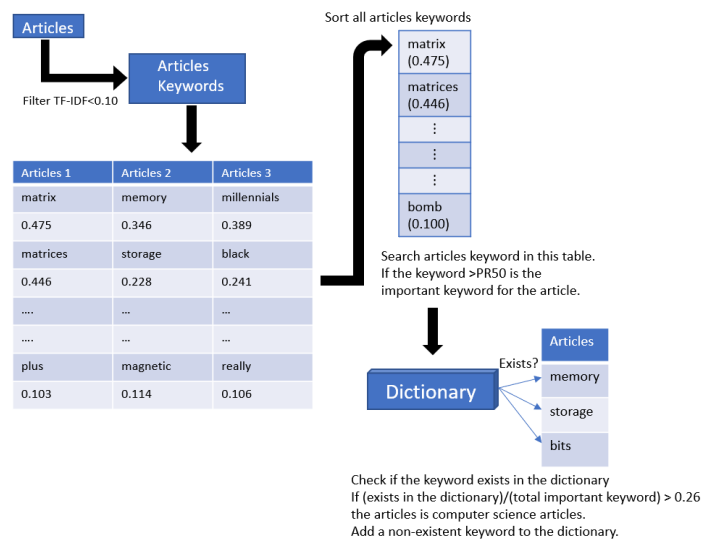


Fig1. Flowchart of keywords extraction and article classification.

Experimental Result

The system found 149 articles from TED about computer category. There are 2452 keywords about computer science in the dictionary. The system filtered 20 articles that meet requirements in these 149 test articles. The articles remove keywords of exist in the dictionary, there are 9 articles with computer science keywords, 9 without computer science keywords, and 2 articles with other keywords.

CONCLUSION

The purpose of this study is to provide a keyword expansion system. The system will slowly expand from a small dictionary into a large dictionary. The number of articles that can be crawled increases when the dictionary keyword is sufficient. Let the system to continuously perform keyword expansion.

References:

- [1] LAHIRI, S., MIHALCEA, R., & LAI, P. (2017). Keyword extraction from emails. *Natural Language Engineering*, 23(2), 295-317. doi:10.1017/S1351324916000231.
- [2] Christian, Hans & Agus, Mikhael & Suhartono, Derwin. (2016). Single Document Automatic Text Summarization using Term Frequency-Inverse Document Frequency (TF-IDF). *ComTech: Computer, Mathematics and Engineering Applications*. 7. 285. 10.21512/comtech.v7i4.3746.
- [3] E. I. Setiawan, A. J. Wicaksono, J. Santoso, Y. Kristian, S. Sumpeno and M. H. Purnomo, "N-Gram Keyword Retrieval on Association Rule Mining for Predicting Teenager Deviant Behavior from School Regulation," 2018 International Conference on Computer Engineering, Network and Intelligent Multimedia (CENIM), Surabaya, Indonesia, 2018, pp. 325-328. doi: 10.1109/CENIM.2018.8710892.

A Numerical Study on Intravascular Pressure Estimation with Convolutional Neural Network

Hikaru KOBAYASHI¹⁾, Kazuhiro SUGA²⁾

¹⁾ Department of Mechanical Engineering, Graduate School of Engineering, Kogakuin University, JAPAN
E-mail: am19019@ns.kogakuin.ac.jp

²⁾ Department of Mechanical Engineering, Faculty of Engineering, Kogakuin University, JAPAN
E-mail: ksuga@cc.kogakuin.ac.jp

Abstract

A prediction method using machine learning was proposed to predict the pressure distribution in the blood vessels in real time during medical treatment. A convolutional neural network (CNN) that predicts the velocity field was trained using sets of velocity and pressure distributions of a two-dimensional steady flow field obtained by computational fluid analysis. The effectiveness of the prediction method was examined by comparing the pressure field predicted by the CNN constructed from the input velocity field with the pressure field obtained by numerical analysis.

1. Introduction

Information of the pressure in the blood vessels during medical treatment can help you plan a safe and efficient medical treatment. However, it is difficult to directly measure the pressure distribution in the blood vessel. Numerical predictions cannot be applied to individual patients because of the high cost of geometry modeling and calculation time.

This study proposes a method for predicting pressure distribution in blood vessels by machine learning from velocity fields measured by MRI and so forth. This report focuses on to show the results of numerical experiments in order to evaluate the effectiveness of the prediction method.

2. Prediction of pressure field from velocity field

2.1 Preparation of machine learning dataset

Fluid analysis is performed by simulating various blood vessel shapes. Blood was assumed to flow 0.63 m/s from the left edge of the analysis area^[1]. The kinematic viscosity of the blood was 3×10^{-6} m²/s. The blood vessels wall is Rigid body. The model dimensions are 0.1m \times 0.03m. Fig. 1 shows an example of velocity and pressure distributions obtained by computational fluid analysis.

Analyze various blood vessel shapes to obtain velocity and pressure distributions. The resulting set of velocity and pressure fields is used as teacher data.

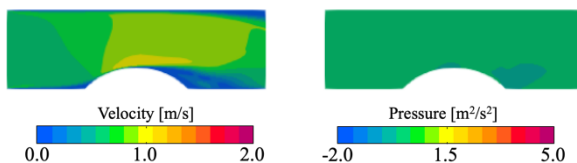


Fig. 1 Training data set.

2.2 Training neural network

The relationship between velocity and pressure field was learned using Pix2Pix^[2], a type of convolutional neural network (CNN). Distribution

data is an image with a resolution of 256×256 .

2.3 Prediction of pressure field

An unknown velocity field was input into the learned CNN and the pressure field was predicted. The effectiveness of the prediction method was examined by comparing the prediction results with the results obtained by numerical fluid analysis. Fig. 2 shows the comparison results. You can see that the prediction results can reproduce the analysis results.

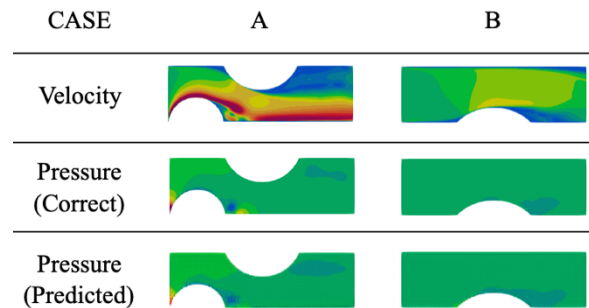


Fig. 2 Comparison between predicted and simulated pressures.

3. Conclusion

We proposed a method for predicting the pressure distribution in blood vessels by machine learning. The relationship between the velocity field and the pressure field obtained by numerical fluid analysis was learned with CNN. The effectiveness of the proposed method was confirmed by comparing the results of predicting the pressure field with the learned CNN and the results of numerical fluid analysis.

References:

- [1] Whitmore RL, Rheology of the Circulation. Pergamon Press, Oxford, 1968.
- [2] Phillip Isola, Jun-Yan Zhu, Tinghui Zhou, Alexei A. Efros, Image-to-Image Translation with Conditional Adversarial Networks, arXiv:1611.07004v1 [cs.CV] 21 Nov 2016.

Threshold Setting Method considering General calls with Waiting Queue under Emergency Trunk Reservation Control

Kenta KAWAI¹⁾, Katsunori YAMAOKA²⁾, and Ken-ichi BABA¹⁾

¹⁾ Major of Electrical Engineering and Electronics, Kogakuin University, Japan

E-mail: cm18015@ns.kogakuin.ac.jp, baba@cc.kogakuin.ac.jp

²⁾ Department of Information and Communications Engineering, Tokyo Institute of Technology, Japan

E-mail: yamaoka@ict.e.titech.ac.jp

Abstract

A huge number of calls are generated in an emergency situation such as an earthquake or a fire. In such a case, congestion of networks occurs and it is difficult for us to connect calls. As countermeasures against congestion, there are a trunk reservation control which accommodate emergency calls into a reserved part of whole capacity, and a call duration control which control call duration time of general calls. In previous works we proposed a trunk reservation control in which we add a waiting queue for general calls in order to reduce blocking probability of general calls. However the call blocking probability of general calls was yet high. In this study we proposed a mathematical analytic approach based on a queuing theory considering a waiting queue to achieve a proper threshold of the trunk. Through simulations, we showed that the proposed trunk reservation control with a waiting queue works effectively.

Introduction

In emergency situations, such as an earthquake or fire, a huge number of calls are generated to confirm the safety of those in the disaster area and to report emergencies in the afflicted area to the police, fire department, and so on. Figure 1 shows these calls cause phone congestion and it is difficult to accommodate all calls over a local telephone network. Thus, undamaged communication resources must be utilized more efficiently. In a telecommunication network, we classify calls as two types: emergency calls and general calls. Emergency calls are used by public institutions, such as the police, fire department, army, and news organizations. Emergency calls have a higher priority and can be accommodated without call admission control. Conversely, general calls are made by typical users for safety confirmation purposes. Certain network resources are preferentially allocated to emergency calls in a telephone exchange or SIP server, where general calls have lower priority than emergency calls. However, because safety confirmation via general calls is also important for individual users, we believe that as many general calls as possible should be accommodated, while still guaranteeing the necessary number of emergency calls. In order to do this, it is necessary to set the number of reserved lines appropriately. Reference [1] predicts the arrival emergency calls and general calls volume, and set the threshold. In Ref [2], general calls were treated as waiting calls, and the call blocking probability for general calls were reduced. But despite having a waiting queue, using the threshold setting in Ref [1].

In this paper, calculate a minimum threshold for accommodating emergency calls by mathematical analytic approach using the queuing theory of trunk reservation control in consideration of the waiting

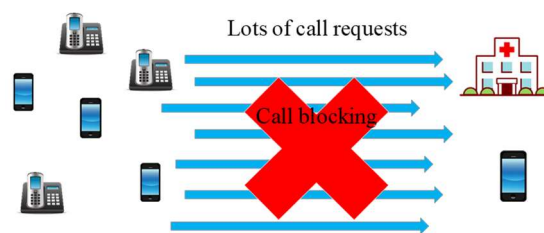


Fig. 1. Trunk congestion.

queue for general calls.

Proposed method

In this section, we assume that a telecommunication system (e.g., telephone exchange or SIP server) has a waiting queue for general calls. We model a telephone exchange as an $M/M/2/S/S, th+m$ queuing system that implements trunk reservation control and general call holding time control based on queuing theory.

1. The maximum accommodation capacity (number of lines) in the telephone exchange system is S .
2. The maximum number of stored calls in the waiting queue is m .
3. The arrivals of emergency calls and general calls follow Poisson distributions with averages of λ_e and λ_g .
4. The holding times of emergency calls and general calls follow an exponential distribution with an average of $1/\mu_e$ and deterministic distribution with a constant value h_g .

5. In trunk reservation control, when the number of lines in use is less or equal to a threshold th at the time of new call arrival, both call requests for emergency calls and general calls are accommodated. However, if the number of lines in use is above the threshold, only the call requests for emergency calls are accommodated and the call requests for general calls are stored in the waiting queue.
6. A general call request stored in the waiting queue is guaranteed to be accommodated by waiting until the arrival at the head of the queue.

When there is no vacancy in the waiting queue, an incoming general call is blocked.

The threshold th is obtained as follows according to Fig. 2.

1. The waiting queue m is always accommodated up to the maximum capacity.
2. Target only reserved lines, normalize only reserved lines. Calculate the state probability of a priority call.
3. The threshold is set so that the call blocking probability for emergency calls is less than P_e .

Performance evaluation

By numerical analysis, the state probability (call blocking probability) of the emergency call is calculated and set the threshold. The ratio of arrival emergency calls and arrival general calls is $\lambda_e:\lambda_g=3:97$ used in [1, 2]. The evaluation parameters are $S=100$, $\lambda_e=30$, $\lambda_g=970$ [calls / min], $1/\mu_e=60$ [sec], $m=10$, $h_g=10\text{--}120$ [sec], $P_e=0.01$. The total number of calls is 1000000. For comparison, the method in Ref. [2] for $m=0$ and 10 is used.

Figure 3 shows the relationship between hg and emergency call blocking probability, and Figure 4 shows the relationship between hg and general call blocking probability. From Fig. 3, it can be seen the call blocking probability Br_e of the emergency call in the proposed method is kept below the set call blocking probability. As shown in Fig. 4, when $hg=30$ [sec], $m=10$ the general call blocking probability is 80.8% in the conventional method and 74.7% in the proposed method, meaning the general blocking probability decreased by 6.1 percentage points. In this way, by setting as few reserved lines as possible through numerical calculations, the call blocking probability for general calls can be greatly reduced.

Conclusion

As a result, the threshold that can accommodate the minimum emergency call was obtained by numerical analysis using queuing theory in trunk reservation control considering the waiting time of general calls. In comparison with the existing method, the effectiveness of the threshold set by the proposed

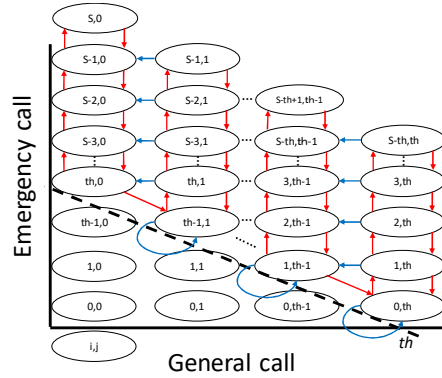


Fig. 2. State transition diagram considering waiting.

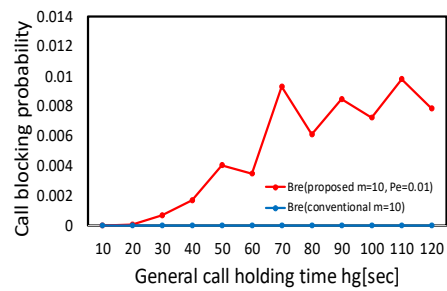


Fig. 3. Emergency call probability using proposed method ($m=10$, $P_e=0.01$).

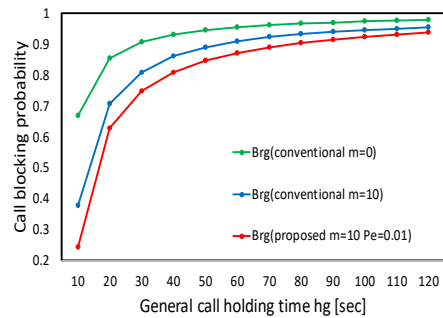


Fig. 4. General call blocking probability using proposed method ($m=10$, $P_e=0.01$).

method was clarified while keeping the call blocking probability in the emergency call below the required value.

References:

- [1] K. Tanabe, et. Al., "Threshold relaxation and holding time limitation method for accepting more general calls under emergency trunk reservation", *IEICE Trans Fundamentals*, pp. 1518–1528, August 2016.
- [2] K. Kawai, et. Al., "Emergency trunk reservation control using waiting queue for accommodating more general calls", Proc. of ICNC2019, pp. 287–291, February 2019.

Black Holes and Beyond, the Taylor Switch Method for Image Filtering

Timothy Ryan Taylor, Chun-Tang Chao, and Juing-Shian Chiou

Department of Electrical Engineering, Southern Taiwan University of Science and Technology, Taiwan

E-mail: sylmstim@gmail.com, tang@stust.edu.tw, and jschiou@mail.stust.edu.tw

Abstract:

This paper proposes the use of the Taylor Switch Method (TSM) image filter for the selected Spitzer Space Telescope image of M87. TSM can perform a high degree of flexible filtering options that can be readily applied to variety of imaging applications and at a relative inexpensive computational cost. One of the features explored in this paper is TSM's ability to reduce noise within a certain bandwidth/color of the image matrix.

TSM Constitutive Matrix Relationships:

In the trichromatic RGB color space, the probabilistic image space can be set up by using the following equation:

$$\psi_n = [0,1](\alpha_n \lambda' - \mu_m \lambda_n'),$$

where λ represents any general color channel. The variables α and μ are scalar multiples of the difference matrix, for this case $\alpha_n = \mu_m = 1$, and ψ_n is the possible image information relation for the compared color channels. In this TSM solution, $[0,1]$ shall represent the on or off state for the activated region of the image matrix.

$$R_n = A_1 R' - K_1 (+\psi_1 + \psi_2 + \psi_3 + \psi_4 + \psi_5 + \psi_6),$$

$$G_n = A_2 G' - K_2 (+\psi_1 + \psi_2 + \psi_3 + \psi_4 + \psi_5 + \psi_6),$$

$$B_n = A_3 B' - K_3 (+\psi_1 + \psi_2 + \psi_3 + \psi_4 + \psi_5 + \psi_6),$$

where A and K are scalar multiples of the generated image matrix, $R', G',$ and B' are the channel components of the original RGB image.

Method:

Using the aforementioned mathematical equations in Matlab, an algorithm was constructed to produce this new robust class of image filters. Table 1 shows the switching states for the generated images.

Table 1. Switch States for TSM.

	ψ_1	ψ_2	ψ_3	ψ_4	ψ_5	ψ_6
Rn	[0,1]	[0,0]	[0,0]	[0,0]	[0,0]	[0,1]
Gn	[0,1]	[0,0]	[0,0]	[0,0]	[0,0]	[0,1]
Bn	[0,1]	[0,0]	[0,0]	[0,0]	[0,0]	[0,1]

Source image courtesy of NASA/JPL-Caltech/IPAC was saved in high resolution TIF format. This image was taken by the Spitzer radio telescope and in the infrared region which lies outside of the visible spectrum^[1].

Table 2. Band Wavelength.

	Wavelength	Telescope
Infrared	3.6 μm	Spitzer IRAC
Infrared	4.5 μm	Spitzer IRAC
Infrared	8.0 μm	Spitzer IRAC

Therefore, the constructed image in the visible spectrum taken from the data in the Infrared region is a representation of what our eyes may approximate from the radio telemetry. Thus, it is a pseudo image and merely one interpretation of the representative data. The Event Horizon Telescope Collaboration team, used an array of radio telescopes in concert with machine learning to generate pseudo images of black hole M87's event horizon^[2]. Their task was to image an object that is so dense that light itself cannot overcome its sheer awesome power. An object that produces gravitational forces rips at the very heart of space and time. This idea of the black hole was born conceptually out of General Relativity^[3].

Results:

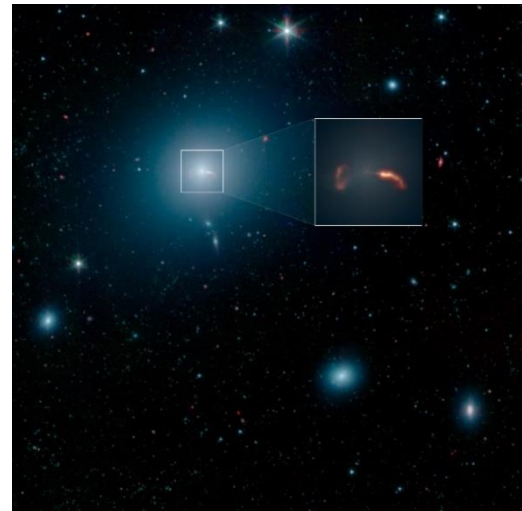


Fig. 1. Spitzer Messier 87 (Jets) Original. (Credit: NASA/JPL-Caltech/IPAC)



Fig. 2. Spitzer Messier 87 (Jets) TSM. (Credit: NASA/JPL-Caltech/IPAC; TSM Credit: Timothy Ryan Taylor)

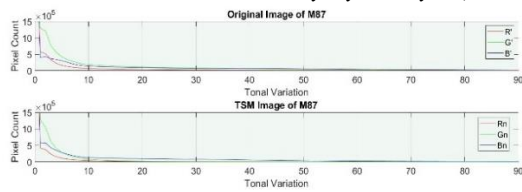


Fig. 3. Comparative Histograms of the color channels between the original and TSM images in Figure 1 and Figure 2.

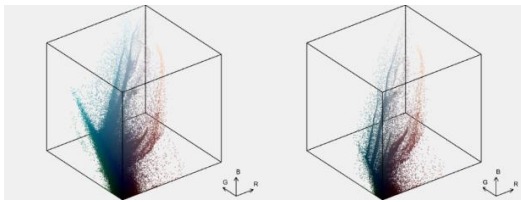


Fig. 4. Color cloud of the original image (left) and the TFM modified image (right).



Fig 5. Spitzer Messier 87 (Jets) original (left) and TSM image (right). (Credit: NASA/JPL-Caltech/IPAC; TSM Credit: Timothy Ryan Taylor)

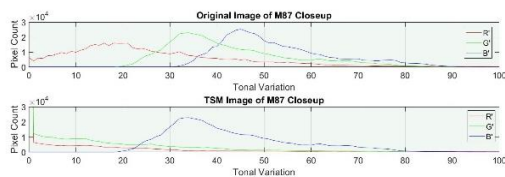


Fig. 6. Comparative Histograms of the color channels between the original and TSM images in Figure 5.

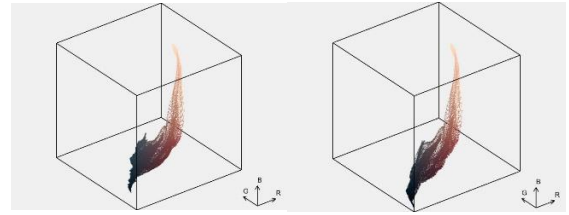


Fig. 7. Color cloud of the original image (left) and the TFM modified image (right) in Figure 5.

Conclusions:

The TSM method has the capability to shed light on previously unobserved astronomical phenomena. One solution and the resulting generated image shows a marked improvement in clarity of the image. The information from the decomposition that contains the glare was reduced to a great extent. However, portions of the images information were lost and transformed in the process. The result although impressive is only a stepping stone, and has been improved upon markedly. This will be addressed in a much more detailed follow up paper.

References:

- [1] NASA/JPL-Caltech/IPAC, <http://www.spitzer.caltech.edu/images/6592-ssc2019-05b-Spitzer-Captures-Messier-87-Jets-> (2019).
- [2] Kazunori Akiyama, Antxon Alberdi, Walter Alef, Keiichi Asada, Rebecca Azulay, Anne-Kathrin Baczko, David Ball, Mislav Baloković, John Barrett, The Event Horizon Telescope Collaboration. First M87 Event Horizon Telescope Results. I. The Shadow of the Supermassive Black Hole. *Astrophys. The Astrophysical Journal Letters*, **875**:L1 (2019).
- [3] A. Einstein, Sitzungsberichte der Königlich Preußischen Akademie der Wissenschaften (Berlin: Deutsche Akademie der Wissenschaften zu Berlin) (1917).

The Anomaly Diagnosis Mechanism for Service Function Chaining Integrity in NFV Environments

Jia-Shing Shih¹⁾, Sheng-Tzong Cheng²⁾, Chong-Yi Zhu²⁾, and Yu-Ming Chen³⁾

¹⁾Department of Electrical Engineering, Southern Taiwan University of Science and Technology, Taiwan

E-mail: jasonshih@stust.edu.tw

²⁾Department of Computer Science and Information Engineering, National Cheng-Kung University, Tainan, Taiwan.

E-mail: stcheng@mail.ncku.edu.tw

³⁾Testing and Network Communications Technology Division, Telecom Technology Center, Kaohsiung, Taiwan.

E-mail: ymchen@ttc.org.tw

Abstract

The emerging container technologies such as Docker can provide more agile service provisioning than virtual machines can in the cloud environments. Also, each network function tends to be deployed in the form of containers. The goal of this work is to diagnosis SFC integrity by the proposed module in a 5G cloud-native environment. If any anomaly is detected, the proposed module will report to NFV orchestrator and take action to deal with this anomaly. The proposed mechanism is evaluated on its performance such as the accuracy of our ELM model.

The Age of the wireless network already advances to the fifth generation (5G) era. The 5G network puts emphasis on the increment of capacity, faster data rate, the decrease of latency and improved quality of service for bringing more intelligence into the network.

Software-defined networking (SDN) and network function virtualization (NFV) both are very important technologies for evolving 5G network. SDN helps decouple the control logic from the data plane; this makes network management easier due to avoiding individual configurations for each networking device [1]. With these technologies, a number of scenarios can be implemented in the 5G network. For example, networking slicing can be realized in a 5G network [2]. The services provided by clouds can be formed by service function chaining (SFC). SFC, in short, is an ordered list consisting of several service functions so as to process traffic flows. The VNFs of an SFC are deployed in the form of virtual runtimes such as virtual machines and are probably placed in devices at geographically different locations. Although SDN and NFV can help the SFC deployment faster as mentioned in [3], there are issues needed to be solved such as providing better performance and optimal resource utilization in function deployment.

The SFC architectural concepts and principles are the main points in this publication. SFCs define that an ordered set of service functions (SFs) representing logical elements serve received packets and how the traffic is steered by constraints. The mapping of SFC concepts in IETF RFC 7665 and ETSI NFV constructs can be found in ETSI Network Service Templates Specification [4]. An SF is equivalent to the deployment of one or more VNFs. Moreover, multiple SFs can be deployed in one VNF as long as an external connection point provides access to this

SF within the VNF. SFC mapping concept can be referred to Network Service Templates Specification [4].

We training our analyzer in our mechanism by using Extreme learning machine (ELM). ELM proposed by Huang et al. [5] is a learning algorithm that is based on single-hidden layer feedforward neural networks (SLFNs).

In order to check the SFC integrity, a framework which is shown as Figure 2 is proposed, and it is named Service Path Checker (SPC) module. The proposed framework here is based on the SIM framework from [6]. Our proposed framework is modified from the SIM framework so as to fit this work.

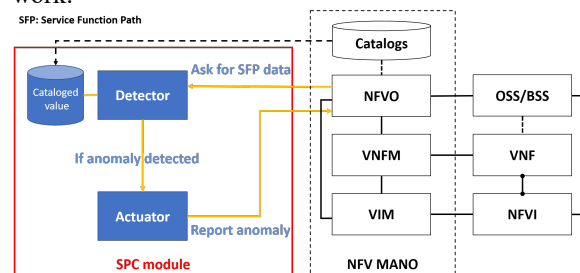


Fig. 2. The proposed framework: SPC module

There are two primary components in SPC module. They are submodule *Detector* and submodule *Actuator* respectively. The core of submodule *Detector* is to make a judgment if the Service Function Path (SFP) is corrupted, that is, to detect whether an anomaly exists in a certain SFC or not. The submodule *Actuator* is mainly responsible for reporting detected anomalies and deciding what corresponding actions should be taken in order to handle those anomalies. The workflow of submodule *Actuator* is as follows. Once *Actuator* receives the alert of anomaly from *Detector*, it will confirm what

kind of anomaly is detected. And then it reports to NFVO and asks NFVO to take corresponding actions to mitigate the harm. The rest of components are secondary parts. There is only one secondary component, the storage Cataloged value. It is for storing the NSDs which already exist.

In Figure 3 shows the diagram of the mechanism of anomaly detection in *Detector*.

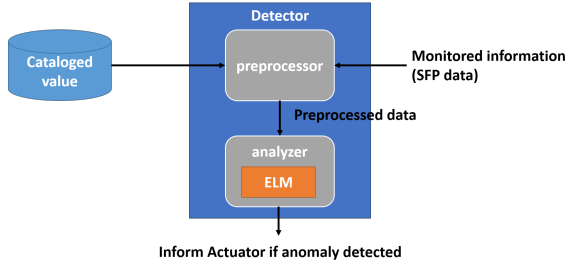


Fig. 3. The mechanism of anomaly detection

Detector has two ways to be triggered for detecting anomalies. But first of all, the predefined NS catalogs need to be backed up into storage (Cataloged value). It can be designed as either event-driven or polling. The event-driven way means NFVO will notify *Detector* to do the job of detection. The polling way, on the other hand, means *Detector* will check the monitored information at regular intervals. The core of *analyzer* is the ELM model which is used as judging whether the monitored SFC is normal or not.

We choose OpenStack Tacker as our NFV orchestrator and use devstack [7] to build up our environment for experiments, though there are many choices such as OPNFV installers (e.g., Apex and Fuel [8]) to help construct the NFV platform. The reason why we choose OpenStack Tacker is that Tacker has integrated with Kubernetes which can be used as VIM.

TABLE 1
THE ACCURACY W.R.T. DIFFERENT ACTIVATION FUNCTIONS AND NUMBER OF NEURONS

activation function	number of neurons				
	4	7	10	12	15
<i>sigm</i>	69.71%	85.68%	93.03%	96.14%	99.12%
<i>tanh</i>	68.53%	81.36%	89.56%	94.31%	99.14%
<i>RBF</i>	59.18%	68.99%	78.19%	83.92%	92.39%

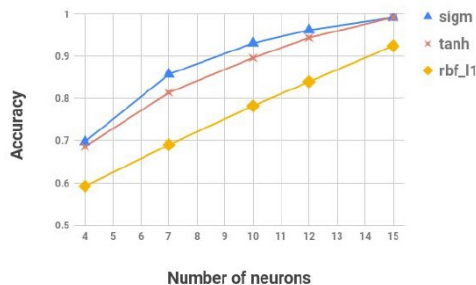


Fig. 4. The accuracy w.r.t. different activation functions and number of neurons

we show how accurate is our ELM model to do the prediction regarding the class of SFC integrity. The dataset we use to do experiment has 650 service chains in total. We divide the dataset into two subsets,

training set and test set. The number of service chains in test set is 20% of the number of service chains in the dataset. Therefore, the training set has 520 samples and the test set has 130 samples. We use 10-fold cross validation to validate our ELM model. After validation, we then use test set to verify the accuracy of our model. Once the number of neurons is determined, we train our model for 500 times with a specific activation function. The accuracy for a determined number of neurons and a specific activation function is the average of 500 results. The results are shown in Table 1. Figure 4 gives an intuitive way to compare the accuracy among those three activation functions.

References:

- [1] W. Stallings, S. Jelassi, and F. Agboma, "Foundations of modern networking: Sdn, nfv, qoe, iot, and cloud," 2016.
- [2] J. Ordonez-Lucena, P. Ameigeiras, D. Lopez, J. J. Ramos-Munoz, J. Lorca, and J. Folgueira, "Network slicing for 5g with sdn/nfv: Concepts, architectures, and challenges," *IEEE Communications Magazine*, vol. 55, no. 5, pp. 80–87, 2017.
- [3] M. S. Bonfim, K. L. Dias, and S. F. Fernandes, "In- tegrated nfv/sdn architectures: A systematic literature review," *ACM Computing Surveys (CSUR)*, vol. 51, no. 6, p. 114, 2019.
- [4] "Network functions virtualisation (nfv) release 2;management and orchestration; network service templates specification," 2018, https://www.etsi.org/deliver/etsi_gs/nfv-ifa/001099/014/02.05.01_60/gs_nfv-ifa014v020501p.pdf.
- [5] G.-B. Huang, Q.-Y. Zhu, and C.-K. Siew, "Extreme learn- ing machine: theory and applications," *Neurocomputing*, vol. 70, no. 1-3, pp. 489–501, 2006.
- [6] L. Bondan, T. Wauters, B. Volckaert, F. De Turck, and L. Z. Granville, "Anomaly detection framework for sfc integrity in nfv environments," in *2017 IEEE Conference on Network Softwarization (NetSoft)*. IEEE, 2017, pp. 1–5.
- [7] OpenStack, "Openstack docs: Install via devstack," 2019, <https://docs.openstack.org/tacker/latest/install/devstack.html>.
- [8] OPNFV, "Downloads - opnfv," 2019,<https://www.opnfv.org/software/downloads>.

A Bus Notifying System – A Proof of Concept

Chia-Nian Shyi¹⁾, Jiun-Yu Tu²⁾, Jia-Xiang Zhao³⁾, Guo-Shun Hong⁴⁾, and Cong-Xun Yan⁵⁾

Department of Computer Science and Information Engineering, Southern Taiwan University of Science and Technology, Taiwan

¹⁾E-mail: shyi@stust.edu.tw

²⁾E-mail: duketu@stust.edu.tw

³⁾E-mail: 4a5g0004@stust.edu.tw

⁴⁾E-mail: 4a5g0035@stust.edu.tw

⁵⁾E-mail: 4a5g0037@stust.edu.tw

Abstract

A mass transit system is one of the most important infrastructures to a modern metropolitan. With a mature and well-developed mass transit system, a metropolitan provides residents with an efficient moving way in their daily live. A mass transit system may be composed of a bus transit sub-system, a mass rapid transit sub-system, and etc. As being a basic component of a mass transit system, a bus transit sub-system plays an important role on commuting. However, by the classic method of calling bus, many issues need to be resolved. In this work, a novel bus calling system is designed. The proposed novel bus calling system invokes the internet of things technology for exactly stopping a bus whenever passengers are waiting for. The proposed novel system deals with a problem that, for some reasons, a bus driver may ignore a sign for calling the bus to stop and to pick up passengers from a bus station.

The prevalence of mass transit systems makes people move more conveniently. A mature and well-developed mass transit system can be composed of a bus sub-system, a mass rapid transit sub-system, and etc. However, there are still some issues to be resolved for making mass transit systems better. For a bus transit sub-system as an example, a bus driver may ignore a sign for stopping the bus.^[1,2]

Traditionally, passengers at a bus station stop a bus by waving their arms when they want to take the coming bus. A bus station is inevitable built for stopping buses routing to many different destinations. When passengers wave their arms to sign to a bus driver for stopping a specific bus, the bus driver maybe ignore or miss the sign because a.) other vehicles obstruct the driver's view of the passengers. b.) many buses routing to different destinations arrive to a bus station at the same time, so the bus drivers misunderstand the signs. c.) passengers wave their arms lightly, so the sign to a driver is not obvious, and etc. Sometimes, for stopping a specific bus, passengers even need to run inside a traffic lane to sign a bus driver for stopping the bus. To avoid these situations that cause bus drivers to ignore or misunderstand stopping signs generated by passengers, this work invokes the technology of Internet of Things (IoT)^[3] to improve the way that passengers stop a bus.

In our design, each bus stations would equip stopping buttons in the way of one route one button. The designed mechanism is described as following:

- a. When a passenger wants to take a bus, he/she need only press on the button which is

mapped to the specific route that he/she wants to go.

- b. Once a passenger presses on a button at a bus station where he/she is standing for a bus, the bus station would deliver the request to a server locating at cloud through a network connection.
- c. The server recognizes where the request came from, figures out the next arrival bus on the desired route through information of the Global Positioning System (GPS), and requests a status changing instruction to the chosen bus.
- d. The information board notifies the bus driver about a "stopping needed" message to let him/her know that on which bus station there are passengers want to take the bus, and he/she should stop the driving bus to pick up the passengers.
- e. The status of the information board stays on the status of "stopping needed" until the bus arrives the specific bus station, and switch on doors on the bus to pick up the desired passengers.
- f. When a button has been pressed, further pression would not change the status of the information board.
- g. If passengers want to cancel the request to the bus, they need only have a long pression on the corresponding button for 5 seconds.

Figure 1 is the flow chart to illustrate our proposed mechanism.

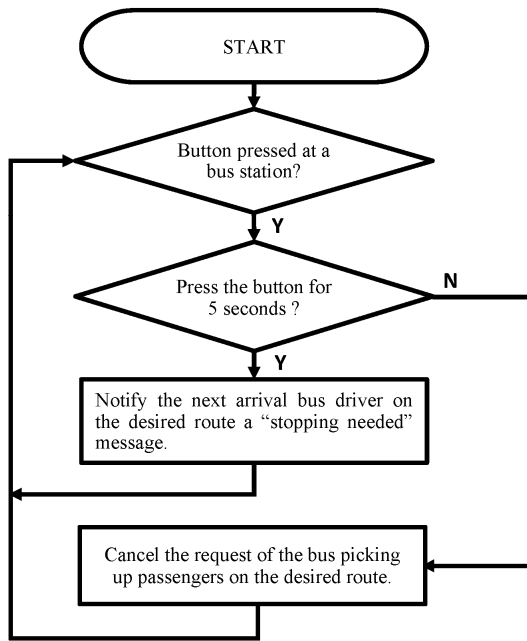


Fig. 1. The flow chart to illustrate our proposed mechanism of the bus notifying system.

References:

- [1] <https://www.ithome.com.tw/news/96948>
- [2] <https://www.peopo.org/news/292573>
- [3] Internet of things - Wikipedia, https://en.wikipedia.org/wiki/Internet_of_things

Surface acoustic wave sensor for outdoor pollution air sensing

Yu-Jen Hsiao

Department of Mechanical Engineering, Southern Taiwan University of Science and Technology, Taiwan

E-mail: yujen@stust.edu.tw

Abstract

Currently, in current research SAW gas sensor with an interdigitated electrode of 20 μm width is combined with doping ZnO nanostructures of four different thicknesses, 50nm, 75nm, 100nm, 125nm at room temperature in order to find out the best manufacture conditions and to achieve the highest detecting sensibility. Since the detecting thin film has good absorption performance, the expected detection range of ammonia concentration is 0.01 ~ 20 ppm. This SAW gas sensor has excellent properties such as recoverability and selectivity. It is also applicable to low gas concentration, and thus can be used in many chemical industry, food process industry, and medical diagnoses. This study intends to enable a wide application of this SAW gas sensor in daily life situations.

Acoustic wave resonator is an important passive electronic component, which can be applied to wave filters and detectors. Currently, the SAW RF wave filters which is composed of SAW resonator accounts for the largest market share for wave filters on cell phones. Due to its small size, SAW filters can be mass-produced with semiconductor technology [1-2]. It is not only low-cost, but also has the advantages of low damages and good filtering effects. The applicable frequency range of SAW devices is 10M-2GHz. To develop SAW devices with high working frequency and high working power, lithography with high resolution and short gate length as well as substrate materials with high SAW speed are used to enhance the working frequency. In this project we intend to develop an air detecting module for industrial area by using SAW gas sensors (see Fig. 1) to detect the gas concentrations in the air and to conduct in-time calculation according to the air quality index by the EPA so that the problem of over-released waste from chemical factories, semiconductor factories, PCB industry, as well as recycling industry can be effectively monitored and controlled. This SAW gas sensor has four features: 1) high sensitivity: the self-developed sensor can precisely detect the air quality pollution index at monitored places; 2) in-time: when the air quality index of the monitored places reaches pollution standards, APP will automatically twitter this warning message immediately so that the neighborhood can take immediate precautions; 3) cloud data: the all-day-round air monitoring data will be saved in cloud so that we can know the air quality of the factory at any time and any distance. 4) data analyzable: historical monitoring data can be searched out at any time and the possible changing trend of air quality can be calculated by way of the AQI big data analysis platform.

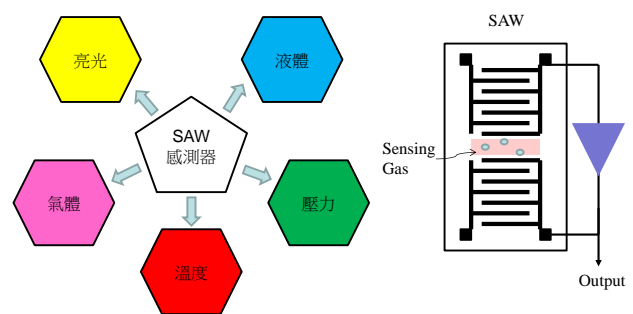


Fig. 1. Applications of the SAW gas sensors

References:

- [1] V. Bhasker Raj, A.T. Nimal, Y. Parmar, M.U. Sharma, K. Sreenivas, V. Gupat, Cross-sensitivity and selectivity studies on ZnO surface acoustic wave ammonia sensor, *Sens. Actuators B* 147 517–524 (2010).
- [2] Y.-T. Shen, C.-L. Huang, R. Chen, L. Wu, A novel SH-SAW sensor system, *Sens. Actuators B* 107 283–290 (2005).

Power and Energy Optimization Strategies of a Wireless Sensor Network (WSN) for 2D Spatio Temporal Temperature Profiling in Marine Environments

Diogenes Armando D. Pascua^{1,2}, and Michael Lochinvar S. Abundo³

¹School of Engineering, Doctor of Engineering, University of San Carlos -Technological Center, Cebu, Philippines

²College of Engineering and Architecture, University of Science and Technology of Southern Philippines, E-mail: diogpascua@gmail.com

³Programme Integration Manager Rolls-Royce@NTU Corporate Lab, Nanyang Technological University, Singapore
E-mail: abundo@ieee.org

Abstract

Energy consumption is one of the biggest constraints of the wireless sensor nodes deployed in marine environment. They are typically used for remote environment monitoring in areas where providing electrical power is difficult. Therefore, the devices need to be powered by batteries and alternative energy sources. Because battery energy is limited, the use of different techniques for energy saving is one of the hottest topics in Wireless Sensor Networks(WSNs.) Various battery optimization schemes have been developed both through hardware and software techniques. The ubiquity of Wireless Fidelity(Wi-Fi) based networks makes for a popular choice for establishing Wi-Fi based sensor networks but the relatively high-power requirements of these systems conflict with the requirement for long battery life and low maintenance. This work considers whether it is possible to reduce Wi-Fi power usage to the point where cheap Wi-Fi based products can be used instead of other protocols. The setup is composed of a wireless sensor which is based on the low cost esp8266 module tasked to gather temperature data in a marine protected area. Energy consumption was analyzed for the nodes at various states along the device firmware as well as the relationship between energy consumption against the rate of sensor data of transmission and system sleep period. The study also compares the energy usage of two network implementation: Message Que Telemetry Transport(MQTT) against Server-Client based system. Test results reveal that the sensor nodes can have a maximum battery life of 15.8 hours for both transmission methods, regardless of transmission rates, if no sleep period is implemented. Transmission rate have a profound effect on the systems battery life if sleep mode is implemented. It was found that battery life can increase up to 43 times for a transmission period of one hour and up to 40 times for a transmission period of one minute. An optimized WSN configuration utilizing MQTT transmission scheme proved to extend battery life more than that of the Server-Client scheme by up to 34 percent. From these analyses, the design of an optimal firmware and choice of network architecture can be derived where battery life can be extended in the longest possible time.

A Software Defined Radio Design Flow for FSK Modulation and Demodulation and Its Implementation Using GNU Radio

Yun-Tai Hsueh¹⁾

¹⁾Department of Electronic Engineering, Southern Taiwan University of Science and Technology, Taiwan
E-mail: ythsueh@stust.edu.tw

Abstract

Software Defined Radio (SDR) has been a popular subject in wireless communication recently. A versatile tool for SDR design projects, called GNU Radio, is very helpful for the designers/engineers to complete their works. But designing a frequency shift keying (FSK) modulation and demodulation (modem) using GNU radio is not an easy job. Hereby, we propose a feasible design flow for an FSK modem using GNU radio. The design flow for FSK modulation is simpler and has two steps: firstly, data is serialized to numbered symbols which can be single or multiple bits like 2-bit or 4-bit etc.; secondly, the carrier frequency is modulated by symbols using a GNU radio custom function block called "FSK Mod" which uses VCO to translate the frequency modulated signal to in-phase signal and quadrature signal and the resulting signal is transmitted. The design flow for FSK demodulation is a bit complicated and described as follows. Firstly, the received signal is filtered by a low pass filter to eliminate any unwanted high frequency signals. And then the filtered signal is demodulated by a custom function block "FSK Demod" which converts in-phase and quadrature signals to symbol information. The results of this step are still noisy and required further filtering. Besides, a clock recovery scheme is also necessary. For clock recovery scheme, we need to estimate the symbol time by using a custom function block "Clock Recovery" which uses some parameters obtained by examining input signal waveform of this block. Finally, the clock recovered signal has to be de-serialized to form the original data and therefore the demodulation flow is finished. At last, the aforementioned process of FSK modem is implemented and verified using USRP B200 SDR developing board which has 56MHz data sampling rate and 70M-6GHz RF coverage. This FSK modem can be applied to a reconfigurable audio walkie-talkie or wireless data transfer.

Key words: SDR, GNU radio, FSK, reconfigurable walkie-talkie

Drying Kinetics and Anticoagulant Activity of Microwave-vacuum, Dehumidified-air and Freeze-dried African Night Crawler (*Eudrilus eugeniae* Kinberg)

***Alfredo F. Fortu Jr.¹, Ernesto P. Lozada², Engelbert K. Peralta³,
Kevin F. Yaptenco⁴, and Delfin C. Sumintrado⁵**

¹²³⁴**Agricultural and BioProcess Division**

⁵**Agricultural Machinery Division**

Institute of Agricultural Engineering,

College of Engineering and Agro-Industrial Technology

University of the Philippines Los Baños, College, Laguna, Philippines

***Corresponding Author: Email: alfred_fortujr@yahoo.com/affortu@up.edu.ph**

Abstract

In this study, the drying kinetics and anticoagulant activity of dried earthworm *Eudrilus eugeniae* were compared using microwave-vacuum, dehumidified-air, and freeze-drying. Data showed that microwave-vacuum and dehumidified-air drying methods have relatively short drying time, higher drying rate and have low operational cost compared with freeze-drying. The Two term, Midilli, and Diffusion models fit the best in describing drying kinetics under microwave-vacuum, dehumidified-air, and freeze drying respectively. The water activity of the dried sample was in the acceptable value for safe storage though the dehumidified-air dried sample was in the critical range. Proximate analysis showed that dried earthworms have high protein content ranging from 60 to 70 percent of its total dry weight. The anticoagulant assay showed that fresh earthworm is potent as heparin showing no coagulation. Microwave-vacuum dried earthworm exhibited strongest anticoagulant activity compared with other drying methods though weaker than the fresh sample. This study suggests that earthworms have anticoagulant activity and microwave-vacuum and dehumidified-air drying could be an alternative method for drying the heat-sensitive sample.

Keywords: african night crawler, anticoagulant, dehumidified-air, drying kinetics, microwave-vacuum.

Involvement of NTH α (IV) in formation of basement membrane-like structures around the endothelial cell network in a novel *in vitro* angiogenesis model

Yongchol Shin^{1), 2)}, Akane Moriya²⁾, Yuta Tohnishi¹⁾, Takafumi Watanabe³⁾ and Yasutada Imamura^{1), 2)}

¹⁾Department of Chemistry and Life Science, Kogakuin University, Japan
E-mail: shin@cc.kogakuin.ac.jp

²⁾Graduate School of Engineering, Kogakuin University, Japan

³⁾Department of Veterinary Medicine, Rakuno Gakuen University, Japan

Abstract

Angiogenesis is a process through which new blood vessels are formed by sprouting and elongating from existing blood vessels. Several methods have been used to replicate angiogenesis *in vitro*, including culturing vascular endothelial cells on Matrigel, and co-culturing with endothelial cells and fibroblasts. However, the angiogenesis elongation process has not been completely clarified in these models. We therefore propose a new *in vitro* model of angiogenesis, suitable for observing vascular elongation, by seeding a spheroid co-cultured from endothelial cells and fibroblasts into a culture dish. In this model, endothelial cells formed tubular networks elongated from the spheroid with a lumen structure and were connected with tight junctions. A basement membrane (BM)-like structure was observed around the tubular network, similarly to blood vessels *in vivo*. These results suggested that blood vessel-like structure could be reconstituted in our model. Laminin and type IV collagen, main BM components, were highly localized around the network, along with non-triple helical form of type IV collagen α 1 chain (NTH α 1[IV]). In an ascorbic acid-depleted condition, laminin and NTH α 1(IV) were observed around the network but not the triple-helical form of type IV collagen, and the network was unstable. These results suggest that laminin and NTH α 1(IV) are involved in the formation of tubular network, and type IV collagen is necessary to stabilize the network.

Introduction

Angiogenesis is a phenomenon in which new blood vessels are formed by sprouting and elongation from existing blood vessels. The basement membrane (BM) covers the endothelial cells of the inner wall of the blood vessel. Type IV collagen is a major component of the BM. At the same time, there is a non-triple helical polypeptide of type IV collagen alpha 1 chain (NTH α 1(IV))^[1]. NTH α 1(IV) was localized uniquely along the new blood vessels in the angiogenesis model of rabbit cornea^[2]. We used an *in vitro* model of angiogenesis suitable for observation of the vascular elongation in a culture dish seeded with co-culture spheroids^[3] using human umbilical vein endothelial cells (HUVEC) and human fetal lung fibroblasts TIG-1. In this presentation, we show the construction of the BM on an *in vitro* angiogenesis model and localizations of BM components along the vascular-like network^[4].

Method

HUVEC (4×10^3 cells/well) and TIG-1 (16×10^3 cells/well) were suspended in corresponding culture medium containing 0.25% (w/v) methylcellulose and cultured in nonadherent round bottom 96-well plates for 7 days. Spheroids formed were reseeded onto a adherent culture dish or cover glass. The cells were cultured in the presence or absence of ascorbic acid.

1. HUVEC was stained with anti-CD31 or anti-VWF antibody. Localization of extra cellular matrix (ECM) proteins were examined using specific antibodies.

2. Adhered spheroids were fixed, dehydrated in graded ethanol, and embedded in epoxy resin. After

48-h heat polymerization at 60°C, ultra- thin sections were prepared with a diamond knife. The sections were examined using a transmission electron microscope (TEM) with electron staining.

Results

1. Localization of type IV collagen, laminin or NTH type IV collagen in the presence or absence of ascorbic acid

In the presence of ascorbic acid, type IV collagen and laminin were highly localized around the tip of the network and the periphery of the network (Fig.1).

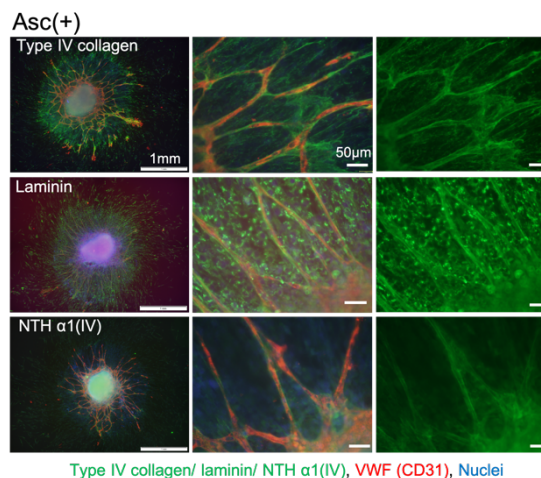


Fig. 1. Localization of ECM proteins around EC network.

NTH $\alpha 1(IV)$ was localized around the periphery of the network. The BM may be formed around the network similarly to the blood vessel *in vivo*.

Since, localization of NTH was observed around the network in the presence or absence of ascorbic acid, the interaction between TIG-1 and HUVEC may induce the NTH $\alpha 1(IV)$ production.

In the ascorbic acid-depleted condition, type IV collagen was hardly localized around the network, while Laminin was localized around the network. NTH $\alpha 1(IV)$ was highly localized inside TIG-1 cells and HUVEC (Fig.2).

From the results, type IV collagen may not be essential for vascular-like network formation.

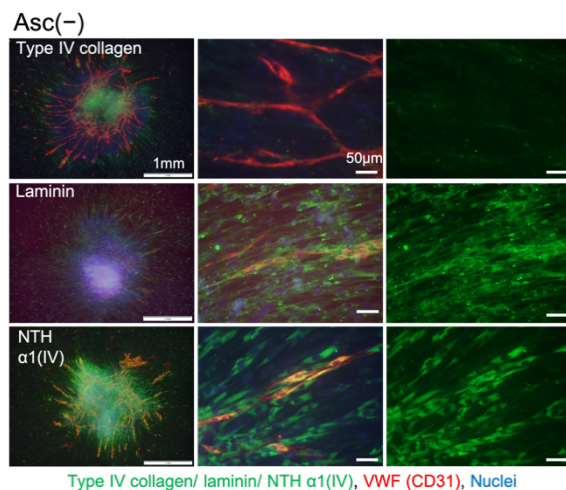


Fig. 2. Localization of extra cellular matrix proteins around EC network in the absence of ascorbic acid.

2. Luminal structures in the vascular-like network

After culturing in the presence of ascorbic acid, lumen-like structures were observed with a TEM (Fig. 3). Cells adhered to each other by tight junctions (*) in three places, and a lumen (L) was formed. In addition, a BM (arrow) was constructed outside the lumen forming cells.

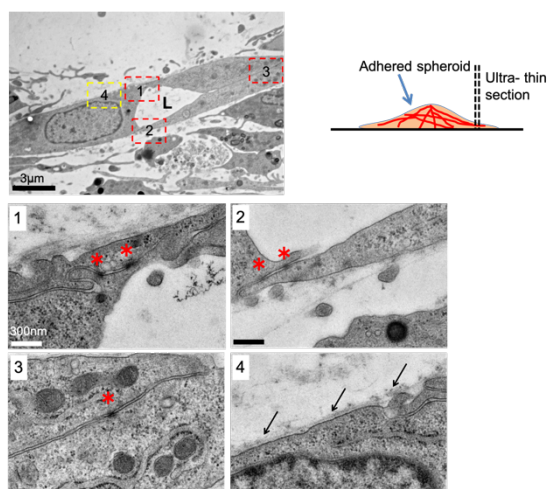


Fig. 3. TEM images of elongating EC network from co-cultured spheroids.

Discussion

Type IV collagen and laminin were localized around the network. Furthermore, the BM-like structure was observed outside the lumen forming cells by a TEM. From those results, we suggest that BM-like structure formed around the network is similar to the BM found in blood vessel *in vivo*.

NTH $\alpha 1(IV)$ was observed around the cellular network of HUVEC and intensely inside TIG-1 cells surrounding the network as well. NTH $\alpha 1(IV)$ might be involved in the angiogenesis.

In a rabbit angiogenic model, NTH $\alpha 1(IV)$ was observed in neovascular region of endothelial cells. In our model, NTH $\alpha 1(IV)$ was observed around the cellular network of HUVEC and intensely inside TIG-1 cells surrounding the network as well. Similarity between our model and a rabbit angiogenic model indicates that the elongation of blood vessel may be reconstituted in our *in vitro* model.

Always laminin and NTH $\alpha 1(IV)$ were co-localized around the network. Interaction of laminin and NTH $\alpha 1(IV)$ may be involved in blood vessel formation.

References:

- [1] Kiwamu Yoshikawa, Seiichiro Takahashi, Yasutada Imamura, Yoshikazu Sado, Toshihiko Hayashi, *J. Biochem.*, **129**, 929–936 (2001).
- [2] Hiroaki Sugiyama, Kazuhiro Tokunaka, Toshihiko Hayashi, Yasutada Imamura, Makoto Morita, Masayuki Yamato, *Heliyon.*, **1**, e00051 (2015).
- [3] Leoni A. Kunz-Schughart, Josef A. Schroeder, Marit Wondrak, Frank van Rey, Karla Lehle, Ferdinand Hofstaedter, Denys N. Wheatley, *Am. J. Physiol. -Cell Physiol.*, **290**, 1385-1398 (2006).
- [4] Yongchol Shin, Akane Moriya, Yuta Tohnishi, Takafumi Watanabe, Yasutada Imamura, *Am. J. Physiol. -Cell Physiol.*, **317**, 314-325 (2019).

Tooth Segmentations from CBCT based on Image Processing with Tooth Smoothness and based on Deep Learning

Kazuhiro SUGA¹⁾, Akira SHINOHARA¹⁾

1) Department of Mechanical Engineering, Faculty of Engineering, Kogakuin University, Tokyo, Japan
E-mail: ksuga@cc.kogakuin.ac.jp

Abstract

It is one of the most essential steps to recognize the 3-D structure of a tooth for safety and efficient dental treatment. The cone beam computed tomography (CBCT) is generally employed in order to recognize the 3-D structure of a tooth then the tooth area is segmented based on CT values. The separation between the tooth root and the alveolar bone is hard task because the limitation of spatial resolution of CBCT and the CT values of a tooth and bone. The research proposes a segmentation method based on image processing with continuity of shape change, and also a segmentation method using a deep learning. The effectiveness of these methods is discussed.

A part of this research is supported by JSPS KAKENHI Grant Number JP 18K11339.

Development of trehalose bioconversion process in *Bacillus subtilis*

Xin-Ru Jiang, Yi-Fen Lin, and Po Ting Chen*

Department of Biotechnology and Food Technology, Southern Taiwan University of Science and Technology,
Taiwan

E-mail: ptchen@stust.edu.tw

Abstract

Trehalose is a non-reducing disaccharide and has a wide range of applications in food and bio-related industry. This sugar can be synthesized from maltose in one step by trehalose synthase.

Bacillus subtilis was used as an expression host, and the various *B. subtilis* signal peptides and chitin-binding domains (ChBD) were fused with the N- and C-termini, respectively, of trehalose synthase gene. Results showed that trehalose synthase was secreted by the YwbN signal peptide of *B. subtilis* and bound specifically to the chitin beads. The conversion yield of the immobilized enzyme was higher than that of the free enzyme. Furthermore, the immobilized enzyme also retained 50% of its residual activity after the 21st repeated use. The chitin beads maintained 55% adsorption capacity after being reused 53 times. The one-step reaction method using trehalose synthase to produce trehalose from maltose was established.

References:

- [1] Krajewska B. Application of chitin-and chitosan-based materials for enzyme immobilizations: a review. *Enzyme Microb Tech*, 35: 126-39 (2004).
- [2] Westers L, Westers H, Quax WJ. *Bacillus subtilis* as cell factory for pharmaceutical proteins: a biotechnological approach to optimize the host organism. *BBA-Mol Cell Res* 1694: 299-310 (2004).
- [3] Chen PT, Chiang CJ, Chao YP. Strategy to approach stable production of recombinant nattokinase in *Bacillus subtilis*. *Biotechnol Progr* 23: 808-13 (2007).
- [4] Chen PT, Shaw J-F, Chao Y-P, David Ho T-H, Yu S-M. Construction of chromosomally located T7 expression system for production of heterologous secreted proteins in *Bacillus subtilis*. *J Agr Food Chem* 58: 5392-99 (2010).
- [5] Brockmeier U, Caspers M, Freudl R, Jockwer A, Noll T, Eggert T. Systematic screening of all signal peptides from *Bacillus subtilis*: a powerful strategy in optimizing heterologous protein secretion in Gram-positive bacteria. *J Mol Biol* 362: 393-402 (2006).

Development of imaging method of biological sample by TOF-SIMS

Kazuva Tamura,¹⁾ Takurou Hasegawa,¹⁾ Masato Morita,²⁾ Tetsuo Sakamoto^{1),2),*}

¹⁾ Graduate School of Electric Engineering and Electronics, Kogakuin University

²⁾ Department of Applied physics, School of Advanced Engineering, Kogakuin University

*E-mail: ct13087@ns.kogakuin.ac.jp

Abstract

We have developed a high resolution imaging method of biological sample by using Ga Focused Ion Beam Time-of-Flight Secondary Ion Mass Spectrometry (FIB-TOF-SIMS). TOF-SIMS analysis requires introduction of a sample into a high vacuum chamber. As a result, water and volatile components in the sample evaporate rapidly, and the shape changes. As a countermeasure of these problems, we have developed a mechanism to freeze the sample and introduce it into the vacuum chamber without contamination from ambient. Hereby the imaging of hydrated samples with TOF-SIMS has been realized. In this study, we have examined analysis technique

1. Introduction

In currently year, the need of analyzing for biological sample is increased, it is studied by many analytical methods. MALDI-MS (Matrix Assisted Laser Desorption/Ionization-Mass Spectrometry) and fluorescence microscopy are popular methods for direct imaging of biological sample. However, MALDI has low spatial resolution. Fluorescence microscopy is difficult multicomponent imaging.

On the other hand, the FIB-TOF-SIMS (Focused Ion Beam Time-of-Flight Secondary Ion Mass Spectrometry) developed by Sakamoto has the maximum spatial resolution of 40 nm and it is possible to detect almost all elements. And it is one of the surface analysis techniques for visualizing the elemental distribution in microscopic view with very high sensitivity. However TOF-SIMS analysis of biological materials has also some problems. In principle, TOF-SIMS analysis requires introduction of a sample into a high vacuum chamber. As a result, water and volatile components in the sample evaporate rapidly, and the shape changes. As a countermeasure of these problems, we have developed a mechanism to freeze the sample and introduce it into the vacuum chamber without contamination from ambient. Hereby the imaging of hydrated samples with TOF-SIMS has been realized.

In this study, we have examined some analysis technique

2. Experimental

The TOF-SIMS used in this study was developed by Prof. Sakamoto^[1]. It is equipped with Ga focused ion beam (FIB). This apparatus has some technique. Sample stage with 5-axes movement can be cooled down to -140°C with liquid nitrogen circulation. Biological sample is analyzed water containing state that prevented evaporation of volatile compounds by homemade TOF-SIMS. And it is possible to analyze inside sample with FIB cross section process.

3. Result and discussion

This figure 1 shows secondary ion maps of red blood cell under frozen condition after cross section by FIB. It shows total ions, ²³Na, ³⁹K, ⁵⁶Fe, ⁸⁷GaH₂O. The distribution of Iron was detected from whole of red blood cells. ⁸⁷GaH₂O is one of the important components. Therefore the discredition of chemical component was detected from red blood cell. Distribution of ⁸⁷GaH₂O shows that water was hold in the cell under the high vacuum. From these results, TOF-SIMS analysis with natural state of water-containing samples became possible.

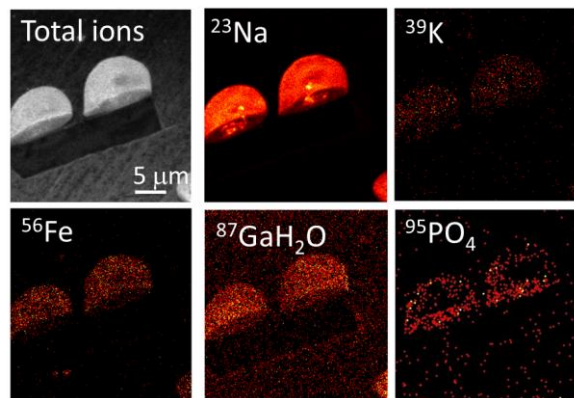


Figure 1 images of red blood cell after cross section

References:

- [1] T. Sakamoto, M. Koizumi, J. Kawasaki, J. Yamaguchi, *Applied Surface Science*, **255**, 1617 (2008).
- [2] G. Marko-Varga et al., *Journal of Proteomics*, **74**, 982 (2011).

Acknowledgment

This work is performed in “Joint-Research of Kogakuin University and Tokyo Medical University”. Authors greatly appreciate to Prof. Ikeda, Prof. Ohira, Prof. Kajiwara, Prof. Kakihana, and Dr. Nagase (Tokyo Medical University).

Electro-Spray Dialysis for TOF-SIMS analysis of aerosol

Toru Murata¹⁾, Shunki Karasawa²⁾, Masato Morita²⁾, and Tetsuo Sakamoto^{1),2)}

¹⁾Graduate School of Engineering, Kogakuin University, Tokyo
E-mail: ct13087@ns.kogakuin.ac.jp

²⁾Department of Applied Physics, Kogakuin University, Tokyo
E-mail: kt13544@ns.kogakuin.ac.jp

Abstract

Because PM_{2.5} and black carbon are very fine particles as a kind of aerosol, there is a possibility that they invade deep human lungs. Therefore, it is necessary to analyze their structure and components, individually. Focused ion beam time-of-flight secondary ion mass spectrometer (FIB-TOF-SIMS) developed by the authors, has a high spatial resolution and low detection limit, and the component imaging of individual particle can be performed. However, since aerosol is very small, the detailed structure of particles cannot be observed satisfactorily with the FIB-TOF-SIMS. In this study, in order to evaluate the structure of aerosol, we combined a new dialysis method and the FIB-TOF-SIMS. In this method, if the lateral resolution is insufficient, the structure of aerosol can be visualized with separating the particles and surface components, respectively.

1. Introduction

The fine particle called PM_{2.5} has a fear that it invades into human lungs deeply. Black carbon (BC) is also very fine particle. One of the forms of BC in atmosphere is diesel soot particles which are emitted from factories and automobile exhaust gases.

Individual analysis of BC requires chemical state analysis with high lateral resolution and high detection sensitivity. In this study, in order to evaluate the structure of BC, we combined the aerosol dialysis method (ESD) and FIB-TOF-SIMS observation. By ESD, particles on a flat substrate, dissolved components remain as stains around the particles. Therefore, it is possible to evaluate the structure approximately by shape observation before and after separating the target component with an appropriate solvent.



Figure 1 Schematic of electro-spray dialysis method

2. Experimental

BC on a Si substrate was dialyzed with acetone and water by ESD. In the FIB-TOF-SIMS analysis, the samples, acetone ESD, water ESD and untreated sample, were compared.

3. Result and Discussion

Figure 2 shows the SEM images of diesel soot particle before and after ESD with the acetone and

water, respectively. In the SEM image before water ESD, there were bright particles and low brightness particles around the diesel soot particles. Formers are sulfate or nitrate aerosol with highly water-soluble. In the SEM image after water ESD, there are no particles with low brightness, and only hydrophobic particles with high brightness remain. Since the relative positions of the undissolved particles have not changed, it can be seen that only the target components can be dialyzed without applying physical impact to the particles. It was found that dialysis is also possible with ESD method. The appearance of diesel soot particles was not changed dramatically by water ESD. On the other hand, in the case of acetone ESD, the particle shape changed dramatically. Also, sulfate aerosol around diesel soot particle did not change. When this method is combined with a surface analysis method such as TOF-SIMS, it is possible to perform component imaging including a chemical state information.

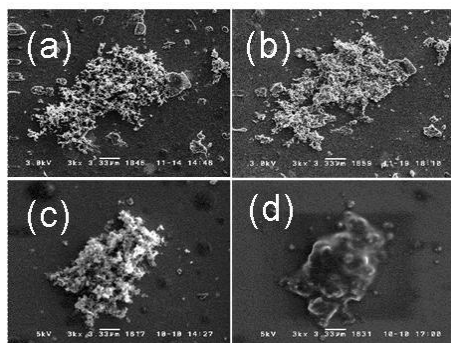


Figure 2 SEM images of diesel soot particle. (a) and (b): before and after water ESD, (c) and (d): those acetone ESD.

References

- [1] Makiko Mukai, Teruyuki Nakajima, Toshihiko Takemura, *J. Geophys. Res.* **113**, D12211 (2008)
- [2] Tetsuo Sakamoto, Masaomi Koizumi, Junji Kawasaki and Jun Yamaguchi, *Appl. Surf. Sci.*, **255**, 1617 (2008)

Practical functional performance of interior finishing wall using plastering material

Tomoko Kanemaki¹⁾, Masaki Tamura²⁾, Yuto Nakamura³⁾

¹⁾ Doctoral Course student, Dept. of Arch., Graduate School of Engineering, Kogakuin Univ., Tokyo, Japan
E-mail: life@neo.nifty.jp

²⁾ Kogakuin University, Dr.Eng, School of Architecture Department of Architecture, Tokyo, Japan

³⁾ Master Course student, Dept. of Arch., Graduate School of Engineering, Kogakuin Univ., Tokyo, Japan

Abstract

The plastering wall is Japan's traditional architectural technology, during usual and disaster situation [1]. The Shikkui finishing is known to be good for the living environment and health due to its excellent deodorizing and humidity performance. However, although the function evaluation of only the plaster material has been carried out, the function of the plaster wall including the substrate material has not been quantified.

The purpose of this study is to grasp the tactical functionality, including the base of plastering walls. The function of plastering materials is clarified by performing a functional evaluation test using plastering wall including a substrate material. We have set 46 types of specimens: conventional plaster wall using Shikkui and diatomite, PVC wallpaper and paint finish, plaster paint used for DIY, plaster wallpaper using Shikkui and diatomite (Table.1/Fig.1). The performance evaluation of each test specimen was conducted by a functional test using a simple experimental facility (Table 2). The functional tests are performed the adsorption of air pollutants: VOC and odor, anti-mold, humidity control, and soundproofing.

As a result, basic information about the functional performance of plastered walls including the base was organized. The plastering wall has a higher air pollutant adsorption function than PVC wallpaper and paint finish, and the ammonia adsorption function has more than twice the adsorption (Fig.2). As a result of the humidity control function test, there were 3 kinds of Shikkui that could be judged as a humidity control building material (Fig.3). The anti-fungal function was higher than that of the PVC wallpaper and paint finish (Fig.4). In the sound-proofing performance, it was confirmed that more than a majority of the plaster specimens had a larger transmission loss and higher sound insulation than the paint finish and PVC wallpaper (Fig.5).

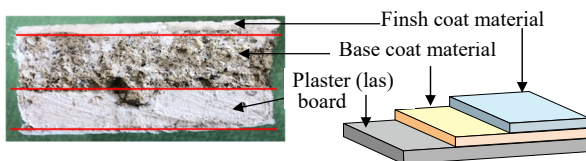


Fig.1: Plastering finishing wall composition

Tabl.1: List of specimens

No.	Plaster base	Base coat material	Finish coat material	Thickness of the finish coat layer (mm)*	Code	
1	Gypsum plaster board				A	
2	Gypsum lath board				B	
3	Gypsum plaster board	Dry type	-	-	Ab	
4		Premixed			Ac	
5	Gypsum lath board	Job site preparation			By	
6		Premixed gypsum			Bd	
7	Gypsum plaster board (T=12.5mm)	Dry type primer coating	Diatomite L	1-2mm	Ab1	
8			Diatomite W		Ab2	
9			Spot kneading on shikkui using Powder	Sand2 +2 = 4mm	Ab3-4	
10			Spot kneading on shikkui using Boild blue	2mm	Ab3-2	
11				Sand2 +2 = 4mm	Ab4-4	
12			Premixed shikkui	2mm	Ab4-2	
13				Sand2 +2 = 4mm	Ab5-4	
14			Premixed gypsum plaster	2mm	Ab5-2	
15				Diatomite L	1-2 mm	Ac1
16			Diatomite W	Ac2		
17			Premixed gypsum plaster	Spot kneading on sikkui using powder tsunomata	Sand2 +2 = 4mm	Ac3-4
18				Spot kneading on Shikkui used boild blue	2	Ac3-2
19					Sand2 +2 = 4mm	Ac4-4
20				Premixed shikkui	2mm	Ac4-2
21	Sand2 +2 = 4mm	Ac5-4				
22	Paint (Acrylic emulsion)	-	2mm	Ac5-2		
23			0.03mm	Ap		
24	Wallpaper(Vinyl chloride)		0.05mm	Ax		
25	paint	Premixed	①	2.03mm	Ax1	
26	Wallpaper	shikkui	②	2.05mm	Ax2	
27	Premixed shikkui	-	①	2mm	A1	
28			②	2mm	A2	
29	Wallpaper (Shikkui)		0.05mm	Axs		
30	Wallpaper(Diatomite)		0.05mm	Axd		
31	Gypsum lath board (t=9.5mm)	Job site preparation plaster	Diatomite L	1-2 mm	By1	
32			Diatomite W		By2	
33			Spot kneading on shikkui using powder	Sand2 +2 = 4mm	By3-4	
34			Spot kneading on shikkui using boild blue	2mm	By3-2	
35				Sand2 +2 = 4mm	By4-4	
36			Premixed shikkui	2mm	By4-2	
37				Sand2 +2 = 4mm	By5-4	
38			Premixed gypsum plaster of thick painting	-	2mm	By5-2
39					Diatomite L	1-2mm
40			Diatomite W	1-2mm	Bd2	
41	Spot kneading on sikkui used powder tsunomata	-	Sand2 +2 = 4mm	Bd3-4		
42			2mm	Bd3-2		
43	Spot kneading on shikkui used boild blue	-	Sand2 +2 = 4mm	Bd4-4		
44			2mm	Bd4-2		
45	Premixed shikkui	-	Sand2 +2 = 4mm	Bd5-4		
46			2mm	Bd5-2		

* : Sand2=Lime sand plaster of 2mm

Tab2: Experimental items and Evaluation methods

Performance test	Evaluation methods					
	Space volume	Adsorption surface area / Specimen size	Temp (°C)	Hum (%RH)	Measurement time	Chemical concentration
Air pollution reduction performance (VOC: AIJES-A0001-2014, Odor: AIJES-A0003-2005)**	Formaldehyde (HCHO)	3.1L	81cm ² /100mm×100mm	20	60	0.2,12,24 (h)
	Ammonia (NH3)					3ppm
	Trimethylamine (C3H9N)					5-15ppm
Humidity absorption and desorption performance (JIS A 1470-1)*	3.1L	81cm ² /100mm×100mm	20	50±10 80±10	Absorption: 3,6,12(h) Release : 12(h)	
Anti-mold performance (AIJES-A0002-2013)**	black mold	Φ90×15mm	16cm ² /50mm×50mm	35	90	0.4,24(h) 0.4ml
Sound insulation performance (Simple experiment in a Styrofoam box)	Box: W840 mm×D420 mm×H500 mm, t100mm, Precision sound level meter: NL-52 Transmission loss (dB) : $TL = L_1 - L_2 - 10\log_{10}(A_2/F)$					

*Japanese Industrial standard ** Architectural Institute of Japan Environmental Standards

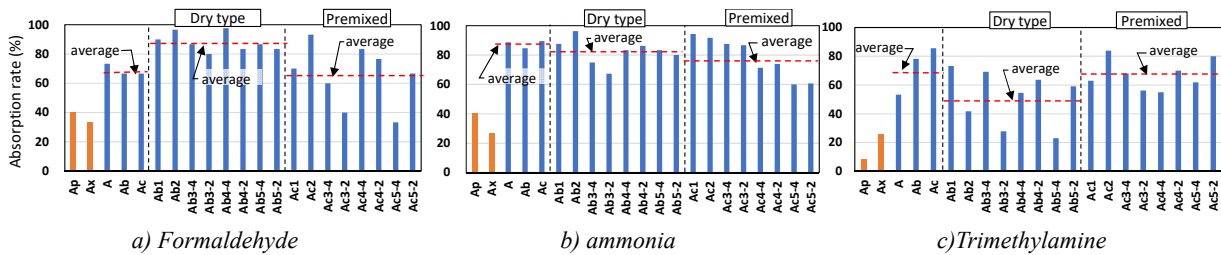


Fig.2 : Results of air pollution absorption performance test of each specimen on gypsum plaster board base

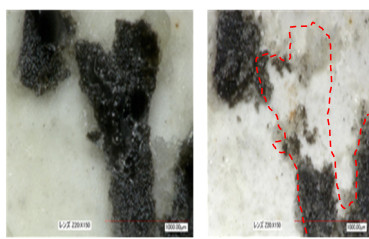


Fig.4: anti-mold performance test (Ab5-2)

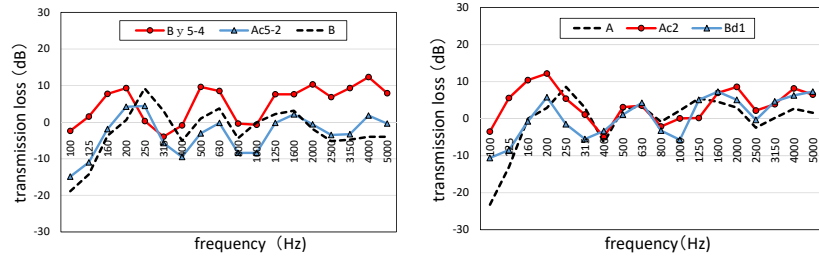


Fig. 5: Comparison of transmission loss of each specimen

References:

- [1] T.Kanemaki, M.Tamura, Construction technologies and systems of shelters and temporary houses for improving the living environment for people with pets in disaster situations, 14th DBMC, pp.337,2017 (in Belgium)
- [2] T.Kanemaki, M.Tamura,et.al, The functional performances evaluation of plaster finishing walls. Part5 The comparison of performances on antimicrobial. papers of AIJ annual meeting, pp.1325-1326,2019 (in Japanese)

Acknowledgement

This research is part of the results of joint research between Kogakuin University and the Tokyo Plasterer Craftsmen Associations.

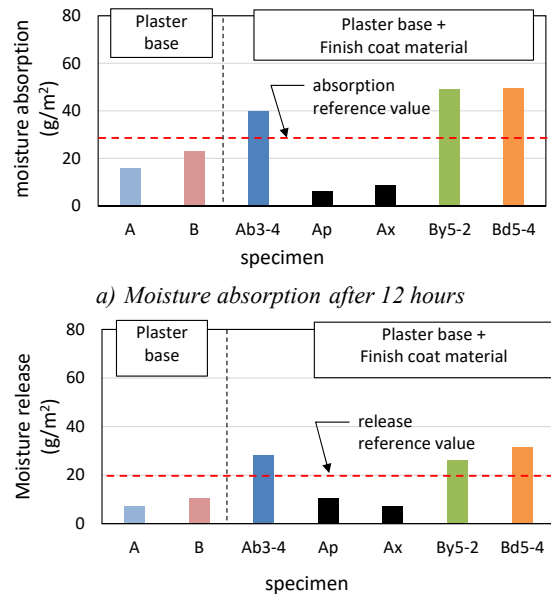


Fig.3: Result of humidity control performance test on Shikkui specimen

Practical functional performance of interior finishing wall using plastering material

Tomoko Kanemaki¹⁾, Masaki Tamura²⁾, Yuto Nakamura³⁾

¹⁾ Doctoral Course student, Dept. of Arch., Graduate School of Engineering, Kogakuin Univ., Tokyo, Japan
E-mail: life@neo.nifty.jp

²⁾ Kogakuin University, Dr.Eng, School of Architecture Department of Architecture, Tokyo, Japan

³⁾ Master Course student, Dept. of Arch., Graduate School of Engineering, Kogakuin Univ., Tokyo, Japan

Abstract

The plastering wall is Japan's traditional architectural technology, during usual and disaster situation [1]. The Shikkui finishing is known to be good for the living environment and health due to its excellent deodorizing and humidity performance. However, although the function evaluation of only the plaster material has been carried out, the function of the plaster wall including the substrate material has not been quantified.

The purpose of this study is to grasp the basic functionality, including the base of plastering walls. The function of plastering materials is clarified by performing a functional evaluation test by a plastering wall including a substrate material and quantifying the function. The functional tests performed are the adsorption of air pollutants (VOC and odor), anti-mold, humidity control, and soundproofing.

Key words – (Functionality evaluation, Shikkui, Plastering wall, including a substrate material)

1. Introduction

In recent years in Japan, PVC wallpaper is often used as a wall material because of the ease of material and construction and ease of construction [2]. However, “plastering wall”, a traditional Japanese building technique, is attracting attention from the viewpoint of comfort and surface texture. Shikkui and diatomite finishes are expected to have functions corresponding to the hot and humid Japanese climate such as odor adsorption function, anti-bacterial / anti-mold and humidity control performance. In an environment where dogs and cats are kept, is very important, and there is a high expectation for the function of plastering walls.

In this study, the reliability of traditional technology rooted in the Japanese climate has been confirmed by quantifying the function of plastering walls, including the substrate materials.

2. Outline of the experiment with the specimen imitating the plastering wall

Tabl.2 shows experimental items and evaluation methods. The functional tests are performed the adsorption of air pollutants: VOC and odor, anti-mold, humidity control, and soundproofing. The performance evaluation of each test specimen was conducted by a functional test using a simple experimental facility.

3. Plastered wall specimens used for experiment

Tabl.1 shows List of specimens, and Fig.1 shows Plastering finish wall composition. We have set 46

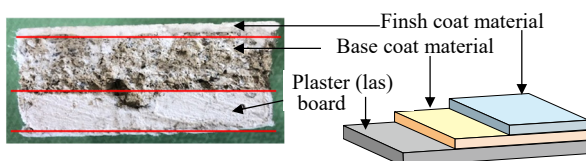


Fig.1: Plastering finishing wall composition

Tabl.1: List of specimens

No.	Plaster base	Base coat material	Finish coat material	Thickness of the finish coat layer (mm)※	Code	
1	Gypsum plaster board				A	
2	Gypsum lath board				B	
3	Gypsum plaster board	Dry type			Ab	
4	Gypsum plaster board	Premixed			Ac	
5	Gypsum lath board	Job site preparation			By	
6	Gypsum lath board	Premixed gypsum			Bd	
7	Gypsum plaster board (t=12.5mm)	Dry type primer coating	Diatomite L	1-2mm	Ab1	
8			Diatomite W		Ab2	
9			Spot kneading on shikkui using Powder tsunomata	Sand2 +2 = 4mm	Ab3-4	
10				2mm	Ab3-2	
11			Spot kneading on shikkui using Boild blue	Sand2 +2 = 4mm	Ab4-4	
12				2mm	Ab4-2	
13			Premixed shikkui	Sand2 +2 = 4mm	Ab5-4	
14			2mm	Ab5-2		
15		Gypsum plaster board (t=12.5mm)	Premixed gypsum plaster	Diatomite L	1-2 mm	Ac1
16				Diatomite W		Ac2
17				Spot kneading on sikkui using powder tsunomata	Sand2 +2 = 4mm	Ac3-4
18					2mm	Ac3-2
19				Spot kneading on Shikkui used boild blue	Sand2 +2 = 4mm	Ac4-4
20					2mm	Ac4-2
21	Premixed shikkui			Sand2 +2 = 4mm	Ac5-4	
22				2mm	Ac5-2	
23				Paint (Acrylic emulsion)	0.03mm	Ap
24				Wallpaper(Vinyl chloride)	0.05mm	Ax
25		paint	Premixed	①	2.03mm	Ax1
26		Wallpaper	shikkui	②	2.05mm	Ax2
27		Premixed shikkui	①	2mm	A1	
28			②	2mm	A2	
29		Wallpaper (Shikkui)		0.05mm	Axs	
30		Wallpaper(Diatomite)		0.05mm	Axd	
31	Gypsum lath board (t=9.5mm)	Job site preparation plaster	Diatomite L	1-2mm	By1	
32			Diatomite W		By2	
33			Spot kneading on shikkui using powder tsunomata	Sand2 +2 = 4mm	By3-4	
34				2mm	By3-2	
35			Spot kneading on shikkui using boild blue	Sand2 +2 = 4mm	By4-4	
36				2mm	By4-2	
37			Premixed shikkui	Sand2 +2 = 4mm	By5-4	
38			2mm	By5-2		
39		Premixed gypsum plaster of thick painting	Diatomite L	1-2mm	Bd1	
40			Diatomite W	1-2mm	Bd2	
41	Spot kneading on sikkui used powder tsunomata		Sand2 +2 = 4mm	Bd3-4		
42			2mm	Bd3-2		
43	Spot kneading on shikkui used boild blue		Sand2 +2 = 4mm	Bd4-4		
44			2mm	Bd4-2		
45	Premixed shikkui		Sand2 +2 = 4mm	Bd5-4		
46		2mm	Bd5-2			

※ : Sand2= Lime sand plaster of 2mm

Tabl2: Experimental items and Evaluation methods

Performance test		Evaluation methods					
		Space volume	Adsorption surface area / Specimen size	Temp (°C)	Hum (%RH)	Measurement time	Chemical concentration
1	Air pollution reduction performance (VOC: AIJES-A0001-2014 , Odor: AIJES-A0003-2005) ** Formaldehyde (HCHO) Ammonia (NH3) Trimethylamine (C3H9N)	3.1L	81cm ² /100mm×100mm	20	60	0,2,12,24 (h)	3ppm
						0,5,15(min)	5-15ppm
2	Humidity absorption and desorption performance (JIS A 1470-1) *	3.1L	81cm ² /100mm×100mm	20	50±10	Absorption: 3,6,12(h)	
					80±10	Release : 12(h)	
3	Anti-mold performance (AIJES-A0002-2013)** black mold (Simple experiment in a styrofoam box)	Φ90×15mm	16cm ² /50mm×50mm	35	90	0,4,24(h)	0.4ml
4	Sound insulation performance Box: W840 mm×D420 mm×H500 mm, t100mm , Precision sound level meter: NL-52 Transmission loss (dB) : $TL = L_1 - L_2 - 10\log_{10}(A_2/F)$						

*Japanese Industrial Standard ** Architectural Institute of Japan Environmental Standards

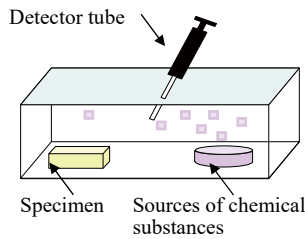


Fig.2: Schematic diagram of Air pollution reduction performance test

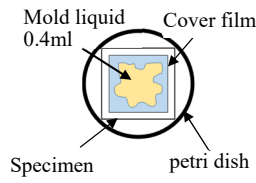


Fig.3: Schematic diagram of Anti-mold performance test

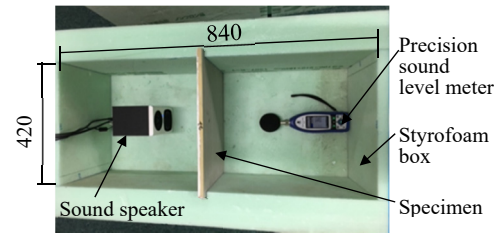


Fig.4: Sound insulation performance test using Simple experiment in a styrofoam box

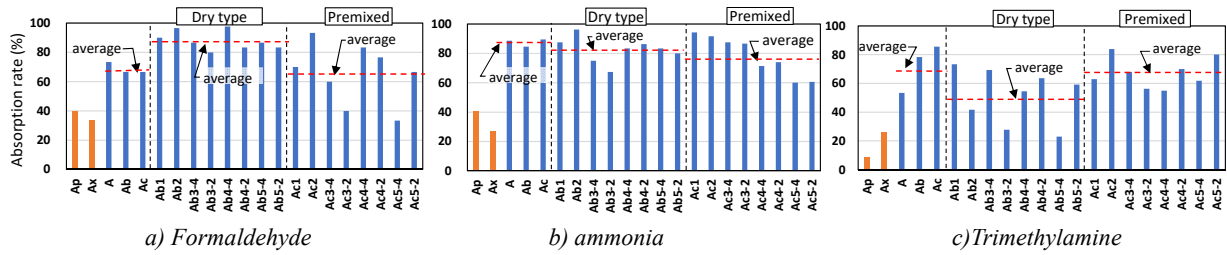


Fig.5 : Results of air pollution absorption performance test of each specimen on gypsum plaster board base

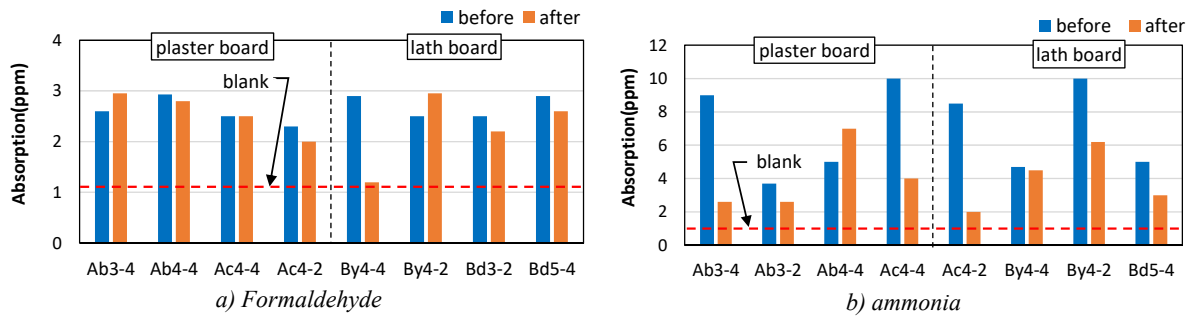


Fig.6: Results of chemical adsorption test after neutralization (Shikkui)

types of specimens: conventional plaster wall using Shikkui and diatomite, PVC wallpaper and paint finish, plaster paint used for DIY, plaster wallpaper using Shikkui and diatomite.

4. Evaluation of air pollutant adsorption functionality (Test1)

4.1 Outline of air pollutant adsorption Performance test

Fig.2 shows Schematic diagram of Air pollution reduction performance test. The performance evaluation

was conducted by a functional test using a simple experimental facility. The chemical substances examined are formaldehyde(VOC) and two kinds of odorous substances, ammonia and trimethylamine.

4.2 Results of air pollution adsorption performance test

Fig.5 shows part of the Results of air pollution absorption performance test of each specimen on gypsum plaster board base, and Fig. 6 shows Results of chemical adsorption test after neutralization (Shikkui). Since the amount of absorption varies in

proportion to the initial concentration of the substance in the air, the comparison was evaluated by the absorption rate (%). Specimens using plastering materials had higher absorption rates of VOCs and odorous components than PVC wallpaper and painted specimens. With trimethylamine, the performance is considered to be greatly affected by the primer.

5. Humidity regulation effects test (Test2)

5.1 Outline of Humidity absorption and desorption performance test

We compared the moisture absorption and desorption amount of each specimen, and grasped the difference in humidity control functionality between those using plastering material and those not using. The performance evaluation was conducted by a functional test using a simple experimental facility.

5.2 Results of Humidity absorption and desorption performance test

Fig.7 shows part of the Result of humidity control performance test on Shikkui specimen, and Fig.8 shows result of Humidity control performance test diatomite specimen. There were three types of specimens that could be judged as humidity control building materials: Ab3-4, By5-2, and Bd5-4.

6. Anti-mold function evaluation method (Test3)

6.1 Outline of anti-mold performance test

Fig.3 shows a schematic diagram of Anti-mold performance test. The antibacterial evaluation test is performed by dripping cultured mold-containing water onto the specimen. The area of mold on the specimen was measured with a microscope immediately after dropping and 24 hours later, and the reduction rate was calculated. The type of mold tested was black mold.

6.2 Results of anti-mold performance test

Fig.9 shows image of anti-mold performance test (Ab5-2), and Fig.10 shows part of the mold reduction rate result. The plastering wall test specimen showed a higher rate of mold reduction than the VOC wallpaper and paint finishing.

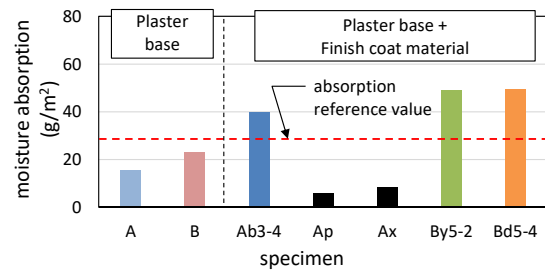
7. Sound insulation performance test (Test4)

7.1 Outline of Sound insulation performance test

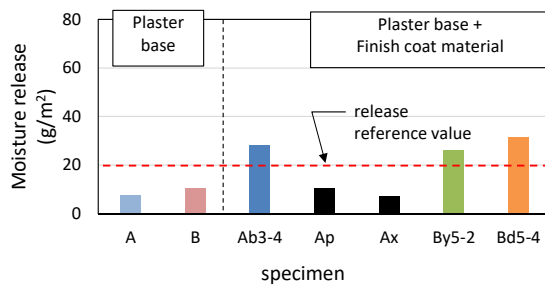
Fig.3 shows Sound insulation performance test using Simple experiment in a Styrofoam box. Using material of dog barking, the acoustic equivalent loss of each specimen was compared to evaluate the soundproofing function.

7.2 Results of Sound insulation performance test

Fig.11 shows part of the Comparison of transmission loss of each specimen. a) is lath board+Shikkui (By5-4, Ac5-2), and b) is flat board+diatomite(Ac2, Bd1). More than half of the plastering finished specimens had greater transmission loss than the PVC wallpaper and paint finished specimens. By5-4, the Shikkui specimen, had the largest amount of transmission loss and had soundproofing properties.

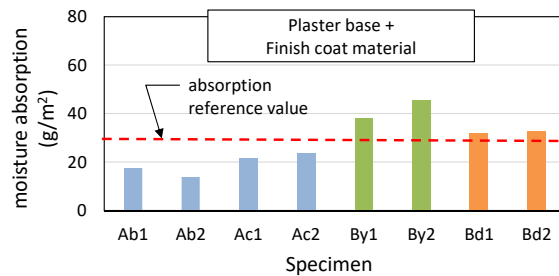


a) Moisture absorption after 12 hours

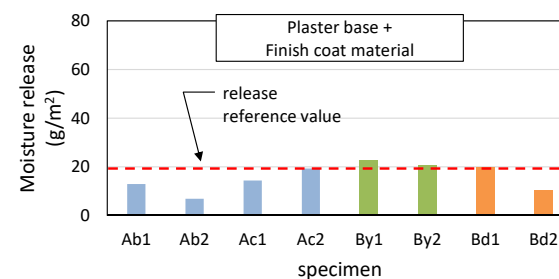


b) Moisture release after 12 hours

Fig.7: Result of humidity control performance test on Shikkui specimen



a) Moisture absorption after 12 hours



b) Moisture release after 12 hours

Fig.8: Result of humidity control performance test on Diatomite

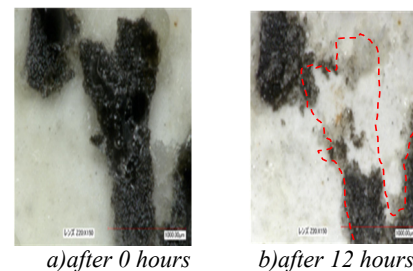


Fig.9: Image of anti-mold performance test (Ab5-2)

8. Summary

As a result, basic information about the functional performance of plastered walls including the base was organized.

- 1) The plastering wall has a higher air pollutant adsorption function than PVC wallpaper and paint finish, and the ammonia adsorption function has more than twice the adsorption. With trimethylamine, the performance is considered to be greatly affected by the primer.
- 2) As a result of the humidity control function test, there were 3 kinds of Shikkui specimen (Ab3-4, By5-2, Bd5-4) that could be judged as a humidity control building material.
- 3) The anti-fungal function was higher than that of the PVC wallpaper and paint finish.
- 4) In the soundproofing performance, it was confirmed that more than a majority of the plaster specimens had a larger transmission loss and higher sound insulation than the paint finish and PVC wallpaper

References:

- [1] T.Kanemaki, M.Tamura, Construction technologies and systems of shelters and temporary houses for improving the living environment for people with pets in disaster situations, *14th DBMC*, pp.337,2017 (in Belgium)
- [2] H.Okuyama, The present and future of plaster, *Journal of the Society of Inorganic Materials, Japan 14*, pp.261-267,2007
- [3] M.Tamura, T.Kanemaki, et.al, The functional performance development and evaluation in living environment on plaster finishing walls. Part1 abstract and Setting of Specimens, *papers of JSFT annual meeting, 2018 (in Japanese)*
- [4] T.Kanemaki, M.Tamura, et.al, The functional performances evaluation of plaster finishing walls. Part5 The comparison of performances on antimicrobial, *papers of AIJ annual meeting, 2019 (in Japanese)*
- [5] Y.Nakamura, T.Kanemaki, M. Tamura, The functional performance development and evaluation in living environment on plaster finishing walls. Part 5 Functional assessment of Building materials for Loving space with Companion animals and human., *papers of JSFT annual meeting, 2019 (in Japanese)*

Acknowledgement

This research is part of the results of joint research between Kogakuin University and the Tokyo Plasterer Craftsmen Associations. We received great support from R.Nakada and M.Makino of undergraduate students of Kogakuin Univ.

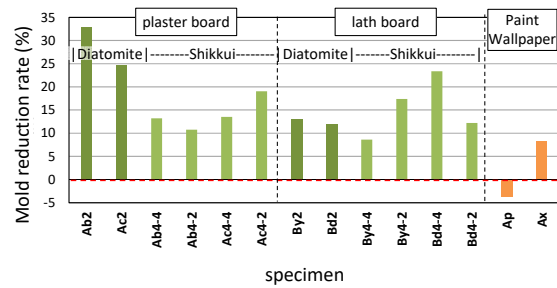
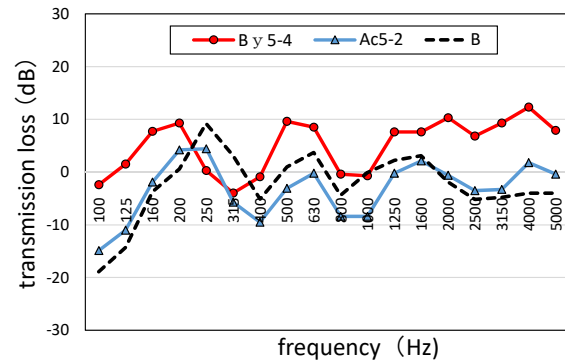
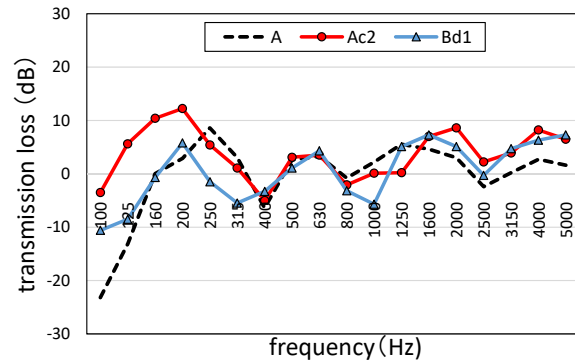


Fig.10 Mold reduction rate result



A) Shikkui (By5-4, Ac5-2)



b) Diatomite (Ac2, Bd1)

Fig.11: Comparison of transmission loss of each specimen



Tomoko Kanemaki

- Practical functional performance of interior finishing wall using plastering material
- Doctoral Course degree, Dept. of Arch., Graduate School of Engineering, Kogakuin University
- first-class architects, Kanemaki & Kokubo Studio
- Plasterer, Building Material, Functionality evaluation, Disaster situation, Living with pets



Masaki Tamura

- Development of Building materials, Structural Concrete, Finishing Materials Evaluation of built environment, environmental load, socio-cultural aspects, Recycling Engineering,
- Professor of building construction group, school of architecture, Kogakuin University



Yuto Nakamura

- Practical functional performance of interior finishing wall using plastering material
- First-year master's degree, School of Architecture, Kogakuin University
- Plasterer, Building Material, Functionality evaluation, Air environment, Living with pets

Study on Improving Residence and Durability of Concrete Block Construction in South East Asia by Using Palm Oil Waste Fiber

Erika Futami¹⁾ and Masaki Tamura²⁾

¹⁾ School of architecture, Kogakuin University, Japan
E-mail: db15412@ns.kogakuin.jp

²⁾ Department of building material, School of architecture, Kogakuin University, Japan
E-mail: masaki-t@cc.kogakuin.ac.jp

Abstract

In this research, we are going to study about EFB fiber which is come out from palm oil industry to use as a part of reinforcing building materials. This material will not only be expected improving durability of housing inexpensively, but also proposing a new method of industrial waste treatment.

1. Introduction

Nowadays, the number of Asian populations is expected that it will be over 50% of world population by 2050. Accordingly, the demand of residence construction is getting higher. However, local Asian people prefer to build their house inexpensively instead of taking safety, so those houses don't have enough strength for any natural disasters such as earthquakes and typhoon.

At the same time, Palm Oil has also increased production in association with world population because palm oil can be a foundation of any foods and daily necessities. Since 2015, over 85% of world production of Palm Oil has been covered by only Malaysia and Indonesia because the cultivating conditions are quite good in those tropical areas and Palm plantations have expanded rapidly. But these have caused serious problems in both environmental and societal aspects. Palm oil waste disposal is one of the environmental problems, although some part of Palm Oil waste has been recycled into biomass fuel, fertilizer and so on. In this study, we have tried to solve this waste disposal problem by considering possibility of using EFB fiber which is one of the Palm Oil waste as a part of building materials. To recycle those waste from agricultural industry into building industry, it will be able to make a system of "Local resources for local consumption" and build high quality housing while world population increasing and resource depletion have been advocated.

2. Research methodology

2.1. Materials in the experiment

In this study, 4 types of fiber such as EFB fiber, straw, coconut fiber and vinylon fiber was used for the experiments to compare their property each other.

2.2. Details of experiments

2.2.1. Fiber Alkali resistance test

The methodology is soaking fibers in Sodium hydroxide aqueous solution for 28 days, and then

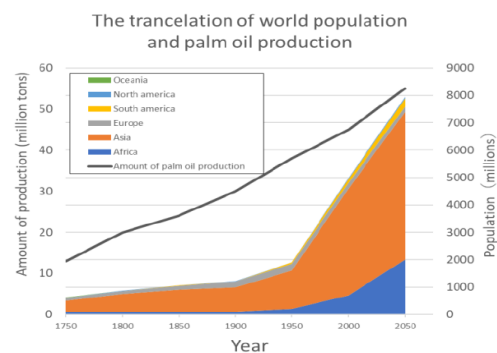


Fig. 1. The trancelation of world population and palm oil production.



Fig. 2. A palm oil trees



Fig. 3. EFB fiber



Fig. 4. Typhoon damages By hagibis 2019



Fig. 5. Underconstruction oconcrete blocks apartment



Fig. 6. An example of different shape of EFB fiber

recording the pH changes of the aqueous solution before soaking and 28 days later. In addition, the soaked fiber and normal fiber will be tested the tensile. The condition of experiment is shown in figure 6.

2.2.2. Water absorption test

Water absorption test has done for researching surface quality of fiber mortar. The method is sticking a funnel filled by water inside on surface of wall body test piece and recording the reduction of water every 1 hour. It has hold on as of 28days material ages.

2.2.3. 3-point bending and compression tests

3-point bending and compression tests have done for researching mortar’s solid state protaerties. These tests use Quadrangular prism test pieces Distinction of test pieces are showed in table 1. The mortar mix proportion is water: cement : sand = 1:2:4. Each size is 40mm*40m*160mm and those ware made three of each. In 3-point bending test, the result has calculated average of 3 test pieces. And also, to research the relationship between load and deflection, test pieses ware connected to Data logger. In compression test, it have tested each half pieces and calculated average value of them.

2.2.4. Shear resistance

Shear resistance test has assumed that fiber mortar wall has been constructed. This test used wall body tests pieces. Making method of these test pieces ware piling concrete blocks up/down and left/right, and then, applying fiber mortar on the surface once or twice. These tested 3-point bending test as of 28 days material ages. To research the relationship between load and deflection, test pieses ware connected to Data logger.

3. Property of Fiber included Mortar

As can be seen from figure 6, the shape of each natural EFB fiber are irregular, it is tend to crack at spherical fiber points and strength is not stable. In

Table 1. Factors and Levels of examinations

Fanter	Level
Type of fiber	EFB fiber (e),coconut fiber(c),straw (w),vinylon (b)
Length of fiber	1cm,2cm
Percentages of Fiber	1%vol,3%vol
W/C	40%,60%
Material ages	7days,28days

Table 2. Method of experiments

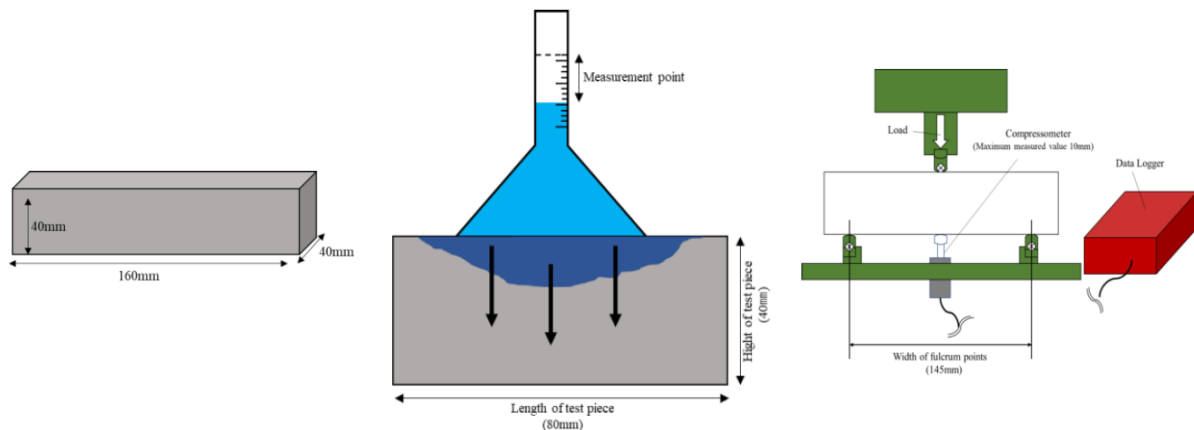
Classification	Method	Content
Mortar test pieces	Making test pieces	Making 64 different types of test pieces which is distinguished by Factors and levels.
Strength tests	3-point bending test JIS R 5201	These tests followed JIS R 5201. At 3-point bending test, Test pieces were connected to Data logger to measure the relationship between load and deflection.
	Compression test JIS R 5201	
	Shear resistance test	Bending wall body test pieces at 3-point and measure the relationship between load and deflection.
Water absorption test	Comparison of absorption speeds	Measuring absorption speeds every 1 hour by attaching funnel with scale on the surface of test pieces.
Fiber Alkali resistance test JIS A 1193	Soaking test	Comparison of pH between normal fiber and soaked one as of 28days.
	Tensile test	Doing tensile test for normal fiber and soaked one.



Fig. 7. Alkali resistance test



Fig. 8. Measuring of Materials



(a) Quadrangular prism test pieces (b) Water absorption test (c) 3-point bending test

Fig. 9. The illustration of condition of experiment

addition, those fiber twined around propeller mixer and accumulate at the bottom, so it was difficult to spread fiber evenly into the test pieces. On the other hand, at a compression test, broken pieces of non-including fiber mortar test piece were scattered energetically after reached maximum load, however it wasn't happened for a test pieces which was including EFB fiber. It is one of the common reason that broken pieces hurt human beings. So there is a possibility to reduce a human damages by any natural disasters.

4. Result of Experiment

At a 3-point bending test, non-fiber test piece caused brittle fracture after reached maximum load, the but EFB fiber test piece kept 10% of maximum load after reached peak point while deflection was changing. At a compression test, non-fiber test piece was stronger than EFB fiber test piece. Possible reason for this result is that spherical fiber made test piece easy to break.

5. Conclusion

Proposing the low-cost method of improving durability of building is providing a stable infrastructure for their cultural lives. In addition, it is not only realizing Local resources for local consumption by using oil palm waste for building materials but also being able to resolve some environmental issues and contributing for sustainable development of oil palm industry. Therefore, this study will create new cycle between agricultural industry and construction industry.

References

[1] Erika Futami, Masaki Tamura, Toward Long Time Use of Stone-based Wall Panel in High-rise Building between Past and Future in Japan, 17th

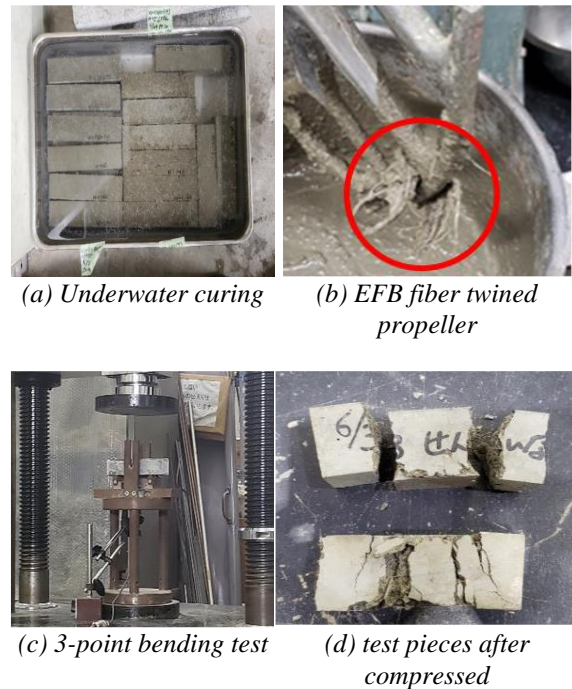
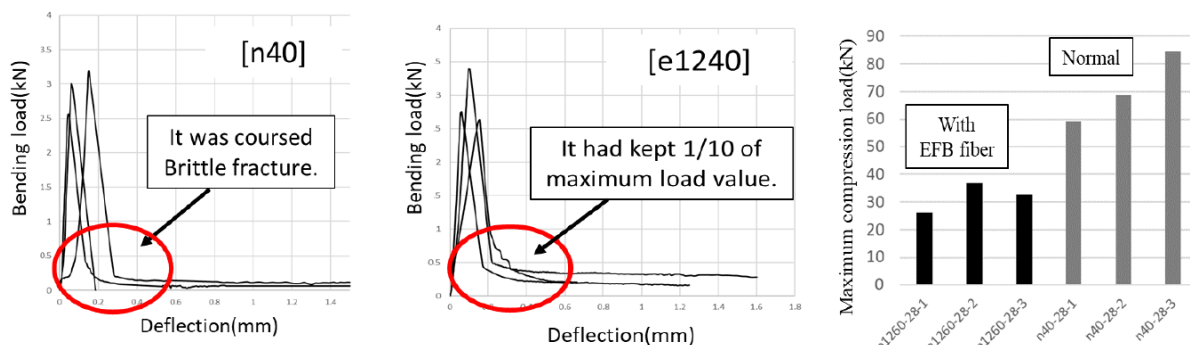


Fig. 10. Picture of Condition of experiments

International Symposium on Advanced Technology (ISAT-17) Engineering Innovation for Sustainable Future, November 13 - 15, 2018
 [2] WWF JAPAN, Science Technology section. <https://www.wwf.or.jp/activities/basicinfo/2484.html>
 [3] Japan Society For Finishing Technology. <http://www.nissaren.or.jp/1232>
 [4] Taiheiyo Cement Corporation. <http://www.taiheiyo-cement.co.jp>



(a) Normal mortar test pieces (b) EFB fiber mortar pieces (c) Comparison of compression test
 Fig. 11. The result of 3-point bending test and compression test

Estimation of Long-Period Ground Motions Containing Permanent Displacement in the Near-Fault Region for 1999 Kocaeli Earthquake

Author1's Takumi Kiryu¹⁾, Author2's Yoshiaki Hisada²⁾, and Author3's Shinya Tanaka³⁾

¹⁾Department of Architecture, Kogakuin University, Japan
E-mail: dm19023@ns.kogakuin.ac.jp

²⁾Department of Architecture, Kogakuin University, Japan
E-mail: hisada@cc.kogakuin.ac.jp

³⁾ Tokyo Electric Power Services Company, Japan
E-mail: s.tanaka@tepsc.co.jp

Abstract

Seismic motion evaluation is performed near the surface earthquake fault based on theoretical methods. The “recipe” by the Headquarters for Earthquake Research Promotion does not take into account the effects of shallower earthquakes. The recurrence analysis of the records of the 1999 Kocaeli earthquake in Turkey was performed by extending the recipe beyond the seismogenic layer.

introduction

The authors have been studying the method of setting the epicenter model for the evaluation of long-period ground motion including permanent displacement near the surface fault (Tanaka et al. (2018) ^[1]). In the proposed method, an earthquake source model is set in the earthquake generation layer using a strong ground motion recipe, the slip distribution is extended to a depth below the earthquake occurrence layer, and a wide slip based on the standardized Yoffe function ^[2] below the earthquake occurrence layer. The speed time function is used. In this study, we investigate the applicability of the proposed method to earthquakes caused by long faults. Here, the examination result for the 1999 Kocaeli earthquake (MW7.5) is shown

Seismic source fault model setting

The macroscopic aspect was set with reference to Sekiguchi and Iwata (2002) ^[3]. Next, the top depth of the seismogenic layer was assumed to be 3 km, and microscopic parameters were set in the seismogenic layer based on the strong ground motion recipe. However, the average stress drop was 3.1 MPa according to Fujii and Matsu'ura (2000) ^[4], and the asperity area ratio was 22%. The asperity position is based on the center of each segment, but for the segment C, here is a model that is located on the west side. The sliding velocity time function below the seismogenic layer uses the standardized Yoffe function by Tinti et al. (2005). Figure 1 shows the positional relationship between the seismic source fault model and the target observation point.

Seismic motion evaluation based on theoretical methods

Figure 2 shows the seismic source model and the

evaluation results obtained by the wavenumber integration method ^[5] with a period of 1 second or longer. Here, Sekiguchi and Iwata (2002) is used as the ground model for seismic motion evaluation. The target period is basically 1 to 10 seconds, but at the YPT and SKR points close to the surface earthquake fault, the period is more than 1 second. It can be seen from Fig. 2 that the observation records can be roughly reproduced. However, since the reproducibility of the velocity waveform is somewhat poor at the SKR point, it will be discussed in the next section.

Evaluation of failure mode at SKR site

Fig. 3 shows the seismic motion in the seismogenic layer at the SKR site and from shallower than that. The contribution of the velocity waveform to the seismogenic layer is large, and the characteristic pulse peak is divided into two. This is probably because the SKR point is far from the destruction start point, and the destruction is not heading to the observation point. According to previous findings, the difference between the arrival times of the P wave and S wave at the SKR point is as short as about 1.8 seconds, indicating that the destruction of asperity near the SKR point may be excited by the P wave from the seismic source ^[6]. Has been. Therefore, the ground motion was evaluated assuming the failure mode shown in Fig. 4. The results are also shown in the figure. It can be seen that the reproducibility of the velocity waveform is improved by reviewing the destruction type. Fig. 5 shows a simpler hypocenter model based on these results. It can be seen that even with this setting, the observation records can be reproduced.

Conclusion

Based on Tanaka et al. (2018) for the 1999

Kocaeli earthquake, a source fault model based on a strong ground motion recipe that takes into account the depth below the seismogenic layer can be set, and observation records with a period of 1 second or more can be reproduced using a theoretical method. showed that. In the future, other earthquakes will be studied.

References:

[1] Tanaka et al. (2018): Architectural Institute of Japan, No.752 [2] Tinti, E. et al.(2005): Bulletin of the Seismological Society of America, Vol. 95, No. 4. [3] Sekiguchi and Iwata(2002): Rupture process of the 1999 Kocaeli, Turkey, earthquake estimated from strong-motion waveforms. Bull. Seis. Soc. Am 92 [4] Fujii, Y. and M. Matsu'ura, (2000) : Regional Difference in Scaling Laws for Large Earthquakes and its Tectonic Implication, Pure and Applied Geophysics, 157 [5] Hisada (1997): Efficient calculation of normal mode solution and Green's function in stratified soil, Architectural Institute of Japan, No.501 [6] Anderson et al.(2000):Implications for seismic hazard analysis, in Kocaeli, Turkey, Earthquake of August 17, 1999, Reconnaissance Report, Earthquake Spectra 16

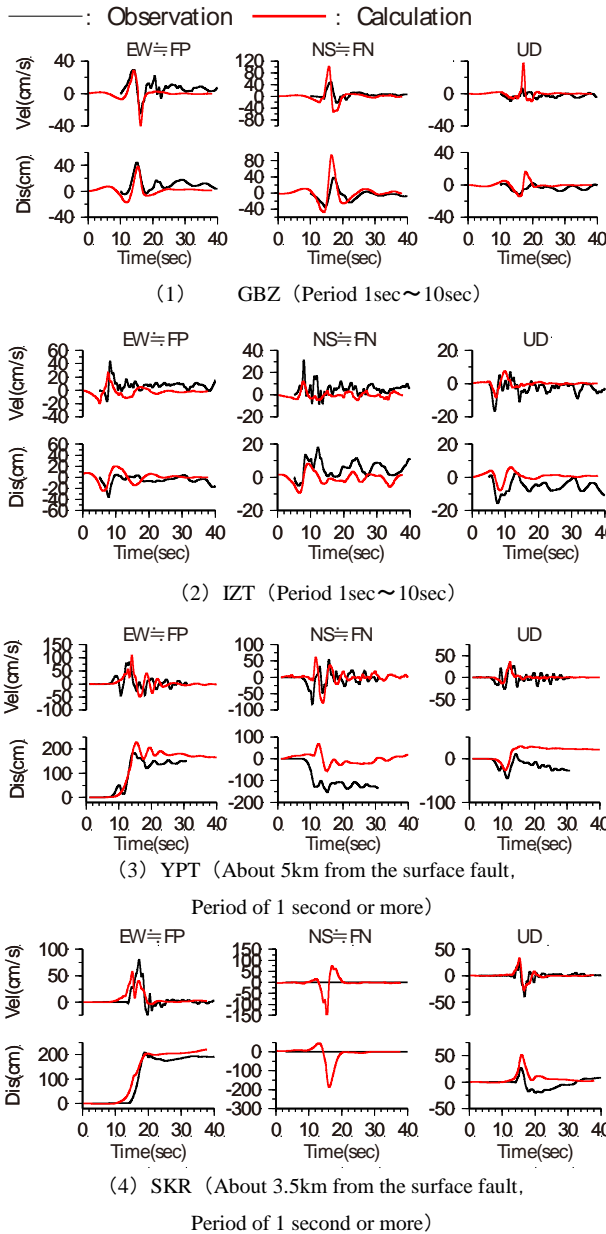


Fig.2 Evaluation results by Hisada and Bielak

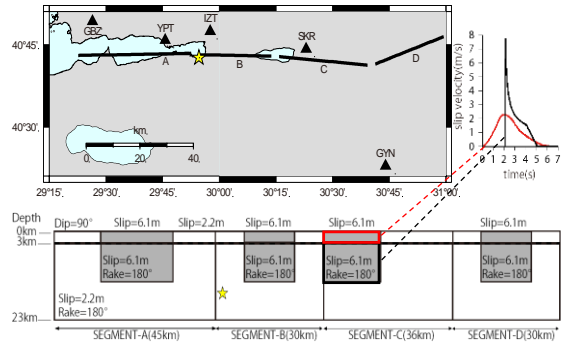


Fig.1 Setting of seismic source fault model and slip velocity time function.

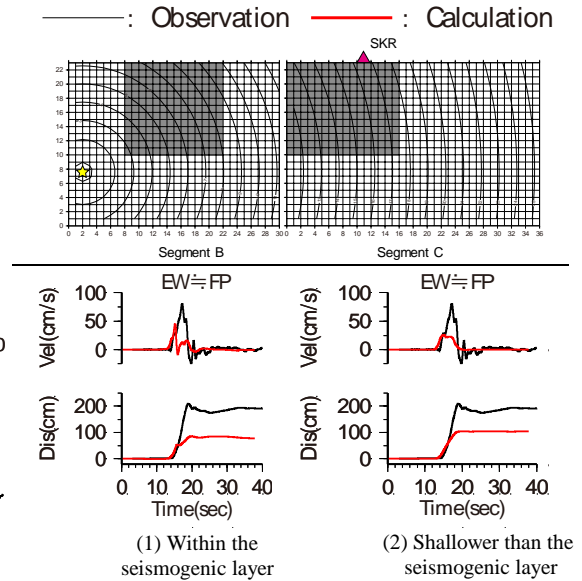


Fig.3 Contribution shallower than seismogenic layer at the SKR site

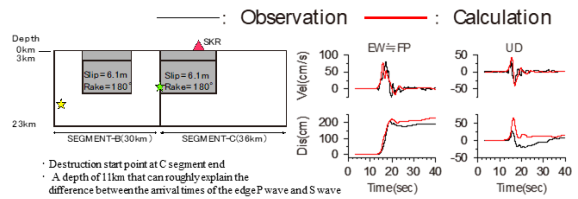


Fig.4 Effect of fracture type on SKR.

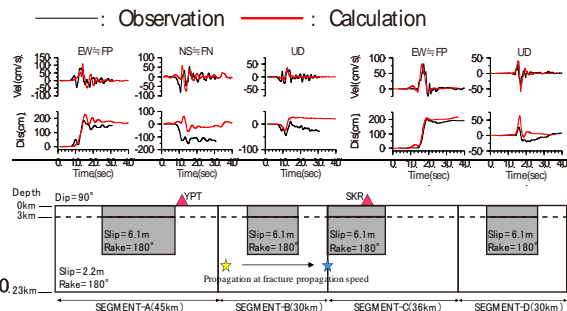


Fig.5 Evaluation results after reviewing the destruction type

Material characteristic evaluation for plastering restoration of Japanese style architecture in Taiwan

Misako Hanza¹⁾, Masaki Tamura¹⁾, Guanhan Jiang¹⁾, Osamu Goto¹⁾, Shigeru Sugasawa¹⁾, Chi-jen Chen²⁾, and Reimi Ishizawa¹⁾

¹⁾Department of Architecture, Kogakuin University, Japan
E-mail: dm18045@ns.kogakuin.ac.jp

²⁾Department of Architecture, National University of Kaohsiung, Taiwan

Abstract

Japanese style architecture is a collective term for a group of buildings built in Taiwan during the period of Japanese rule from 1895 to 1945. Its accounts for half of the buildings currently designated as cultural assets in Taiwan. One of these is Shoyoen, which is targeted this time. Table 1 shows an overview of Shoyoen. Shoyoen is a Japanese-Western mixed type villa architecture built in Kaohsiung, Taiwan, as a villa for the Japanese noble Kozui Otani^[3]. In this research, to focus on the plastering finish part of Shoyoen, the composition and construction method at the beginning of construction will be examined by conducting chemical component analysis on the finishing layer collected locally. From this result, the purpose is to create a construction procedure for restoration work.

Outline of experiment

The target of this analysis is the three places plastering finish. Fig. 1 shows three target elements. The surface of the first internal wood lath was covered with house paint, and it was not clear whether the interior was Japanese lime plaster (Shikkui) or gypsum. In addition, in order to analyze what the green component used in the internal wood lath ceiling and the outside brick masonry groundwork pillar was analyzed using a fluorescent X-ray analyzer^[1]. Fig. 2 shows the analysis results. It can be seen that plaster (Ca(OH)₂) was used instead of gypsum (CaSO₄) because sulfur (S) was not detected on the wall of c). The ceiling a) and the pillar b) constructed in green both detected chromium oxide (Cr₂O₃) in common. That is, it is considered that the green pigment was a chrome green pigment.

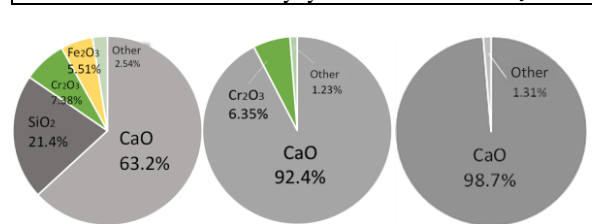
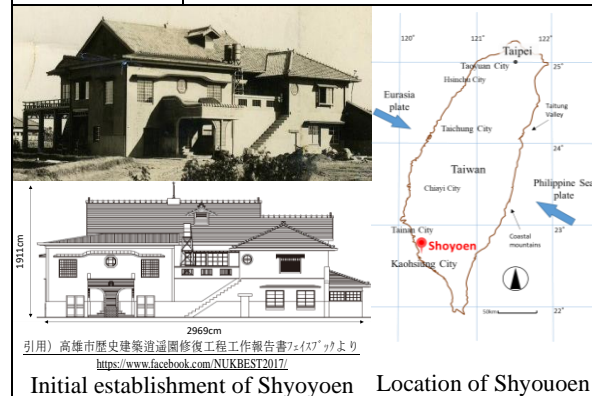
Determine the chrome pigments used in Shoyoen. Shoyoen was built with craftsmen and materials from Japan. Therefore, it is thought that the pigment was also Japanese products. The mine series was the first to use chrome green as a pigment in Japan^[2]. The mine green component is 100% chrome, and it is highly possible that it was used in the Shoyoen.



a) Internal ceiling b) Outside pillar c) Internal wall
Fig. 1. Actual element of Shoyoen

Table 1. Summary of Shoyoen

location	No. 64-8, Fuxing 1st Road, Xinxing District, Kaohsiung City
Designer	Kojiro Nikaku
Construction	Construction in 1939
Structure and format	Structure : 1st floor brick, 2nd floor RC and wooden format : Rebar truss, tile-roofing, shingle the roof
Cultural property classification	Historic architecture



a) Internal ceiling b) Outside pillar c) Internal wall
Fig. 2. Component analysis results by X-ray fluorescence analyzer

In addition, the green color often seen in Taiwanese buildings is often green-blue, which is the color of rust produced by oxidation of copper. The green-blue color changed over the years and was considered a noble color due to its beauty. Kozui Otani is thought to have made the entire Syoyoen green based on the characteristics of patina and the culture of Taiwan's patina. The mine was the same shade as this green-blue. Determine the amount of pigment to reproduce the original color. First, test specimens were created to bring the pigment content of a) the internal ceiling and b) the outer pillar closer. Table 2 shows the mixing proportion of the specimen. Fig. 3 shows represents the green color a^* values of the test specimen and the actual element. a) The ceiling had an original a^* value of -5.9. The chromium content was 0.68% when the numerical curves from the test specimens intersected. b) The pillar also had an original a^* value of -4.2, and the value that intersected the curve was 0.93%. The amount of pigment calculated from this graph is considered to be the same as the original color, and in actual construction, construction site compounding is performed based on this value.

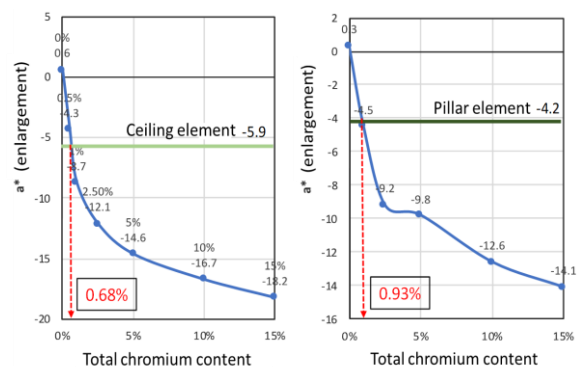
From June 14th to 17th, 2019, construction was performed by Japanese craftsmen on the plastering finish surface at Shoyoen. The amount of pigment added to the compounding was adjusted from the results of this study. Table 3 shows the job site compounding and the results of color values of the plastered places. Looking at the table, it can be seen that numerical results that are quite close to the original color were obtained even with the amount of site compounding. Shikkui ceiling has an original a^* value of -5.5, compared to -5.9, and mortar pillar have an original value of -4.2, this time -4.4. Fig. 4 shows the construction location after painting. The shikkui ceiling was unique in its original texture, but its characteristics could be reproduced, and the color became quite close even visually. In addition, the mortar pillar is not inferior to the original element. Job site compounding is based on the craftsman's senses, and it is thought that work efficiency will be improved by analyzing and digitizing it. And this Soyoen restoration work will lead to research to improve historical architectural repair technology in the future.

References:

- [1] Misako Hanza, Masaki Tamura and others: Evaluation and verification experiment of the deterioration state of the lath plaster ceiling in heritage buildings, Kanto branch research report of the Architectural Institute of Japan, March 2018
- [2] Mine, Cement / Concrete Pigment Technical Report, Yabuhara, 2019 quote
- [3] Kaohsiung City Historic Building Xiaoyao Garden Restoration Project Entrusted Construction Case [Service Proposal] April 27, 2013

Table 2. Test specimen mixing proportion

a) Internal shikkui ceiling				
Materials used (g)	lime	shell lime	tsunomata	fibers for plastering
	200	80	6	8
Total chromium pigment content (%)		15 / 10 / 5 / 2.5 / 1 / 0.5		
b) Outside mortar pillars				
Materials used (ratio)	silica sand		cement	
	1		1	
Total chromium pigment content (%)		15 / 10 / 5 / 2.5 / 1 / 0		



a) Internal shikkui ceiling b) Outside mortar pillar
Fig. 3. Chromium content and a^* value of ceiling and pillar specimens

Table 3. Site compounding and color value results

a) Internal shikkui ceiling			
Materials used	lime	shell lime	pigment (mine green)
	20kg	8kg	196g
a* value result	original : - 5.9 → result : - 5.5		
b) Outside mortar pillars			
Materials used	silica sand	cement	pigment (mine green)
	25kg	30kg	562g
a* value result	original : - 4.2 → result : - 4.4		



a) shikkui ceiling b) mortar pillars
Fig.4. After painting the target construction site

Collapse Prevention of a Lath and Plaster of Ceiling: Seismic Retrofitting of the Main Building of the Former Ibaraki Prefectural Tsuchiura First High School

Guanhan Jiang, Masaki Tamura, Osamu Goto and Naohiro Kobayashi

¹⁾Graduate School of Architecture, Kogakuin University, Japan E-mail: nephele_iknak@icloud.com

²⁾School of Architecture, Kogakuin University, Japan E-mail: masatamu2007@jcom.home.ne.jp

³⁾⁴⁾Research Institute, Kogakuin University, Japan

E-mail: ogoto@cc.kogakuin.ac.jp, kobana016@gmail.com

Abstract

To prevent the possible collapse of the lath and plaster ceiling for the Main Building of the former Ibaraki Prefectural Tsuchiura First High School, this study examined preventative measures and developed a reinforcement method as practical application and evaluated it.

Background

In recent years, published research* has emphasized the extension of building life and effective use of building stock, increasing demand for long-term use of buildings, while repair work has been undertaken due to various constraints such as technology, costs, human resources, and materials. It is known that many buildings have been demolished and have reached the end of their lives. Under these circumstances, Kogakuin University has been focusing on research to repairing cultural properties, and has established a method of restoration for plastered walls and ceilings, which obtained a patent approved by the JPO.

A front view of the former Ibaraki Prefectural Tsuchiura Junior High School main building before the start of earthquake-proof reinforcement work is shown in Photo 1, and an overview is shown in Table 1. In this study, two types of construction were performed on the former Ibaraki Prefectural Tsuchiura Junior High School main building, the reinforcement work by the patent construction method and the reinforcement work by the applied construction method determined by applying the patent construction method.

Construction

Fig. 1 shows a schematic cross-sectional view of the construction method based on the patent method, and Photo 2 and Photo 3 summarizes the procedure of the construction method. In this construction, it is divided into a place where construction is possible from the ceiling and a place where construction is necessary from the finished surface because construction is difficult from the ceiling. Therefore, repair methods and construction procedures suitable for each location were studied. Since it is difficult to predict the thickness of the wooden member that is the base in the moldings on the four sides of the room, it was impossible to construct from the ceiling, and the construction method on the finished surface was examined.

Fig. 2 shows a schematic cross-sectional view of the construction by applying construction method. Table 2 summarizes the procedure of the construction method. Only the ceiling plane is removed from the ceiling part plane and part of the molding part, and the cross section is exposed at the boundary part

between the molding part and the plane. It was confirmed that this occurred. Table 4 summarizes the construction procedures and photos. In order to prevent collapse, a method for repairing gaps in existing parts was studied, and this was tentatively named the sealing method. In this construction method, the basic principle is the same as that of the patent construction method, and the resin is filled in the gap between the wood slide base and the existing plaster layer, and the cured resin and the filler mixed with the resin serve as the anchor.



Photo 1. A front view of the former Ibaraki Prefectural Tsuchiura Junior High School main building

Table 1. an overview

address	4-4-2 Manabe, Tsuchiura-shi
architect	Komatsu Kinji (1877-1919 Ibaraki Prefectural Government Repair Department)
Completion date	1904 (Meiji Method 37)
Structure and format	Wooden one-storied house, concave plane, gothic style Wall / ceiling: plaster finish
Cultural properties status	1976 (Showa Method 51) Designated as an important cultural property of the nation's first country as an old junior high school building
Construction location	Entrance: Ceiling center decoration, ceiling molding section
Background	During the Great East Japan Earthquake, the entrance ceiling plane collapsed. (Public property) Requested repair to Kogakuin University from the Cultural Properties Building Conservation Technology Association

In this construction, both the patent method and the conventional sealing method were combined. In addition, almost no change on the curing rate of the material due to weather effect was observed. Nevertheless, in this construction, the considerations on safety, enhancement of work environment, resin handling, etc. remained as problems, although construction can be done without impairing the aesthetics of the finished surface, and the degree of freedom in technical operation is still relatively high. In order to improve the workability, it was considerable that to understand the construction method and familiarity with the work are necessary, this project also examined above problems and improvements related to the tools and equipment used in the construction.

Result

This project established a new construction method to prevent the collapse of the plastered wooden plaster ceiling for the former Ibaraki Prefectural Tsuchiura Junior High School. During the construction, not only the previous mentioned patent method for the central decoration part has been done, but also the current situation and all practical considerations are undertaken.

References

[1] Kentaro Oka, Masaki Tamura, Osamu Goto, Hiroaki Maruyama and Junichi Yokoshima, Experimental Study on Conservation a Preservation for historical Architecture using Plaster Finishing Material, SCMT4 The Fourth International Conference on Sustainable Construction Materials and Technologies, Las Vegas, USA, 2016

[2] Maintenance and Conservation Strategy for Building and constructed assets in Life Cycle Management Part 10 - Prevention Construction of Wooden Lath and Plaster of Ceiling Boards of Tsutiura junior high school building, Guanhan Jiang, Masaki Tamura, Osamu Goto and Naohiro Kobayashi, Academic Lecture of Architectural Institute of Japan, 2019

Table 2. the procedure of the construction method

1 st Apply resin	4 th Fill the hole
2 nd Filling the material	5 th Putting the hemp rope
3 rd Apply resin	6 th Apply resin

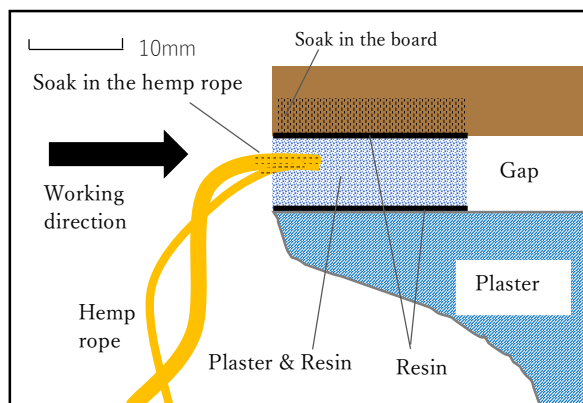


Fig 2. a schematic cross-sectional view of the construction by applying construction method

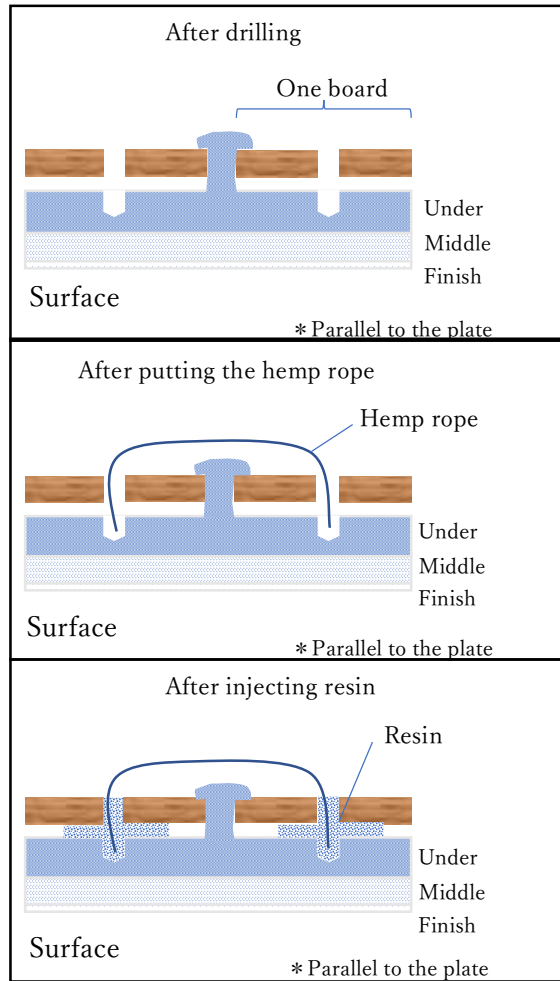


Fig 1. a schematic cross-sectional view of the construction method based on the patent method



Photo 2. drilling



Photo 3. After all steps

Design a Robot to Inspect Faults on the High Voltage Power Lines

Nguyen Hoang Mai¹⁾

¹⁾Department of Electrical Engineering, Danang University of Science and Technology, Vietnam

Email: nhmai@dut.udn.vn

Abstract

Our country as of July 26, 2018 has 7,503km of the 500kV line of circuit 1 and circuit 2 and is continuing to draw circuit 3 in recently. Therefore, when completed, the total length of the 500kV line can reach 10,000km. The length of 220kV line is 16.903km. Line parameters need to be monitored continuously to ensure power supply reliability. But now that job is using workers with very slowly speed and discontinuous parameters. Therefore, if an automatic parameter monitoring robot is built, the number of self-monitoring devices will need a lot. The continuous and accurate parameter monitoring will allow transmission companies to make better maintenance, repair, replacement, operation decisions, saving time and effort. Therefore, the economic and technical efficiency will be great. The paper presents a smart self-propelled robot study that moves on high-voltage and high-voltage lines to support monitoring of line operation.

Keyword: Optimization, Robot, DC motor, inductance, electromagnetic field, automatic control, drone, high voltage power line process

I. INTRODUCTION

These two types of High voltage power lines, one single wire and one multi-wire. Single wire type for medium power and voltage below 400Kv. For power lines with higher voltages, the phase division to reduce halo loss and increase the current in the wire. The line has support columns and cross-ties columns. Each column has a different way of hanging porcelain, the support pillars can be hung vertically or horizontally, while the crossbar only hang horizontal and pull porcelain, shown that Figure 1. Due to the terrain passing through many mountainous areas, the slope of the road large wire, there are negative deflections, that is, the point of the conductor is lower than the foot of the column as shown in Figure 1.

The operation process of the line is 24/24h. Therefore, it is important to watch the line parameters. During operation, the conductor is hot, struck by lightning, the wire is broken, discharges damage the surface of wires, porcelain, aluminum - irregular steel, oxidation, rust ... make conductor characteristics unlike the original, resulting in reduced operating quality. Therefore, it is necessary to have equipment to observe and record parameters continuously. The parameters are:

- Measure temperature
- Measure a surface of the wire
- Measure current of the wire if has broken
- Measure the robust of the wire.

This is a difficult problem for Vietnam electricity industry as well as other countries in the world.

From that requirement, the authors have built a project to research, design, build automatic robots to move on the line and record the parameters to pass to the processing line monitoring center, avoiding broken down and reduce potential problems that can cause long-term harm.



Figure 1. The 500kV power line of Vietnam

The requirement of the robot is able to move on the wire for a long time, so the energy problem is very important. Obviously, it is impossible to use batteries or batteries in this case to supply robots. So, the idea of the project is to design the source that directly extracts the energy on the line to make the robot supply work. The second problem is moving through the column ranges, because the types of columns are not the same so it is impossible to share the same migration principle. Here the column transfer design is used by drones (UAV) to control the robot to fly up and move to the new column place.

II. DESIGN MECHANISM OF ROBOT

Robot only moves on one wire, whether or not the electrical line is in division phase. This is because the need is that the robot must be light to UAV carry, and must have balanced motion, while the line does not always have to balance. Since then, the team has designed the robot mechanical part including parts as shown in Figure 2. The robot mechanical design focuses on moving wheels and chassis, durable balancing parts when hanging on a point. To calculate the robot to overcome a positioning frame on the 500kV line,

we must decide the drag to calculate the engine power just enough, ensuring light weight.

Consider a two-wheel vehicle running on a wire and the center of gravity as a standing point on a rigid bar

The principle of balance applied is that of stable equilibrium, which means that the center of the robot must be lower than the set point here. To do that, the moving parts, including the body of the frame, the wheels, and the engine, are located above the line point of contact, and the source and circuit board are located below the line. Induction coil is placed horizontally across the line and is always in equilibrium when moving normally, only when crossing the positioning frame, the center of gravity will shift to the contact point.

Call the mass of the upper part of the contact point m_1 , the mass of the part below the contact point is m_2 .

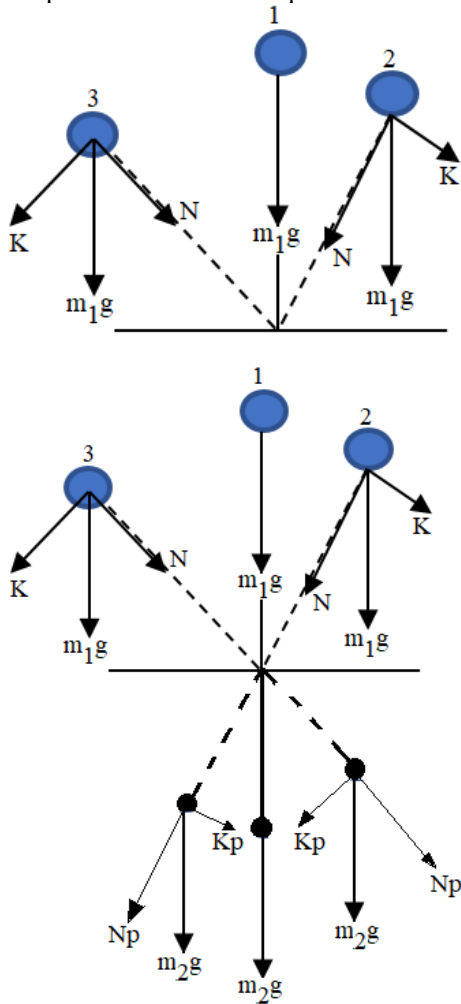


Figure 2. Description of balance principle.

Then, if the car is vertical, if $m_2 > m_1$, the focus will shift below the contact point.

If the vehicle deviates to the left or right by a certain angle, the torque will be:

Above torque:

$$M_1 = Nl_1 = m_1gl_1\cos\beta \quad (1)$$

Below torque

$$M_2 = -Npl_2 = m_2gl_2\sin\beta \quad (2)$$

For robust balance then $|M_2| > |M_1|$, that is:

$$m_2gl_2\sin\beta - m_1gl_1\cos\beta > 0 \quad (3)$$

From that we have a condition balance of the β is:

$$\tan\beta > m_1l_1/m_2l_2 \quad (4)$$

We see a condition with horizontal wind: call square area wind is S.

Wind speed is v, weight density of air is σ , then press force of wind into square S is:

$$F = S.P.C_d \quad (5)$$

Here:

S is a main square area for wind

P is a wind pressure

C_d is an opposition factor.

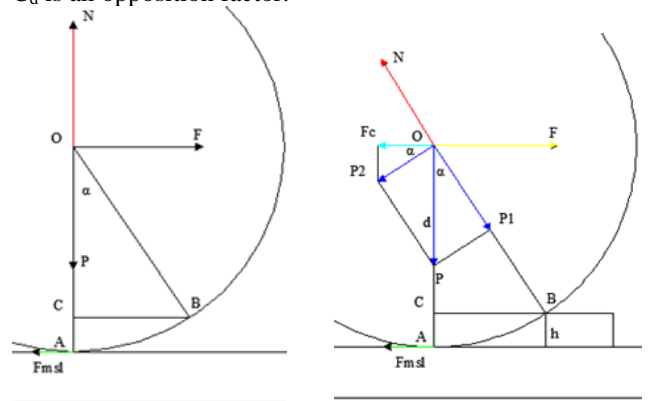


Figure 3. Description of passing position frame

Robot frame is made by 20x20mm shaped aluminum. This type of aluminum has a relatively low specific gravity, high mechanical strength, easy assembly so it is very suitable for making Robot frames.

Robot is built with 2 wheels, front wheel and rear wheel. It is specially built to help the robot move smoothly on the line. When the UAV brings the robot down the new pole, the wheels can also easily access the new line.

The transmission for the robot consists of a pulley + roller and a DC motor. When calculating the motor, it is necessary to calculate the load torque so that the motor can help the robot operate and cross the positioning frame.

If exposed at A: Robot running on the wire, the obstacle for stopping the movement is only the rolling friction, in this case the drag is not the largest. We do not use to calculate engine choice.

- Gravity and reaction force cancel each other out.

- Rolling friction force

$$F_{mst} = \mu . N' = \mu . N = \mu . m . g \quad (6)$$

If contact at B: Assuming the wheel is moving on the line, there is an obstacle (positioning frame) of height h.

Analysis of forces yields forces:

Gravity P, then P is analyzed into 2 forces P_1 and P_2 . Jet N

Rolling friction force, in this case $F_{msl} = 0$. Thrust of the F engine. The resistance F_c is the projection of P_2 force in the horizontal direction.

We call d is the length of OC:

Jet N and P_1 cancel each other out

Rolling friction force $F_{msl} = 0$.

Drag

$$F_c = P_1 \cdot \cos(\alpha) = P \cdot \sin(\alpha) \cdot \cos(\alpha) = M \cdot g \cdot \sin(\alpha) \cdot \cos(\alpha) \quad (7)$$

The main force F act onto robot to run pass fix frame

$$F \geq F_c = M \cdot g \cdot \sin(\alpha) \cdot \cos(\alpha) \quad (8)$$

A torque of motor:

$$M \geq F_c \cdot R \cdot \frac{2}{3} = M \cdot g \cdot \sin(\alpha) \cdot \cos(\alpha) \cdot R \cdot \frac{2}{3} \quad (9)$$

Here:

R is a radius of the wheel.

III. DESIGN ELECTRIC SOURCE

Based on the principle of electromagnetic induction, the robot power source is designed by an open ferrite core induction coil. The induction coil is controlled so that when it reaches the positioning frame, it opens itself and the robot passes over the positioning frame, after which it closes. Similarly, at the end of the column, the robot starts to touch the anti-vibration barbell or the ceramic head, it will take pictures of the porcelain and then open the sensor circuit for the UAV to pick up the robot, move to the new column range. From there, We designed the source as shown in Figure 3.

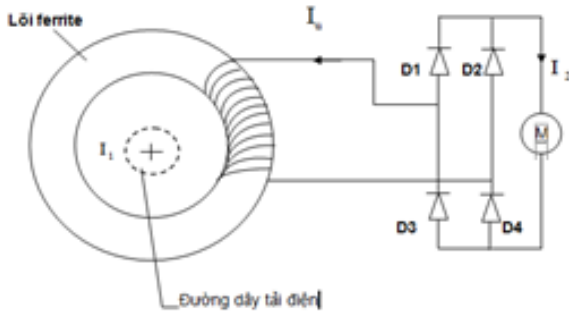


Figure 4. Description inductance coil

In Figure 3, to avoid the use of battery batteries in robot movement, to solve two problems, the first is to increase the robot load, the second is the battery or battery with finite power, can't move long, while with sensors, robots can move for a very long time, maybe up to months.

We have the following parameters, the current running on the 500kV line is in the range 400A to 800A when operating, this is the parameter provided by the transmission company.

$$i_{1min} = 400\sqrt{2} \cdot \sin(100\pi t) \quad (A)$$

$$i_{1max} = 800\sqrt{2} \cdot \sin(100\pi t) \quad (A)$$

Power of motor: $P = 300W$

We have:

$$B = \mu\mu_0 \frac{I_1}{4\pi R} \cos\theta_1 - \cos\theta_2 \quad (10)$$

Because power line 500kV is long too. Therefore, we see current line is unlimited line. $\theta_1 = 0$ and $\theta_2 = \pi$, so (5) is:

$$B = \frac{\mu \cdot \mu_0 \cdot I}{2 \cdot \pi R} \quad (11)$$

With I_1 is a primary current (A). It is about 400 A to 800A by experiment.

In this way, the team has figured out the actual parameters of the source device and ensures enough for the robot to work long term, as well as provide embedded computers and induction motors to lift the steel core.

With this design structure, after completion, the robot was tested on a sample line at Danang University of Technology. The result for the parameter is as follows:

- Electric current pumped on line 629A
- Voltage obtained on the two motor poles: 7.7 volts
- Operating motor current: 7.9A

The motor completely passes the positioning bracket and line angle below 30 degrees of the slope scale.

The Faraday cage:

Because the robot operates in high voltage environment with the frequency of 314 rad/s, the minimum electric field strength is 80kV/m, the protection of electromagnetic shielding for the electronics inside the robot is very important. The magnetic field around the conductor is closed-loop, but the electric field is inclined to the outside, so the magnetic shield must ensure both. Based on [3], it was proved that the magnetic field passing through the magnetic shield will cause the gradient magnitude of the magnetic vector as shown in Figure 4. This will be the basis for the design of the magnetic shield. The theory of Faraday magnetic shielding has been perfected for a long time, so in this design, we only use the existing research results to calculate the magnetic barrier, not go against the research process. However, the evaluation can return empirical results to compare with theory and determine applicability.

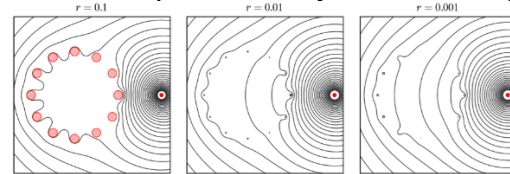


Figure 5. Description of magnetic in cage.

Electromagnetic:

$$\phi = K \cdot \log|z - z_s| - \sigma(z) \quad (12)$$

Where z is the position that identifies the magnetic field, $\sigma(z)$ is the proportional quantity that characterizes the ability to touch between turns of the wires, K is the characteristic factor for the magnetic field.

We have the gradient vector of the magnetic field through the wire cross sections:

$$|\nabla\phi(0)| = \frac{-2 \log r}{n|z_s|} \quad (13)$$

Where r is the radius of the wire ring sections and n is the number of sections. According to [3] one calculates the

value of the magnetic field in the screen as shown in Figure 5. According to Figure 5 we see that when the size of the wire is small, the magnetic field can pass through the screen. The fact that the Faraday screen works only with modified magnetic fields, while static magnetic fields such as the earth's magnetic field or fixed magnets can still pass through the screen.

Table 1. Description of the word chest in the Faraday level

	$r=10^{-1}$	$r=10^{-2}$	$r=10^{-3}$	$r=10^{-4}$	$r=10^{-5}$	$r=10^{-6}$
$n = 5$	0.1118	0.2663	0.3348	0.3723	0.3959	0.4122
10	0.0236	0.1582	0.2399	0.2902	0.3241	0.3486
20	0.0003	0.0699	0.1406	0.1916	0.2300	0.2598
40	0	0.0229	0.0693	0.1082	0.1406	0.1681
80	0	0.0047	0.0297	0.0539	0.0757	0.0954
160	0	0.0000	0.0112	0.0246	0.0372	0.0492
320	0	0	0.0036	0.0105	0.0173	0.0239

Thereby we will design magnetic shield with a mesh structure of 0.1mm in diameter. That is, the mesh thickness is 0.1mm, with the number $n = 40$ fibers. However, knitting such a mesh is not effective, so we will replace it with a sheet metal screen with the corresponding thickness. When the dimensions shown in Table 1 are reached, compared to Figure 4, the magnetic field of the alternating source will be completely eliminated in the Faraday screen. Design Drone process

We use drone to bring robot onto wire and while robot run to end of segment line then drone will bring robot to next segment line. The main problem is control drone on the power line 500kV. This is an electrical field too. We have completed an experiment drone onto power line with good result.

IV. SIMULATION RESULT

After designing the mechanical part, the source part. We conduct the robot's motion trajectory on the line including:

- Positioning Framework
- Regular straight wire
- Strings in large 30-degree deflection.

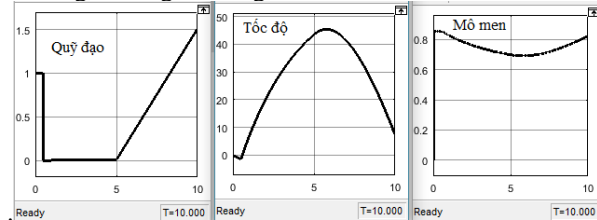


Figure 6. Simulation of state action cases.

The simulation results of motor movements are shown in Figure 5. In which the motor speed when running on straight conductors reaches a maximum of 40 rpm through the reduction gear box. Initially due to the positioning frame, the engine has a speed of seeing, after passing the positioning frame, the motor is reversed due to the movement going forward, then the engine accelerates on the braking line and up to time 5 sec, the wire started to slope up to 30 degrees, then the engine speed decreased until the end of the simulation. Accordingly, the torque of the engine

also changes accordingly to control the robot moving through obstacles on the line

V. EXPERIMENT

After simulation, the team built a robot and experimented with the name of the non-live line, with the line size and positioning frame being the field of 500Kv line. The robot is manufactured as shown in Figure 6



Figure 7. The body of robot.

Experiments show that the robot has operated well and passed the positioning frame very well, ensuring the speed and torque as required.

The experimental results were measured as in Figure 7



Figure 8. Experiment data of the robot.

The data measured when the robot is operating shows that the pumped current is 629A, the sensor generates 7.56VDC voltage, the current through the motor is 3.53A, approximately 30% of the motor rated current. This is a result consistent with the theory of electric drive and allows the engine to operate in long-term mode.

We have repeated experiments before presented a final result. There are difficult when contact to high electromagnet on power line. We have seemed difficulty control when happened a change of electric power in wire. The drone has been oscillation and can not drop on the wire. So that only short state and drone become balance after some time.

We use drone to fly on power line 500KV as figure 9.



Figure 9. Experiment of drone parked on the power wire 500kV



Figure 10. Drone flies near power line.

VI. DISCUSSION

The research project of the group has basically designed the working robot part. Theoretical calculations of the electromagnetic field show that the source part meets the requirements with a no-load voltage of up to 20 volts. However, in reality, the current of the line will be between 400A and 800A so the voltage of the induction source has a minimum of 10V, then the robot can still run.

The robot mechanical part has not taken into account the bearing capacity of the material is shaped aluminum. But with a robot weight of 4kg it is within the tolerable load range of the aluminum-shaped material capable of being purchased in the Vietnamese market.

Experimental results show that the robot mechanical frame withstands the impact of environment such as wind and robot oscillation when the wind is strong to level 7, which is an equal to 1/3 of the radius of oscillation along the vertical guide bar of the robot.

VII. CONCLUSION

This is the first study, so some designs are not completely complete and accurate model, as well as the process of both designing and testing, many parameters have been experimentally manipulated and revised. In the near future, the team continues to develop batteries for embedded computers and attached drones to the control by image recognition to automatically bring the robot through the

ceramic string, as well as high-slope columns. I can't run up the slope.

Reference

- [1]. Dr C. T. Whelan, 2000, The Principles of Dynamics, Pembroke College, Cambridge publishing.
- [2]. Rodney Hill, 1964, Principles of Dynamics 1st Edition, ISBN: 9781483185279, Pergamon 1964 publishing.
- [3]. D. P. Hewett and I. J. Hewitt, 2017, Homogenized boundary conditions and resonance effects in Faraday cages, Mathematical Institute, University of Oxford, UK.
- [4]. S. Jonathan Chapman, David P. Hewett, Lloyd N. Trefethen, 2015, Mathematics of the Faraday Cage, 2015 Society for Industrial and Applied Mathematics, Vol. 57, No. 3, pp. 398–417.
- [5]. Tran Van Chinh, 2011, Electromagnetics field, The Construction publishing, Hanoi
- [6]. John J. Craig, 2005, Introduction to Robotics, Pearson Education International, Pearson Prentice Hall®
- [7]. Mark W. Spong, Seth Hutchinson, and M. Vidyasagar, 2004, Robot Dynamics and Control, McGraw Hill publishing

Design of 3 DoF Statically Balanced Articulated Manipulator Based on a New Gravity Balancer

Hong-Nguyen Nguyen¹⁾

¹⁾Faculty of Project Management, The University of Danang, University of Science and Technology, Vietnam
E-mail: nhnguyen@dut.udn.vn

Abstract

A statically gravity balanced manipulator can shift to any position with only little or no initial force/torque as in a gravity-free environment. Based on the theory of conservation of potential energy, concept of the gravity balancer and the virtual-ground scheme, this research proposes the design of 3 DoF balanced manipulator.

1. Concept of Scotch Yoke type balancer

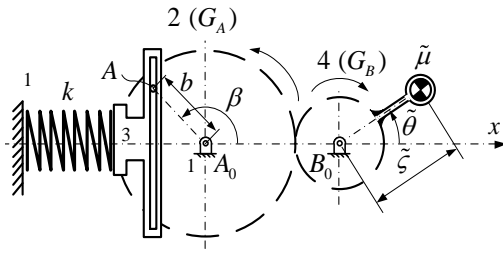


Fig. 1. Scotch yoke type gravity balancer

The static balance of a system as shown in Fig. 1 can be achieved if the summation between the gravity potential energy and elastic potential energy is constant. Hence, two conditions must be satisfied:

$$C1: \tilde{\mu}g\tilde{\zeta} = \frac{1}{4}kb^2$$

$$C2: \sin \tilde{\theta} = -\cos 2\beta$$

2. Virtual-Ground Scheme

Based on the virtual base scheme proposed by Lin et., al. [1], series of spatial RSSR parallelogram linkages can be used in an articulated system to emulate a virtual ground for fitted springs. However, such construction is considered overdesigned. In this research, a much simpler, generalized, planar RRRR parallelogram linkage can also provide a virtual-ground for each distal primary link i .

3. Numerical Modelling and Simulation

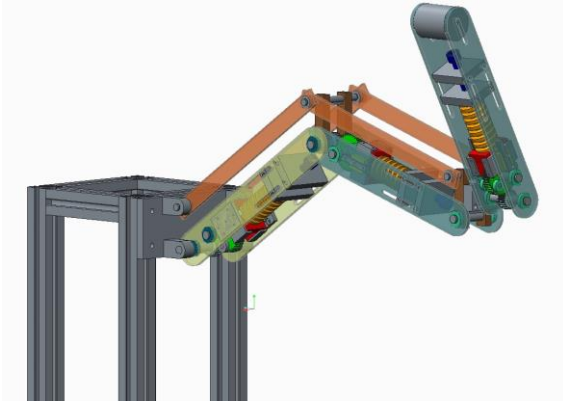


Fig 2. The design of 3 Dof Balanced Articulated Manipulator

Table 1. D-H parameters and mass properties of the mechanism

i	d_i	$\tilde{\Theta}_i$	a_i	α_i	m_i	m_i'	m_i''
1	0	$\tilde{\Theta}_1$	240	0	0.92	0.08	0.15
2	0	$\tilde{\Theta}_2$	0	90	0.85	0.08	0.25
3	240	$\tilde{\Theta}_3$	240	0	1.5	0	0

Data given in mm, degree and kg

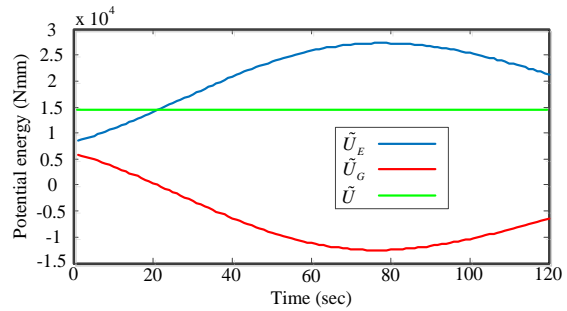


Fig 3. Potential energies of the overall system

References:

- [1] Lin, P. Y., Shieh, W.B., and Chen, D. Z., "Design of a Gravity-Balanced General Spatial Serial-Type Manipulator", *ASME J. Mech. Rob.*, 2(3), pp. 031003 (2009)
- [2] Nguyen, H. N., Shieh, W. B., "On the Design of the Gravity Equilibrator Using Scotch Yoke Derivative Mechanism", *New Advances in Mechanism and Machine Science: Proceedings of the 12th IFToMM International Symposium on Science of Mechanisms and Machines (SYROM 2017)*
- [3] Nguyen, N. H., "Design, Manufacturing and Justification of Spatial, Articulated, Gravity-Balancing Manipulators Based on a Novel Spring Type Equilibrator", *M.Sc. Thesis, Ming Chi University of Technology, New Taipei, Taiwan (2017)*

Evaluation of a locally-fabricated small-scale pyrolizer for bio-oil and bio-char production of seaweeds (*Sargassum sp.*) from Roxas City, Capiz, Philippines

Romel A. Arrobang¹⁾, Rossana Marie C. Amongo¹⁾, Delfin C. Suministrado¹⁾ and Marisa J. Sobremisana²⁾

¹⁾ Agricultural Machinery Division, Institute of Agricultural Engineering, College of Engineering and Agro-Industrial Technology, University of the Philippines Los Baños 4031, Philippines
E-mail: raarrobang@up.edu.ph

²⁾ School of Environmental Science and Management, University of the Philippines Los Baños 4031, Philippines

Abstract

This study served as a continuous effort to further investigate the fuel characteristics of seaweeds from Roxas City, Capiz, Philippines through pyrolysis. The physicochemical properties of the bio-oil and bio-char produced from a locally-fabricated small-scale pyrolizer through proximate analysis and heating value determination. Dried raw samples of *Sargassum* were subjected to proximate analysis and heating values were obtained to quantify the biomass potential of seaweeds. Moisture content determination and proximate analysis were done through gravimetric method for obtaining the percent composition of each component. The heating values were obtained using a bomb calorimeter. The heating value obtained from the analysis of dried raw *Sargassum* is 10.95 MJ/kg. A small-scale pyrolizer was fabricated using local materials for the conduct of an experimental pyrolysis in which *Sargassum* is the feedstock. A three-valve burner stove connected to a liquid petroleum tank was used as the heat source for the process. Results from the experiment showed that as the temperature increases, the amount of bio-oil collected also increases while the quantity of bio-char produced decreases. From the results of the proximate analysis of the bio-char, it was evident that volatile matter and fixed carbon content decreases while ash content increases with the increase in temperature. In conclusion, this study proves that *Sargassum* has fuel potential—as raw feedstock as well as for bio-oil and bio-char production through pyrolysis.

Keywords: seaweeds, *Sargassum*, pyrolysis, bio-oil, bio-char

References:

- [1] Chhiti Y, Kemiha M. 2013. Thermal Conversion of Biomass, Pyrolysis and Gasification: A Review. The International Journal of Engineering and Science. 75-85.
- [2] Choi J, Woo HC, Suh DJ. 2014. Pyrolysis of seaweeds for bio-oil and bio-char production. The Italian Association of Chemical Engineering.37: 121-126.
- [3] Michalak I. 2018. Experimental processing of seaweeds for biofuels. WIRES Energy and Environment. 1-25.
- [4] Novak J, Busscher W, Laird D, Ahmedna M, Watts D, Niandou M. 2009. Impact of biochar amendment on fertility of a southeastern coastal plain soil. Soil Science. 105-112.
- [5] Zhang J, Liu J, Lui R. 2014. Effects of pyrolysis temperature and heating time on biochar obtained from the pyrolysis of straw and lignosulfonate. Bioresource Technology.

Investigation of Optimum Geometry for Synthetic Jet Fan

Ryoichi Moriyama¹⁾, Takeru Shinohara²⁾, Koichi Nishibe³⁾, Hiroshi Ohue⁴⁾, and Kotaro Sato⁵⁾

¹⁾Graduate School of Integrative Science and Engineering, Tokyo City University, Japan
E-mail: g1881061@tcu.ac.jp

²⁾Graduate School of Integrative Science and Engineering, Tokyo City University, Japan
E-mail: g1881028@tcu.ac.jp

³⁾Department of Mechanical Engineering, Tokyo City University, Japan
E-mail: knishibe@tcu.ac.jp

⁴⁾Department of Mechanical Engineering, Tokyo City University, Japan
E-mail: hohue@tcu.ac.jp

⁵⁾Department of Mechanical System Engineering, Kogakuin University, Japan
E-mail: at12164@ns.kogakuin.ac.jp

Abstract

As a first step to establish optimum geometry of the synthetic jet fan, this paper elucidates the influence of the duct width on the performance and internal flow fields for synthetic jet fan under constant representative velocity and dimensionless stroke by conducting computational fluid dynamics (CFD).

Last two decades, as an alternative to a flow control using a continuous jet, that using synthetic jet has been investigated. Because the synthetic jet is generated by a more compact and lightweight actuator than that of the continuous jet. To date, the flow characteristics including jet structure and formation /development criterion have been demonstrated experimentally and numerically [1-2]. In addition, the fundamental study on a fluid machinery such as a fan driving by the synthetic jet has begun and discussed an influence of the dimensionless stroke, $L = l/b$ (l and b are the stroke and slot width, respectively) on its performance [3-4], but many issues to be solved remain to establish the optimal design for synthetic jet fan.

As a first step to establish it, this paper elucidates the influence of the dimensionless mixing duct width, $W = w/b$ (w is the mixing duct width) on the performance and internal flow fields for the synthetic jet fan under constant representative velocity (Reynolds number) and dimensionless stroke by

conducting computational fluid dynamics (CFD).

Figure 1 shows the simulation domain with boundary conditions for CFD. Panel (a) and (b) show an overall calculating domain and magnified view with mesh around secondary inlet in case of $W = 10$, respectively. CFD performed using a commercial thermo-fluid simulation code SC/Tetra (MSC Corporation) assuming three-dimensional incompressible viscous flow and the internal flow field was symmetric to both x - y and x - z planes. Governing equation and turbulence model are Navier–Stokes equation and standard k - ϵ model, respectively, and boundary conditions was applied as shown in Fig. 1 in accordance with previous work of Nishibe et al. [4]. Total number of mesh for $W = 10$ and $W = 20$ are approximately 2,360,000 and 3,880,000. In addition, we confirmed the results obtained from CFD and experiments are qualitatively consistent by comparing the performance curve. The representative velocity, U , and dimensionless stroke, L , are defined as following

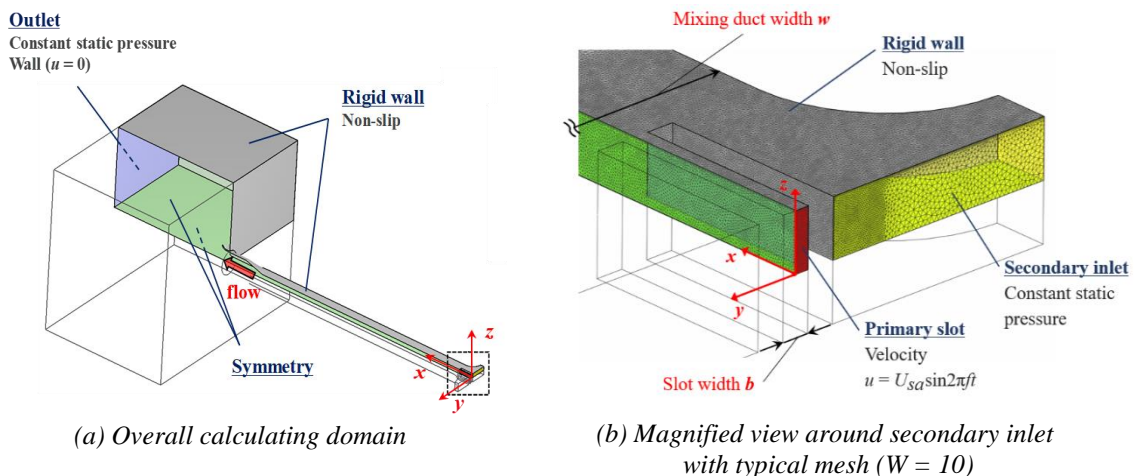


Fig. 1 Calculating domain with boundary conditions for CFD.

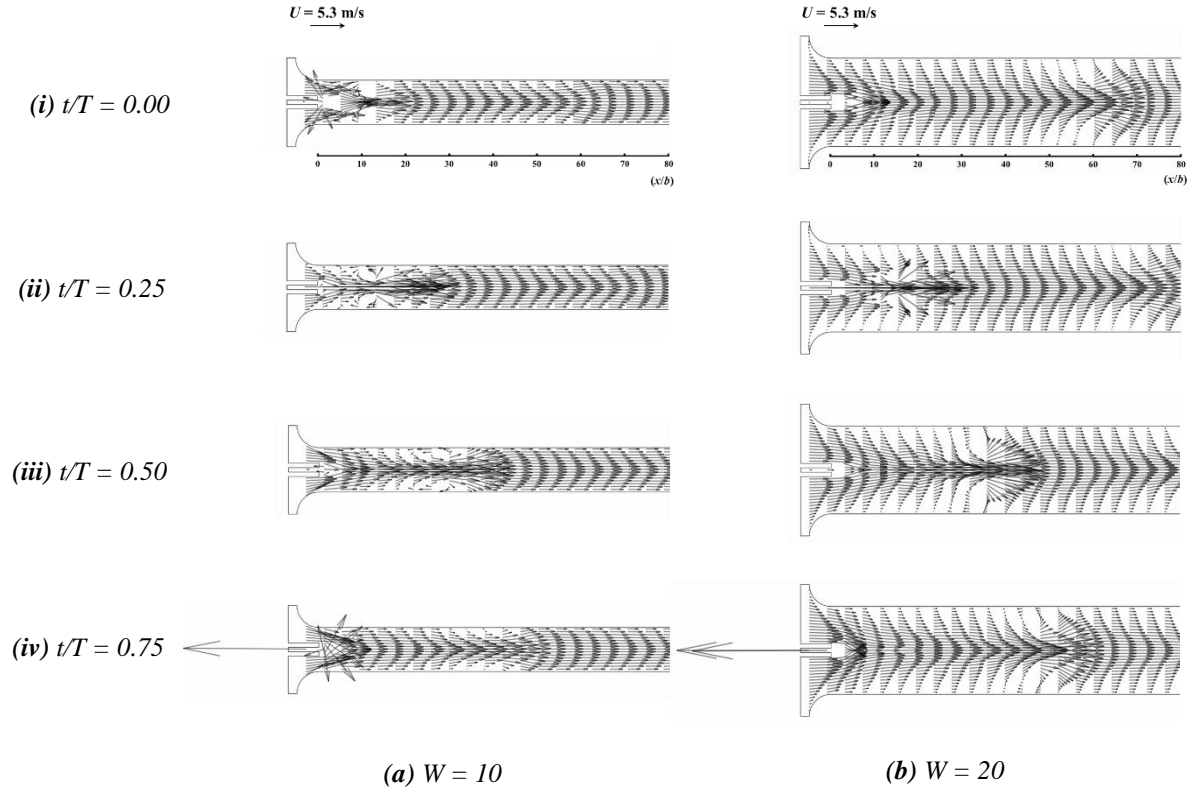


Fig. 2 Time variation of the velocity vectors at x - y plane in case of maximum flow rate ($L = 82$)

equations in accordance with Holman et al. [1]:

$$U = \frac{1}{T} \int_0^T U_{sa} \sin 2\pi f t dt = f l \quad (1)$$

$$L = \frac{l}{b} \quad (2)$$

where f , T , U_{sa} are the frequency, period and velocity amplitude at the primary slot, respectively, and l the stroke.

Figure 2(a) and 2(b) show the time variation of the velocity vectors at x - y plane in case of $L = 82$ and at maximum flow rate (no pressure difference between the secondary inlet and outlet of CFD domain) for $W = 10$ and 20 , respectively. Panels (i)-(iv) show the results in case of dimensionless time $t/T = 0.00$, 0.25 (maximum blowing), 0.50 and 0.75 (maximum suction), respectively. From both panels (a) and (b), it is observed that a vortex pair is generated downstream of the primary slot at $t/T = 0.25$. And then it translates further downstream of the mixing duct even in $t/T = 0.75$ (maximum suction). Because its induced velocity overcome the suction from the primary slot. In a free synthetic jet, it has been reported that the translation velocity of the vortex pair only depends on L under the same slot geometry and Reynolds number [2]. On the hand, that of the vortex pair from the primary slot for both panels (a) and (b) are different even though L is constant unlike that in the free synthetic jet. Furthermore, we also investigated time-averaged

maximum flow rate at outlet of the mixing duct in the same condition as Fig. 2 and obtained the maximum flow rate for $W = 20$ is approximately 1.4 times as much as that for $W = 10$. We assume that one of the reasons above results is an entrainment from the secondary inlet for $W = 20$ during the suction cycle is larger than that for $W = 10$ because the flow resistance around the secondary inlet probably reduces by the extending width of the secondary inlet.

From these results, the mixing duct width W affects to the internal flow characteristics and performance of the synthetic jet fan deeply.

References:

- [1] Holman, R. et al. (2005). "Formation criterion for synthetic jet", *AIAA Journal*, Vol. 43, No. 10, pp. 2110–2116.
- [2] Nishibe, K. et al. (2011). "Experimental and numerical study on the flow characteristics of synthetic jets", *Journal of Fluid Science and Technology*, Vol. 6, No. 4, pp. 425–436.
- [3] Ishizawa, T. et al. (2015). "Performance characteristics of a fan using synthetic jets", *Springer Proceedings in Physics*, Vol. 185, pp. 109–115.
- [4] Nishibe, K. et al. (2018). "Influence of Stroke on Performance Characteristics of Synthetic Jet Fan", *Journal of Applied Fluid Mechanics*, Vol.11, No.4, pp. 945-956.

[Li-doped C₆ | S₈] cells for long-cycle-life Li-S batteries

Yusuke Ushioda¹⁾, Kohei Inaba¹⁾, Keitaro Takahashi¹⁾, Yuki Ishino¹⁾, Kazuki Machida¹⁾, Hibiki Miyauchi¹⁾, Tatsuya Kawamura¹⁾, Masayoshi Watanabe²⁾, Shiro Seki¹⁾,

¹⁾ graduate school of Applied Chemistry, Kogakuin University, Japan

E-mail: bm19006@ns.kogakuin.ac.jp

²⁾ Department of Chemistry and Biotechnology, Yokohama National University, Japan

Abstract

Recently, demands of renewable energy are increasing with against lack of energy resources. However, power generation of renewable energies (solar and wind-power) drastically change with meteorological variation, and have poor stability of output performances. Therefore, large-scale and high-energy-density energy storage devises are strongly desired for stabilization of power system, and lithium-sulfur (Li-S) batteries are expected as the one candidates. Main advantages of Li-S batteries are low-cost of elemental sulfur (S₈) and their high capacity (1,672 mAhg⁻¹). On the other hand, intermediate compound of positive electrode material with charge-discharge process (Li₂S_x) can be easily dissolved into electrolyte solution with significant degradation of cells. Therefore, we used to electrolyte that can be expected to suppress the dissolution of Li₂S_x for lithium-sulfur battery. Moreover, lithium dendrite grows up at the Li metal anode and causes internal short-circuit. In this study, to prevent the Li dendrite, Li-incorporated negative electrode, such as C₆Li_x (Li-doped graphite electrode) (Fig. 1) was proposed as a stable electrode.

Experimental

C₆Li_x electrodes were prepared by reconstructed process of electrochemical cells (C₆ | electrolyte | Li) and washed with DMC solvent that does not react with Li-doped C₆Li_x electrode. In order to improve the efficiency of Li-S battery, we investigated applying C₆Li_x electrode as a negative electrode, and [Li(SL: sulfolane)₂]TFSA + 2HFE as a electrolyte. We fabricated coin cell ([C₆Li_x | [Li(SL)₂]TFSA + 2HFE | S₈]), and evaluated charge-discharge performances.

Results and discussion

Fig. 2 shows charge-discharge profiles for [C₆Li_x | [Li(SL)₂]TFSA + 2HFE | S₈] coin cell. Relatively high capacity (ca. 700 mAhg⁻¹), and quite sufficient reversibility (coulombic efficiency: ca. 100%) were obtained. Proposed Li-doped C₆Li_x negative electrode have the possibility, to make a low degradation Li-S cells even in the case of long cycle charge-discharge operations.

In the presentation, we will report Li-S battery

performances of [C₆Li_x | [Li(SL)₂]TFSA + 2HFE | S₈] cells, and other electrolyte systems.

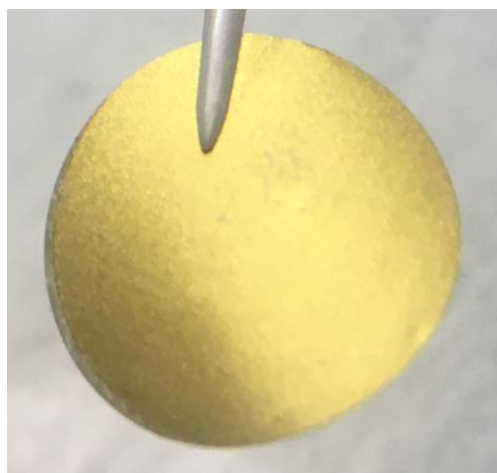


Fig. 1 Appearance of C₆Li_x electrode. The color of electrode changed black to gold by Li-doping.

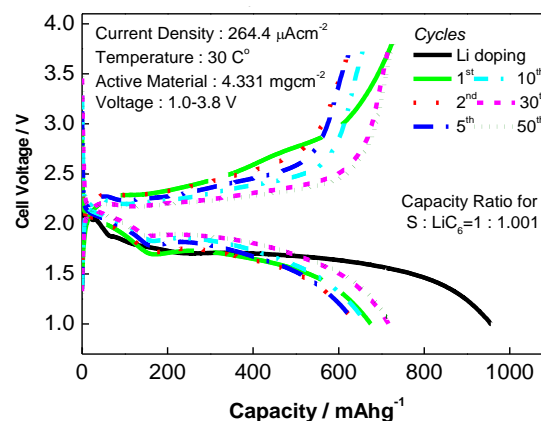


Fig. 2 Charge-discharge profiles [C₆Li_x | [Li(SL)₂]TFSA + 2HFE | S₈] coin cell.

Development of sensitive ionization method for Sr isotopes imaging by R-SNMS

Takeru Yoshida¹⁾, Yuzuka Ohmori²⁾, Yuta Miyashita²⁾, Yue Zhao³⁾, Masato Morita^{1,2)},
Tetsuo Sakamoto^{1,2,*}, Kotaro Kato⁴⁾, Volker Sonnenschein⁴⁾, Hideki Tomita⁴⁾, Toshihide Kawai⁵⁾,
Takeo Okumura⁵⁾, Yukihiro Satou⁶⁾, Masabumi Miyabe⁶⁾ and Ikuo Wakaida⁶⁾

¹⁾Department of Applied Physics, Kogakuin University, 2665-1 Nakano-machi, Hachioji, Tokyo, 192-0015 Japan

²⁾Grad. Sch. of Electrical and Electronic Eng., Kogakuin Univ., 2665-1 Nakano-machi, Hachioji, Tokyo, 192-0015 Japan

³⁾Collabarative Open Reserch Center, Kogakuin University, 2665-1 Nakano-machi, Hachioji, Tokyo, 192-0015 Japan

⁴⁾Nagoya University, Furo-cho, Chikusa-ku, Nagoya, 464-8601 Japan

⁵⁾Japan Neutron Optics Inc., 20-5, Takeshima-cho, Gomagori, Aichi, 443-0031, Japan

⁶⁾Japan Atomic Energy Agency, 790-1, Motooka Otsuka, Tomioka, Futaba-gun, Fukushima, 979-1151, Japan

*ct13087@ns.kogakuin.ac.jp

Abstract

Radioactive Sr is a β -rays-emitting nuclide and doesn't emit γ -rays. Therefore, it is difficult to analyze by radiation measurements such as imaging plate and γ -ray camera. Time-of-flight secondary ion mass spectrometry (TOF-SIMS) is suitable for the analysis of multi-elements and unknown samples. However, it has a problem of isobaric interference which derives from non-ionization-selectivity. Resonance laser sputtered neutral mass spectrometry (R-SNMS) is very effective method for radioactive materials with element selectivity. By using this method, the isobaric interference is avoided. In this study, the images of Sr isotopes were obtained selectively and efficiently by R-SNMS. This result provides a useful reference for the future analysis of radioactive ⁹⁰Sr.

1. Introduction

In Fukushima Daiichi nuclear disaster, the reactors hurled large amounts of radioactive material into the air. These radioactive materials exist in the environment as particulate matters. Among them, some nuclides are difficult to analyze, because they hardly radiate γ -rays. Time-of-flight secondary ion mass spectrometry (TOF-SIMS) is effective for analyzing particles. However, it has a serious problem of isobaric interference due to non-selective ionization with focused ion beam (FIB) sputtering. For example, it is impossible to distinguish between ⁹⁰Sr (radioactive) and ⁹⁰Zr (stable) by the mass spectrum of SIMS due to the limitation of mass resolution. The resonant laser ionization sputtered neutral mass spectrometry (R-SNMS) can overcome this problem [1]. It was reported that the isotopes of radioactive Cs were analyzed successfully by using R-SNMS [1]. In this study, we report an R-SNMS result of another element Sr. We have already reported an R-SNMS result of Sr [2]. However, this time, we investigated excitation of Sr to autoionizing Rydberg states in order to realize efficient ionization by R-SNMS. Here, we validated the R-SNMS of ⁸⁸SrCO₃ reagent.

2. Results and Discussion

The sample was ⁸⁸SrCO₃ reagent powder. We tuned a wavelength from lab-made Ti:Sapphire laser

corresponding to the ⁸⁸Sr transition level to selectively ionize the target element. Here, we selected the 5s² (ground state) to 5s5p orbital and the 5s5p to 5p² (autoionizing state) orbital as the resonance absorption scheme of Sr by using two wavelength-tunable Ti:Sapphire lasers (fundamental wavelength 700~1000 nm, and second order harmonic wavelength 350~500 nm). The resonance absorption occurs due to the photon energy was matched to the energy levels of Sr, and subsequent absorption of either photon results in ionization. The light source was incorporated into our FIB-TOF-SIMS equipment. We succeeded in obtaining the mapping of the reagent of ⁸⁸SrCO₃ by resonant ionization with two-color two photons scheme.

References

- [1] T. Sakamoto, *et al.*, *Anal. Sci.* **34**, 1265-1270 (2018).
- [2] Y. Zhao et al., "Microarea imaging of Sr by two-color resonant ionization sputtered neutral mass spectrometry", abstract of SIMS-22, 23-SP-12 (2019).

Study on Swirling Flow Produced by Annular Guide Vanes

Kotaro Yamanaka¹⁾, Ryota Kobayashi²⁾, Koichi Nishibe³⁾, and Kotaro Sato⁴⁾

¹⁾ Graduate School of Engineering, Kogakuin University, Japan
E-mail: am19061@ns.kogakuin.ac.jp

²⁾ Graduate School of Engineering, Kogakuin University, Japan
E-mail: ad18001@ns.kogakuin.ac.jp

³⁾ Department of Mechanical Engineering, Tokyo City University, Japan
E-mail: knishibe@tcu.ac.jp

⁴⁾ Department of Mechanical System Engineering, Kogakuin University, Japan
E-mail: at12164@ns.kogakuin.ac.jp

Abstract

Annular inlet guide vanes are installed in various turbomachines, and effects on the flow rate adjustment, inlet pressure control, and reduction of collision loss for impellers are measured. It has been reported by many researchers that flow instability with abnormal noise occurs under the condition of a small exit angle of the guide vane. Annular guide vanes are also used to generate swirling jets. However, the detailed flow characteristics of the swirling jets generated by annular guide vanes remain unclear. In this study, the behavior of the swirling jets generated by the annular inlet guide vanes, as well as the flow structure, are investigated.

Because the behavior of swirl flow is closely related to the behavior of flame propagation in the combustor, many studies have been reported, mainly in the field of combustion [1],[2]. The flow field of swirling flow greatly depends on the ratio of angular momentum to axial momentum per unit length, i.e., the swirl number. In the case of a swirling flow open to a semi-infinite space, the flow under a low-swirl-number condition becomes a jet structure with swirling, whereas the flow does not become a jet structure under a large-swirl-number condition and spreads radially by centrifugal force. However, the detailed flow characteristics of swirling jets remain unclear.

Annular guide vanes are sometimes applied to produce the swirl flow. However, when the outlet vane angle is small, a peculiar flow instability may occur and should be handled with careful attention [3]. There are few reports on the relationship between the flow characteristics downstream of the annular guide vanes and the structure of the swirling jet.

This study is a preliminary investigation to clarify the effects of annular guide vanes on the behaviors of swirl flows released into the atmosphere. In this study, the fundamental flow characteristics of the swirl flow generated by annular guide vanes between two disks were numerically investigated. The relationship between the conditions of the guide vanes and the structure, including the radial spreading flow with the backflow region, was mainly investigated.

As the numerical simulation code, SC/Tetra (Software Cradle Co., Ltd.), which is a commercial computational fluid dynamics (CFD) code for thermohydrodynamic analysis based on an unstructured grid, was utilized. The calculation model, boundary conditions, and typical mesh examples used

in the present calculation are shown in Figs. 1 and 2. In this study, the calculated mesh number is approximately ten million. The inlet flow rate is defined as $Q = 0.01 \text{ m}^3/\text{s}$, and the outlet pressure is defined as $P = 0 \text{ Pa}$. The no-slip condition is applied to a solid wall surface. The standard $k-\varepsilon$ model is applied as the turbulence model.

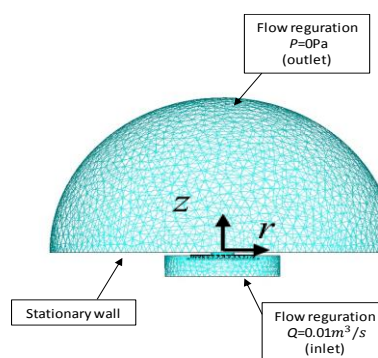


Fig. 1. Boundary conditions of the numerical calculation

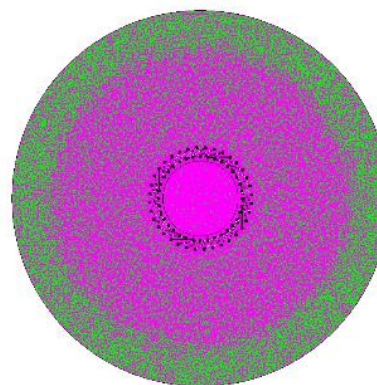


Fig. 2. Typical meshes on $x-y$ plane
($r_2/r_3 = 1.1$, $\beta_2 = 10^\circ$, $L = 15 \text{ mm}$)

Figures 3–6 show the numerical results for the radius ratio of the outlet vane and device exit $r_2/r_3 = 1.1$ and vane angle $\beta_2 = 10^\circ$. Fig. 3 shows time-averaged velocity vectors on the meridian plane. Fig. 4 shows an enlarged view of the flow downstream of the guide vanes and the device outlet where the flow is released to the atmosphere. In Figs. 5 and 6, the time-averaged velocity distributions on the x - y plane are shown. Fig. 5 indicates the velocity vectors at the midspan of the annular guide vane, and Fig. 6 is velocity vectors at $z/r_3 = 0.1$ ($z = 5$ mm) downstream of the apparatus outlet. Fig. 5 shows the inward flow, and it can be seen that the circumferential velocity is generated by passing through the guide vanes. Figs. 3 and 4 show that the flow after passing through the guide vanes (leftward flow in Fig. 4) is deflected upward in the axial direction and is released to the atmosphere; at the same time, the flow spread radially outward because of the centrifugal force. Furthermore, Fig. 4 shows that the large-scale reverse flow (suction flow) occurs to satisfy the continuity equation near the central axis. Consequently, the stagnation point is formed on the lower wall surface. This is considered to be one of the major features of the swirling jet generated by the annular guide vanes sandwiched between two disks. Figs. 3 and 6 show that the streamlines downstream of the outlet of the apparatus become the jet sheet attached to the wall by the centrifugal force.

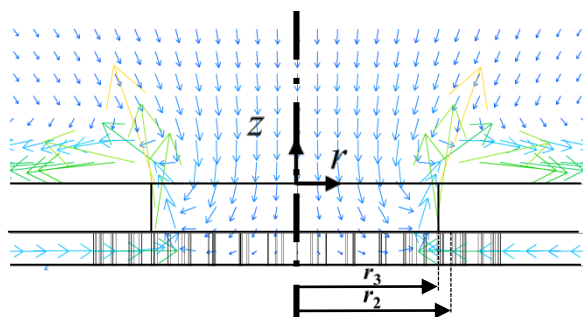


Fig. 3. Velocity vectors on the meridian section ($r_2/r_3 = 1.1$, $\beta_2 = 10^\circ$, $L = 15$ mm)

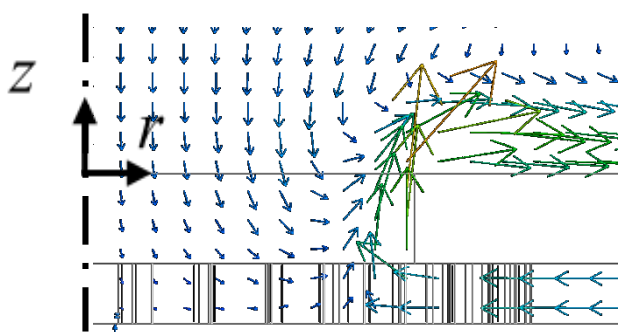


Fig. 4. Enlarged view of the flow field at the outlet of vanes and device ($r_2/r_3 = 1.1$, $\beta_2 = 10^\circ$, $L = 15$ mm)

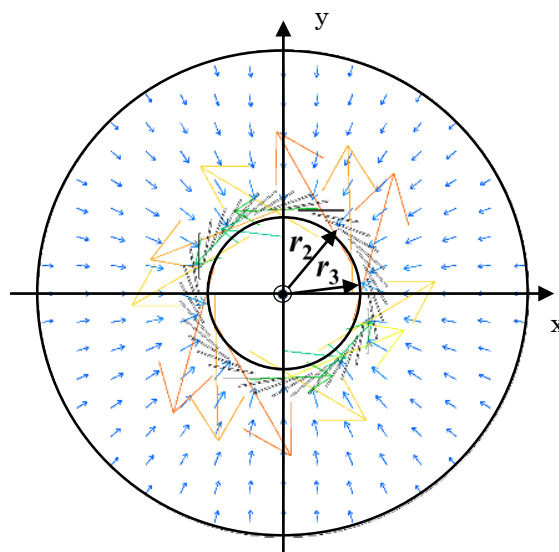


Fig. 5. Upstream and downstream flow of vanes on x - y plane ($r_2/r_3 = 1.1$, $\beta_2 = 10^\circ$, $L = 15$ mm, midspan)

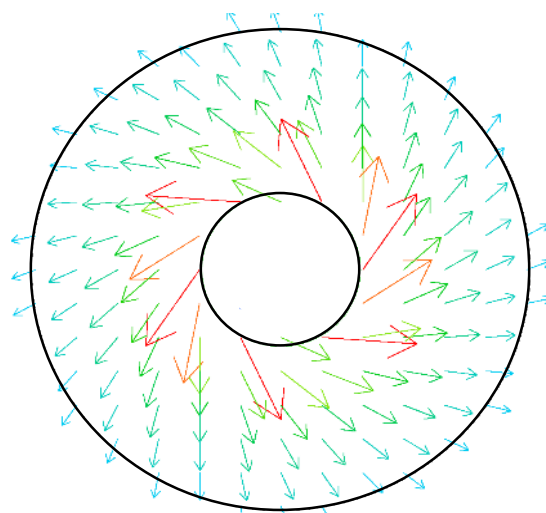


Fig. 6. Swirling flow downstream of device on x - y plane ($r_2/r_3 = 1.1$, $\beta_2 = 10^\circ$, $L = 15$ mm, $z/r_3 = 0.1$)

References

- [1] Gupta A K, Lilley D G, Syred N (1984) Swirl flows. Turnbridge Wells, UK: Abacus Press.
- [2] Sudo K, Kuwahara H, Tsukada M (1997) Diffusion characteristics of swirling jet. *Japan Society of Mechanical Engineers*, vol. 63 (609), pp. 1620–1627.
- [3] Fujiwara A, Tatsumi A, Yokota K, Sato K (2015) Study of unsteady flow generated by whirl of swirling jet. *Proceedings of the Fluid Engineering Division Lecture Series*, p. 12.

Consideration of large capacity high voltage direct current transmission from photovoltaics in the desert area

Ryo Tabei¹⁾, Yasuhiro Noro²⁾

¹⁾ Department of Electrical and Electronic Engineering, Kogakuin University, Japan
E-mail:cm18025@ns.kogakuin.ac.jp

²⁾ Department of Electrical and Electronic Engineering, Kogakuin University, Japan
E-mail:noro@cc.kogakuin.ac.jp

Abstract

This paper shows whether long-distance, high-voltage DC transmission can transmit high power from desert photovoltaics (PV) to destinations. And it is proved that power transmission loss at multiple terminals is small and is practical.

1. Introduction

Due to increasing population and energy demand, environmental problems such as global warming are becoming more serious. One way to solve this is to use renewable energy. However, it is rare to generate huge-capacity electric power with these energies. This is because a large area is required to generate a large amount of power. Therefore, this study focus on to introducing large-scale photovoltaic power generation (PV) in the desert. And it is clarified whether a realistic system can be constructed assuming long-distance power transmission across countries. DC transmission is suitable for long-distance transmission. In addition, when installing large-scale PV plants in desert areas, a multi-terminal power transmission system is suitable for installing multiple conversion stations in a wide area. Therefore, it is necessary to establish a control and protection system with multiple terminals. In the case of a multi-terminal DC power transmission system, the circuit configuration is such that a plurality of converter stations connect to each other. In addition, it is necessary to continue operation without stopping the all system in the event of some failure or accident. Therefore, when an accident occurs in a part of the DC power transmission system, the accident section should be separated.

2. Target system

In this study, we suppose to install PV station in the Sahara Desert in Africa. Then, we think about the power transmission system to Europe across Mediterranean. In addition, DC transmission that is suitable for long-distance transmission is studied. This time, the feasibility of long-distance large-capacity power transmission with a three-terminal configuration is confirmed. The route is shown in Fig. 1. The power transmitted from the PV plant is assumed to be the highest capacity self-excited converter possible in the near future, referring to a literature survey^[1]. The rated capacity on the receiving side in Spain is 3000MW, the DC voltage is ± 500 kV,

and the current is 3000A.

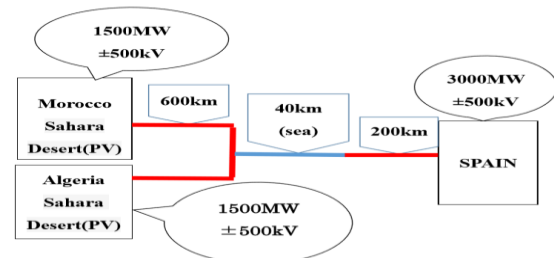


Fig.1 Power Transmission route Spain - Morocco and Algeria

3. Model building

As the DC transmission system, we assume a multi-terminal structure^[1] using a bipolar configuration with neutral wire conductor return system as shown in Fig. 2. From the entso-e Europe Power System^[2], the Spanish system voltage is assumed to be 400kV. Regarding converter control method, the power sending side controls AC system voltage and frequency, and the power receiving side controls DC voltage and reactive power.

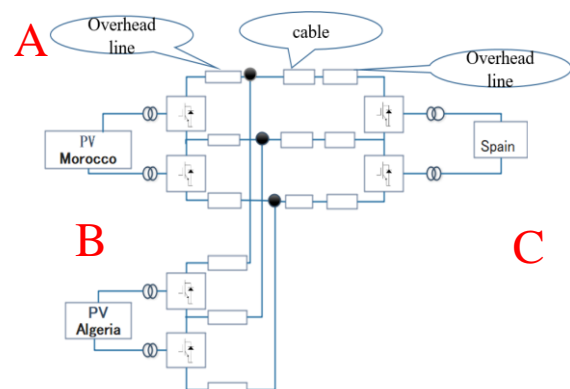


Fig.2 HVDC system model

Each parameter of the overhead line for the land route and the oil-filled cable for the sea route is shown in table 1 and 2.

Table 1. Oil-filled cable parameter

resistance(Ω/km)	0.00386
capacitance ($\mu\text{F}/\text{km}$)	0.37
inductance(mH/km)	1.6
number of parallel	2

Table 2. Overhead line parameter

esistance (Ω/km)	0.0101
capacitance ($\mu\text{F}/\text{km}$)	0.013
inductance (mH/km)	0.84
number of conductors	6

4. Simulation system

Electro-Magnetic Transients Program (EMTP) is used for the simulation. The capacity of the DC system is 1500MW on the power transmission side, DC voltage $\pm 500\text{kV}$, and current 1500A. The receiving side capacity is assumed to be 3000MW, DC voltage $\pm 500\text{kV}$, and current 3000A.

4.1 Simulation contents

Case 1: When the PV output is rated capacity, we check the voltage drop error between the theoretical value and the simulation result.

Case 2: We check the response of the system when the output power on the PV side changes from the steady state suddenly.

5. Simulation results

5.1 Case 1

Fig. 3 shows the simulation result of the DC voltage in the steady state.

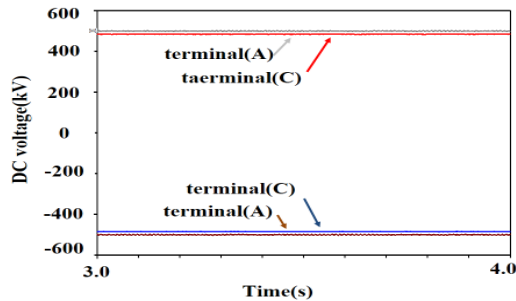


Fig.3 DC voltage

From Tables 1 and 2, the theoretical value of the voltage drop between the receiving side and the sending side is 15.6 (kV). From the simulation results of Fig. 3, the voltage drop between the power receiving side and the power sending side is 15.3 (kV), which is a value close to the simulation. Moreover, from this result, the loss in the transmission line is considered to be an acceptable range of about 3% for the DC voltage of 500kV. Therefore, it can be said that 3-terminal long-distance transmission is possible.

5.2 Case 2

Fig. 4 and Fig. 5 show the simulation results assuming that the PV side output current on the A side in Fig. 2 changes from 1530A to 765A at 3.2s. In Fig. 5, capacity on the power transmission side is 1500 MW, and base capacity on the power receiving

side is 3000MW.

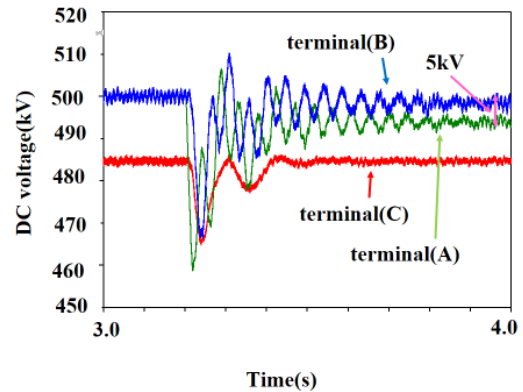


Fig.4 DC voltage

In Fig 4, there is a 5kV drop in the voltage at terminal A at 4s. After the voltage drops, the voltage at terminal B on the transmitting side returns to a value of 500kV at 4s.

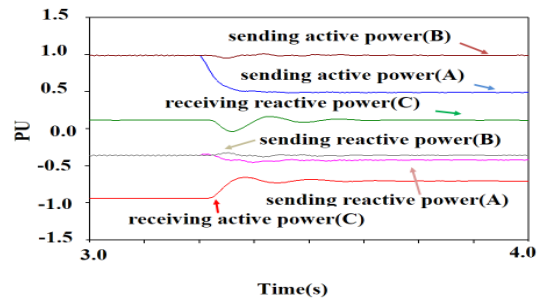


Fig.5 active power and reactive power

The active power and reactive power are shown in Fig.5. Sending active power A changes from 1pu to 0.5pu after 3.2s. This corresponds to changing the PV output current from 1530A to 765A. The change in receiving active power C corresponds to the change in capacity on the A side. Fig. 4 and 5 show a stable transition even after the current change.

6. Summary

A simulation using three terminals was performed. It was proved that transmission loss is small at long distances. This system was stable when the PV output changed suddenly.

7. References

- [1]Kunihiko Machiyama, *DC transmission*, 63-132(1999)
- [2] entso-e, *Europe Power System* <https://www.entsoe.eu/1> (2018/06/20 browse)
- [3]ABB, *reference list*, <https://new.abb.com/jp> (2018/06/20 browse)
- [4] Yoshihiro Kushima, *Electrical Engineering Handbook*, 547, 1221, 1271 (2001)
- [5]DESERTEC Foundation, <http://www.desertec.org/>, (2018/05/30 browse)

Investigation of soundness evaluation method of electrode interface structure of all-solid-state battery using electrochemical simulation

Shodai Ban¹⁾, Ayato Sakamoto²⁾, Kazuhiro Suga³⁾

¹⁾Department of Mechanical Engineering, Graduate School Kogakuin University, JAPAN

E-mail: am19049@ns.kogakuin.ac.jp

²⁾Department of Mechanical Engineering, Kogakuin University, JAPAN

E-mail: a116048@ns.kogakuin.ac.jp

³⁾Department of mechanical engineering, Faculty Engineering Kogakuin University, JAPAN

E-mail: ksuga@cc.kogakuin.ac.jp

Abstract

The correlation between the mechanical properties of the electrode-electrolyte interface of the all-solid-state battery and the Cole-Cole plot obtained by electrochemical measurement is examined using electrochemical simulation. First, material constants is identified in order to reproduce the experimental results by simulation.

Introduction

In all-solid-state batteries, the bonding properties at the interface decrease due to deterioration phenomena such as oxide film and structural changes of reactants^[1] at the electrode-electrolyte interface due to charge and discharge. The decrease in bondability affects the structural integrity of the interface due to vibration and impact, and battery performance may be significantly lost. In this study, the correlation between the mechanical properties of the electrode-electrolyte interface and the Cole-Cole plot obtained by electrochemical measurement is investigated using electrochemical simulation. First, material constants necessary for simulation are identified. Next, we examined whether the experimental results could be reproduced by electrochemical simulation.

Methods

The electrode materials used were LiCoO₂ for the active material of positive electrode and Graphite for the active material of negative electrode. LiPF₆ EC:DEC 1:1 was used as the electrolyte. The thickness of the positive and negative electrodes was 0.08 [mm], the thickness of the separator was 0.05 [mm], and the height was all $h = 16$ [mm]. The electrode reaction was analyzed using the Butler-Volmer equation^[2], and the mass transport was analyzed using the Nernst-Planck equation^[2].

The AC impedance was measured with the frequency range of the AC voltage from 0.05 to 200000 [Hz] and the temperature $T = 303.15$ [K]. Table 1 and Fig. 1 show the numerical data and the Cole-Cole plot obtained by experiments and simulations using the identified material constants.

Table 1. Comparison of Cole-Cole Plots between Simulation and Experimental results

	Simulation	Experiment	difference
Electrolyte resistance	1.663 [Ω]	2.222 [Ω]	25.2 [%]
Positive electrode Charge transfer resistance	59.82 [Ω]	57.94 [Ω]	3.24 [%]
Negative electrode Charge transfer resistance	14.57 [Ω]	1.558 [Ω]	835 [%]

Conclusions

The impedance was simulated using the material constants identified by experiments and the material constants^{[2],[3]} identified with reference to the literature. The shape of the Cole-Cole plot did not match the experimental results. In particular, the charge transfer resistance of the negative electrode, which had a large error, is often identified from literature, and will be identified in future experiments.

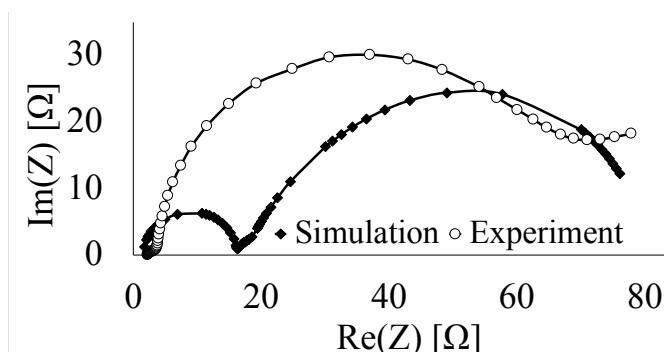


Fig. 1. Comparison of Cole-Cole Plots between Simulation and Experimental results

References:

- [1] M. Broussery, Ph. Biensan, F. Bonhomme, Ph. Blanchard, S. Herreyre, K. Nechev, R. J. Blanchard, *Main aging mechanisms in Li ion batteries*, J. Power Sources, **146**, 90-96(2005)
- [2] N. Wolff, F. Roder, U. Krewer, *Model Based Assessment of Performance of Lithium-Ion Batteries Using Single Ion Conducting Electrolytes*, Electrochim. Acta, **284**, 639-646(2018)
- [3] S. Brown, N. Mellgren, M. Vynnycky, and G. Lindbergh, *Impedance as a Tool for Investigating Aging in Lithium-Ion Porous Electrodes*, J. Electrochem. Soc., **155**, A320-A338(2008)

Genetic Algorithm and Fuzzy Multi-objective Programming for Optimizing Maintenance Policies of Offshore Wind Systems

Thi Huynh Anh Le¹⁾, Thi Kim Oanh Le¹⁾

¹⁾Department of Project Management, The University of Danang – University of Science and Technology, Vietnam

E-mail: lthanh@dut.udn.vn; ltkoanh@dut.udn.vn

Abstract

The maintenance strategy is more complex so that maintenance actions might not always return the system to new condition. Additionally, the maintenance threshold plays an importance key to determine the optimal maintenance scheduling that reduces the maintenance cost. However, the limited researches determine the maintenance threshold for multiple components of offshore wind system. Optimal maintenance policy aims to provide optimum maintenance threshold with the most possible maintenance cost. Therefore, this paper proposes approach to determine the optimal maintenance threshold for offshore wind system such that minimizes the maintenance cost while increase the system reliability. The proposed approach aims to provide the optimal maintenance threshold for multiple components of wind system by proposing a two-step approach to optimize maintenance policy. The number of impacted parameters such as weather condition, system reliability, power generation loss during maintenance and market electric price are all considered to enhance the accuracy of estimating the maintenance cost in the proposed method. First, dynamic maintenance strategy is proposed to determine the maintenance threshold for component of the offshore wind turbines in which failure rate and maintenance cost are vital parameters for the cost model. Genetic algorithm is developed to find the optimal maintenance threshold for the component. Then, the optimal maintenance threshold for offshore wind system is determined by using fuzzy multi-objective programming. The result indicates that the optimal maintenance threshold of whole system may save an average 1.19% on maintenance cost and increase 1.62 % on system reliability over the maintenance threshold based on individual component.

This research builds a mathematical model to find the optimal maintenance threshold for an individual component independently. The individual maintenance threshold is subsequently utilized to determine the optimal maintenance threshold for a whole offshore wind system where all components are considered. The influence among components is considered carefully to establish the optimal maintenance threshold of the offshore wind system. The proposed approach adheres to the following assumption:

All turbines of the offshore wind system are identical

The system has to be shut down whenever there are maintenance activities even if for one component. The state of components that are not maintained remains unchanged during the maintenance of other ones.

A particular component either is similar for all wind turbines or has the same failure distribution. The failure rate of all components follows the Weibull distribution and increases over the time.

A component failure is noticed immediately without any inspection activities.

Table 1. The optimal total number of maintenance activities for whole system during 240 months

Components	Number maintenance activities
Rotor system	4
Bearing	9
Generator	12
Gearbox	10
Total maintenance Activities	35

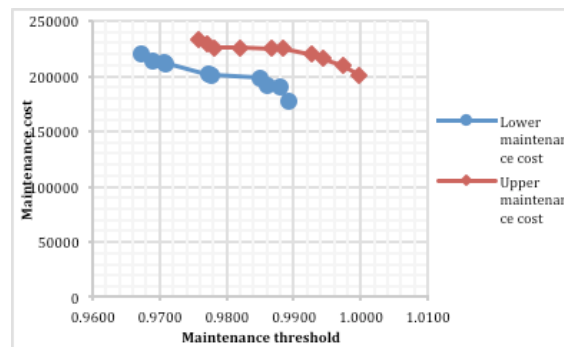


Fig. 1. Maintenance cost as a function of maintenance threshold

References:

- [1] Astariz, S. and G. Iglesias (2015). "Accessibility for operation and maintenance tasks in co-located wind and wave energy farms with non-uniformly distributed arrays." *Energy Conversion and Management* 106: 1219-1229.
- [2] Poppe, J., Boute, R. N., Lambrecht, M. R. (2018). "A hybrid condition-based maintenance policy for continuously monitored components with two degradation thresholds." *European Journal of Operational Research* 268(2): 515-532.
- [3] Tuyet, N. T. A. and S. Y. Chou (2018). "Maintenance strategy selection for improving cost-effectiveness of offshore wind systems." *Energy Conversion and Management* 157: 86-95.

Relationship between aerodynamic characteristics of soccer balls and their panels

Yuki Sakamoto¹⁾, Shinichiro Ito²⁾, and Masaki Hiratsuka²⁾

¹⁾Department of Mechanical Engineering, Graduate School of Kogakuin University, Tokyo, Japan

E-mail: am19022@ns.kogakuin.ac.jp

²⁾ Department of Mechanical Engineering, Kogakuin University, Tokyo, Japan

E-mail: ito@cc.kogakuin.ac.jp

Abstract

The design of the soccer balls continues changing almost every world cups. The difference in panel shape gives a major influence on the aerodynamic characteristics that affect ball trajectory. The purpose of this research is to investigate the aerodynamic characteristics of these balls, to investigate their factors, and to propose a predisposing factor for designing a ball with high controllability. Regarding 11 kinds of soccer balls, the measurement of the fluid force and panel groove as panel shape measurement were performed. The differences in flow separation position were confirmed by an oil film method and compared with the drag coefficient of each ball. The landing position was also measured using a roller type ball launcher in the same spin rate launch speed and launch angle constant. As a result, it was found that the rapid change of drag characteristics in the Reynolds number differs depending on the shape of the panel groove and the panel shape that also relates to the controllability of the ball. This is found to be related to the turbulent transition position on the ball surface.

1 Introduction

The difference in panel shape will have a major influence on the aerodynamic characteristics that affect ball trajectory. Passmore and many researchers reported various aerodynamic studies on soccer balls [1]. The purpose of this research is to investigate the aerodynamic characteristics of 11 balls of different shapes, including the newest 2018 balls, to investigate their trajectories, and to propose a predisposing factor for designing a ball with high controllability.

2 Method

2.1 Fluid force experiment

Drag measurement was performed on 11 kinds of different soccer balls with a wind tunnel and a 3 component load cell. This device conducted sampling at 1000 Hz for 9 seconds from wind speed 3 to 29 [m/s] under computer control, and the experimental values were averaged. Balls bonded with double-sided tape attached with a support cup were supported with a cobra type support shown in Fig.1. The support rod connecting the ball to the load cell was covered with an airfoil case to eliminate the influence of the fluid force of the support rod, and each fluid force of model was obtained accurately by removing the fluid force of the sting that supported the model separately.

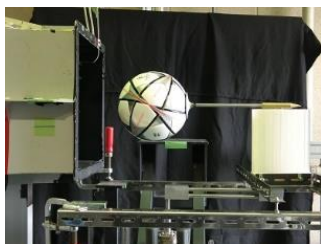


Fig.1 Wind tunnel test

2.1 Groove shape measurement

The cross-sectional area of the groove in the panel joint of each ball were taken with one-shot 3D shape instrument by VR-3000, KEYENCE as shown in Fig.2. As for the groove length, the string was put in all grooves and the total length was measured as shown in Fig.3. The cross sectional area and depth of the grooves were calculated as shown in Fig.4. The total groove volume was calculated for each groove volume with the groove length having the same cross-sectional area, and the groove volumes for different cross-sectional areas were added.



Fig.2 VR-3000



Fig.3 The string was put in all

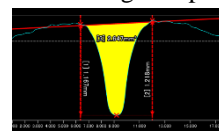


Fig.4 Analysis area

2.3 Oil film experiment

To confirm the flow separation on the panels of each ball, a mixture of oleic acid, liquid paraffin and tetra-tri-iron oxide as oil film was coated on the surface of the balls with the same system at a wind speed of 29.6 [m/s]. A representative panel-shaped four-ball type was used.

2.4 Ejection test

In order to evaluate the performance of the soccer ball, an ejection experiment using a roller ejection machine as shown in Fig.5 was conducted. This

ejection machine puts the fixed stand as shown in Fig.6 to reduce the installation position due to the reaction of the ejection. Two different trajectories were measured horizontal rotation (curve rotation) and vertical rotation (drive rotation). The curve and drive ejection test was conducted under the condition as shown in Table 1. This is the same with the actual game speed.



Fig.5 Ejection machine Fig.6 The fixed stand

Table 1 Condition of ball ejection

Rotor speed [rpm]	Left	Right
	2650	2150
Injection angle [°]	20, 35	
Injection speed [km/h]	80	
Speed of ball [rps]	8.3	

3 Result and Discussion

3.1 Fluid force experiment

Fig.7 is The C_D diagram of each ball. It can be seen that the tendency of drag crises are greatly different depending on the difference of the ball panels. In order to clarify this cause, the end of the drag crisis was defined as the End Reynolds number.

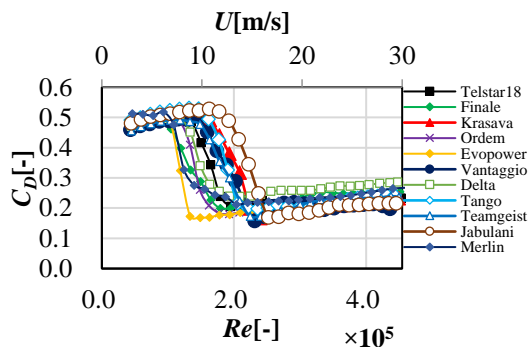


Fig.7 Drag coefficient of each ball

3.2 Groove shape measurement

The measurement results are shown in Fig.8. Large groove volume balls like Evopower have the small end-Reynolds number compared with the smaller volumes like Jabulani. It has a tendency that the larger the groove volume is, the smaller the end-Reynolds number becomes. The correlation between the total volume and the End-Reynolds number was strongly correlated with -0.83.

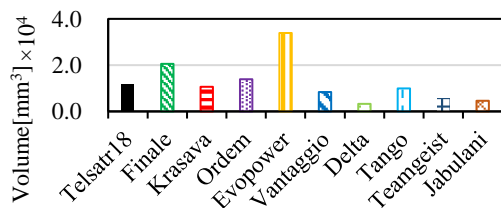


Fig.8 Total groove volume of each ball

3.3 Oil film experiment

Fig.9 showed the characteristic oil film results of balls. In the case of a true sphere, the true sphere had the first and second separation points. Since the positions of the separation points of all the balls were almost the same, the C_D was almost the same at the wind speed 29.6 [m/s].



Fig.9 Oil film results of balls

3.4 Ejection test

Fig.10 is the results of curve balls. The correlation coefficient between the C_D value and the flight distance at 23 [m/s] of the ejection velocity showed a positive correlation of 0.55. Since it is not thought that the greater the drag the greater the distance, it seems that there is a difference between the spinning C_D and the stationary C_D . Concerning the lateral displacement, we could not obtain any relation with lateral displacement of landing position and groove specification, either.

Fig.11 is the result of the drive. It was found that the longer the distance was, the smaller the total volume (Fig.8) was. The correlation factor was -0.75. Correlating the standard deviation of the variation of x, y axis (σ_x and σ_y) with the groove data. The most correlated are $\sigma_x \cdot \sigma_y$ and the volume and the correlation factor was -0.52. It was found that the larger the total volume was, the smaller the variance of distance became. The total volume is important for ball controllability.

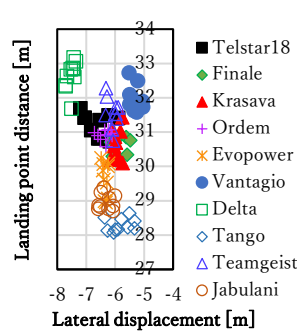


Fig.10 Curve result

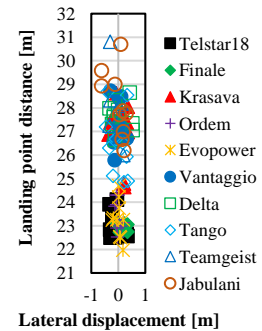


Fig.11 Drive result

4 Conclusion

1. The total groove volume effects with the end Reynolds number of drag.
 2. The total groove volume effects with the landing distance in drive spin.
 3. The total groove volume effects with the landing distance variance in drive spin.
- In order to design a ball with high controllability, it is necessary to increase the groove volume.

References

[1] Goff, J. E. (2013). A review of recent research into aerodynamics of sport projectiles, Sports Eng., 16:137-154.

Numerical Study on Fundamental Flow Characteristics of Excited Jets

Chisato Ichihara¹⁾, Daiki Yamaguchi²⁾, Ryota Kobayashi³⁾, Koichi Nishibe⁴⁾, and Kotaro Sato⁵⁾

¹⁾Department of Mechanical System Engineering, Kogakuin University, Tokyo, Japan

E-mail: a216013@ns.kogakuin.ac.jp

²⁾Graduate School of Engineering, Kogakuin University, Tokyo, Japan

E-mail: am18065@ns.kogakuin.ac.jp

³⁾Graduate School of Engineering, Kogakuin University, Tokyo, Japan

E-mail: ad18001@ns.kogakuin.ac.jp

⁴⁾Department of Mechanical Engineering, Tokyo City University, Tokyo, Japan

E-mail: knishibe@tcu.ac.jp

⁵⁾Department of Mechanical System Engineering, Kogakuin University, Tokyo, Japan

E-mail: at12164@ns.kogakuin.ac.jp

Abstract

The fundamental flow characteristics of excited jets were investigated by numerical simulation. As the excitation jet, a pulsating jet with a sine wave velocity fluctuation component added to the steady velocity was considered. The effect of the velocity fluctuation frequency on the flow pattern was mainly examined, and an attempt was made to clarify the relationship between the jet structure and the unsteady characteristics.

Jet technology is applied to flow control in many fields, and investigations on the flow characteristics of various types of jet are still widely conducted^{[1], [2]}. The pulsating jet, which adds a fluctuation velocity component to the steady jet, is a typical excited jet^[3]. It has different characteristics from steady jets because of the behavior of the vortexes formed in the velocity shear layer, and the promotion of diffusion and mixing of the flow is expected because of this. However, many unclear points remain regarding the effect of oscillating characteristics on the jet structure.

In this study, the flow characteristics of a pulsating jet in which the unsteady velocity component of the sine wave is added to the steady velocity were investigated by numerical analysis. The velocity vectors and vorticity distributions calculated under typical conditions are shown, assuming a two-dimensional plane jet. The behavior of large-scale vortexes generated by the pulsation of jets is discussed.

The main symbols are shown below.

- b_0 : Slot width ($= 5.0 \times 10^{-3}$ m)
- u : Velocity in the x -direction [m/s]
- u_0 : Velocity in the x -direction at slot exit [m/s]
- f : Frequency [Hz]
- f^* : Dimensionless frequency ($= fb_0/U_{p0}$ [-])
- t : Time [s]
- T : Period [s]
- U_{p0} : Characteristic velocity in pulsating jets [m/s]
- U_{c0} : Steady velocity on slot exit [m/s]
- U_{pa} : Velocity amplitude on slot exit [m/s]
- v : Velocity in the y -direction [m/s]
- v_c : Inlet velocity at upper/lower boundary [m/s]
- ω : Vorticity [1/s]
- Re : Reynolds number ($= U_{p0} b_0/\nu$ [-])

In the numerical simulation code, SC/Tetra (Software Cradle Co., Ltd.) was used, which is a commercial computational fluid dynamics code for thermohydrodynamic analysis based on an unstructured grid. A two-dimensional incompressible viscous flow was assumed, and the k - ϵ model was applied as a turbulent flow model. The mesh number was approximately 200,000. Figs. 1 and 2 show an example of the mesh in the analysis region and an example of the mesh near the slot, respectively. The boundary conditions of the analytical model are shown in Fig. 3 (full view) and Fig. 4 (enlarged view). The computational domain is $400b_0$ in the x -direction and $200b_0$ in the y -direction. In this study, the velocity boundary condition at the nozzle inlet was given so that the slot exit velocity was $u_0 = U_{c0} + U_{pa} \sin(2\pi ft)$. The constant static pressure ($p = 0$) condition was imposed at the exit of the computational domain. Furthermore, the velocity conditions of $v_c = -0.05U_{c0}$ and $v_c = 0.05U_{c0}$ corresponding to entrainment of the jet were given at the upper and lower boundaries, respectively. A nonslip condition was also imposed on the wall surface, and meshes of more than 10 layers are discretized in the regions where the velocity gradient on the wall surface is large.

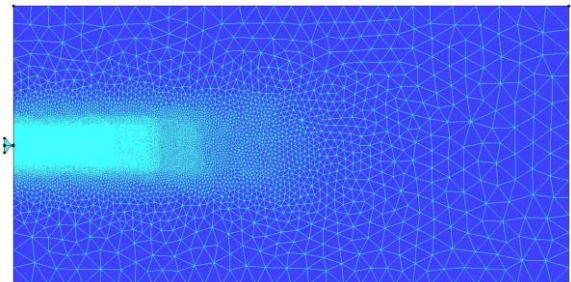


Fig. 1. Calculation domain overview

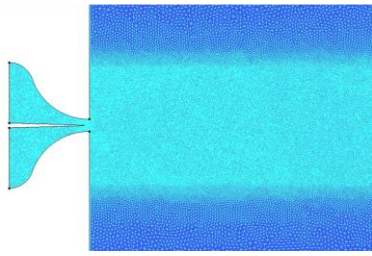


Fig. 2. Typical meshes near the slot

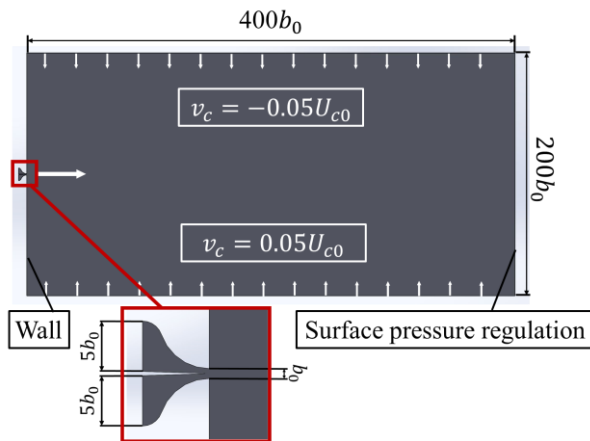
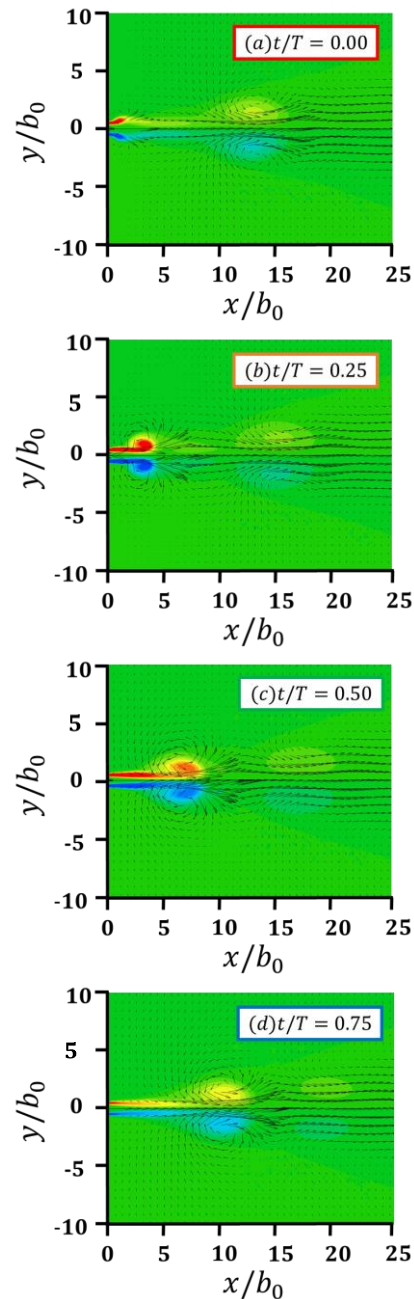


Fig. 3. Boundary conditions for numerical analysis

Fig. 5 shows the calculation results obtained for the slot width $b_0 = 5$ mm under the conditions of the jet steady velocity $U_{c0} = 6.0$ m/s, the velocity fluctuation amplitude $U_{pa} = 3.0$ m/s, the ratio $U_{pa}/U_{c0} = 0.5$, the Reynolds number $Re = 2050$, the frequency $f = 50$ Hz, and the dimensionless frequency $f^* = 4.17 \times 10^{-2}$. The velocity vectors and the vorticity distributions are shown in the same figure. The flow patterns of $t/T = 0.0$, 0.25 (maximum velocity), 0.5 , and 0.75 (minimum flow rate) are shown in Figs. 5(a), (b), (c), and (d), respectively. Because the velocity shear layer with a large velocity gradient is formed around (b) $t/T = 0.25$, the velocity shear layer is rolled up. Consequently, a vortex pair is formed from the vorticity distribution in (c) $t/T = 0.5$. Comparison of (c) $t/T = 0.5$, (d) $t/T = 0.75$, and (a) $t/T = 0$ (corresponding to $t/T = 1.0$) shows that the vortex pairs are immigrating translationally because of the induced velocity of each other's vortices, even under the phase with a small slot exit velocity. The x -direction velocity on the jet centerline rapidly increases at the position where the vortex pair exists. However, in the vicinity of the vortex pair, the existence of the reverse flow region with x -direction velocity $u < 0$ is also observed. These are similar to the flow characteristics observed in synthetic jets^[4], suggesting that the same control method as that for synthetic jets can be applied to pulsating jets with a nonzero net flow rate.


 Fig. 5. Velocity vectors and vorticity distributions ($Re = 2050$, $U_{pa}/U_{c0} = 0.5$, $f^* = 4.17 \times 10^{-2}$)

References:

- [1] Rajaratnam, N. 1976 Turbulent Jets (Developments in Water Science, Volume 5). Elsevier Science.
- [2] Shakouchi, T. 2004 Jet flow engineering – fundamentals and application, Morikita Publishing Co., Ltd. (In Japanese).
- [3] Riley, N., Sánchez-Sanz, M., and Watson, E. J., “A planar pulsating jet,” *Journal of Fluid Mechanics*, Volume 638, 10 November 2009, pp. 161-172.
- [4] Nishibe, K., Fujita, Y., Sato, K., Yokota, K., and Koso, T., “Experimental and Numerical Study on the Flow Characteristics of Synthetic Jets,” *J. Fluid Sci. Tech.*, 6, 425-436 (2011).

Dissociated ammonia as a sustainable energy source

Takashi Saika¹⁾

¹⁾Department of Mechanical Science and Engineering, School of Advanced Engineering, Kogakuin University, Tokyo, Japan

E-mail: saika@cc.kogakuin.ac.jp

Abstract

Ammonia is mostly used as a nitrogen feedstock for agriculture or as a refrigerant, but it is occasionally used as fuel for internal combustion engines and fuel cells. Because it is a carbon-free substance there is currently a renewed interest for using ammonia as a fuel. This paper describes the potential of ammonia as a sustainable energy source.

Ammonia energy system

Figure 1 shows a system diagram of an ammonia energy system. Ammonia is supplied directly as a hydrogen carrier or after being converted into hydrogen at a hydrogen production plant, and supplied as fuel for fuel cells and fuel for combustion at home.

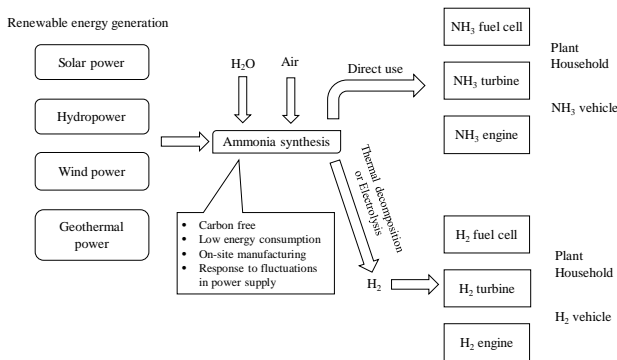


Fig. 1. Conceptual diagram of an ammonia energy system.

In home-use distributed power generation, it is easy to use electricity and heat together, and energy efficiency is greatly improved. Home fuel cells include polymer electrolyte fuel cells (PEMFC) and solid oxide fuel cells (SOFC).

Ammonia, which is easy to store and transport, is transported to a hydrogen station where it is converted to hydrogen and used as fuel for fuel cell vehicles. Hydrogen transportation costs are greatly reduced, and the spread of fuel cell vehicles can be promoted.

Manufacturing and transportation

The manufacturing capacity of ammonia in the world is about 159 million tons. Eighty percent of the production is used as raw materials of manure and it is not usually used for an energy source. In the present production process of ammonia, CO₂ of about 2.623 ton is more released for ammonia of 1 ton than 0.564 ton in natural gas or 0.781 ton in petroleum.

Hydrogen is produced by the steam reforming from coal, LPG, LNG, naphtha, natural gas or offgas at present. Ammonia is then synthesized by the Haber-Bosch method using the hydrogen and nitrogen in the air. Ammonia has better to be produced not by the method using fossil fuel but by new methods to emit no CO₂. The electricity generated by renewable energies such as solar energy, wind power energy, etc. will produce hydrogen by electrolysis of water, and synthesize the hydrogen and nitrogen to ammonia. The ammonia transportation system is proposed to use the hydrogen dissociated from the ammonia at a demand side. In addition, there are production methods considered from raw materials by abolished plastic and collecting ammonia from a sewage disposal plant etc.

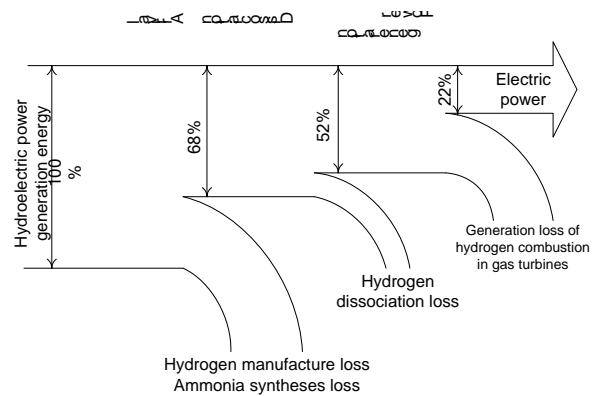


Fig. 2. Estimation of generating system on ammonia fuel.

Figure 2 shows estimation of production and transportation of ammonia in the World Energy Network (WE-NET) plan by the New Energy and Industrial Technology Development Organization (NEDO) in Japan^[1]. The energy of hydroelectric power generation becomes about 68% as ammonia at the demand side, about 52% with the loss in dissociation process to hydrogen and about 22% in power generation by hydrogen combustion turbine. The energy loss consists of the ammonia dissociation

and the refinery process of about 15%, and the ammonia syntheses process of about 15%, the production process of hydrogen and nitrogen of about 15%, and the hydrogen combustion in gas turbines of about 30%.

Ammonia as a fuel

There is little advantage of ammonia made with conventional ammonia syntheses process, because the hydrogen is obtained from fossil fuel. However, ammonia would have a possibility as a liquid fuel for fuel cells, if the following new methods of ammonia syntheses are practically developed without using fossil fuel to save the energy and to reduce environmental effects.

- Ammonia generation from urea contained in liquid waste of human and animals
- Ammonia synthesis by carbon molecule C60 and γ -cyclodextrin molecule

The synthesis of ammonia with molecule C60 carbon (the alias: buckminsterfullerene) and γ -cyclodextrin molecule was developed by Prof. S. Uemura of Kyoto University [2]. Ammonia can be synthesized on energy saving and mild conditions by using nitrogen, water, visible light and a reducing agent.

As a result, the total efficiency of the liquid hydrogen system was 15% lower and that of the methanol system was about 2% lower than that of a conventional system, when the output of power generation was 1,000 MW. The generation cost of the ammonia system was about 33 yen/kWh as the same level as the liquid hydrogen system and 8 yen/kWh higher than that of the methanol system. However, ammonia is practically an attractive fuel for transportation and storage as a hydrogen carrier, because ammonia is advantageous in the aspect of environmental impacts.

Problems and solutions of ammonia fueled engine

In comparison with combustion characteristics between ammonia and hydrocarbon fuels such as gasoline, ammonia for automobile fuel has remarkable problems in the maximum laminar burning velocity and the minimum ignition energy. The maximum laminar burning velocity and the minimum ignition energy of ammonia are 1.5 cm/s and 8.0 mJ. Therefore ammonia is dissociated under Rh-Al₂O₃ catalyst to hydrogen, and the ignition and flame propagation characteristics can be improved by using the hydrogen.

Figure 3 show cylinder pressure in comparison with methane and ammonia operations [3]. If the supplied rate is equivalent in ammonia and dissociated ammonia, the engine shows almost the same combustion process as in the methane operation. It is reasonable that the laminar burning velocity is 30 cm/s in the equivalent flow rate.

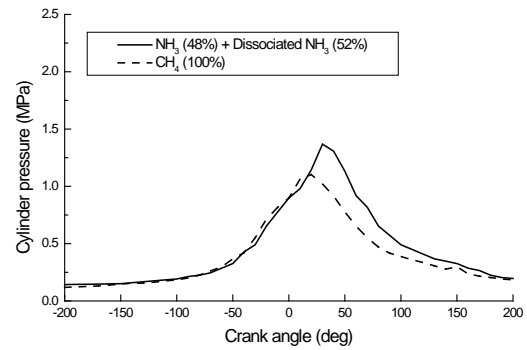


Fig. 3. Cylinder pressure diagram.

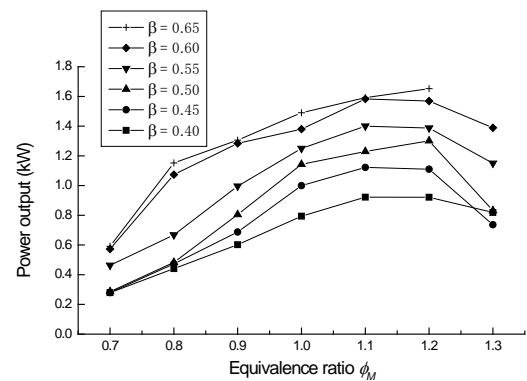


Fig. 4. Effect of equivalence ratio on power output.

Figure 4 shows results of net outputs for various equivalence ratios. ϕ_M is the equivalence ratio mixed fuel of ammonia and hydrogen, and β is hydrogen fraction of the fuel supplied to an engine. The engine output increases by raising the hydrogen fraction. However, in the rich mixture at $\phi_M = 1.3$ and $\beta = 0.65$, the plosive sound from the engine and the engine rotational speed decreased. It seems to be generating backfire then, and there is the limit to the hydrogen fraction β of 0.65 for the rich mixture. Therefore, the maximum output is obtained at the equivalence ratio from 1.1 to 1.2, because the output decreases at 1.3. There was no much different change in output characteristics affected by equivalence ratios, even if hydrogen fractions are changed.

References:

- [1] "1996 Annual Report: International Clean Energy System Technology on Hydrogen Application" (in Japanese), NEDO-WE-NET-9631, (1997).
- [2] S. Uemura et al, Nature, **428**, 279-280 (2004).
- [3] Takashi Saika, Koji Korematsu, Sixth International Conference on Technologies and Combustion for a Clean Environment, **28.3**, 857-862 (2001).

Birefringent PET Transducers for Non-contact Liquid Concentration Measurements by Heterodyne Metrology

Ruey-Ching Twu*, Kai-Hsuan Li, and Bo-Lin Lin

Department of Electro-Optical Engineering, Southern Taiwan University of Science and Technology, Taiwan
E-mail: rctwu@stust.edu.tw

Abstract

A Birefringent PET transducer is proposed to be used for non-contact liquid concentration measurements in a heterodyne interferometer. The experimental results show that the measurement resolutions are 4.5×10^{-5} and 4.2×10^{-6} RIU for the attached single and two layers of PET film, respectively.

In the liquid concentration measurements, a non-contact technique has advantages of remote monitoring and non-contamination during the liquid transportation. Especially, the liquids with corrosive or viscous cause the necessary to clear the sensing heads for the next usage. Typically, optical and electromagnetic techniques have been successfully demonstrated for the purpose^[1,2]. In the past decades, it is well known that a polyethylene terephthalate (PET) polymer can be used for the flexible displays and photonic sensors^[3]. Besides, the PET materials are birefringence^[4]. When an obliquely incident light with two orthogonal waves passes through such birefringent materials, the phase delay between two orthogonal waves is dependent on the incident angle and the environmental refractive index (RI)^[5].

To further explore the birefringent polymer for the application of optical sensors, a non-contact sensor is proposed to be used in a common path heterodyne interferometer as shown in Fig. 1. In the Fig. 2, a simple fluidic container (FC) of triangular shape was made by the single attached PET film of $188 \mu\text{m}$ through a UV-cured layer on the hypotenuse. The FC can provide the sensitive measurement of liquid concentrations by the optimization on the cell designs. Usually, a quasi-linear relationship between RI and concentration is existed for the most of liquid solutions. The varied concentrations of the injection liquids can make the incident angle changes of probe light while passing the PET film. The corresponding phase values were obtained through the measurements in the heterodyne interferometer. Figure 3 gives the phase dependence on the different concentrations of salt solutions. The zero phase level is the injected pure DI waters.

According to the experimental results, the mean values of measured phase and the injected liquid concentrations have linear relations between them. In the test salt solutions with the weight percentage ranging from 0% to 2.5%, the measurement resolutions are 4.5×10^{-5} and 4.2×10^{-6} RIU for the single and two layers of PET film, respectively. Moreover, the dynamic ranges of measurement can be adjusted by the incident angle and PET layers.

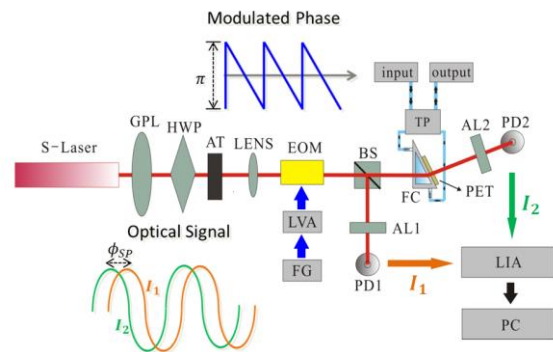


Fig. 1. Non-contact liquid concentration measurement setup.

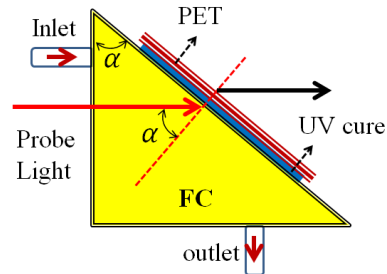


Fig. 2. Fluidic container with attached PET film.

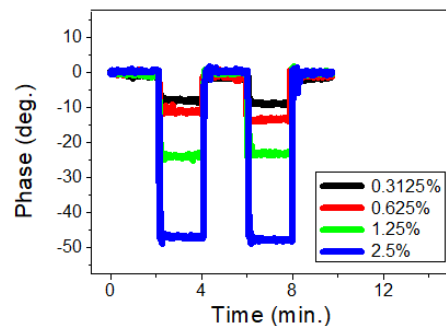


Fig. 3. Phase variations under different salt concentrations exchanged for the single layer PET transducer.

References:

-
- [1] R. C. Twu and J. Y. Chen, *Sens. and Actuators A*, **2017**, 267, 424-430.
 - [2] T. Susa, T. Watanabe, M. Sohigawa, and T. Abe, *IEEJ Trans. on Sens. and Micromachines*, **2015**, 135, 210-213.
 - [3] G. Zhang, C. Lan, H. Bian, R. Gao, and J. Zhou, *Opt. Express*, **2017**, 25, 22038-22045.
 - [4] B. L. Van Horn and H. H. Winter, *Macromolecules*, **2003**, 36, 8513-8521.
 - [5] R. C. Twu and C. W. Hsueh, *Sens. and Actuators A*, **2017**, 253, 85-90.

Reinforcement of Epoxy Thermoset Composite Using Epoxidized Kraft Lignin from Sugarcane Bagasse

Rayman T. Alamag¹), Myra G. Borines¹), Ronniel D. Manalo²), Jerico Z. Alcantara¹)
and Jovita L. Movillon¹)

¹)Department of Chemical Engineering, College of Engineering and Agro-industrial Technology,
E-mail: mgborines@up.edu.ph

²)Department of Forest Products and Paper Science, College of Forestry and Natural Resources,
University of the Philippines Los Baños, Laguna, Philippines

Abstract

The use of natural fiber as reinforcing material in polymer composites is now gaining attention due to its sustainability and abundance. Epoxy is a polymer with a wide variety of applications. But due to its cross-linked structure, it has high tendencies to fracture and impact resistance if used as the lone component [1].

To enhance its mechanical properties, reinforcing materials or fillers are being added to epoxy composites but these fillers are commonly synthetic and derived from non-renewable resources [2,3]. In this study, epoxidized Kraft lignin from sugarcane bagasse, a by-product of sugar manufacture, was used as a reinforcing material to enhance the flexural strength and hydrophobicity of epoxy thermoset composites.

Sugarcane bagasse was subjected to Kraft pulping for the recovery of lignin and obtained a yield of 9.82%. Epoxidation of Kraft lignin with Poly(ethylene glycol) diglycidyl ether was done to enhance the compatibility with polymer. Functionalization of lignin was verified using FT-IR analysis as shown in Fig.1.

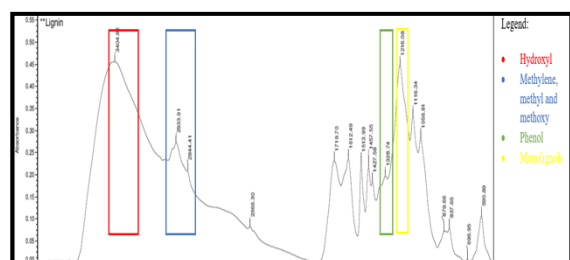


Figure 1. FT-IR spectrum of Kraft lignin samples

Different loadings of unmodified and epoxidized Kraft lignin (1%, 3% and 5% v/v) were used as filler at varying curing time (45 minutes, 60 minutes and 90 minutes). The effects of filler modification, filler loading and curing time on flexural strength (MPa) and %water absorption of composites were investigated. Thermoset that were reinforced with epoxidized Kraft lignin generally exhibited high flexural strength and hydrophobicity relative to that of unmodified Kraft lignin especially at 1% filler loading and at 90 minutes of curing. Factors were all found significant to the responses at 0.05 significance level except the modification of filler to the hydrophobicity of the thermoset. Reinforced

thermosets showed relatively higher flexural strength (Fig. 2) but have lower hydrophobicity compared with neat epoxy, specifically at 1% filler loading and 90 minutes curing time (Fig. 3). These results showed that epoxidized lignin from bagasse is a promising filler for epoxy thermosets.

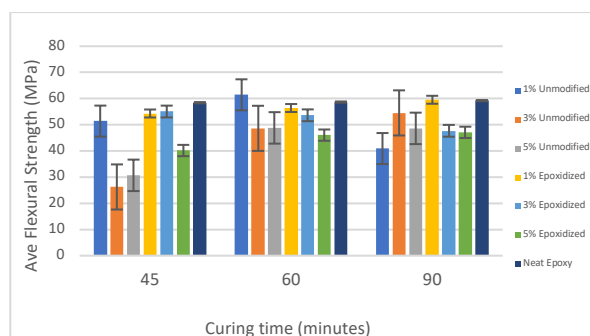


Figure 2. Average flexural strength of neat epoxy and composites produced at different curing time.

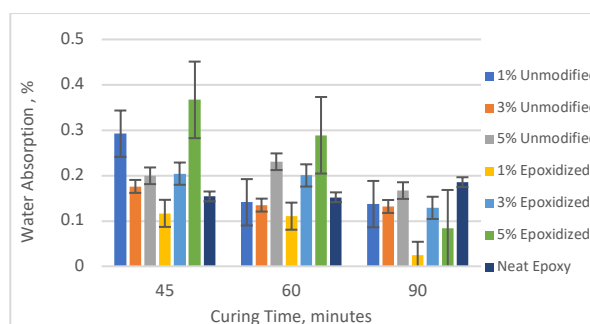


Figure 3. Average water absorption of neat epoxy and composites produced at different curing time.

References:

- [1] Hodd, K. Epoxy Resins. *Comprehensive Polymer Science and Supplements*, 667–699. doi: 10.1016/B978-0-08-096701-1.00178-6 (1989).
- [2] Saba, N., & Jawaid, M. Epoxy resin based hybrid polymer composites. *Hybrid Polymer Composite Materials: Properties and Characterisation*. Elsevier Ltd. doi:

-
- 10.1016/B978-0-08-100787-7.00003-2 (2017).
- [3] Woodcock, J., Fox, D. M., Davis, C. S., Zammarano, M., Matko, S., Gilman, J. W., Davis, R. D. Epoxy Composites Using Wood Pulp Components as Fillers. *Composites from Renewable and Sustainable Materials*. doi: 10.5772/65261 (2016)

Super-Hydrophilic Interface - Zwitterionic Structure Design for Multiple Application

Ying-Nien Chou^{1,*}

¹)Department of Chemical and Materials Engineering, Southern Taiwan University of Science and Technology, Taiwan

*E-mail: ynchou@stust.edu.tw

Abstract

We introduced a thermo-settable zwitterionic copolymer to design a high temperature tolerance biomaterial as a general antifouling polymer interface. The original synthetic fouling-resistant copolymer, poly(vinylpyrrolidone)-co-poly(sulfobetaine methacrylate) (poly(VP-co-SBMA)), is both thermal-tolerant and fouling-resistant, and the antifouling stability of copolymer coated interfaces can be effectively controlled by regulating the VP/SBMA composition ratio. We studied poly(VP-co-SBMA) copolymer gels and networks with a focus on their general resistance to protein, cell, and bacterial bio-adhesion, as influenced by the thermo-setting process. Interestingly, we found that the shape of the poly(VP-co-SBMA) copolymer material can be set at a high annealing temperature of 200°C while maintaining good antifouling properties. However, while the zwitterionic PSBMA polymer gels were bio-inert as expected, control of the fouling resistance of the PSBMA polymer networks was lost in the high-temperature annealing process. A poly(VP-co-SBMA) copolymer network composed of PSBMA segments at 32 mol% showed reduced fibrinogen adsorption, tissue cell adhesion, and bacterial attachment, but a relatively higher PSBMA content of 61 mol% was required to optimize resistance to platelet adhesion and erythrocyte attachment to confer hemocompatibility to human blood. We suggest that poly(VP-co-SBMA) copolymers capable of retaining stable fouling resistance after high temperature shaping have a potential application as thermo-settable materials in a bio-inert interface for medical devices, such as the thermo-settable coating on a stainless steel blood-compatible metal stent investigated in this study.

Most biomaterials have a lack of a simple, efficient and robust antifouling modification approach that limits their potential for biomedical applications. The challenge is to develop a universal surface grafting solution to meet the antifouling requirement. In this work, a new formulation of zwitterionic sulfobetaine-based copolymer, poly(glycidyl methacrylate-co-sulfobetaine methacrylate) (poly(GMA-co-SBMA)), is designed as a chemical for grafting onto material and is introduced for the surface zwitterionization of versatile biomaterials, including ceramic, metal, and plastics. The grafting principle used to stabilize the poly(GMA-co-SBMA) on the target surfaces is based on the base-induced ring opening reaction between epoxide and hydroxyl groups. A universal surface modification procedure was developed and performed from an optimized sequence of ultra-violet ozone pretreatment and trimethylamine-catalyzed zwitterionization on a selective case of versatile surfaces including silicon wafer, ceramic glass, titanium, steel, and polystyrene. The prepared poly(GMA-co-SBMA) with an optimum PGMA/PSBMA ratio of 0.23 and a molecular weight of 25 kDa exhibited the best resistance to fibrinogen adsorption with over 90% reduction as well as blood cell activation, tissue cell adhesion and bacterial attachment on the zwitterionic copolymer grafted surfaces. The developed antifouling grafting introduces a universal modification method to generate zwitterionic interfaces on versatile biomaterial substrates, providing great potential for application in medical device coating.

For surface-based diagnostic devices to achieve reliable biomarker detection in complex media such as blood, preventing nonspecific protein adsorption and incorporating high loading of biorecognition elements are paramount. In this work, a novel method to produce nonfouling zwitterionic hydrogel coatings was developed to achieve these goals. Poly(carboxybetaine acrylamide) (pCBAA) hydrogel thin films (CBHTFs) prepared with a carboxybetaine diacrylamide crosslinker (CBAAX) were coated on gold and silicon dioxide surfaces via a simple spin coating process. The thickness of CBHTFs could be precisely controlled between 15 and 150 nm by varying the crosslinker concentration, and the films demonstrated excellent long-term stability. Protein adsorption from undiluted human blood serum onto the CBHTFs was measured with surface plasmon resonance (SPR). Hydrogel thin films greater than 20 nm exhibited ultra-low fouling (<5 ng/cm²). In addition, the CBHTFs were capable of high antibody functionalization for specific biomarker detection without compromising their nonfouling performance. This strategy provides a facile method to modify SPR biosensor chips with an advanced nonfouling material, and can be potentially expanded to a variety of implantable medical devices and diagnostic biosensors.

1. Thermal-tolerant zwitterionic material

2. Universal coating via epoxytated zwitterionic copolymer

3. Zwitterionic hydrogel-thin-film SPR biosensor

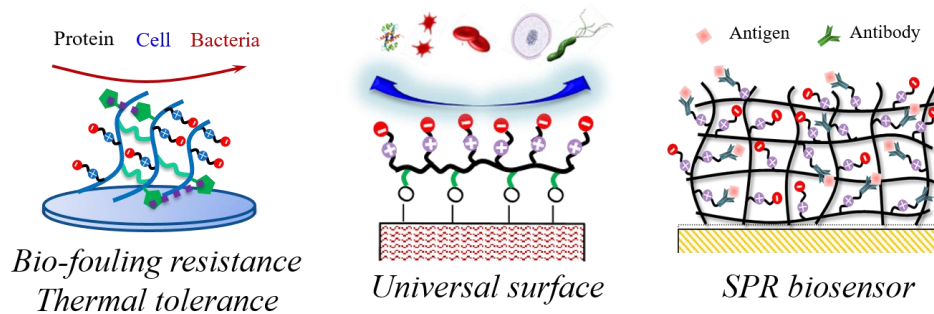


Fig. 1. Novel super-hydrophilic application with zwitterionic antifouling surfaces.

References:

- [1] Ying-Nien Chou, Yung Chang, and Ten-Chin Wen, *ACS Appl. Mater. Interfaces*, **7**, 10096–10107 (2015).
- [2] Ying-Nien Chou, Ten-Chin Wen, and Yung Chang, *Acta Biomaterialia.*, **40**, 78–91 (2016).
- [3] Ying-Nien Chou, Fang Sun, Hsiang-Chieh Hung, Priyesh Jain, Andrew Sinclair, Peng Zhang, Tao Bai, Yung Chang, Ten-Chin Wen, Qiuming Yu, Shaoyi Jiang, *Acta Biomaterialia.*, **40**, 31–37 (2016).

Optimization of Performance of a Sweet Sorghum Threshing Cylinder

Reynold M. Caoili¹⁾, Delfin C. Suministrado²⁾, Rossana Marie C. Amongo²⁾, Arsenio N. Resurreccion²⁾, and Engelbert K. Peralta³⁾

¹⁾Department of Agricultural and Biosystems Engineering, College of Engineering, Mariano Marcos State University, City of Batac, 2906 Ilocos Norte, Philippines

E-mail: reynoldmcaoili@yahoo.com

²⁾Agricultural Machinery Division, Institute of Agricultural Engineering, College of Engineering and Agro-industrial Technology, University of the Philippines Los Baños, College, 4031 Laguna, Philippines

E-mail: dcsuministrado@yahoo.com; rnc_amongo@yahoo.com; archieresu@yahoo.com.ph

³⁾Agricultural and Bio-process Division, Institute of Agricultural Engineering, College of Engineering and Agro-industrial Technology, University of the Philippines Los Baños, College, 4031 Laguna, Philippines

E-mail: engelbert.peralta@gmail.com

Abstract

A rice thresher was initially evaluated as sweet sorghum thresher. Results of preliminary test showed inefficiency having a lower threshing efficiency of 96.28 percent and higher amount of mechanically damaged grain of 6.08 percent compared to allowable standard values of thresher. This signified the need to improve the threshing cylinder as it was further reiterated during the interview of farmer-user of the rice thresher. Response surface methodology was used to characterize the performance of the peg-tooth type threshing cylinder by Box and Behnken Design. Independent variables include the number of peg-tooth, threshing cylinder speed, and concave clearance. Response variables were threshing recovery, threshing cylinder efficiency, and amount of mechanically damaged grain. Optimization revealed that the ideal region of operation was at 36 peg-teeth, threshing cylinder speed settings of 830 to 840 rpm, and concave clearance of 15 mm. Models were validated and found 99.66%, 99.59%, and 92.08% accurate for predicting threshing recovery, threshing cylinder efficiency, and amount of mechanically damaged grain, respectively.

Sweet sorghum (*Sorghum bicolor* (L.)) is the only crop that provides grain and sugary juice at the same time. Postproduction operations like threshing and cleaning remained serious problems to the farmers. A lot of threshing studies in the Philippines were done for a long time for different crops but no adequate research conducted for threshing sweet sorghum. In the Philippines, farmers used and adopted the rice thresher to thresh sweet sorghum grains, however, results of preliminary test showed inefficiency for sweet sorghum threshing.

Generally, the study aimed to design and establish the optimum operating conditions of sweet sorghum thresher. Specifically, the study aimed to: 1) study the effects of operating parameters such as number of peg-teeth, threshing cylinder speed, and concave clearance on the threshing cylinder performance; 2) develop empirical equations or regression models to relate the different operating parameters with the threshing performance parameters; and 3) determine the optimum areas of operation of the threshing parameters.

Sweet sorghum samples were collected in the field following an approved method of sampling and characterized in term of variety, moisture content, straw length, and grain to straw ratio^[1].

Basic performance parameters such as threshing recovery, threshing efficiency, and amount of mechanically damaged grains were determined.

There were three independent variables

considered in analyzing the performance of sweet sorghum thresher. These include the number of peg-tooth, threshing cylinder speed, and concave clearance. Three levels of each independent variables were used in the experimental design (Table 1).

Table 1. The coded values of each factors.

Coded Value	Number of peg-tooth	Cylinder speed (rpm)	Concave clearance (mm)
-1	32	700	5
0	36	800	10
+1	40	900	15

Data gathering and its subsequent analysis followed the Box and Behnken design. The results of Box and Behnken design of experiment were analyzed using a response surface regression analysis^[2].

After identifying the optimal operational setting, model validation was conducted by making three experimental runs within the model design space. The accuracy of the models' prediction was evaluated by comparing the experimental values of threshing recovery, threshing efficiency, and mechanically damaged grain to the predicted values of the model.

The mathematical models that best characterized threshing recovery, threshing efficiency, and amount of mechanically damaged grains were a reduced and modified cubic models. This means that interaction between factors were present and the relationships

were non-linear.

Threshing recovery. Results revealed that the threshing recovery increases as the concave clearance setting increases as shown in Fig. 1. This implies that the decreased of concave clearance caused the intensity of compression leading to a more damaged grains that lessen the recovery, thus increasing the clearance caused the threshing recovery increased.

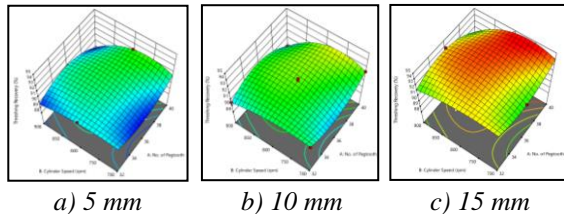


Fig. 1. Response surfaces of threshing recovery at different concave clearance settings

Threshing efficiency. The threshing efficiency decreased as the concave clearance setting increased because the closer the clearance the higher the intensity of compression, thus the amount of unthreshed grains decreased (Fig. 2). Moreover, the threshing efficiency was increased with increased of number of peg-tooth because of more peg-teeth that hit the grains that create higher collision energy (Fig. 3). Furthermore, the threshing efficiency was increased with increased of threshing cylinder speed since the peripheral speed at the tip of the peg-teeth was increased leading to more impacts on the grains (Fig. 4).

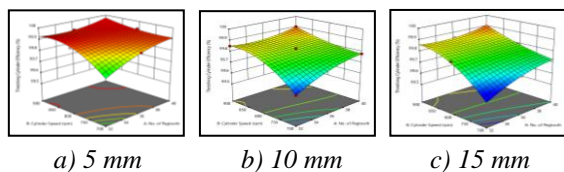


Fig. 2. Response surfaces of threshing efficiency at different concave clearance settings.

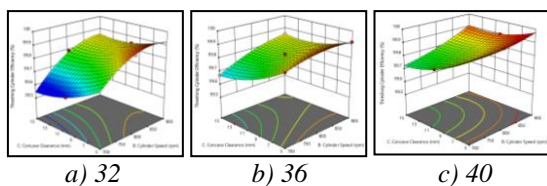


Fig. 3. Response surfaces of threshing efficiency at different number of peg-tooth settings

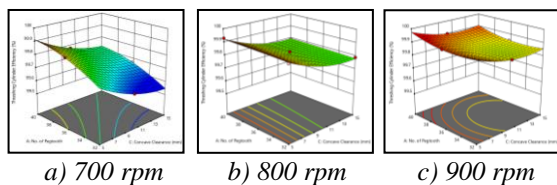


Fig. 4. Response surfaces of threshing efficiency at different threshing cylinder speed settings

Mechanically damaged grain. The amount of mechanically damaged grain decreased as the

concave clearance setting increased as shown in Fig. 5. The decreased of concave clearance caused the intensity of compression resulted to higher amount of mechanically damaged grains. Moreover, the mechanically damaged grain was increased with increased of number of peg-tooth (Fig. 6) because the increased in number of peg-teeth had caused more impacts with the grains leading to more grains being cracked or dehulled with each impact. Furthermore, the mechanically damaged grain was increased with increased of threshing cylinder speed (Fig. 7) because the peripheral speed at the tip of the peg-teeth was increased leading to more impacts on the grains.

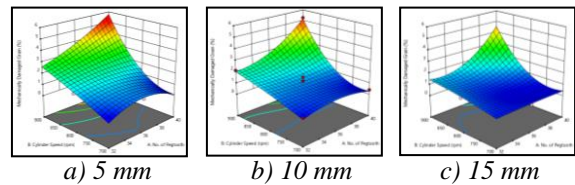


Fig. 5. Response surfaces of mechanically damaged grain at different concave clearance settings.

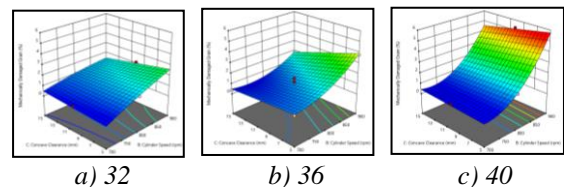


Fig. 6. Response surfaces of mechanically damaged grain at different number of peg-tooth settings

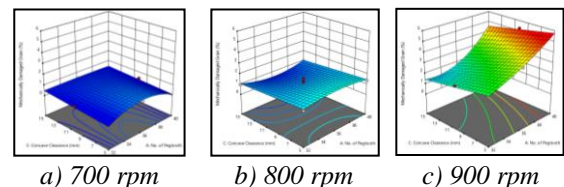


Fig. 7. Response surfaces of mechanically damaged grain at different threshing cylinder speed settings

Optimal operational setting. Result of numerical optimization revealed that the ideal region of operation was at 36 peg-teeth, threshing cylinder speed of 830 to 840 rpm, and concave clearance of 15 mm. The validation experiment supported validity of the model because of the close fit of actual and predicted responses. Accuracy of the models' prediction was 98.56%, 99.59%, and 93.81% for threshing recovery, threshing efficiency, and amount of mechanically damaged grain, respectively.

References:

- [1] Philippine Agricultural Engineering Standard (PAES) 205:2000. Agricultural Machinery – Mechanical Rice Thresher – Methods of Test, UPLB.
- [2] Cavazzuti, M. 2013. Optimization methods: From theory to design scientific and technological aspects in mechanics. XVIII, 262 pp.

Investigation on Deformation Behavior of Photomask Protective Film

Yu-Ching Lee

Department of Mechanical Engineering, Southern Taiwan University of Science and Technology, Taiwan
E-mail: ycllee@stust.edu.tw

Abstract

Photomask protective film is an important device for photomask protection in photolithography process. In this paper, surface profile and deformation of photomask protective film is measured by fringe reflection method. Protective film devices with and without damage were investigated during measurement. Experimental results show that the trend of out-of-plane displacement for thinner membrane is more nonlinear than thicker one.

Photomask is an indispensable component and requires considerable skill and expense in manufacturing and maintenance during the lithography process in advanced semiconductor process [1, 2]. Deformation of the protective film on the photomask may occur whenever equipment or users hold it. However, there is scarce literature on measurement of the protective film on the photomask subjected to external flow and force. This study focused on the establishment of a non-destructive system for out-of-plane displacement measurement on photomask protective film devices by fringe reflection method [3, 4]. The thin film on the photomask has improved wafer yield and protected the pattern from fall-on particles in the clean room, reducing the cost of photomask repair and cleaning. Therefore, investigations on deformation of the protective thin film will help to extend the life of the photomask and reduce costs [5, 6].

In this research, A Fringe reflection method was used to measure out-of-plane deformation of photomask protective film subjected to external force. A fringe reflection system contains an LCD, a CCD and a signal processing system. The transverse fringe patterns are presented on an LCD. If the specular surface of sample is not flat relative to a reference mirror, the fringe patterns captured by the CCD will shift or deform due to the slope variation of the surface. Fig.1 shows the schematic diagram of fringe reflection system. The fringe shift distance can be calculated by using phase shifting and phase unwrapping techniques in the processing system. Accordingly, the phase difference between the sample and reference mirror can be found and the relation between the slope variation and the phase difference. By integrating the slope variation along the x and y direction, the surface topography can be thus constructed.

In our experiment, photomask protective film devices with and without damage were selected for measurement. It shows that the scrape part of film is unresolvable in the surface topography due to no interference fringes produced on the scrape part. In addition, the film was exerted by the external flow from the nozzle head. The movable stage was used to control the distance between the nozzle head and film.

The experimental result shows that the out-of-plane deformation increases as the distance between the nozzle and film decreases. It is also noted that the out-of-plane displacement curve are non-linear up to displacement.

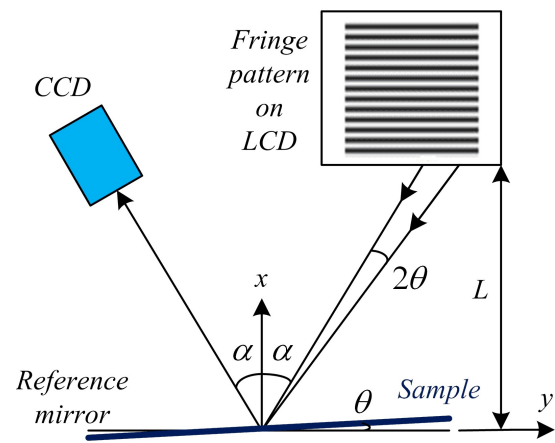


Fig. 1. Schematic diagram of fringe reflection system.

References:

- [1] B.J. Lin., The Future of Subhalf-Micrometer Optical Lithography, *Microelectronic Engineering*, **6**, 31-51 (1987).
- [2] B.J. Lin, Immersion Lithography and Its Impact on Semiconductor Manufacturing, *Journal of Micro/Nanolithography, MEMS, and MOEMS*, **3**, 377-395 (2004).
- [3] X. Zhang and W. North, Retroreflective grating generation and analysis for surface measurement, *Applied Optics*, **37**, 2624-2627, (1998).
- [4] X. Zhang and W. North, Retroreflective projection gratings, *Optics & Laser Technology*, **35**, 369-372, (1999).
- [5] B. J. Grenon. , C. Peters, K. Battacharyya, and W. Volk, Formation and Detection of Sub-pellicle Defects by Exposure to DUV System Illumination, *Proceedings of SPIE*, (1999).
- [6] I. Pollentier, J. U. Lee, M. Timmermans, C. Adelman, H. Zahedmanesh, C. Huyghebaert, and E. E. Gallagher, Novel membrane solutions for the EUV pellicle: better or not, *Proceedings of SPIE*, (2017).

Optical characteristics of high-In-incorporated GaInN MQWs grown by RF-MBE

R. Yoshida, Y. Nakajima, H. Hirukawa, S. Ohno, T. Yamaguchi, T. Onuma, and T. Honda

Department of Electrical Engineering and Electronics, Graduate School of Engineering, Kogakuin University,
Tokyo, Japan

e-mail: cm19051@ns.kogakuin.ac.jp

-Introduction-

GaInN is an alloy semiconductor of InN and GaN with bandgap energies of about 0.7 eV and 3.4 eV, respectively, at room temperature (RT). This indicates that GaInN can emit the lights over the entire visible spectral range by controlling its composition ratio. Therefore, GaInN is applicable to use for semiconductor material in full-color μ -LED flat panel display [1]. However, rapid decrease in the internal quantum efficiency (IQE) in high-In-incorporated GaInN/GaN multi quantum wells (MQWs)[2] emitting in red color region is serious problem compared to those for the LEDs in blue or green color region due mainly to the quantum confined Stark effect (QCSE) induced in the strained quantum wells[3]. Moreover, growths of high-In-incorporated GaInN alloys by metal organic chemical vapor deposition (MOCVD) are suffered from a phase separation.

Behind this background, we have been proposing to employ high-In-incorporated $\text{Ga}_{1-x}\text{In}_x\text{N}/\text{Ga}_{1-y}\text{In}_y\text{N}$ ($x>y$) MQWs grown by radio-frequency plasma-assisted molecular beam epitaxy (RF-MBE) since the structure can suppress QCSE, which is one of the causes of deterioration of IQE as mentioned above[4]. In this study, photoluminescence (PL) spectra of high-In-incorporated $\text{Ga}_{1-x}\text{In}_x\text{N}/\text{Ga}_{1-y}\text{In}_y\text{N}$ MQWs are measured to assess an impact of growth temperature (T_G) on their optical characteristics.

-Experiment-

Approximately 0.4- μm -thick $\text{Ga}_{0.75}\text{In}_{0.25}\text{N}$ film was grown as an underlayer by RF-MBE on the commercially available GaN/ Al_2O_3 templates, in which T_G of 720°C was monitored by a thermocouple setting in the vicinity of backside of the substrate. The growth time was 1 hour. Subsequently, 5-periods of 2-nm-thick $\text{Ga}_{1-x}\text{In}_x\text{N}$ / 5-nm-thick $\text{Ga}_{0.75}\text{In}_{0.25}\text{N}$ MQWs were grown by varying T_G from 580 to 720°C with fixed Ga/In flux ratio, nitrogen gas flow rate and RF plasma power. The substrate holder was rotated during the whole growth process to suppress in-plane inhomogeneity. The MQWs and a single layer ($\text{Ga}_{0.75}\text{In}_{0.25}\text{N}$ film grown at 720°C) were characterized by the X-ray diffraction (XRD) 2θ - ω and PL measurements. The PL was excited by 325.0 nm line of He-Cd laser with an excitation power of 50 mW, and was dispersed by a 64 cm focal-length Czerny-Turner monochromator equipped with a 600 groove/mm grating. Then, the dispersed light was detected by a photomultiplier tube using the lock-in detection technique.

-Results and Discussion-

As shown in Fig. 1, $\text{Ga}_{1-x}\text{In}_x\text{N}$ (002) diffraction peak for the samples grown at $T_G = 700^\circ\text{C}$ and 720°C exhibits a shift toward higher diffraction angle compared to that of the single layer. A diffraction peak was additionally observed in between the GaN (002) and $\text{Ga}_{1-x}\text{In}_x\text{N}$ (002) diffraction peaks though its origin is unknown at present. Such additional peak disappeared for the samples grown at $T_G = 580^\circ\text{C}$, 620°C , and 660°C , and predominant $\text{Ga}_{1-x}\text{In}_x\text{N}$ (002) peak moderately shifted toward lower diffraction angle. PL spectra at RT are summarized in Fig. 2. The single layer exhibited a peak at 580 nm, and the peak wavelength showed blueshift for the sample grown at 720°C. The peak wavelength showed gradual increase from 551 nm to 675 nm with decreasing T_G from 720°C to 580°C. Note that the spectra for the samples grown at $T_G = 620^\circ\text{C}$ and 580°C are superimposed by a PL peak at around 580 nm from the $\text{Ga}_{0.75}\text{In}_{0.25}\text{N}$ underlayer. The sample grown at the lowest T_G eventually showed PL wavelength in a wavelength range of 620-750 nm. The results demonstrate successful growths of high-In-incorporated GaInN MQWs emitting in red color region by employing the appropriate $\text{Ga}_{0.75}\text{In}_{0.25}\text{N}$ underlayer.

-Reference-

- [1] J. Day *et al.*, Appl. Phys. Lett. **99**, 031116 (2011).
- [2] S. Nakamura *et al.*, J. Appl. Phys. **74**, 3911 (1996).
- [3] T. Takeuchi *et al.*, Appl. Phys. Lett. **73**, 1691 (1998).
- [4] M. Siekacz *et al.*, J. Cryst. Growth **310**, 3983(2008).

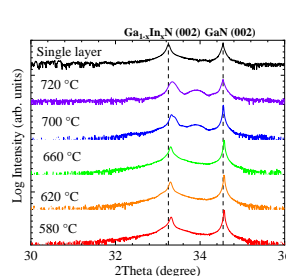


Fig. 1 XRD 2θ - ω patterns for samples grown at 580°C to 720°C and single layer.

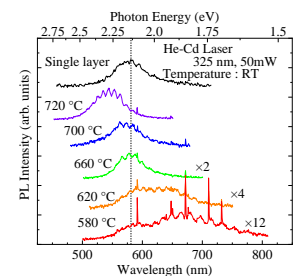


Fig. 2 PL spectra for samples grown at 580°C to 720°C and single layer.

Preparation of cellulose nanocrystals and microfibrillated cellulose from bakong (*Hanguana malayana* (Jack) Merr.)

Glenn Christian P. Acaso¹⁾, Veronica P. Migo²⁾, and Ramon A. Razal³⁾

¹⁾Department of Chemical Engineering, University of the Philippines Los Baños, Laguna, Philippines
E-mail: gpacaso@up.edu.ph

²⁾ Department of Chemical Engineering, University of the Philippines Los Baños, Laguna, Philippines
E-mail: vpmigo@up.edu.ph

³⁾ Department of Forest Products and Paper Science, University of the Philippines Los Baños, Laguna, Philippines
E-mail: rarazal@up.edu.ph

Abstract

Nanocellulose is a renewable material with a potential for applications in advanced materials due to its highly reactive surface and mechanical properties. *Hanguana malayana* (Jack) Merr., commonly known as Bakong, is one promising source of cellulose due to its abundance in one region of the Philippines. In this study, cellulose nanocrystals (CNC) and microfibrillated cellulose (MFC) were produced from Bakong fibers. The fibers were ground using a Wiley mill, pulped using 10% sodium hydroxide, and then bleached with 5% sodium hypochlorite. For preparing the CNC, the bleached fibers were treated with 17.5% sodium hydroxide, then hydrolyzed using 46, 55, and 64% sulfuric acid. For the MFC, the bleached pulp was subjected to mechanical grinding using a Masuko Supermasscolloider at 1500 rpm for 15 passes. The overall CNC and MFC yields were 0.0353% and 41.57%. The nanocellulose products were characterized using optical microscopy, scanning electron microscopy, dynamic light scattering, and infrared spectroscopy. The CNCs have lengths of 102 nm and widths of 22 nm on average, while the MFCs were composed of large 20 μm fibers with evidence of defibrillation on the surface.

I. INTRODUCTION

Cellulose is the main component of the cell wall of most plant species. It can form an ordered crystalline structure giving it good mechanical properties. [1]. Nanocellulose is a form of cellulose wherein the size of at least one dimension is in the nanometer scale. They are classified as either cellulose nanocrystals (CNCs) or cellulose nanofibrils (CNFs). CNCs, produced by acid hydrolysis, are 5-70 nm wide, between 100 nm to several microns long, and 54-88% crystalline [2,3]. On the other hand, CNFs are produced upon treatment with mechanical refining equipment usually accompanied by a significant increase in viscosity after several passes [4]. One source of cellulose used for this study is *Hanguana malayana* (Jack) Merr., commonly known as Bakong. It is a species of perennial herbaceous plant native than can be found in Cagayan in the Philippines. It has since been popular in the area and is projected to become a great source of livelihood for the people.

II. METHODOLOGY

Pulping and Bleaching

For the production of CNC, pre-bleached fibers were used, while unbleached fibers were used for the production of MFC. The fibers were cooked in a pressure cooker at 120°C for 3 hours using 10% NaOH by weight. The pulp fibers were then bleached by treating with 5% NaClO (10 g per 100 mL) for 30 minutes.

Production of cellulose nanocrystals (CNC)

Three grams of bleached pulp underwent alkali treatment using 60 mL of 17.5% NaOH at 20°C for 30 min. to produce alkali-insoluble cellulose (AIC). The solution was then neutralized with 10% CH₃COOH. 50 mL of H₂SO₄ at 46, 55, and 64% v/v were added to 1 g samples of the AIC. The mixtures were then immersed in a water bath for 30 min. at 45°C. 500 mL of cold distilled water was added, and the mixtures were left to settle for 24 hours. The products were then centrifuged, subjected to dialysis for 24 hours, and sonicated for 30 minutes.

Production of microfibrillated cellulose (MFC)

Bleached pulp in water at 1 gram per 1000 mL ratio was subjected to a mechanical grinding process for 15 passes using the Masuko Supermasscolloider, model MKCA6-2. The grinder was operated at a speed of 1500 rpm.

Characterization of the samples

The pulp, bleached pulp, AIC, CNC, and MFC were subjected to Fourier-Transform Infrared Spectroscopy (FTIR). To observe the morphology of the CNC and MFC, optical microscopy and scanning electron microscopy (SEM) were used. Dynamic light scattering (DLS) using a Malvern Instruments Zetasizer Nano-ZS90 was also performed.

III. RESULTS AND ANALYSIS

CNC and MFC yields

Table 1 shows the summary of the material yields.

Table 1. CNC and MFC production yields.

Process	Yields (%)	
	CNC	MFC
Pulping	81.5	71.45
Bleaching	71.7	66.47
Alkali treatment (CNC)	43.1	-
Acid hydrolysis (CNC)	14.0	-
Grinding at 15 passes (MFC)	-	87.52
Overall	0.0353	41.57

Concentrations of 46 and 55% v/v sulfuric acid were initially applied to the AIC. The solution did not turn clear indicating that large molecules were still present. Only after treatment with 64% v/v did the solution turn translucent indicating that the hydrolysis products are nanoparticulate. The yield after acid hydrolysis was only 14.0% with an overall yield of 0.0353%. This is low, as yields up to 88% have been reported [5].

On the other hand, the yield after producing MFC was 87.52% with an overall yield of 41.57%. This is a good value for the yield, but increasing this is still very likely, as further improvements in the pulping and bleaching processes may be done.

Morphology of the CNC and CNF

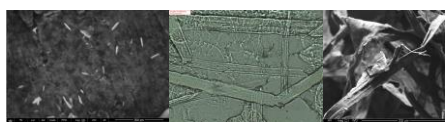


Fig. 1. SEM image of the CNC (left), optical microscope image of the MFC (middle), and SEM image of MFC (right)

Figure 1 shows the scanning electron microscope of the CNC and MFC. It was observed that the CNC consisted of rod-like particles with lengths of around 102 nm and widths of 22 nm on average. The particles may be considered cellulose nanoparticles [2]. The low aspect ratio of the obtained samples suggested that the treatments may have been harsh, and that the particles have significantly degraded.

On the other hand, the MFC were 700 μm long and 20 μm wide, but much smaller fibers and evidence of microfibrillation were visible. The SEM image of the freeze-dried suspension suggests that significant defibrillation occurred during grinding. However, the drying method was not able to successfully isolate the individual microfibrils, agglomerating and forming sheet-like structures.

Fourier Transform Infrared Spectroscopy

Figure 2 shows the FTIR spectra of the CNC, MFC, and intermediate products.

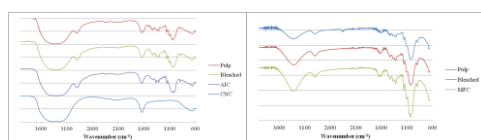


Fig. 2. FTIR spectra of the intermediates leading to the CNC (left) and the MFC (right)

The characteristic peaks are compared to the nanocellulose peaks described in another study [6]. The functional groups present in the spectra confirm that the products are made up of cellulose. It was observed that there were no significant differences in the FTIR spectra different samples. Thus, it can be concluded that the cellulose backbone of the Bakong fibers was not altered significantly during the processes.

Size analysis by Dynamic Light Scattering

The size distribution peaks of the suspended particles are shown in Figure 3. Three peaks were present. The lowest sized peaks were at around 300 nm, the mid-sized peaks were at around 1000 nm, and the largest sized peaks were at 5000 nm. This shows that the friction grinder was able to produce cellulose fibrils to the nanometer range. However, the uniformity of the fibers was not very good since no further treatments were made to improve the size distribution of the sample.

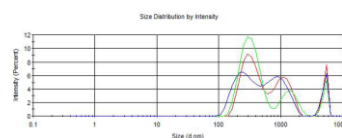


Fig. 3. Size distribution of the particles in the MFC suspension

IV. CONCLUSION

Cellulose nanocrystals (CNC) and microfibrillated cellulose (MFC) were produced from Bakong (Hanguana malayana (Jack) Merr.) fibers. CNC was successfully prepared by hydrolysis using sulfuric acid. Upon treatment, using less than 64% v/v on the samples was ineffective. Further purification by centrifugation and dialysis produced CNCs of almost uniform sizes. However, the yield and the aspect ratio of the samples were low, so further optimization of the processes is recommended. On the other hand, MFC was produced friction grinding. The grinding yield was 87.52% after 15 passes, while optical microscopy and scanning electron microscopy supported that microfibrillation occurred. Dynamic light scattering analysis was performed on the MFC and a non-uniform size distribution was observed. The high yields obtained showed that the method used for producing the MFC was promising. FTIR analysis of the samples showed that the cellulose backbone of the intermediates did not change significantly during the treatments. Overall, the Bakong fibers showed promise as a source of cellulose nanocrystals and microfibrillated cellulose. Finding further applications of the CNC and MFC from Bakong for advanced materials is recommended.

ACKNOWLEDGMENT

The author would like to thank the Design Center of

the Philippines for providing the Bakong fibers. The author would also like to thank the Department of Chemical Engineering and the Department of Forest Products and Paper Science of the UPLB. Lastly, the author would also like to thank the DOST-ERDT Program for providing the scholarship used in the study.

References:

- [1] Borjesson, M., & Westman, G. Crystalline nanocellulose – preparation, modification, and properties. In M. Poletto (Ed.), *Cellulose – Fundamental Aspects and Current Trends*, 159-191. London, United Kingdom: InTech (2015)
- [2] Brinchi, L. Cortana, F., Fortunati, E. & Kenny, J. Production of nanocrystalline cellulose from lignocellulosic biomass: technology and applications. *Carbohydrate Polymers*, **94(1)**, 154-169 (2013).
- [3] George, J., & Sabapathi, S.N. Cellulose nanocrystals: synthesis, functional properties, and applications. *Nanotechnology, Science and Applications*, **8**, 45-54 (2015).
- [4] Kargarzadeh, H., Ioelovich, M., Ahmad, I., Thomas, S., & Dufresne, A. Methods for extraction of nanocellulose from various sources. In H. Kargarzadeh, I. Ahmad, S. Thomas, & A. Dufresne (Eds.), *Handbook of Nanocellulose and Cellulose Nanocomposites*, 1-49, Weinheim, Germany: Wiley-VCH (2017)
- [5] Lu, Q., Cai, Z., Lin, F., Tang, L., Wang, S., & Huang, B. Extraction of cellulose nanocrystals with a high yield of 88% by simultaneous mechanochemical activation and phosphotungstic acid hydrolysis. *ACS Sustainable Chemistry & Engineering*, **4(4)**, 2165-2172 (2016).
- [6] Sofla, M.R.K., Brown, R.J., Tsuzuki, T., & Rainey, T.J. A comparison of cellulose nanocrystals and cellulose nanofibres extracted from bagasse using acid and ball milling methods. *Advances in Natural Sciences, Nanoscience and Nanotechnology*, **7(3)**, 1-9 (2016).

Development of various techniques for aerosol analysis by TOF-SIMS

Masato Morita,¹⁾ Ryota Koiwai,²⁾ Toru Murata,²⁾ Tetsuo Sakamoto^{1),2),*}

¹⁾ Department of Applied physics, School of Advanced Engineering, Kogakuin University

²⁾ Graduate School of Electric Engineering and Electronics, Kogakuin University

*E-mail: ct13087@ns.kogakuin.ac.jp

Abstract

For the aerosol analysis, the bulk analysis method of collected particles on a filter is widely used. In the bulk analysis, the information with high accuracy as the averaged value of collected particles can be obtained, but the information of individual particle is not obtained. In this study, aerosol was analyzed with a high resolution by means of TOF-SIMS developed by our group. This study introduces aerosol sample collection methods suitable for surface analysis techniques such as TOF-SIMS, and statistically reliable particle analysis while preserving individual particle information.

Introduction

Various fine particles (aerosol) exist in the atmosphere. In recent years, by the economic development of the Asian region, harmful aerosol emitted from industrial region becomes a serious problem. Particularly, the interest in human health impact and environment issues such as acid rain cause in relation to aerosol increase. In case of analysis of aerosol, bulk analysis method of all the collected particles on a filter is widely used, such as ICP-MS for inorganics, GC-MS for organics and so on. In the bulk analysis, information with high accuracy as the average values of collected particles can be obtained. However, there is a slight difference in the same kind of aerosol particles, and an analytical technique that can analyze individual particle is required. Therefore, we developed high resolution TOF-SIMS apparatus for individual particle analysis[1]. Moreover, the aerosol sampler for TOF-SIMS and the other surface analysis techniques was developed.

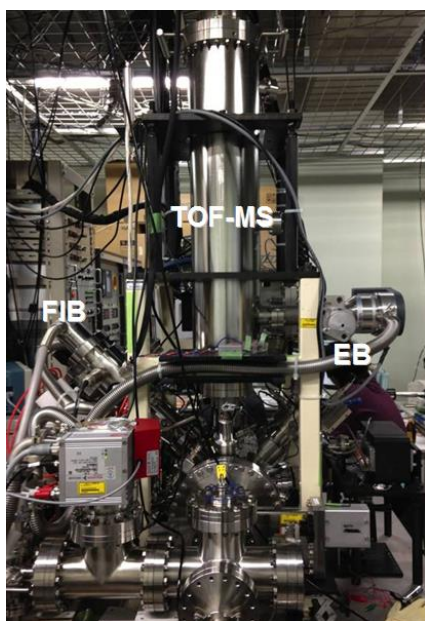


Fig. 1 Photograph of our TOF-SIMS apparatus

High resolution TOF-SIMS

Figure 1 shows the photograph of our developed TOF-SIMS apparatus. This apparatus equips the gallium focused ion beam for primary ion beam and in situ micro machining, FE-SEM for non-destructive observation, and the cooling stage with liquid nitrogen for the volatile component analysis. The maximum lateral resolution is less than 40 nm in TOF-SIMS mode.

Result and discussion

Figure 2 shows the result of TOF-SIMS analysis for yellow sand. There were two types of yellow-sand particles, namely, dissolved particles and dry one. Dissolved particle is thought to be the reaction product of yellow sand chlorination. The shapes of these two types are quite different. The ratio of chlorination will provide us the information on the trajectory of the particle during the emission and collection.

References

[1] T. Sakamoto *et al.*, *Applied Surface Science*, **255**, 1617 (2008).

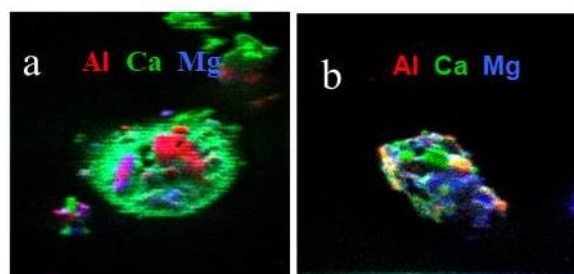


Fig. 2 TOF-SIMS maps of (a) dissolved yellow-sand (chlorinated yellow sand), (b) dry yellow-sand.

Photoluminescence Au NDs—PNIPAM Hybrid Microspheres: Synthesis and Application as Hg²⁺ Sensor

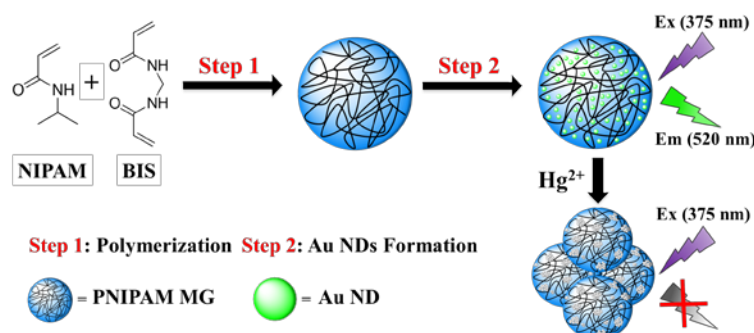
Wei-Yu Chen¹⁾

¹⁾Department of Chemical and Materials Engineering, Southern Taiwan University of Science and Technology, Tainan, Taiwan

E-mail: weiyuchen@stust.edu.tw

Abstract

In the present study, we unveil an approach for producing PNIPAM microgel particles hybridized with photoluminescence gold nanodots (Au NDs). Transmission electron microscopy (TEM) images showed that photoluminescence Au NDs ($d: 1.8 \pm 0.2$ nm) have been successfully loaded on the PNIPAM microgel particles ($d: 615 \pm 15$ nm) (denoted as Au NDs—PNIPAM microspheres). Compared with the original 11-MUA—Au NDs, the Au NDs—PNIPAM exhibited the same optical properties, including absorption and photoluminescence, but displayed higher stability under high ionic strength media. Using PNIPAM particles as carrier of Au NDs, which not only provide the ability of Hg²⁺ adsorption but also provide high sensitivity of Hg²⁺ detection based on luminescence quenching of Au NDs. This approach provided a limit of detection for Hg²⁺ (at a signal-to-noise ratio of 3) of 0.21 nM, with great selectivity (at least 90-fold) over other metal ions. We also demonstrated the feasibility of using developed hybrid materials for determination of mercury in fish sample.



References:

- [1] Li-Yi Chen, Chung-Mao Ou, Wei-Yu Chen, Chih-Ching Huang, Huan-Tsung Chang, *ACS Appl. Mater. Interfaces*, **5**, 4383–4388 (2013).

Determination of Water Vapor Transmission Rate Using Nitrogen Encapsulated Calcium Sensor

Ching-Ming Hsu, Wen-Tuan Wu, Geng-Wei Zhou, and Yei-Hang Tsai

Department of Electro-Optical Engineering, Southern Taiwan University of Science and Technology, Taiwan
E-mail: tedhsu@stust.edu.tw

Abstract

This work utilized an over-pressurized mechanism to protect calcium (Ca) sensors and achieve more accurate measurements of water vapor transmission rate (WVTR). The results showed WVTR $< 1 \times 10^{-6}$ g/m²/day is possible with the proposed mechanism, and the commercialization of this technique is highly expected.

It has been well demonstrated that flexible organic electronic devices require encapsulations to ensure a high device reliability, and this is generally realized using gas barrier films with an extremely low vapor transmission rate (WVTR). The level of water vapor and oxygen permeation through the gas barrier films must be then accurately monitored in the development of flexible organic electronics, such as organic light-emitting diodes or organic solar cells. Unfortunately, the existing commercial tool can only measure WVTR to a level of 5×10^{-5} g/m²/day, that is not qualified for organic device applications, where WVTR $< 1 \times 10^{-5}$ g/m²/day is required. Some other techniques [1,2] have ability to determine WVTR $< 1 \times 10^{-5}$ g/m²/day, however, they are either too expensive or have safety issues. It is hence important to develop a commercial WVTR measurement technique for flexible organic electronics applications. Calcium test is a laboratory tool capable of measuring WVTR to a level $< 1 \times 10^{-6}$ g/m²/day. Traditional Ca sensors are generally frame encapsulated by a glass backplate using edge glue [3]. Such an architecture usually leads to a measurement instability due to the penetration of moisture through the edge glue. In this work, we employed an over-pressurized mechanism to protect Ca sensors, and that resulted in an improved WVTR measurement accuracy.

As reported elsewhere [4], the measured WVTR for glass substrate using the over-pressurized mechanism could reach WVTR $< 1 \times 10^{-6}$ g/m²/day, superior to a traditional Ca-test device ($\sim 1.0 \times 10^{-4}$ g/m²/day). We then measured gas barrier films using the newly developed Ca-test mechanism. Figure 3 shows the G-t characteristics of SiN/1,1,2,2,9,9,10,10-Octafluoro[2.2]paracyclophane (parylene, AF4) and Al₂O₃/AF4 stacked gas-barrier films on PET substrates. The gas barrier films consist of 1 ~ 2 pairs of SiN/AF4 and 1 ~ 2 pairs of Al₂O₃/AF4 stacking to each other. The calculated WVTR is 1.3×10^{-2} , 1.1×10^{-3} and 8.5×10^{-3} g/m²/day for the gas-barrier films with a stacking structure of 1 pair of SiN_x1, (SiN/AF4)_x2/ (Al₂O₃/AF4)_x1, and (SiN/AF4)_x2/ (Al₂O₃/AF4)_x1, respectively. It is interesting to observe that the WVTR is reduced when more

SiN/AF4 pairs are introduced. Nevertheless, WVTR increases as more Al₂O₃/AF4 pairs are added to the stacked structure. This indicates that adding more gas resistive films does not guarantee a lowered WVTR. Since the Ca-test were conducted on the samples with the same structures for several times and showed the similar G-t characteristics, we believed the results shown in Fig. 3 stand true. The figure then suggests that the stacked films may have pinholes or maybe not dense enough. In addition, film stress may increase as more films are stacked, and that can induce structural defects, leading to deteriorated WVTR. Therefore, the Ca-test confidently gives a message that film quality should be improved before investigating the effect of stacked film pairs.

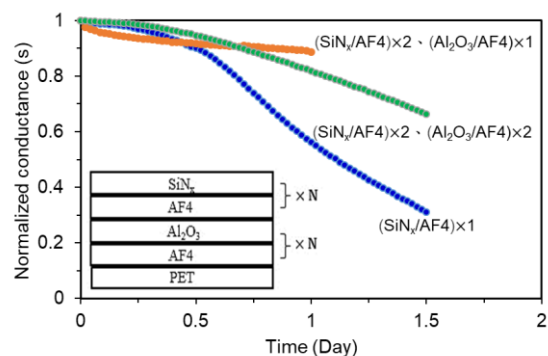


Fig. 1. WVTR Measurement of SiN/AF₄ and Al₂O₃/AF₄ based Gas barrier films using Ca-test.

References:

- [1] A. A. Dameron, S. D. Davidson, B. B. Burton, P. F. Carcia, R. S. McLean, and S. M. George, *J. Phys. Chem. C*, **112**, 4573 (2008).
- [2] M. Norrrahim, H. Ariffin, M. A. Hassan, N. A. Ibrahim, and H. Nishida, *RSC Advance*, **3**, 24378 (2013).
- [3] J. H. Choi, Y. M. Kim, Y. W. Park, J. W. Huh, B. K. Ju, I. S. Kim and H. N. Hwang, *Rev. Sci. Instrum.*, **78**, 064701 (2007).
- [4] C.M. Hsu, W.T. Wu, G.W. Zhou, K.C. Wu, *Proc. 2nd International Conference on Microelectronic Devices and Technologies*, May, 22-23, (2019)

Poster Session

A Study of Japanese-text Compression and Punctuation Prediction with Natural Language Processing

Ryota Tominaga¹⁾, and Hideoshi Saito²⁾

¹⁾Graduate School of Engineering, Kogakuin University, Tokyo, Japan
E-mail: cm18027@ns.kogakuin.ac.jp

²⁾Department of Electrical and Electronic Engineering, Faculty of Engineering, Tokyo, Japan
E-mail: h-saito@cc.kogakuin.ac.jp

Abstract

Recently, the application fields of natural language processing (NLP) has been studied. Developing various NLP systems, machine learning techniques have been expected to play an important role. In this report, we propose a method of improving compression ratios for machine translated Japanese texts with NLP and machine learning prediction of the use of a punctuation mark (comma). Our proposed method can be applied to information compression for any Japanese plain text data.

1. Introduction

Recently, mobile, content, and cloud-based data traffic has been rapidly growing on communication networks^[1]. In order to handle enormous amounts of data on these networks, information compression technology for digital media is an indispensable technology. In addition, the research field of natural language processing (NLP) is attracting attention as a method of analyzing the concept of natural language that we use on a daily basis by use of a computer. NLP is highly useful for machine translation (MT) and has an impact on predictive analytics, etc.^[2]

In this research, we discuss about an effective information compression method using NLP for the document of Japanese (the translated text) into which a MT device translates the document of prescribed language (the original text). In a Japanese text, there is a mark in a sentence, called a punctuation mark. It is important for us to know the way or manner in which punctuation is or has been used^[3]. That is, it needs to insert a punctuation mark into the translated Japanese text exactly if we recognize the clear and unmistakable meaning of the original text. Even among punctuation marks, we focus on the usage of a *comma* in a Japanese document. There are several detailed rules for the usage of a comma in Japanese^[3]. It is possible to make an NLP device predict insertion positions of commas in Japanese texts because a machine learning approach is capable of adapting a method of automatically inserting commas into Japanese texts based on usage classification of commas. Then, we propose and evaluate a Japanese-text compression method using prediction of punctuation marks by NLP.

2. Natural Language Processing

NLP is a field that has been inspired by the concept of communicating with non-human devices as human language research has evolved. NLP is designed and developed to recognize, understand, analyze, learn and synthesize any human language. Therefore, NLP is an artificial intelligence field because its purpose is to

recognize character strings as meaningful character strings in human languages rather than just character strings. Many applications using NLP such as speech recognition and language have been developed over the years.

Especially, Japanese NLP consists of following two major processes: morphological analysis and syntactic analysis. In these processes, morphological analysis is a technique in which a sentence is divided into minimum words and classified into parts of speeches. As a result, the type of the constituent elements of the sentences can be determined. Parsing is a technique for obtaining grammatical relationships between several sentences based on the results of morphological analysis. As a result, parsing makes it possible to know and clear which word has a specific meaning. Then, the reason why we need such a processing is that Japanese sentences don't leave a space between words. In English, there is a space between words written in sentences. We know which letter belongs to a specific word is obvious. However, if a document consists of sentences with unseparated words, such as Japanese, it is necessary to investigate whether we get a meaning word to which letters or characters are connected or not. For this above reason, we need morphological analysis to decide the position of a space between words in a given sentence. Fig.1 shows that an English sentence is translated to the corresponding Japanese sentence and final sentence leaves a space between words by morphological analysis.

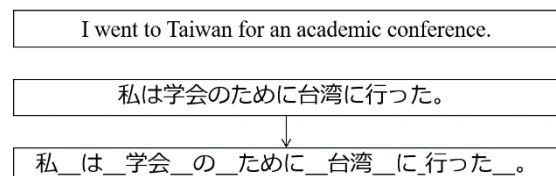


Fig.1 An example of a Japanese sentence leaving a space between each two words.

3. Commas in Japanese Texts

In Japanese, a comma is one of punctuation marks which is called a delimiter character. The Japanese comma is called “*tooten*” formally or “*ten*” informally. Commas are used to separate components such as words and phrases in a sentence. But, rules for the usage of the Japanese comma are relatively loose. Table 1 shows categorization of general usages of commas in Japanese. Commas are commonly used to improve the readability of a Japanese text as shown in Table 1. Commas may be placed wherever a natural break in the sentence might occur.

In Table 2, we show an example of the usage of commas both of in English and Japanese. As can be seen in an example of a common place in Table 2, the comma is right after a subordinate clause. In addition, the Japanese comma should not be placed immediately before a particle or conjunction.

4. Proposed Method

In this section, we explain our proposed method. At first, we remove commas from a translated Japanese document into which a MT device translates the English document. Removing commas from a document in data compression, we expect that the information compression ratio for the document is improved in proportional of the amounts of deleted commas. In encoding of the aimed data file, we can use the encoders implemented with existing lossless data compression algorithms to convert the aimed document files without commas into much smaller compressed files.

Moreover, in decoding, the decoders decode the compressed files to obtain uncompressed files. After we get the documents in the uncompressed files, NLP analyzes each Japanese sentence in these Japanese documents. As a consequence of NLP analysis, we can

Table 1. Categorization of usage of commas [4].

#	Usage
1	Comma for clause divisions
2	Comma to clarify dependency relations
3	Comma to avoid obfuscation and misreading
4	Comma indicating the subject
5	Comma for sentence head conjunction or adverb division
6	Comma to clarify parallel words or phrases
7	Comma for adverb division that represents time
8	Comma to emphasize thw last word
9	Others (Comma for quotation, etc.)

Table 2. Differences in the usage of commas between English and Japanese sentences.

Propriety	Example Sentence
Ok	As an example, I will show one example sentence.
No	As an example, I will show one example sentence.
Ok	例として、私は一つの例文を示します。
Ok	例として、私は一つの例文を示します。

get the complete Japanese sentences with reinserted commas.

5. Evaluation Results

In our proposed compression method, lossless data compression schemes are used in the encoders. In this compression scheme, a decompression function can restore the original file exactly with no loss of data. In this research, following lossless data compression algorithms such as ZIP, BZIP2, LZMA, LZW, LZT are used. We use translated Japanese articles on entertainment, economics, science news provided by general public networks as test data. Table 3 shows the results of information compression of test data. From these results, it is found that information compression ratio varies depending on the news categories. ZIP or BZIP2 is superior compression scheme in comparison with the other scheme. If we use apply our method to original Japanese articles, our method gives average recall and precision for reinserted commas as about 40% and 90%, respectively.

6. Conclusion

In this report, we propose and evaluate a new Japanese-text compression method based on lossless compression schemes and punctuation prediction for “Japanese commas” using NLP. As a result, it is found that the compression ratios for newspaper articles depend on the news categories and there is an essential difference between the compression ratios of news categories. Our method will give nearly equal average recall or average precision for the conventional method [3],[4]. At the end, if we will conduct any corpus-based analyses for Japanese documents, the performance of the proposed method will be improved.

References:

- [1] Cisco Visual Networking Index: Global Mobile Data Traffic Forecast Update, 2017–2022, Feb. 2019.
- [2] J. Hirschberg and C. D. Manning, “Advances in natural language processing,” vol. 349, issue 6245, pp.261-266, July 2015.
- [3] M. Murata, T. Ohno and S. Matsubara, “Automatic comma insertion based on usage classification on commas,” vol. 2010-NL-196, no. 8, pp. 1-8, May 2010 (*in Japanese*).
- [4] M. Murata, T. Ohno, and S. Matsubara, “Automatic comma insertion into Japanese texts based on usage classification of commas,” IEICE Trans. Inf.& Syst. (*Japanese Edition*), vol. J95-D, no. 9, pp. 1783-1793, Sept. 2012.

Table 3. Compression results of newspaper articles. Compression ratio: [%]

scheme	Entertainment	Economy	Science
ZIP	71.99	60.69	48.82
BZIP2	75.48	63.47	44.48
LZMA	74.46	63.20	47.99
LZW	88.83	85.79	68.20
LZT	88.83	85.79	68.20

Root shape prediction from crown shape using machine learning

Yutaro ISO¹⁾, Kazuhiro SUGA²⁾

¹⁾ Department of Mechanical Engineering, Faculty of Engineering, Kogakuin University, JAPAN
E-mail: a116007@ns.kogakuin.ac.jp

²⁾ Department of Mechanical Engineering, Faculty of Engineering, Kogakuin University, JAPAN
E-mail: ksuga@cc.kogakuin.ac.jp

Abstract

In order to realize safe and effective orthodontic treatment, it is important to grasp the root shape. Because the method using X-ray CT may be exposed to X-rays, the development of a less invasive grasp method In this study, we propose a method for predicting root shapes from crown shapes that can be photographed with visible light using machine learning. In this report, we investigated the feasibility of the proposed method by predicting the root shape from the crown shape of panoramic X-rays.

1. Introduction

The purpose of this study is to propose a method of predicting the root shape from the crown shape using machine learning. In this report, the problem of predicting the root shape from the crown shape of panoramic X-rays is studied. We examine the feasibility of the proposed method.

2. Root shape prediction from crown shape

2-1. Learning data

As shown in Fig. 1, learning images are learned only for the crown and those that can see both the crown and root. The training data was saved in PNG format. The data size was set to 256 x 256 resolution.

2-2. Learning network

In this study, machine learning is performed using a learning model called Pix2Pix^[1], which is a type of convolutional neural network. Pix2Pix is an algorithm that uses GAN and functions by combining a network called U-Net^[2]. It is improving.

The learning data used at this time is a combination of Fig. 1.

2-3. Forecast results

Figure 2 shows the results of prediction using panoramic X-ray images. In Fig. 2, A shows the predicted results and correct answers for molars and B for premolars. It can be seen that the root shape of the premolars can be accurately predicted. On the other hand, bifurcated molars tended to have a lower prediction accuracy than premolars, probably due to the fact that the number of learning teeth with bifurcated roots was smaller than that of a single tooth.

3. Conclusion

In order to propose a method to predict the root shape from the crown shape using machine learning, we examined the feasibility of the proposed method using panoramic X-rays. Future research goals include improving the

accuracy of predicting teeth that have a bifurcated root, and predicting accuracy.

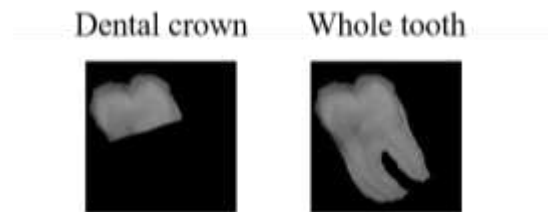


Fig. 1. Learning data

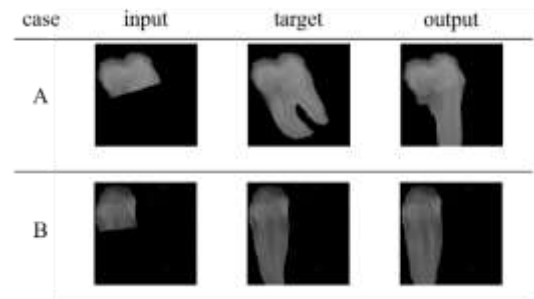


Fig. 2. Forecast results

References:

- [1] Phillip Isola, Jun-Yan Zhu, Tinghui Zhou, Alexei A. Efros; The IEEE Conference on Computer Vision and Pattern Recognition (CVPR), 1125-1134,(2017)
- [2] Olaf Ronneberger, Philipp Fischer, Thomas Brox Medical Image Computing and Computer-Assisted Intervention – MICCAI , 234-241(2015)

A Study of Modified Belief Propagation Decoding for Polar Codes

Naoya Takahashi¹⁾, and Hideoshi Saito²⁾

¹⁾Graduate School of Engineering, Kogakuin University, Tokyo, Japan
E-mail: cm19029@ns.kogakuin.ac.jp

²⁾Department of Electrical and Electronic Engineering, Faculty of Engineering, Tokyo, Japan
E-mail: h-saito@cc.kogakuin.ac.jp

Abstract

Recently, polar codes have attracted much attention as a candidate of the high performance error correction codes because the fifth generation wireless systems standardization process of the third generation partnership project chose polar codes as a channel coding scheme. This report shows a modified decoding method for polar codes based on belief propagation and the evaluated error rate performances of the proposed decoding method .

1. Introduction

Polar codes introduced by Arikan are designed by the theory of *channel polarization* [1]. It is well known that polar codes can be strictly proven to achieve the theoretical limit for the capacity of symmetric binary-input memoryless channels. In both of polar encoding and decoding, computational complexity for a given polar code with codeword length N is $\mathcal{O}(N \log N)$. Especially, it is known that successive cancellation (SC) decoding, originally proposed in [1], is sub-optimal for finite length polar codes. When we use a short-length polar code, the SC decoding performance is significantly degraded and inferior to the other decoding performance [2]. Then, in order to improve polar code decoding performance, we propose a new modified or effective belief propagation (BP) decoding scheme because BP decoding is a promising candidate for both of high data rate and low latency demanding applications [3].

2. Polar Coding

The concept of channel polarization transforms $N = 2^m$ independent channels into polarized channels by *channel combining and splitting* [1]. As a result, we can observe a set of more reliable and a set of less reliable channels. Then, the K most reliable channels are now used to transmit information bits, while the other $N - K$ channels are frozen and set to zero. For a given code rate $R = K/N$, the K information bits are mapped into the decided K non-frozen bit positions of information bits and all other positions are *frozen bits*. In generating a polar codeword \mathbf{x} with length $N = 2^m$, the encoding process is described by a generator matrix \mathbf{G}_N which can be recursively defined as

$$\mathbf{G}_N = \mathbf{F}^{\otimes m}, \mathbf{F} = \begin{bmatrix} 1 & 0 \\ 1 & 1 \end{bmatrix}$$

where $\mathbf{F}^{\otimes m}$ denotes the m^{th} Kronecker power of \mathbf{F} .

A polar code is specified by $(N, K, \mathcal{A}, \mathbf{u}_{\mathcal{A}})$, where the notation \mathcal{A} describes a set of K indices called information bit (*user data* or *message*) locations from $\{1, 2, \dots, N\}$ and the notation $\mathbf{u}_{\mathcal{A}}$ describes the set of K information bits, respectively. On the other hand, we

define that the notations \mathcal{A}^c and $\mathbf{u}_{\mathcal{A}^c}$ represent a set of $N - K$ indices called parity bit (frozen bit) locations from $\{1, 2, \dots, N\}$, and the set of $N - K$ parity bits which are frozen at the beginning of the session and made known to the decoder. For an $(N, K, \mathcal{A}, \mathbf{u}_{\mathcal{A}})$ polar code, a codeword is expressed as

$$\mathbf{x} = \mathbf{u}_{\mathcal{A}} \mathbf{G}_{\mathcal{A}} + \mathbf{u}_{\mathcal{A}^c} \mathbf{G}_{\mathcal{A}^c}$$

where the notations $\mathbf{G}_{\mathcal{A}}$ and $\mathbf{G}_{\mathcal{A}^c}$ are the submatrices of \mathbf{G}_N consisting of rows with indices in \mathcal{A} and \mathcal{A}^c , respectively. This mapping defines a non-systematic encoder which satisfies $\mathbf{u}_{\mathcal{A}} \mapsto \mathbf{u}_{\mathcal{A}} \mathbf{G}_{\mathcal{A}} + \mathbf{c}$ where $\mathbf{c} \triangleq \mathbf{u}_{\mathcal{A}^c} \mathbf{G}_{\mathcal{A}^c}$ is a fixed vector. The code rate can be adjusted by choosing the size of the set \mathcal{A}^c .

3. Belief Propagation Decoding

The BP decoding algorithm is well known as the message passing algorithm and usually described in terms of operations on factor graphs. BP decoding of a polar code is based on the factor graph representation of the given polar code's generator matrix \mathbf{G}_N , where subsequent iterations are conducted on the polar code encoding factor graph [3]. BP decoding using the factor graph can be estimate the polar codeword $\hat{\mathbf{x}}$ and the message $\hat{\mathbf{u}}_{\mathcal{A}}$. In [3], the factor graph of polar codes can be obtained by adding N check nodes to each column of the first $m = \log_2 N$ columns from left to right in the encoding factor graph. Thus, this factor graph consists of an $m + 1$ stages containing N node per stage. Fig.1 shows an example of the factor graph representation for the polar code with $N = 4$.

In Fig.1, the nodes of the factor graph are labeled with pairs of integers (i, j) , $1 \leq i \leq N$, $1 \leq j \leq m + 1$. Soft messages (LLRs: log-likelihood ratios) $\hat{\mathbf{x}}_{LLR}$ and $\hat{\mathbf{u}}_{LLR}$ are updated and propagated among adjacent nodes from the rightmost column to the leftmost column during the whole BP iteration process. Then, the decoder reverses the course and updates schedule toward the rightmost column. This procedure makes one round of *BP iteration*. In the concrete, the BP decoding treats associating two messages with each node (i, j) for every round of BP iteration: a right-propagating message $R_{i,j}^t$ and a left-propagating

message $L_{i,j}^t$, where $t = 0, 1, \dots$ is a round of BP iteration index. These two messages correspond to LLRs at round t and are initialized as follows:

$$L_{i,m+1}^0 = \ln \frac{P(y_i | x_i = 0)}{P(y_i | x_i = 1)}$$

$$R_{i,m+1}^0 = \begin{cases} 0 & \text{if } i \text{ is an information bit} \\ \infty & \text{if } i \text{ is a frozen bit} \end{cases}$$

All other $R_{i,j}^0$ and $L_{i,j}^0$ are set to equal 0. During BP decoding, these messages are propagated and updated among adjacent nodes using min-sum algorithm as follows:

$$L_{i,j}^t = \alpha \cdot f \left(L_{i,j+1}^{t-1}, L_{i+2^{m-j},j+1}^{t-1} + R_{i+2^{m-j},j}^{t-1} \right)$$

$$L_{i+2^{m-j},j}^t = L_{i+2^{m-j},j+1}^{t-1} + \alpha \cdot f \left(L_{i,j+1}^{t-1}, R_{i,j}^{t-1} \right)$$

$$R_{i,j+1}^t = \alpha \cdot f \left(R_{i,j}^{t-1}, L_{i+2^{m-j},j+1}^{t-1} + R_{i+2^{m-j},j+1}^{t-1} \right)$$

$$R_{i+2^{m-j},j+1}^t = R_{i+2^{m-j},j}^{t-1} + \alpha \cdot f \left(L_{i,j+1}^{t-1}, R_{i,j}^{t-1} \right)$$

where $\alpha = 0.9375$ and $f(a, b) \triangleq \text{sign}(a) \cdot \text{sign}(b) \cdot \min(|a|, |b|)$ for any reals a, b .

After reaching the predefined number of BP iteration itr_{max} , the decision sequence $\hat{\mathbf{x}}$ is determined based on the hard decision of messages from the nodes in the leftmost column. Alternatively, we terminate BP iteration if the condition that $\hat{\mathbf{x}} = \hat{\mathbf{u}}\mathbf{G}_N$ is satisfied by checking out hard decision results of $\hat{\mathbf{x}}$ and $\hat{\mathbf{u}}$ before reaching itr_{max} .

4. Proposed Belief Propagation Decoding

In order to improve both of the bit error rate (BER) and frame error rate (FER) performances of polar codes using BP decoding, we propose a following modified method. If BP decoding reaches a multiple of the specified number of BP iteration itr_{sp} ($t_0 = n \times itr_{sp}$), the BP decoder performs repeating another LLR updates continuously between each stages with the predetermined number of setting iterations itr_{in} ($n = 1, 2, \dots, \lfloor itr_{max}/itr_{sp} \rfloor$). Then, we check the sum values of LLRs for each node. If the total sum of absolute values of LLRs for the target node is lower than δ , local updating LLRs is executed using a local right-propagating message $R_{i,j}^{t_0,t'}$ and a local left-propagating message $L_{i,j}^{t_0,t'}$. If $|R_{i,j}^{t_0,t'} + L_{i,j}^{t_0,t'}| < \delta$ in the node (i, j) , we can update LLRs as follows:

$$L_{i,j-1}^{t_0,t'+1} = f \left(R_{i,j}^{t_0,t'} + L_{i,j}^{t_0,t'}, R_{i+2^{m-j},j}^{t_0,t'} + L_{i+2^{m-j},j}^{t_0,t'} \right)$$

$$L_{i+2^{m-j},j-1}^{t_0,t'+1} = (-1)^{R_{i,j-1}^{t_0,t'} + L_{i,j-1}^{t_0,t'}} \left(R_{i+2^{m-j},j}^{t_0,t'} + L_{i+2^{m-j},j}^{t_0,t'} \right) + R_{i,j}^{t_0,t'} + L_{i,j}^{t_0,t'}$$

$$R_{i,j}^{t_0,t'+1} = f \left(R_{i,j-1}^{t_0,t'} + L_{i,j-1}^{t_0,t'}, R_{i+2^{m-j},j-1}^{t_0,t'} + L_{i+2^{m-j},j-1}^{t_0,t'} \right)$$

$$R_{i+2^{m-j},j}^{t_0,t'+1} = (-1)^{R_{i,j}^{t_0,t'} + L_{i,j}^{t_0,t'}} \left(R_{i+2^{m-j},j-1}^{t_0,t'} + L_{i+2^{m-j},j-1}^{t_0,t'} \right) + R_{i,j-1}^{t_0,t'} + L_{i,j-1}^{t_0,t'}$$

where $L_{i,j}^{t_0,0} = L_{i,j}^{t_0}$, $R_{i,j}^{t_0,0} = R_{i,j}^{t_0}$ and $t' = 0, 1, \dots, itr_{in}$.

4. Simulation Result

Fig.2 shows the BER and FER performances of (1024,512) polar codes using proposed decoding method with $itr_{sp} = 200$, $itr_{in} = 10$, $itr_{max} = 6,000$ and conventional method. In this simulation, we assume the additive white Gaussian noise channel model and binary phase shift keying modulation. The BER and FER performance of the proposed method is superior to that of conventional method at a high signal-to-noise ratio (SNR). If $\delta = 0.1$, the proposed decoding method is able to improve the BER and FER performances compared with the conventional method. However, the results with the other δ values are close to the performance of conventional decoding method.

5. Conclusion

In this research, we propose the effective modified BP decoding method. As a result, proposed decoding method is able to improve the SNRs in both of the BER and FER performances by computer simulation.

References:

- [1] E. Arıkan, *IEEE Trans. Inf. Theory*, **55**, 7, pp. 3051-3073, July 2009.
- [2] A. Ekelesh *et al.*, *IEEE Commun. Lett.*, **22**, 8, pp.1536-1539, Aug. 2018.
- [3] E. Arıkan, in *Proc. 4th Int. Symp. on Broad. Commun.*, pp.11-14, July 2010.

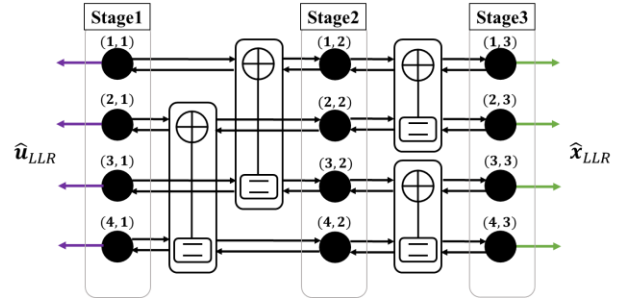


Fig.1 The factor graph representation for \mathbf{G}_4 .

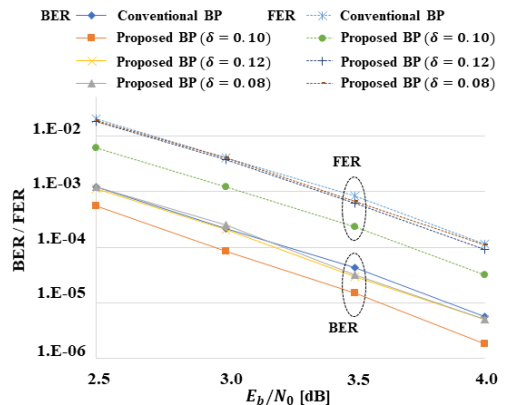


Fig.2 BER and FER performances.

Development of a Smart Device for V2X Driving Assistance

Zhao Li¹⁾ and Koyo Katsura, Ph.D.²⁾

1) Department of System Design Program, Kogakuin University, Japan
E-mail: gm18005@ns.kogakuin.ac.jp

2) Department of System Design Program, Kogakuin University, Japan
E-mail: koyokatsura@cc.kogakuin.ac.jp

Abstract

Some countries, such as Japan, America, and Germany are planning to build a V2X society around 2020. V2X, vehicle-to-everything, system is a communication system that enables a vehicle to connect with other vehicles, road infrastructure, network, and people [1]. By using this system, the obstacles can be detected faster than conventional sensors, reducing traffic accidents. Without a doubt, newly produced cars can be equipped with the V2X system. However, most of the 1.3 billion vehicles running around the world [2] are non-equipped with V2X systems. To solve the issue of the vehicles without V2X system, the research aims to develop a smart device that will enable the vehicles without a V2X system to be incorporated into the V2X system. This paper focuses on how to use ESP8266 for V2X simulation experiment.

1. Materials and Method

To develop the V2X device, an intersection simulation experiment plan as Fig. 1 is designed. In this experiment, we will make four identical devices to be mounted on remote control cars. The remote control cars will pass through the intersection at different speeds and in different directions. They share data, and when they approach each other at a certain distance, a warning message will appear on display.

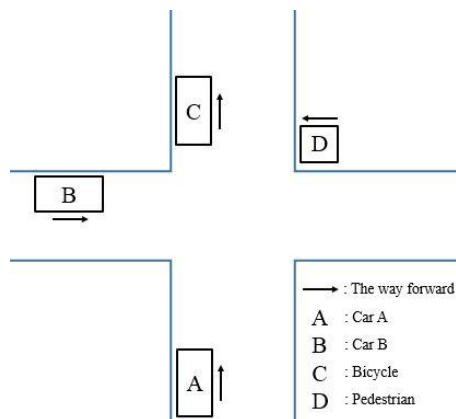


Fig. 1. Intersection simulation experiment plan.

At the beginning, the V2X module (made by U-Blox) was considered to develop the V2X device. Unfortunately, that module was not sold to individuals. Thus, we used an ESP8266 (AE-ESP-WROOM02-DEV) Wi-Fi module instead of the V2X module for transmitting data to each other. A GPS module (AE-GYSFDMAXB) was used for collecting location information. A 1.5-inch OLED module (made by XinTaiWei Electronic) was used to display a warning message. The experimental device was redesigned as a result of the replacement of the

communication module, as shown in Fig. 2.

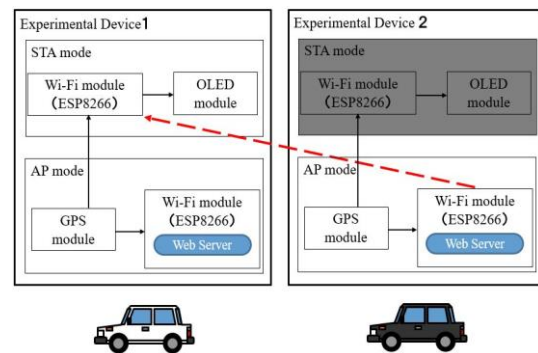


Fig. 2. Experimental device design.

The ESP8266 Wi-Fi module has three modes of operation, namely access point (AP) mode, station () mode, and AP+STA mode. AP is “a device that provides access to a Wi-Fi network to other devices (stations) and connects them to connect a wired network” and STA mode is used “to get the ESP module connected to a Wi-Fi network established by an access point” [3].

Therefore, to simulate the working slot of the V2X system, we carried two ESP8266s in an experimental device. One is working in AP mode; another is working in STA mode. The GPS module provides location data for both ESP8266s at the same time. In the AP mode ESP8266, a web server is set up where data from the GPS module is stored, and the location data is sent to other experimental devices. ESP8266, which is in STA mode, is responsible for receiving location data sent from other experimental devices, and then these location data of their position are compared with the data sent to calculate the distance between the two cars.

2. Experiment

At this stage, a communication experiment between multiple experimental devices cannot be started because the program is under development. However, to proceed with future experiments smoothly, we have conducted some basic experiments as follows:

- Test of the accuracy of the GPS modules (AE-GYSFDMAXB) and confirmation of a level of 1m accuracy on the road in an urban area.
- Communication speed experiment of the Wi-Fi module (AE-ESP-WROOM02-DEV) and confirmation of data update time.
- Test of the program to calculate the distance with 10 meters of accuracy.

To ensure normal communication between the experimental equipment, the experiment will be carried out in an open space. According to the Wi-Fi module (AE-ESP-WROOM02-DEV) communication distance test conducted by Andy Reischle, in an open space, the communication distance of it can reach more than 300 meters^[4]. Two remote control cars to carry the two devices. The initial link distance of the two experimental devices was set within 100 meters because the remote control cars will move at slow speed (under 10km/h) in this simulation experiment. When the experimental devices are set up, two remote control cars keep approaching each other. If the straight-line distance between the two devices is less than 30 meters, a message will appear on their respective displays, indicating that a vehicle is approaching.

3. Discussion

Because the communication module used by the experimental device is not the V2X module, the communication ability and data processing ability are weaker than the V2X module, the function is single, and the Data Encryption is poor. It is hoped that the V2X module will be equipped with more features in the future, such as the priority control to display approaching objects at intersections to avoid disturbing the driver, an alarm for approaching vehicles from the side lane at the ramp of the highway, and improvement of data encryption to increase the practicality of the device.

In addition, when developing the V2X driving assistance smart device, the privacy of users should be considered. The data collected by the devices should only be used in a driving assistance system, not for other purposes, and burned in a short period of time.

References:

- [1] STMicroelectronics. (n.d.). Vehicle-to-Everything (V2X). Retrieved October 31, 2019 from

<https://www.st.com/en/applications/telematics-and-networking/vehicle-to-everything-v2x.html>.

- [2] Japan Automobile Manufacturers Association. (n.d.). Number of four-wheeled vehicles in the world. Retrieved October 31, 2019 from <http://www.jama.or.jp/world/world/index.html>.
- [3] Ivan Grokhotkov Revision b4c28e74. ESP8266WiFi library. Retrieved October 31, 2019 from <https://arduino-esp8266.readthedocs.io/en/latest/esp8266wifi/readme.html>.
- [4] Andy Reischle. UDP-Ranger - a simple ESP8266 range tester. (2016, 26 March). Retrieved October 31, 2019 from <https://www.areresearch.net/2016/03/udp-ranger-simple-esp8266-range-tester.html>.

Control of Multiple, Linked Air Conditioning Devices Using Deep Reinforcement Learning that Considers Both Power Saving and Comfort

Naotoshi OKUYAMA ¹⁾ and Koyo KATSURA, Ph.D. ²⁾

1) Department of System Design, Graduate School of Engineering, Kogakuin University, Japan
E-mail: gm18002@ns.kogakuin.ac.jp

2) Department of System Design, Graduate School of Engineering, Kogakuin University, Japan
E-mail: koyokatsura@cc.kogakuin.ac.jp

Abstract

In recent years in Japan, there is a shift from air conditioning control that pursues only power saving to control that saves electricity while maintaining in-room comfort. In some office buildings, this control linking a plurality of devices is introduced. However, in homes, it is limited to control of single air conditioners only. A control that considers both power saving and comfort by linking by multiple devices is not performed. Therefore, we are aiming to develop a control system that links multiple home appliances to solve problems that prevent such a system's introduction to homes. This paper reports the interim results of this development.

1. Introduction

We are developing a smart controller to optimize power saving and comfort by linking air conditioning devices. There are numerous reasons for utilizing a smart controller. If you did not need to save electricity, you could improve comfort in a house by operating individual home appliances with individual settings. However, there are many inefficient operations that result in wasted power. For example, in the case of two air conditioning devices operating separately, they will operate excessively.

In order to balance power saving and comfort, it is necessary to have a controller that manages all related devices together and optimizes them as a whole. Currently, such controllers are sold as smart thermostats like Nest Learning Thermostat [1]. These can also be seen in office buildings in Japan. In contrast, their introduction to homes is only seen in some luxury homes. This is due to the fact that central air conditioning is not popular in Japan and because of a number of factors affecting optimization. For example, environmental factors, which include temperature, humidity, brightness, concentration of oxygen, and concentration of carbon dioxide, etc. The degree of influence of these factors varies among people, and varies with clothes, activities, age, and culture. This makes it difficult to optimize both comfort maintenance and power savings. The current devices are observing these factors, and based on this, control is performed to balance power saving and comfort. However, it is not efficient because each device is controlled separately.

The aim of this research is to achieve both power saving and comfort by managing and optimizing the factors that are not considered in individual devices as a whole, using a smart controller. As optimization changes depending on the use situation, we aim for a solution by using deep reinforcement learning for optimization that requires calculation in each home.

2. Methods

An outline of the control system to be developed is shown in Fig. 1. Multiple sensors are installed in the home. The room equipment is prepared so that the controller can operate multiple devices remotely. Necessary data for deep reinforcement learning is collected. Finally, the controller is automatically controlled by deep reinforcement learning. The sensors to be installed are temperature, humidity, air pressure, carbon dioxide concentration, air quality, illuminance, and power consumption.

The controller is made using the ESP-32 (Microcontroller made by Espressif Systems, China) Development Board to read the sensors and send the data to the server via Wi-Fi or Bluetooth. It is possible to calculate environmental sensing and control based on the existing home devices. However, it is not possible to control the home appliances automatically from the calculation results because the existing devices hardly support external operations. Therefore, we developed a controller that enables automatic operation of home devices while utilizing existing products. Existing product systems are closed to other systems. We selected an existing product that supports IFTTT that is a service that connects the product system via the Internet. The controller enables operation via IFTTT. Some device

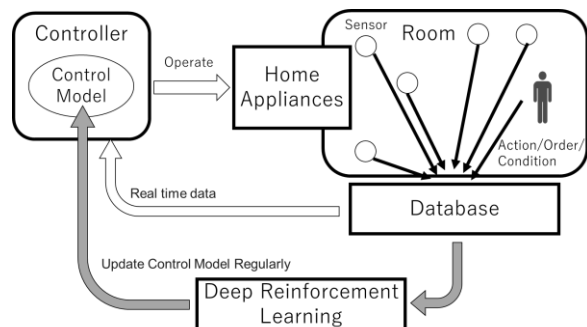


Fig. 1. System diagram of the smart controller

functions are omitted because not all functions of the devices support IFTTT. In addition, deep reinforcement learning is performed to update the control model of a controller using the accumulated data.

3. Results

A range of smart controllers was compared with similar products and services. The IR Learning Remote is a product that operates home appliances by simulating the operation of an infrared remote control. Although it is simple, it can be set to operate automatically from its own temperature sensor. There is also a product that can save up to 30% while maintaining comfort based on the research [2]. A Smart House uses a product such as CASPER.AI. This makes it possible to automate the operation of home appliances by installing a camera and sensor group in the room and detecting human behavior. HEMS (Home Energy Management System) allows remote operation of home appliances using dedicated wireless communication. However, HEMS does not support automatic control at present. Fig. 2 is a graph that shows the results of comparing these three and the smart controller from 16 points and summarizes them into 6 items.

The progress of system development is as follows. The sensors used in the sensor system are

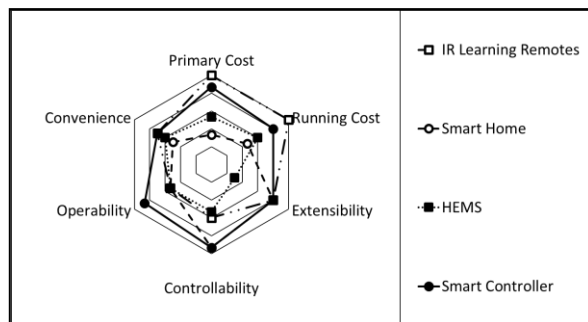


Fig. 2. Radar chart comparing smart controllers

Table 1. List of sensors in the room

Model Number	BME280	DS18B20	CCS811	BH1750
Measuring Range	Temp. -40~85[degC] Humid. 0~100[%] Air Pressure 300~1100[hPa]	Temp. -55~125 [degC]	eCO2*1 400~8192[ppm] TVOC*2 0~1187[ppb]	0~65535[lux]
Measurement Accuracy	± 1[degC] ± 3[%] ± 1[hPa]	± 0.5[degC]	No guarantee	Automatic noise elimination
Optical Resolution	0.01[degC] 0.008[%] 0.18[hPa]	0.0625~0.25 [degC]	No guarantee	0.5~4[lux]
Output Interface	Digital I ² C/SPI	Digital 1-Wire	Digital I ² C	Digital I ² C

*1 equivalent CO₂

*2 Total Volatile Organic Compound

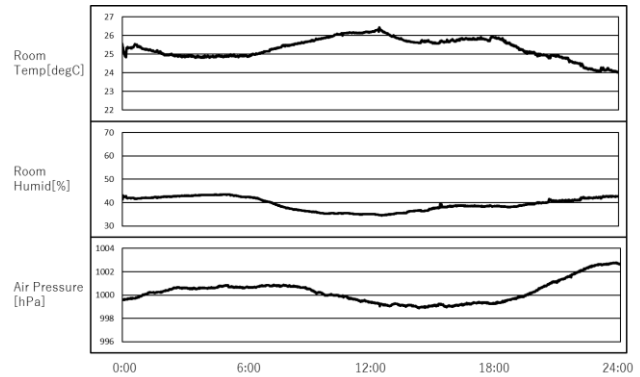


Fig. 3. Changes in temperature, humidity, and pressure in a room for a day

summarized in Table 1. The sensor information is sent to the data server in real time using Wi-Fi. Fig. 3 is a graph of the results, which can be checked in real time on the web. Devices can be operated through IR for infrared remote control, from Smart Plug for outlet ON / OFF, and from a circuit using a self-made solid-state relay for outlet output control. Human actions are collected from physical buttons, smartphones, and smart speakers. The control model by deep reinforcement learning currently under development is composed of ChainerRL [3], and uses a room environment simulator under development to learn basic operations. After that, we move on to learning about the room environment where it is actually installed, and optimize it for each individual environment.

4. Conclusion

It has been demonstrated that even air conditioning devices that do not accept external operations can be operated by simulating a remote control, or via a linked service, or controlling the power at the outlet. In the future, we will verify the effects of control by deep reinforcement learning and basic learning by simulation.

References:

- [1] A thermostat that can be linked with wearable devices provided by Google Nest in only U.S.A. and Europe.
- [2] Tomoya Imanishi, Mio Fukuta, and Hiroaki Nishi, Information Processing Society of Japan, 1, 7-8 (2016).
- [3] Chainer is an open source deep learning framework written by Python. ChainerRL adds state of art deep reinforcement learning algorithms.

Applying IoT Technology in An Intelligent Guiding System for Blind People

Jiun-Yu Tu¹⁾, Chia-Nian Shyi²⁾,

¹⁾Department of Computer Science and Information Engineering, Southern Taiwan University of Science and Technology, Taiwan

¹⁾E-mail: duketu@stust.edu.tw

²⁾E-mail: shyi@stust.edu.tw

Abstract

Walking on streets is not an easy task for blind people. Nowadays, the main guiding system designed for blind people is setting up tactile floor tiles on pavements along streets. Then while blind people walk along streets, they tap pavements with their cane. The main advantage of canes is that blind people can use their cane to probe unknown obstructs toward their walking directions. However, traditional guiding canes for blind people cannot interact with surrounding environments to provide more safety to blind people. For example, when blind people arrive intersection of roads, they cannot know the status of traffic lights. Thus, they cannot determine whether they should stop to wait for red lights or go strictly across because of green lights if they want to go across the intersection. To increase safety to blind people when they use guiding canes to assist their movement, this work proposes an intelligent guiding system for blind people. The proposed intelligent guiding system invokes technology of internet of things (IoT). It is composed of intelligent traffic lights and intelligent guiding canes to interact with each other. The proposed intelligent guiding system can significantly increase safety when blind people want to go across intersection of roads.

Walking on streets is not an easy task for blind people. Nowadays, the main guiding system designed for blind people is setting up tactile floor tiles on pavements along streets. Then while blind people walk along streets, they tap pavements with their cane. The main advantage of canes is that blind people can use their cane to probe unknown obstructs toward their walking directions. However, traditional guiding canes for blind people cannot interact with surrounding environments to provide more safety to blind people.

For example, when blind people arrive intersection of roads, they cannot know the status of traffic lights. They cannot determine whether they should stop to wait for red lights or go strictly across because of green lights if they want to go across the intersection. Otherwise, while blind people are walking across intersections of roads and suddenly hearing sounds of sirens from emergent rescue vehicles, such as coming ambulances, coming fire trucks, and etc., at the same time, they would be at their wits end.

To increase safety to blind people when they use guiding canes to assist their movement, this work proposes an intelligent guiding system for blind people. The proposed intelligent guiding system invokes technology of internet of things (IoT). It is composed of intelligent traffic lights and intelligent guiding canes to interact with each other. The proposed intelligent guiding system can significantly increase safety when blind people want to go across intersections of roads.

In the first part of the proposed intelligent guiding

system, an intelligent guiding cane sticks a Bluetooth beacon ^{[1][2]} broadcaster. The stuck beacon broadcaster broadcasts approaching information about a blind person. The approaching information would include an identifier that can be used to recognize a blind person, the blind person's average moving speed, the variation of the speed, and positioning information of the global positioning system (GPS).

On the other hand, in the second part, each intelligent traffic lights would equip Bluetooth beacon receivers to retrieve broadcasting beacon messages which are sent by intelligent guiding canes. While a traffic light receives a broadcasting message from an intelligent guiding cane, it knows that a blind person is approaching by parsing the identifier packaged in the retrieved beacon message. Once the traffic light parses the values of the blind person's moving speed, variation of the speed, and GPS position information from the retrieved message, it would estimate how much time should the blind person spend to across a specific intersection. The traffic light would adjust the period of green light in the coming turn dynamically to guarantee that the green light period would persist until the blind person going across the intersection of the roads safely.

In the case of encountering rapidly coming emergent rescue vehicles while a blind person wants to go across an intersection of roads, a traffic light can deliver a waiting message to the blind person's guiding cane to stop the blind person's movement once he/she arrives at the intersection of the roads.

By the proposed intelligent guiding system, blind

people could go across intersections of roads more safely. The proposed intelligent guiding system invokes the IoT technology to make intelligent traffic lights and intelligent guiding canes communicate mutually.

References:

- [1] <https://www.beaconstac.com/what-is-a-bluetooth-beacon>
- [2] Texas Instruments, “Bluetooth low energy beacons”, SWRA475A-January 2015-Revised, October 2016.

Development of an Agricultural Automatic Spraying IoT System with Utilizing the Bluetooth Mesh Networking

Jeng-Han Li¹, Wei-Che Ho, Wei-Ting Wu, Ming-Jie Cheng, Yin-Fong Wang

¹)Department of Electrical Engineering, Southern Taiwan University of Science and Technology, Taiwan
E-mail: jenghanli@stust.edu.tw

Abstract

The paper mainly addresses a development of an agricultural automatic spraying IoT system with utilizing the Bluetooth mesh networking. The control board we select is the product, nRF52DK, of Nordic Semiconductor. The nRF52 series SoC products have a 64Mhz Cortex-M4 CPU as their computation core and can support the protocol of Bluetooth 5 with Bluetooth mesh networking. The reasons for adopting the mesh networking are mainly its high scalability and flexibility of network topologies. The control boards of nRF52DK have rich peripheral supports, such as A/D converters, GPIOs, SPI, QDEC and etc., which can give good help for the integration design of agricultural automatic spraying systems. The designed spraying nodes have functions of soil moisture sensing, soil PH-value sensing, sunshine sensing, water flow sensing, solar power storage, and electromagnetic valve control. With the distribution of these spraying nodes, we can collect the relevant sensing information and control the watering conditions. Further, we can apply statistic processes to count the associated information to understand the impacts of various state changes on crop growth.

Fig. 1 Shows the scenario of agricultural automatic spraying IoT control system. The field electrical and mechanical room has pressurized motor and associated control system that can pump irrigation water to each spraying node, and the node controllers can control the volume of irrigation water within the control scopes. And Fig. 2. shows the 3D shape design of spraying node, the base part has irrigation water lines and the top has a shower mechanism. The node controller can control whether the valves are switched ON or not, and according to the information of flow meter, can determine the amount of water to be poured in the charging areas. Fig. 3. shows the hardware architecture of spraying node, that applying the Nordic nRF52DK control board as the computation core to collect the sensing information, such as soil moisture, soil PH-value, sunshine, water flow, and etc., control the electromagnetic valves, and utilizing Bluetooth mesh networking to communicate with each node.

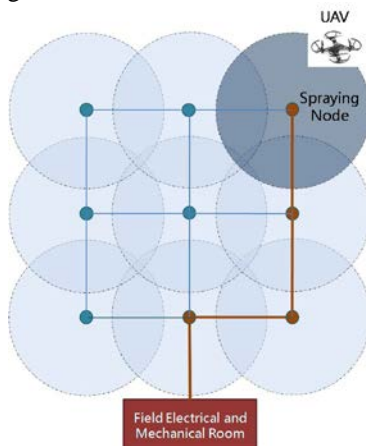


Fig. 1. The scenario of agricultural automatic spraying IoT control system



Fig. 2. The shape design of spraying node of IoT control system

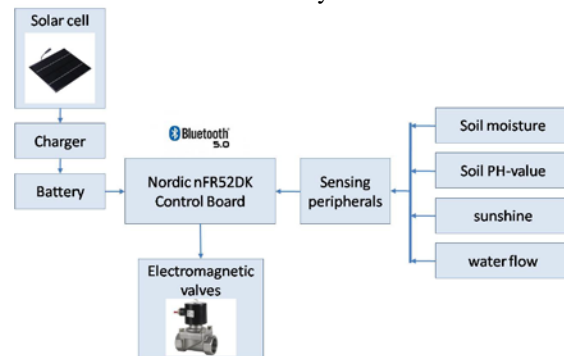


Fig. 3. The hardware architecture of spraying node of IoT control system

References:

- [1] Mathias Baert, Jen Rossey, Adnan Shahid, and Jeroen Hoebeke, The Bluetooth mesh standard: an overview and experimental evaluation, *sensors*, 18, 2409, 2018.
- [2] Hsin-Ru Tsai, *Development of Intelligent Agriculture Monitoring and Automation Control System Based on LPWAN*, Master thesis of National Tsing Hua University, 2018.
- [3] Nordic website: nRF5 DSK for mesh, <https://www.nordicsemi.com/Software-and-Tools/Software/nRF5-SDK-for-Mesh>

Activation of chitinolytic activity of mouse acidic chitinase by sodium chloride

Shiori Takebe^{1,*}, Eri Tabata^{1,2}, Fumitaka Oyama¹

¹Department of Chemistry and Life Science, Kogakuin University, Hachioji, Tokyo, Japan.

²Research Fellow of Japan Society for the Promotion of Science (DC1), Koujimachi, Chiyoda-ku, Tokyo, 102-0083 Japan

*Corresponding author E-mail : bm19029@ns.kogakuin.ac.jp

Abstract

Chitin, a linear polymer of β -1, 4-linked *N*-acetyl-D-glucosamine (GlcNAc), is the second most abundant polysaccharide in nature and functions as a major structural component in crustaceans, insects, nematodes and fungi. Chitinases hydrolyze the β -1, 4 glycoside bonds of chitin. Although mammals do not produce chitin, humans and mice express two active chitinases. Chitotriosidase was the first identified and purified mammalian chitinase. Acidic chitinase (Chia) was the second discovered mammalian chitinase. Chia has attracted substantial attention due to its expression fluctuations under certain pathological conditions such as asthma, allergic inflammation, ocular allergy, dry eye syndrome and gastric cancer. Chia is highly expressed in mouse stomach tissues. Chia has the highest activity at pH 2.0 and lower activities at more neutral pH (pH 3.0~7.0). Recently we showed that Chia can function as a protease-resistant major glycosidase under the gastrointestinal conditions in mouse. Here, we tested the effect of sodium chloride on the chitinolytic activity of mouse Chia. The chitinolytic activity of mouse Chia increased considerably under higher salt concentrations at pH 2.0. This activation was not observed at pH 7.0. These results suggest that mouse Chia has pH dependence of sodium chloride activation mechanism *in vivo*.

The Strategy of Exopolysaccharide Production by Lactic Acid Bacteria

Yu-Xuan Zheng, Tux-Han Lin, Wei-Cheng Wang, Chia-Yu Lin, Po-Ting Chen*

Department of Biotechnology and Food Technology, Southern Taiwan University of Science and Technology,
Taiwan

E-mail: ptchen@stust.edu.tw

Abstract

Polysaccharides are polymers which are polymerized from monosaccharides and their molecular weight distribution. Since the 1950s, scientists began to study the structure, physicochemical properties, and functions of polysaccharides and found the polysaccharides have many benefits for human health. Exopolysaccharide (EPS) from lactic acid bacteria (LAB) is a carbohydrate compound, which synthesized and secreted to extracellular during the cell growth process. Due to its anti-oxidation, antibacterial and other characteristics, EPS can be used as health care products, water retaining agent, stabilizer, thickener, gel, and medical plasma alternatives. The response of surface methodology (RSM) was used to optimize the fermentation condition of EPS. The main component of EPS secreted from *Weissella cibaria* 27 is dextran, it has a high degree of commercial application value in the fields of food, cosmetics and medicine industries. In this study, the production of EPS from *W. cibaria* 27 was successfully improved by fermentation strategy, and the production could reach over 65 g/L. The production of EPS by *W. cibaria* 27 would have potential in the commercial field.

References:

- [1] Das Deeplina, Goyal Arun. Characterization and biocompatibility of glucan: a safe food additive from probiotic *Lactobacillus plantarum* DM5. *Journal of the Science of Food and Agriculture*, 94: 683-690 (2014).
- [2] Ahmed Rifat Z, Siddiqui Khaizran, Arman Muhammad, Ahmed Nuzhat. Characterization of high molecular weight dextran produced by *Weissella cibaria* CMGDEX3. *Carbohydrate polymers*, 90: 441-446 (2012).
- [3] Kim Min Ju, Seo Ha Na, Hwang Tae Sik, Lee Sung Hun, Park Doo Hyun. Characterization of exopolysaccharide (EPS) produced by *Weissella hellenica* SKkimchi3 isolated from kimchi. *The Journal of Microbiology*, 46: 535-541 (2008).

Examination of Cupulolithiasis Treatment Method by Using Vibration Response of Cupula to Detach Otoconial Mass

Kiyomasa Miura¹⁾, Hirotooshi Hishida²⁾, and Koji Otsuka³⁾

¹⁾ Department of System Design, Graduate School of Engineering, Kogakuin University, Japan
E-mail: gm18004@ns.kogakuin.ac.jp

²⁾ Department of Mechanical Engineering, Faculty of Engineering, Kogakuin University, Japan
E-mail: at13307@ns.kogakuin.ac.jp

³⁾ Department of Otolaryngology · Head and Neck Surgery, Tokyo Medical University, Japan
E-mail: otsuka@tokyo-med.ac.jp

Introduction

Benign paroxysmal positional vertigo (BPPV) accounts for 40 [%] to 50 [%] of those suffering from dizziness. It is a pathological condition caused by the inner ear. As a symptom, as soon as a person moves one's head, the person feels as if the person or the surroundings are rotating^[1]. This is caused by the vestibular organs at the back of the tympanic membrane. The vestibular organ consists of the otolith organ that senses the movement, back and forth, left and right, of the body and the ampulla that senses the rotation of the body. However, when otoconial mass is peeled off from the otolith organ, and they enter the semicircular canal, dizziness will occur. Then, it is called the semicircular canal calculus type: the state that an otoconial mass floats in the inner lymph fluid. When the otoconial mass is attached to cupula, then it is called the Cupulolithiasis^[2].

In the medical field, physical therapy that expels the otoconial mass from the semicircular canal is used as a treatment method. Effective treatment for Cupulolithiasis disease has not yet been established. Medical institutions are currently suggesting detaching the otoconial mass from cupula by applying vibration from outside the body. The problems, however, are that the mechanisms of the cupula and otoconial lump adhesion and isolation are not yet elucidated. Also, applying what kind of vibration to which part can safely work to detach the otoconial mass are not clear.

Therefore, to detach the otoconial mass safely, the basic research that investigates the principle of vibration transmission of a cupula is necessary. Therefore, in this paper, vibration load experiments and numerical analysis using pseudo cupula are conducted.

Conventional knowledge and issues

Otoconia are present on the otolithic membrane of the oval and spherical sac in the vestibular organ. Otoconia are like a fine sandy crystal on the sensory hair, which is covered and protected by a jelly-like substance. If otoconia fall off for some reason, they are presumed that they gather at the bottom of each semicircular canal to form an otoconial mass^[3].

Cupula is located in the ampulla of the semicircular canal and it covers the sensory hair of the crista ampullaris. The sensory hair senses the direction of endolymph flow by the cupula's inclination and transmits it to the brain. It is shaped like a membrane that blocks the flow of endolymph and is in contact with the inside the ampulla. Also cupula is a viscous substance mainly composed of mucopolysaccharide. It is presumed to be viscoelastic because it has been confirmed to be deformed by an external stimulus and return to its original state by unloading.

However, because the cupula has a high water content and the actual size is extremely small, it is very difficult to observe the fine form and analyze the constituents, and the detailed shape and physical properties are not known. Also, the behavior of cupula when different vibrations are applied is unknown.

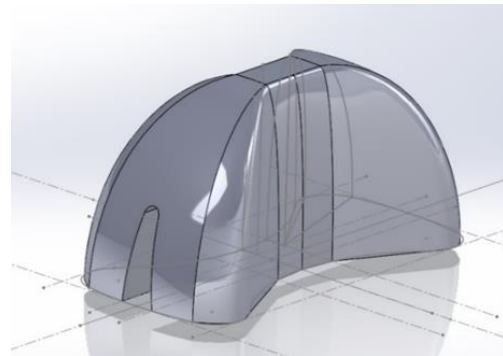


Fig. 1. Pseudo cupula 3D model.

Preparation of pseudo cupula

In this study, it is assumed that the physical property value of cupula is viscoelastic, and pseudo cupulas that reproduce viscoelasticity are created by using gel material. Using a dimensional effect, multiple pseudo cupulas with different sizes, shapes, and materials are compared and examined.

The pseudo cupulas are created by referring to the shape estimated from the measured values from the surrounding tissues of a cupula. Fig. 1 shows the characteristic shape of the cupula created by using SolidWorks, a general-purpose 3D CAD program. A pseudo cupula made of PLA filament was modeled

with a 3D printer (Fig. 2). These are used to make a silicone rubber mold to prepare a gel-like pseudo cupula.



Fig. 2. PLA filament pseudo cupula with different sizes.

Vibration load experiment

To investigate the mechanism of detaching which the otoconial mass by vibration an experiment device is assembled. As shown in Fig. 3, a speaker is used to generate the vibration. A vibrating plate is installed on the top of the speaker to enhance the resonance from the output sound. The sound data is created and controlled by MATLAB. The equipment and peripherals are assembled so that the frequency, amplitude, and waveform can be recorded automatically. While controlling the sound with a PC, the time and amplitude are measured with a sound level meter. Pictures are taken with a 3-axis smartphone to record pseudo cupula's motion during vibration.

A preliminary experiment needs to be conducted to grasp the resonance phenomenon of the material used to vibrating the plate. In this preliminary experiment, vibration will be applied for a certain period of time with salt placed on the vibrating plate. The Chladni Figures of salt that changes with each frequency with a smartphone will be recorded. Then, a pseudo cupula places on the vibrating plate to measure to measure considering the Chladni Figures.

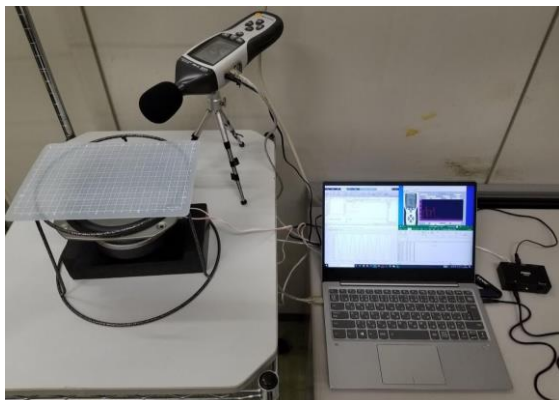


Fig. 3. Vibration device and peripheral equipment.

To investigate the correlation between cupula behavior and otoconial mass, the vibration frequency, resonance amplitude (A_c), waveform, and vibration

mode will be recorded when vibration is applied to the pseudo cupula and resonance phenomenon is observed. The strength of the resonance from the obtained vibration amplitude (A_a) of the experimental device and the resonance amplitude (A_c) of the pseudo cupula will then be calculated.

An experiment with pseudo otoconia attached to a pseudo cupula will be conducted. As an alternative to otoconia, we are considering adopting solid materials such as beads with the same shape and different sizes. The number of exfoliations of otoconial mass will be investigated when vibration is applied. The cupula behavior as the otoconial mass detach will be recorded to examine the correlation between the obtained parameters and the number of liberations of otoconial mass detachment.

FE Analysis

By using each model of the pseudo cupulas and the parameters obtained in the vibration load experiment, the experimental data are studied to obtain further knowledge about the mechanism of the detachment phenomenon of otoconial mass.

It is hoped that the otoconial mass detachment mechanism is physically caught in the experiment, which may lead to a better understanding of a hypothesis: the surface of a cupula is uneven, and the otoconial mass is detached from the cupula when a certain strain occurs.

Import the data created in SolidWorks into the analysis program, fix the bottom face of the pseudo cupula data used secondary tetrahedral elements, and give vibration to it. Besides the vibration response experiment of the cupula should be also conducted by changing the model shape to further analyze the conditions, the natural frequency, and frequency response. Then, for each model, a modal analysis for obtaining the natural frequency and a frequency response analysis for obtaining the distortion concerning the vibration will be performed. Frequency response analysis will be conducted by changing analysis settings and changing Young's modulus, density, and Poisson's ratio.

References:

- [1] Koji Otsuka, Clinical features and treatments of benign paroxysmal positional vertigo, *The Journal of Tokyo Medical University*, 76, 328-337 (2018).
- [2] K Otsuka, M Suzuki, M Negishi, S Shimizu, T Inagaki, U Konomi, T Kondo, Y Ogawa, Efficacy of physical therapy for intractable cupulolithiasis in an experimental model, *The Journal of Laryngology & Otology*, 127, 463-467 (2013).
- [3] Kohichiro Shigeno, Canalith repositioning maneuvers for cases of Benign Paroxysmal Positional Vertigo, *Equilibrium Research*, 77, 583-591 (2018).

Enhancement of the tumor cell migration on fibronectin by the metalloproteinase from *Ovophis okinavensis* snake venom

Yuna Saito¹⁾, Yongchol Shin^{1), 2)}, and Yasutada Imamura^{1), 2)}

¹⁾Graduate School of Engineering, Kogakuin University, Japan

²⁾Department of Chemistry and Life Science, Kogakuin University, Japan

Abstract

We demonstrated that migration of human fetal lung-derived fibroblasts, TIG-1, on FN were enhanced by the metalloproteinase, named MP09, from *Ovophis okinavensis* snake venom. We speculate that the partial cleavage of FN by MP09 causes the detachment of pseudopod that bound FN fragments, and the enhancement of cell migration. In this study, we elucidate the mechanism of the tumor cell migration on FN by MP09. The migration distance of HT-1080 for 6 hours with 3nM of MP09 was 2.6 times longer than the migration distance of cells without MP09. However, on FN pretreated with MP09, HT-1080 migration was not promoted. Furthermore, treatment of MP09 after seeding cells onto intact FN showed a tendency to dilate the gap of cells in proportion to the concentration of MP09. In low-density cell culture, the migration speed of HT-1080 with 3nM of MP09 was shown a tendency to get faster compared to the migration speed without of MP09, though the difference was not statically significant. From these results, we suggest two hypotheses about the mechanism of cell migration, (1) in high-density cell culture on the intact FN, the pseudopod adhered to FN significantly elongated. The partial cleavage of FN by MP09 causes the detachment of pseudopod that bound FN fragments, and the enhancement of cell migration; (2) MP09 enhance the cell migration by cleavage of not only FN but also cell-cell adhesion partially.

Introduction

The extracellular matrix, formed by complex molecular networks, provides cells with a scaffold. The process of binding of cells to extracellular matrix is essential for a variety of cell functions such as cell survival, proliferation, differentiation or migration. The process mainly mediated by integrins, transmembrane receptors, that enhance the adhesion of cell to extracellular matrix [1].

In the cell migration, not only integrins and matrix metalloproteinases (MMPs) also are involved. MMP-2 is known to contribute to tumor cell migration by cleavage of integrins and fibronectin (FN) [2]. Previously, we demonstrated that migration of human fetal lung-derived fibroblasts, TIG-1, on FN were enhanced by the metalloproteinase, named MP09, from *Ovophis okinavensis* snake venom. In addition, we demonstrated that the cleavage sites of fibronectin by MP09 are identical or close to the cleavage sites of fibronectin by MMP-2. We speculate that MP09 promote the fibroblast migration by cleavage of FN which bind to integrin, and MMP-2 also enhance tumor cell migration by similar mechanism. In this study, we elucidate the mechanism of the tumor cell migration on FN by MP09.

Method

[1] Wound healing assay

① Human fibrosarcoma cells, HT-1080, was seeded

on FN-coated plates and cultured for 1 days. The confluent cell monolayer was then scratched to create a wound in a straight line across the center of the dish and incubated with DMEM containing MP09 for 6 h. Images were taken immediately after the treatment of MP09 and 6 hours after the treatment. The areas of gaps without cell coverage were measured using an image analyzer, Image J, and the cell migration distance was calculated from the areas of gaps.

② Wound healing assay was performed on intact FN or precleaved FN by MP09 without addition of MP09. [2] Measurement of cell migration speed using time-lapse imaging in low-density cell culture

HT-1080 cells were seeded at low-density on FN-coated plates and cultured for 1 days. The cells were incubated with 3nM of MP09 for 6 hours. The migration of cell was imaged at 4min intervals for 6 hours using time-lapse microscopy and the migration speed of each cell was measured using automatic tracking tool, Trackmate.

Results

[1] Wound healing assay

① The migration distance of HT-1080 for 6 hours with 3nM of MP09 was 2.6 times longer than the migration distance of HT-1080 without MP09 (Fig. 1). We also observed that the migration distance of TIG-1 became the longest when 3nM of MP09 was added (data not shown).

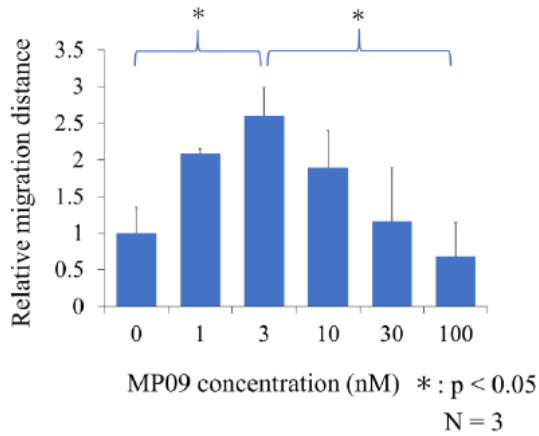


Fig. 1. Effect of MP09 on HT-1080 migration on FN.

② On FN pretreated with MP09, HT-1080 migration was not promoted (Fig.2). The migration of TIG-1, as well as HT-1080, were not promoted by treatment of MP09 (data not shown).

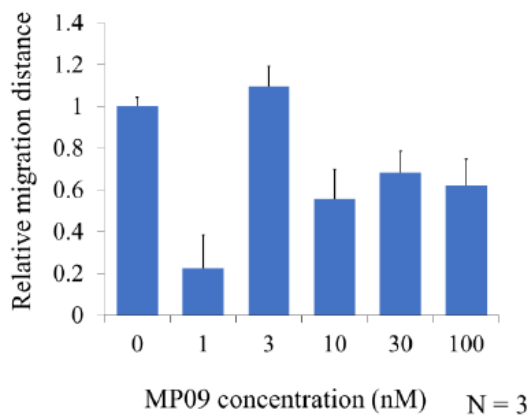


Fig. 2. Effect of MP09 on HT-1080 migration on cleaved FN.

Furthermore, treatment of MP09 after seeding cells onto intact FN showed a tendency to dilate the gap of cells in proportion to the concentration of MP09. However, cells seeded on pretreated FN with MP09 did not show the tendency as written above.

[2] Measurement of cell migration speed using time-lapse imaging in low-density cell culture

Average migration speeds of HT-1080 was $1.38\mu\text{m}/\text{min}$ or $1.42\mu\text{m}/\text{min}$ without or with treatment of MP09, respectively. The migration speed with 3nM of MP09 showed a tendency to get faster compared to the migration speed without MP09, though the difference was not statically significant (data not shown).

From these results, we suggest two hypotheses about the mechanism of cell migration,

(1) when the cells are seeded at high density on the intact FN-coated plates, the pseudopod adhered to FN significantly elongated. The partial cleavage of FN by MP09 causes the detachment of pseudopod that bound FN fragments, and the enhancement of cell migration;

(2) MP09 enhance the cell migration by cleavage of not only FN but also cell-cell adhesion partially.

References

- [1] Fukai F, *Yakugaku Zasshi* **137**, 137– 139.(2017)
 [2] Jiao Y, et al. *PLoS One* **7**: e41591.(2012)

Inhibitory activity of sekothrixide on a drug efflux via P-glycoprotein

Ryoki Haruyama¹, Yongchol Shin^{1,2}, Yasutada Imamura^{1,2}

Kogakuin University ¹Graduate School of Engineering,

²School of Advanced Engineering, Department of Chemistry and Life Science

Abstract

Multidrug resistance(MDR) is a major cause of failure in cancer chemotherapy. P-glycoprotein (P-gp), a promiscuous drug efflux pump, induces MDR. In this study, we developed the methods to measure drug efflux activity using cell-based assay with fluorescent reagents as drug equivalents. Sekothrixide was shown to inhibit the efflux via P-gp.

Introduction

Sekothrixide is a macrolide isolated from a microorganism (*Saccharothrixide* sp) and has been reported to overcome MDR with colchicine-resistant cell line, KB-C2[1]. Since total synthesis of sekothrixide was achieved by a laboratory in Kogakuin, the reagent is available for further experiments[2]. Cells that develop MDR often express multi-drug efflux factors, such as P-gp. In this study, we developed cell-based assay methods to measure drug efflux activity and applied to evaluate inhibitory activity of sekothrixide.

Methods

[Calcein-AM efflux assay]

Madin-Darby canine kidney cell line, MDCK, was provided by the RIKEN BRC through the National Bio-Resource Project of the MEXT/AMED, Japan. MDCK cells were cultured to confluence. They were incubated with Calcein-AM. Simultaneously, sekothrixide or P-gp inhibitors, Verapamil or Cyclosporin A, was added. Cells were washed with PBS(phosphate buffered salts) and solubilized with 10 mM HEPES buffer containing 2 mM CaCl₂ and 0.5% Triton X-100. The amount of Calcein in the lysate was measured as the fluorescence intensity.

[SYTO16 efflux assay]

MDCK cells were prepared exactly the same as above. Then, they were stained for 60 minutes with SYTO16. After cells were washed with PBS, sekothrixide, Verapamil, or Cyclosporin A was added simultaneously with containing 5% fetal calf serum. After 30 minutes, the supernatant was recovered and the fluorescence intensity was measured.

Results & Discussions

[Calcein-AM efflux assay]

We evaluated the Calcein-AM efflux in the presence of sekothrixide, Verapamil, or Cyclosporin A. The values of apparent IC₅₀ for sekothrixide, Verapamil and Cyclosporin A are $0.73 \pm 0.54 \mu\text{M}$, $0.45 \pm 0.52 \mu\text{M}$ and $0.30 \pm 0.13 \mu\text{M}$, respectively.

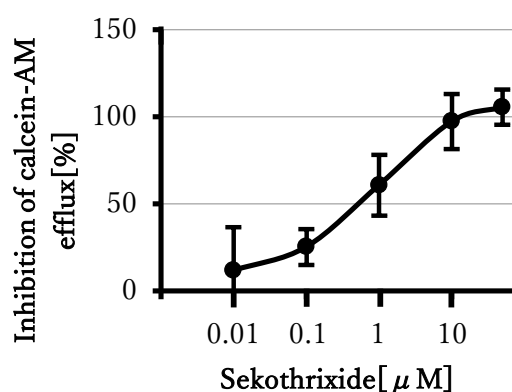


Fig.1 Inhibition of Calcein-AM efflux by sekothrixide

Calcein-AM is a hydrophobic molecule that is taken into the cell membrane, where Calcein-AM is hydrolyzed by resident esterase and converted to fluorescent Calcein. In cells expressing P-gp and MRP1(Multidrug resistance-associated Protein 1), Calcein-AM is partly transported back to medium by these proteins before being converted to Calcein. Since the active P-gp and MRP1 excrete Calcein-AM and decrease intracellular Calcein, the less fluorescence intensity is recovered. However, the suppression of these transporters, enhances the fluorescence recovery^[3]. As shown in Fig.1, sekothrixide inhibited the efflux of Calcein-AM in the concentration dependent manner. Verapamil and Cyclosporin A also showed similar inhibitions(data not shown). These 3 inhibitors show almost the same apparent IC₅₀. This suggests that in assays using Calcein-AM, sekothrixide inhibits either or both of P-gp and MRP1.

[SYTO16 efflux assay]

Verapamil and Cyclosporin A are P-gp inhibitors but their specificity and affinity are not convincing enough. So we tested another assay method using a fluorescent dye, SYTO16. The assay using SYTO16 was carried out as the same cell condition as Calcein-AM assay. Fig.2 shows the SYTO16 concentration of the supernatant at 30 minutes after adding PBS containing 5% fetal calf serum. As shown in Fig.2, the addition of

0.1 μ M sekothrixide or 0.1 μ M Verapamil decreased SYTO16 efflux by 50%.

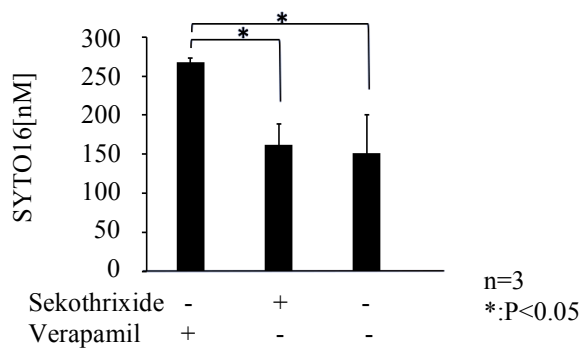


Fig.2 Inhibition of SYTO16 efflux by sekothrixide

SYTO16 was incorporated into the cell during the staining period and thought to reach a concentration equilibrium between both sides of the cell until 60 min. Residual dyes outside cells were washed away with PBS and then their secretion was measured. Since SYTO16 is thought to be effluxed by P-gp[4], the results suggest that sekothrixide inhibited P-gp and decreased the effluxed fluorescence intensity.

From the above two evaluation methods, we concluded that sekothrixide inhibits the efflux by P-gp.

Reference

- [1] Kim, YJ., Furihata, K., Shimazu, A. & Seto, H. Isolation and structural elucidation of sekothrixide, a new macrolide effective to overcome drug-resistance of cancer cell. *J Antibiot.* **45**, 1280-1282 (1991)
- [2] Terayama, N., Yasui, E., Mizukami, M., Miyashita, M. & Nagumo, S. Total synthesis and structural revision of sekothrixide. *Org. Lett.* **16**, 2794–2797 (2014).
- [3] Feller, N. *et al.* Functional detection of MDR1/P170 and MRP/P190-mediated multidrug resistance in tumour cells by flow cytometry. *Br. J. Cancer* **72**, 543–549 (1995).
- [4] Broxterman, H. J. *et al.* Highly sensitive and specific detection of P-glycoprotein function for haematological and solid tumour cells using a novel nucleic acid stain. *Br. J. Cancer* **76**, 1029–1034 (1997).

Analysis of the Factors Affecting the Implementation of Construction Quality Reports in Building Project through Case study of Danang City in Vietnam

Trung Quang Nguyen¹⁾, Oanh Thi Kim Le²⁾, Chau Quynh Truong³⁾, and Pham Nguyen Ngan Hanh⁴⁾

¹⁾Faculty of Project Management, The University of Danang - University of Science and Technology, Viet Nam

E-mail: nqtrung@dut.udn.vn

²⁾Faculty of Project Management, The University of Danang - University of Science and Technology, Viet Nam

E-mail: ltkoanh@dut.udn.vn

³⁾Faculty of Project Management, The University of Danang - University of Science and Technology, Viet Nam

E-mail: paduc@dut.udn.vn

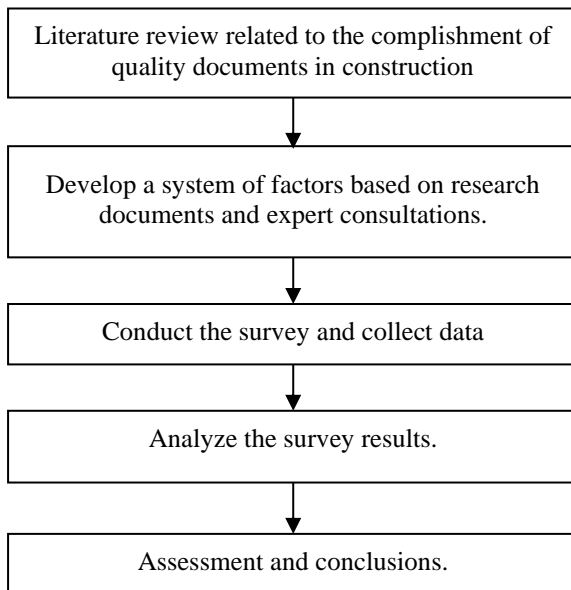
⁴⁾Faculty of Project Management, The University of Danang - University of Science and Technology, Viet Nam

E-mail: phamnganhanh@gmail.com

Abstract

Construction is a special commodity product for production and the requirements of human life. Due to its specific nature, managing construction quality during a project life-cycle will face many risks as well as encounter difficulties and challenges. Certainly, there have been many factors affecting the quality of the construction. This paper studies the factors affecting the process of conducting quality reports in construction projects, thus we will propose measures to improve the quality of construction profiles as well as contributing to improve construction quality management process

* Research Diagram



* Results

Factors influencing the application of green specifications				
No	Factors	Ranking	Mean	Std.
1	Time for documenting quality management.	1	4.11	0.801
2	Inconsistency in the process of project management and administration	2	4.07	0.838
3	Volume, instructional documents and forms for making documents provided by investors.	3	4.04	0.807
4	Process of solving arising problems during construction process	4	4.03	0.816
5	Project management model	5	4.01	0.787

References:

- [1] Ministry of Construction, *The conference evaluated the performance of tasks in 2018 and implemented the 2019 plan of the construction industry.*
- [2] Government, *Decree 46/2015/ND-CP on quality management and construction maintenance*
- [3] Ministry of Construction, *Overview of research on construction risks*
- [4] SPSS software (2012) Statistical package, version 20. SPSS Inc., Chicago. <http://www.spss.com>

Factors influencing the equipment cost estimation in the beginning stage building projects: case in Vietnam

Nguyen Thi Thao Nguyen¹⁾, Oanh Thi Kim Le²⁾, and Tuyet Phuoc Anh Mai³⁾

¹⁾Department of Project Management, The University of Danang-University of Science and Technology, Danang, Viet Nam

E-mail: ntnguyen@dut.udn.vn

²⁾Vice-Rector, The University of Danang-University of Science and Technology, Danang, Viet Nam

E-mail: ltkhoanh@dut.udn.vn

³⁾Department of Civil Engineering, The University of Danang-University of Technology and Education, Danang, Viet Nam

E-mail: mpatuyet@ute.udn.vn

Abstract

In Vietnam, many construction investment projects have recently had to adjust the total investment to increase compared to the initial approval. This not only makes it difficult for project consultants and investors to plan the allocation the capital but also negatively affects the financial efficiency of the Project. Equipment cost is one of seven cost components in the estimation of total project investment. In fact, the proportion of equipment cost accounts for 20% to 30% in the beginning stage building projects. Therefore, the accurate estimation of the equipment cost greatly affects the accuracy of the total investment. This study is conducted to assess the importance of factors influencing the equipment cost estimation from the perspective of the project investor and consultants. Since then, the authors identify important influencing factors and propose solutions to improve the accuracy of the estimation of the equipment cost to limit the adjustment of total investment compared to initial approval and increase investment efficiency for the projects.

Methodology

The data are collected via the survey method. The survey tables are used to record the data of 160 samples. After collecting data, they will be encoded and analyzed by SPSS statistical software.

Result

After the process of surveying and collecting data, the authors offer the following regression analysis table:

Model	Unstandardized Coefficients		Standardized Coefficients	t	Sig.
	B	Std. Error	Beta		
(Constant)	1.482	0.157		9.413	0.000
Project Complexity - TB1	0.008	0.032	0.018	0.259	0.796
Financial Capabilities Of The Investor - TB2	-0.016	0.032	-0.034	-0.478	0.633
Project Location - TB3	-0.013	0.040	-0.038	-0.318	0.751
Availability Of Cash Flow - TB4	0.022	0.039	0.050	0.581	0.562
Guidelines on current calculation methods - TB5	0.142	0.045	0.298	3.146	0.002
Availability of equipments - TB6	0.107	0.043	0.118	2.494	0.014
Accuracy and reliability of market prices - TB7	0.137	0.035	0.251	3.877	0.000
Communication in The Project Team - TB8	0.053	0.034	0.100	1.573	0.118
Experience of project consultants - TB9	0.120	0.035	0.199	3.465	0.001

The standardized regression equation is derived from the regression analysis table as follows:

$$TCX = 0.298 \times TB5 + 0.118 \times TB6 + 0.251 \times TB7 + 0.199 \times TB9$$

Of all 9 independent variables, 4 variables with sig <0.05 are accepted in the regression equation, and they have effects on independent variables. The coefficients in the regression equation are marked with (+), indicating that all four factors have a positive effect on the accuracy of the estimation of equipment costs in the total investment of the project.

Conclusion

Based on analytical results, Accuracy and reliability of market prices, Guidelines on current calculation methods, Experience of project consultants and Availability of equipments are the most influential factors to the accuracy of the equipment cost. Besides, the factors related to project characteristics are not of great importance to the accuracy of the estimation of equipment costs.

From the results of this study, the authors suggest that the project consultants and investors need to improve expertise, enable employees to accumulate knowledge and experience in planning projects and estimating costs; the authorities need to focus on creating market information smoothly and reliably, provide unified, clear guidelines to improve the accuracy of the estimation of the equipment cost

Reference

- [1] H.P. Loh, Jennifer Lyons and Charles W. White, *Process Equipment Cost Estimation Final Report*, DOE/NETL-2002/1169, 6-40 (2002).
- [2] Enshassi, A., Mohamed, S. and Abdel-Hadi, M, "Factors affecting the accuracy of pre-tender cost estimates in the Gaza Strip", *Construction in Developing Countries*, Vol. 18 No. 1, 73-94 (2013).
- [3] Larson, E.W. and Gray, C.F. (Ed.), "Project management", *The Managerial Process*, Sixth ed, (2010)
- [4] Mahamid, I, "Factors affecting cost estimate accuracy: evidence from Palestinian construction projects", *International Journal of Management Science and Engineering Management*, Vol. 10 No. 2, 117-125 (2015).
- [5] Akintoye, A, "Analysis of factors influencing project cost estimating practice", *Construction Management & Economics*, Vol. 18 No. 1, 77-89 (2000).
- [6] Shash, A.A. and Ibrahim, A.D, "Survey of procedures adopted by A/E firms in accounting for design variables nearly cost estimates", *Journal of King Saud University*, Vol.18No.1, 1-17 (2005)

Developing the model for multiple-criteria decision-making for stakeholders in construction projects towards sustainable development

Ngoc Son Truong¹⁾, Anh Duc Pham²⁾, and Le Thi Kim Oanh²⁾

¹⁾Faculty of Project Management, University of Science and Technology, The University of Danang, Vietnam
E-mail: tnson@dut.udn.vn

²⁾ Faculty of Project Management, University of Science and Technology, The University of Danang, Vietnam
E-mail: paduc@dut.udn.vn

³⁾ Faculty of Project Management, University of Science and Technology, The University of Danang, Vietnam
E-mail: ltkoanh@dut.udn.vn

Abstract

Making decision under multiple criteria is a fertile research area with lots of scope for real-life applications. However, the decision-making process is limited on subjective assessments and it has not been balanced between costs and benefits. This study presents a supporting tool for the decision-making process based on the Analytic Hierarchy Process (AHP) in construction management. This tool is built in Visual Basic for Applications (VBA) language. It will provide a convenient, reliable and faster way for the user to make a decision and get the final result of the decision by showing the best alternative based on the most important criteria. This tool is time-saving and reduces errors in decision-making process in many fields, especially in construction management towards sustainable development.

EXPERIMENT ON A MASS CHANGE AND SHRINKAGE OF CONCRETE DUE TO CARBONATION

Masaru OYAMA¹⁾, Masaki TAMURA²⁾, Michihiko ABE³⁾

¹⁾ Graduate school student, Kogakuin University, Tokyo, Japan;
E-mail: dm19010@ns.kogakuin.ac.jp

²⁾ Professor, School of Architecture, Kogakuin University, Tokyo, Japan

³⁾ Professor Emeritus, School of Architecture, Kogakuin University, Tokyo, Japan

Abstract

One of the deterioration factors of reinforced concrete is the neutralization of concrete. This is a phenomenon in which the alkalinity of concrete is lost due to atmospheric carbon dioxide and acid rain. If this neutralization reaches the position of the rebar and water is present, the rebar will corrode and the strength will be severely impaired. In addition, it is known that a large shrinkage strain occurs due to neutralization, and if cracks occur due to this, moisture tends to enter the inside and affect the corrosion of the reinforcing bars.

The purpose of this study is to measure shrinkage and mass change when concrete is neutralized and to summarize the properties.

1. Introduction

After hardening, the concrete loses its mass due to drying and shrinkage strain (dry shrinkage) occurs. It is also known that neutralization increases mass and causes shrinkage strain (carbonation shrinkage)^[1]. These behaviors are complex, but no systematic studies have been found^[2].

In an actual building, it is easier to neutralize the indoor side where it is dry and has a higher CO₂ concentration than outdoors where it rains, but because the moisture content is low, corrosion of the indoor rebar is less likely to occur. In addition, although the progress of neutralization is delayed due to the presence of the finishing material, it is difficult to expect an effect especially in finishing.

Therefore, in this experiment, accelerated carbonation tests were performed on concrete specimens to investigate mass changes and shrinkage behavior. Here, this paper reports until the age of 101 weeks, following our previous studies^[3].

2. Experimental outlines and methods

Table 1 shows the concrete mix proportion. The mixing and materials are according to the experiments by Suzuki et al.^[4] and the unit water quantity is 172kg/m³. AE water reducing agent and AE agent mixed 0.25% and 0.0045% of the cement quantities. The test specimen was a 100 × 50 × 400 (mm) prism with a strain gauge buried inside.

All test specimens removed from the mold at the day following pouring concrete, and cured in water at 20°C until the age of 4 weeks. After that, they dried in constant temperature and humidity chamber at 20°C and 60%R.H., until the age of 8 weeks. At the age of 8 weeks, 4 surfaces except for both sides of the test specimen were sealed with epoxy resin, and the following day, some specimens were moved to an

accelerated neutralization tank at 20 ° C, 60% R.H., CO₂ concentration 5%. The remaining test specimens were returned to the constant temperature and humidity chamber and keep drying. Table 2 shows the combinations of the test specimens.

The test method of concrete is as shown in Table3. The carbonation depth was measured when expect the carbonation depth reaching of 10 mm and 20 mm based on the experiments by Suzuki et al^[4].

Table 1. Concrete mix proportion

W/C	s/a	unit mass (kg/m ³)			
%	%	W	C	S	G
70	49.1	172	344	812	952
60	48.1		287	859	
50	46.1		246	893	

Table 2. Combination of test specimens

Preservation condition	W/C		
	50%	60%	70%
Neutralization	N50	N60	N70
Drying	D50	D60	D70

Table 3. The test method of concrete

Test case	Method
Length change	Strain gages
Mass change	Electronic balance (scale interval : 0.1g)
Accelerated carbonation test	According to JIS A 1153
Carbonation depth	According to JIS A 1152

3. Test results and discussion

3.1 Results of length change

Fig. 1. shows rate of change in length since accelerated carbonation test start. Some data are atypical value because constant temperature and humidity chamber is breakdown. The shrinkage

strains of N series were larger than D series. It is assumed that carbonation shrinkage caused by neutralization of concrete is occurring. Also, in the early stage of accelerated carbonation test, the larger the water-cement ratio, the larger the shrinkage strain occurs, but this tends to reverse as the promotion period becomes longer.

3.2 Results of mass change

Fig. 2. shows rate of change in mass since accelerated carbonation test start. The mass of D series decreased gradually, but the mass of N series increased greatly. It is assumed that because concrete absorbs CO_2 , and neutralization occurs. In the early stage of accelerated carbonation test, the larger the water-cement ratio, the larger the mass increase occurs, but this tends to reverse as the promotion period becomes longer. Also, N series tends decrease slowly since the mass reaches a maximum. From this, it is assumed that the water generated with neutralization slowly dissipates.

3.3 The relation between carbonation depth and mass change

Fig. 3.(A) shows the relation between carbonation depth and rate of change in mass. This rate of change in mass here is subtraction D series from N series. It became a linear relationship in the any water-cement ratio. Also, it get the larger the water-cement ratio, the smaller that ratio of carbonation depth to rate of change in mass. Fig. 3.(B) shows dividing rate of change in mass for (A) by unit cement quantities. They became linear regardless of the water-cement ratio. Because of these things, it may estimate that carbonation depth by mix proportion of concrete and mass change.

4. Summary

- 1) It is assumed that the concrete treated with CO_2 is neutralized and accompanied by carbonation shrinkage.
- 2) The water generated by neutralization is considered to dissipate very slowly.
- 3) The maximum value of length and mass change due to neutralization is related to the unit cement quantity, and it is possible that the carbonation depth can be estimated from this

References:

- [1] Katsuro Kamimura, Shrinkage and weight change of mortar by drying and neutralization. *cement concrete*, 207, 2-6 (1964), and 208, 12-20 (1964).
- [2] Michihiko Abe, Tatsuya Saito, Study on the relation between neutralization and mass change of concrete, *Proceedings of the JUSS Congress on Cement and Concrete*, 44, 13-18 (2017).
- [3] Ooyama Masaru, Michihiko Abe, Masaki Tamura, The experiment on a mass change and shrinkage of concrete due to carbonation Part 2,

Summaries of technical papers of annual meeting, 737-738 (2019).

- [4] Suzuki Yoshihisa, Michihiko Abe, Effect of temperature conditions on the neutralization of concrete. (Comparison between 20°C and 40°C), *Proceeding of the architectural research meetings, Kanto Chapter, Architectural Institute of Japan*, 125-128 (2017).

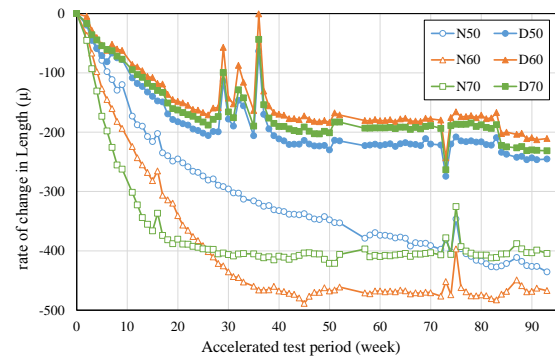


Fig. 1. Aging of the Length on concrete

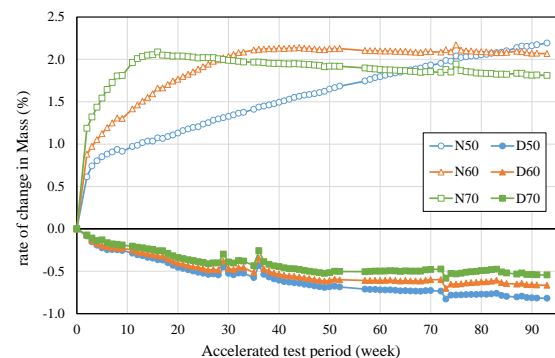


Fig. 2. Aging of the Mass on concrete

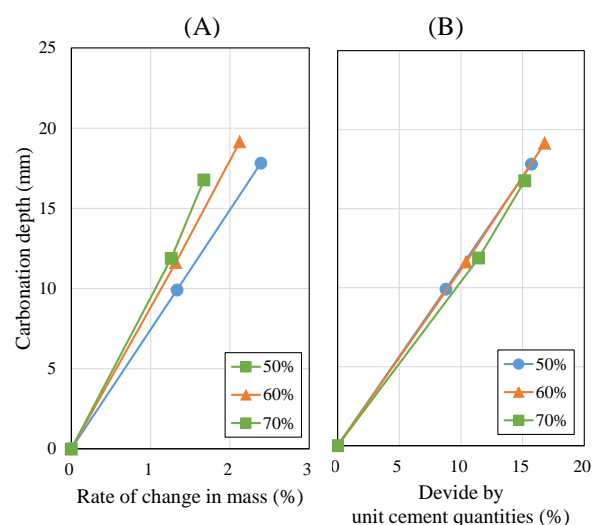


Fig. 3. The relation between carbonation depth and mass change

An Embedded Real-time Monocular SLAM System Utilizing a Dynamically Reconfigurable Processor

Koki Kawashima¹⁾ and Koyo Katsura, Ph.D.²⁾

- 1) Department of Systems Design Program, Graduate School of Engineering, Kogakuin University, Tokyo, Japan
E-mail: gm18003@ns.kogakuin.ac.jp
- 2) Department of Systems Design Program, Graduate School of Engineering, Kogakuin University, Tokyo, Japan
E-mail: koyokatsura@cc.kogakuin.ac.jp

Abstract

Autonomous mobile robots must be able to estimate and maintain the pose of the robot and the map of the environment. SLAM (Simultaneous Localization and Mapping) performs those tasks using one or more external sensors (e.g., LiDAR, Camera, and Inertial Measurement Unit). The previous SLAM system had problems with a sensor size, high power consumption, and high cost. Thus, it is hard to implement on a small indoor robot. We propose an Embedded Real-time Monocular SLAM System utilizing a dynamically reconfigurable processor. This system realizes real-time, low-power (less than 2W), and small size. In the future, we will examine the speed-up of all processing and build it into a device.

Autonomous mobile robots are expected to solve the social problems of the decrease of workers and increase of aging population. According to a market trend report released by Boston Consulting Group (BCG), the global robotics market will grow at CAGR (Compound Average Growth Rate) of 11.2 percent until 2025 [1]. Especially, the personal segment is the most growing segments at CAGR of 17.9 percent. Thus, the demand of an indoor use robots will increase. The future personal robots that help people need to be able to run autonomously and need to be built in small size.

When autonomous mobile robots are running, the robots must be able to estimate and maintain the pose and the map of the environment. The technologies are called “Simultaneous Localization and Mapping (SLAM)”. The previous system has a lot of problems; sensor size, high power consumption, and high cost. It is hard to implement on a small indoor robot. To build on a small indoor robot, it is necessary to realize a small, low-power consumption and low-cost system.

We propose an Embedded Real-time Monocular SLAM System. The proposed system combines an ORB feature extraction-based SLAM (ORB-SLAM), a monocular camera, and a dynamically reconfigurable processor (DRP). This system realizes real-time visual SLAM utilizing a hardware acceleration and a dynamic reconfiguration of the DRP. The DRP is programmable hardware which has both the flexibility of software and the speed of hardware. A DRP product is produced by Renesas Electronics Corporation; it is called “RZ/A2M”. DRP can speed up some complicated processing by hardware acceleration technology (such as parallel processing and pipeline processing), and DRP can change the hardware configuration at any time and at high speed (it is called “Dynamic Reconfiguration”). Therefore, DRP enables to realize the embedded

SLAM system by using the hardware acceleration and the dynamic reconfiguration of the DRP efficiently. Fig. 1 shows the flow of DRP function.

In the current status, we examined the hardware acceleration of FAST (Features from Accelerated and Segments Test) corner detection (which is a part of SLAM processing) using FPGA processor. As a result, the processing time is 0.94ms, and speed-up by 12.6x than CPU (General purpose processor). Fig.2 shows the input image and the result. Additionally, we evaluated that the proposed system could realize small size and low-power consumption (less than 2W).

In future, we would examine the speed-up of all processing and build into the DRP device.

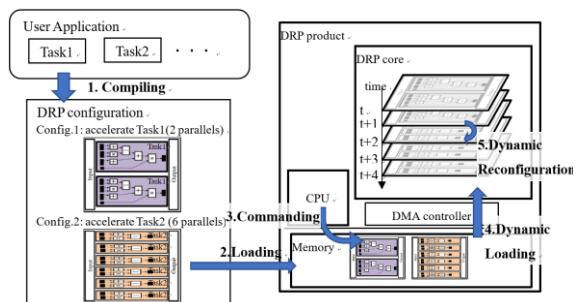


Fig. 1. The flow of DRP function



Input image Detected feature point
Fig.2. Input image and the result

References:

- [1] Frank Tobe, <https://robohub.org/latest-research-report-shows-10-4-cagr-for-robotics-to-2025/>, last accessed Jul. 21, 2019.

Design and Achievement of a small Automatic Mapping Vehicle with a LiDAR Scanning Method

Sheng-He Wang¹⁾, Yong-Qi Zhang, Kai-Cheng Hu Xu, and Chia-Pang Wei

¹⁾ Department of Electronic Engineering, Southern Taiwan University of Science and Technology, Tainan, Taiwan

E-mail: sunhur0315@stust.edu.tw

Abstract

Recently, according to the development of automation technology, automatic manufacturing factory was been focused and developed for the fast and various production. In order to improve to be a full automatic manufacture from self-automatic, the related position for each one of the process machine should be defined precisely, then the coupling machine can be built to let the different automatic process connect together. However, in the most of manufacturing factory, the position measurement was adopted by human hands, which will result in some mistakes and fault, and the coupling machine is difficult to setup. Therefore, LiDAR (Light Detection and Ranging) scanning machine was proposed and build on a small mobile vehicle. When the mobile vehicle is moving, the LiDAR will be activated and scanned to obtain the environment information. By coordinate transformation and array extension method, the environment information can be transferred into digital array dynamically, and the automatic map construction technology can be achieved. According to testing result, the designed mobile vehicle with a LiDAR scanning laser can be achieved and it demonstrated the accuracy of the proposed dynamic map construction technology, which the maximum estimated error was small than 1% for measuring a 50cmX50cm box. Therefore, based on the wireless transmission technology, the digital environment map can be demonstrated on the mobile device by Wi-Fi, and the dimension and position of all process machine in the factory can be estimated.

Keyword: Small automatic vehicle, LiDAR, Array extension method, Dynamic map construction

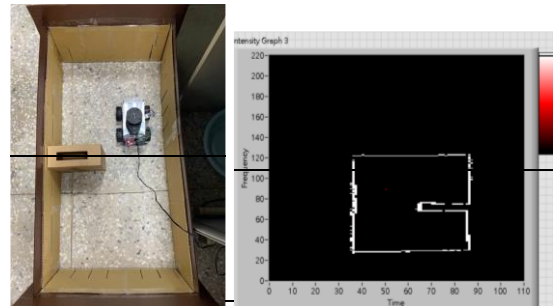
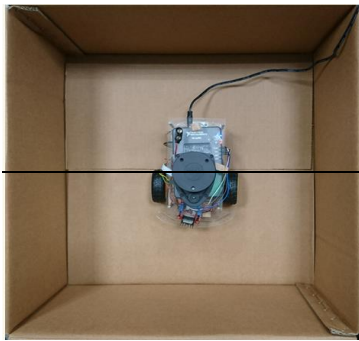


Fig. 2. Dimension estimation with one obstruction

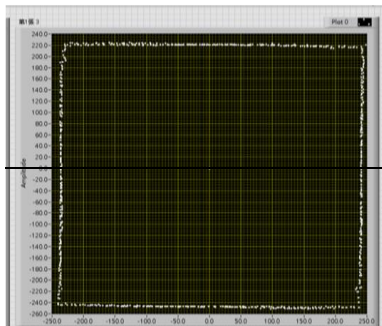


Fig. 1. Dimension estimation of 50cmX50cm box.

References:

- [1] <https://www.ipinlaser.com.tw/blog/t-3d-ldm>.
- [2] <http://blog.udn.com/mhwu1/7534030>
- [3] 林建忠，雷射測距技術與研究現況(1999)
- [4] 林忠杰，自走車專題研究，臺北城市科技大學電機系專題報告。

The Study of Optical Phenomenon of a Rectangular Integrating Rod with a LED by Kaleidoscope Imaging Modelling and Experiment

Min-Yu Tsai[†], Zun-Xiong Ke, Jeng-Fneg Lin, and Chih-Chieh Kang*

Department of Electro-Optical Engineering, Southern Taiwan University of Science and Technology, Tainan, Taiwan

E-mail: kangc@stust.edu.tw

ABSTRACT

In this study, experiments and optical simulations were performed to validate the accuracy of an ASAP simulation model for a rectangular integrating rod with a LED based on kaleidoscopic approach. The simulation results reveal that not all the mirror light sources are required to achieve high illuminance uniformity of output light.

A rectangular integrating rod is widely used in optical systems of industrial and commercial applications, such as lithography, projectors, and automated optical inspection, etc. In addition to illuminance uniformity issue of output light from the integrating rod, the formation of an array of mirror images away from the integrating rod did also attract some attention due to its implication in optical computing. In this study, our aim is to construct an accurate ASAP simulation model for a rectangular integrating rod with a LED based on kaleidoscopic approach to reveal the complexity and form a foundation for the design of an LED AOI light source using multiple spherical lenses. Experiment was performed to validate this simulation model with multiple mirror light sources. It was also compared with another ASAP simulation model directly emulating its physical counterpart

A typical LED AOI light source consists of two parts, an integrating rod with a LED and a set of spherical lenses, as shown in Fig. 1. Nevertheless, the main focus in this study was to address the complexity nature of output light from an integrating rod. Therefore, the experimental setup was only mainly comprised of a LED and a rectangular integrating rod, as shown in Fig. 2. The detection screen was positioned at various distances (increasing from near to zero to 60 mm) from the output end of the integrating rod. The dimension of integrating rod ($n = 1.5$) implemented was $25 \times 25 \times 90$ mm. The size of LED was 5×5 mm. The images of multiple angularly expanded squares overlapping based on kaleidoscopic mechanism at various measurement distances were formed on that screen and recorded. Some typical experimental results were shown in Fig. 3.

An accurate ASAP ray-tracing simulation model I was developed according to the experimental scenario, as shown in Fig. 4. Both lambertian point light source and surface light source was applied in simulations. Though, it was accurate but was unsuccessful in clarifying the overlapping phenomenon of multiple angularly expanded squares. However, it was used to facilitate the verification of

our another ASAP simulation model II based on kaleidoscopic approach, as shown in Fig. 5, which could be a crucial mechanism in the analysis and design of LED AOI light source. The overlapping mechanism of multiple angularly expanded squares could be satisfactorily explained and illustrated by just a simplified 2-D graph in Fig. 6. A more elegant 3-D simulation model illustration based on kaleidoscopic approach with multiple mirror light sources was presented in Fig. 7 which was fully coincided with our concept of angular light ray grouping by partitioning. Each mirror light source represented angular light ray group with zero bounce, one bounce, two bounces, etc., respectively.

The particular simulation results with a point light source corresponding its experiment counterpart by using ASAP model I and II were shown in Fig. 8 and Fig. 9, respectively. To compare to each other and to compare with the experimental results, it showed high-degree of conformity. The illuminance uniformity of the surface proximity to the output end of the rod with ASAP model II was also investigated. It demonstrated that high illuminance uniformity still can be maintained without including large-angle angular light ray group.

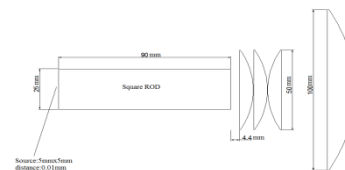


Fig. 1 Schematics of a typical LED AOI light source with a LED and an integrating rod and a set of spherical lenses.

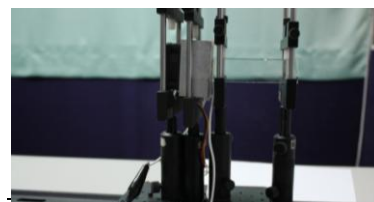


Fig. 2 Experimental setup for validating ASAP simulation models.

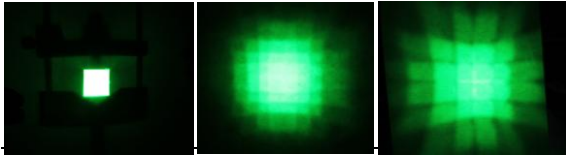


Fig.3 Experimental results: (a-c) images of multiple angularly expanded squares overlapping at different distances (increasing from near to zero to 10 mm, to 60 mm, respectively) from the output end of the rectangular integrating rod.

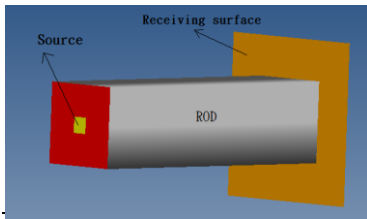


Fig. 4 Schematics of ASAP simulation model I emulated the experiment setup.

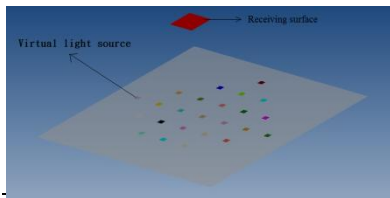


Fig. 5 Schematics of ASAP simulation model II based on kaleidoscopic approach with multiple mirror light sources.

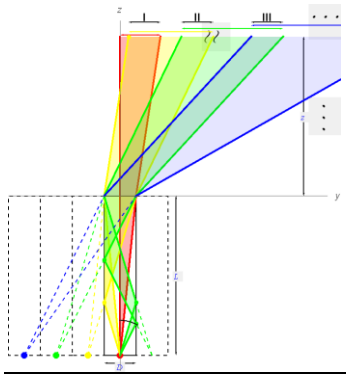


Fig. 6 A simplified 2-D illustration for overlapping angular light-ray groups.

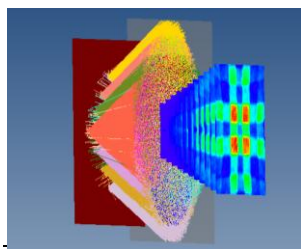


Fig. 7 Illustration of ASAP simulation using ASAP simulation model II.

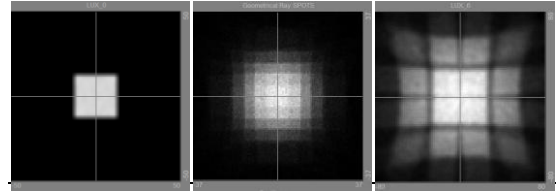


Fig. 8 Simulation results of ASAP simulation model I: (a-c) images of multiple angularly expanded squares overlapping at different distances (increasing from near to zero to 10 mm, to 60 mm, respectively) from the output end of the rectangular integrating rod.

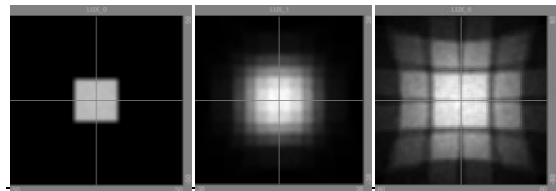


Fig. 9 Simulation results of ASAP simulation model II: (a-c) images of 25 angularly expanded squares overlapping at different distances (increasing from near to zero to 10 mm, to 60 mm, respectively) from the output end of the rectangular integrating rod.

References:

- [1] B. A. Jacobson, R. D. Gengelbach, and J. M. Ferri, *Proc. SPIE*, 3139, pp. 141–150, 2019.
- [2] C. F. Dimas, S. Read, J. J. Kuta, *Proc. SPIE*, 4768, pp. 82-92, 2002.
- [3] Z. L. Jin, D. X. Xiong, J. F. Dong, H. Y. Wang, W. M. Li, L. Q. Guo, and P. P. Wang, *Appl. Opt.*, Vol. 58, no. 2, pp. 317-324, 2019
- [4] Chu-Ming Cheng and Jyh-Long Chern, *Appl. Opt.*, Vol. 23, no. 12, 3123-3132, 2006.

Applied to the intelligent ring pressure sensing system

Lee, Da-Hue¹⁾, Lin, Chia-Huang²⁾, and Wang, Pi-Zhi³⁾

¹⁾Department of Electronic Engineering, Southern Taiwan University of Science and Technology, Taiwan
E-mail: dhlee@stust.edu.tw

²⁾Department of Electronic Engineering, Southern Taiwan University of Science and Technology, Taiwan
E-mail: ma730123@stust.edu.tw

³⁾Department of Electronic Engineering, Southern Taiwan University of Science and Technology, Taiwan
E-mail: ma630121@stust.edu.tw

Abstract

The purpose of this study was to investigate the ring system with pressure sensor. This system works with the back-end signal processing technique, and transfer the result of the operation to the presentation in software program via wireless communication. It also records the the change of pressure with big data analysis, such that the rehabilitation can observe each status, and can use the system to get a reminder of strength feedback, resulting in better rehabilitation performance.

This system uses a piezoresistive film pressure sensor, where the deformation can change the resistance value. This piezoresistive device is a passive sensor. When the component is not under load, the resistance value is very close to infinite. When the force increases, the resistance value decreases. With a series resistor, the voltage division law is used to extract the voltage value between the two impedances.

This system is implemented by the STM MCU system to read the value of the pressure sensor and convert the 15 channels analog signal into a bit string. Through the Bluetooth, the signal is wirelessly transmitted to Labview for signal processing, and is divided into individual channel pressure values. The signal is presented in three ways, percentage, weight, and Newton. We use the value as records, and compare them with the subsequent force sensing value. When the force is insufficient, the force feedback reminds the rehabilitation as a reference.

In this study, 12-bit capacitive successive approximation analog-to-digital converter is used to convert the pressure signal. The principle of successive approximation analog-to-digital converter is to use the binary search method. Compare each time with an intermediate value, the record is compared with the register. As a result, the input values are successively compared successively to obtain an exact value. The capacitive array uses a MOM (Metal-oxide-Metal) architecture to implement capacitive components.

Key word: Pressure sensor; Piezoresistive; Capacitive successive approximation analog-to-digital converter

Use deep learning for polycrystalline solar panel defect detection

You-Teh Lin^{1†}, Keh-Moh Lin^{2*}, Harshad Dandage³, Horng-Horng Lin⁴

^{1,2}Department of Mechanical Engineering, Southern Taiwan University of Science and Technology, Tainan, Taiwan

E-mail: MA810205@stust.edu.tw

³Department of Electrical Engineering, Southern Taiwan University of Science and Technology, Tainan, Taiwan

⁴ Department of Computer Science and Information Engineering, Southern Taiwan University of Science and Technology, Tainan, Taiwan

E-mail: harshadkdandage@gmail.com

[†]Presenter: **You-Teh Lin**

*Corresponding author's email: kemo@stust.edu.tw

ABSTRACT

In recent years, many countries, including Taiwan, have paid great efforts to replace nuclear power with green energy, and solar power is generally considered the primary option. Thus, a large number of solar panels are installed in Taiwan. In addition to conversion efficiency, and the lifespan of solar panels will also be an important factor. Defect such like dirt, cracks, and bolt will lead to shortened product life. Thanks to many of the advantages of electroluminescence, which is widely used for monitoring the manufacturing process. Even so, the monitoring is still done manually. If this manual monitoring step can be replaced by automation, it will save manpower and detection time.

Due to the difference in the crystal structure of the materials, images of polycrystalline silicon solar panels obtained through EL are more complex than those of single-crystal silicon solar panels, as shown in fig. 1. Due to this reason, it is difficult to find the defect part of the polycrystalline silicon solar panels quickly. Therefore, this project plans to develop an automatic detection program combined with deep learning for the inspection of polycrystalline silicon solar panels. Whole EL images of solar panels were first manually divided into two groups, those without defects and with defects. These were used to train the CNN to identify defects. Fig. 2 (a) is the original image of the defect, and fig. 2 (b) is the image after the defect is colored by the program. According to the different defect types, the images are cropped into three sizes, respectively, 160*160, 224*224, 448*448, as shown in fig. 3. The CNN model used for deep learning is Resnet101. Experimental results show that the accuracy in the training mode approaches 100% and the loss approaches 0. However, in the validation experiment, the accuracy falls to 55% and the loss is as high as 2.2, as shown in fig. 4. Since there are insufficient images, it is inferred that the results may be obtained through overfitting. In the future, more training images will be used to solve the current problems.

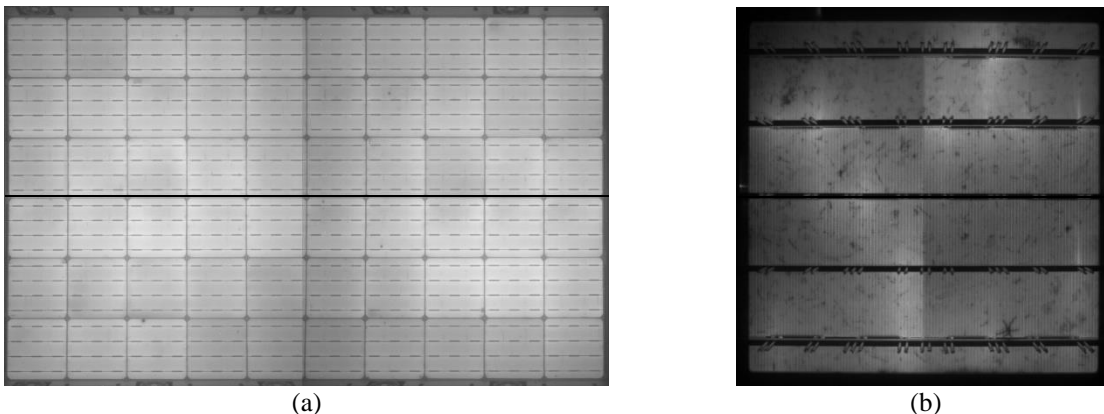


Fig. 1: solar panel EL image (a)single crystalline silicon, (b) polycrystalline silicon

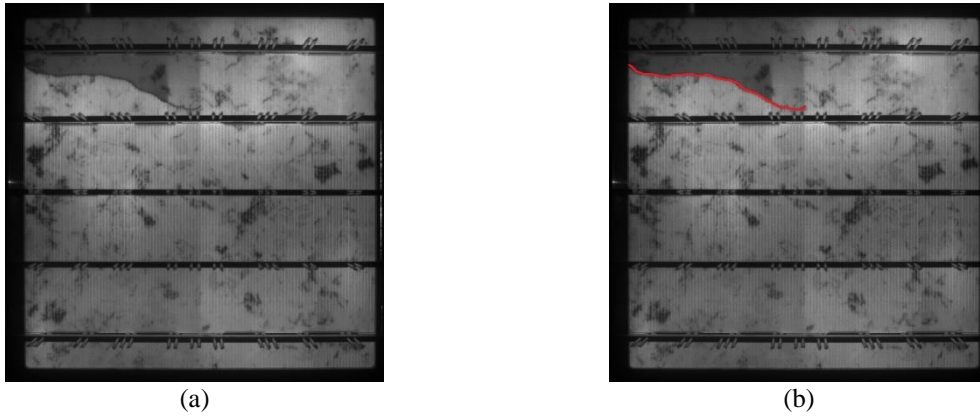


Fig. 2: solar panel EL image (a) original image, (b) colorised image

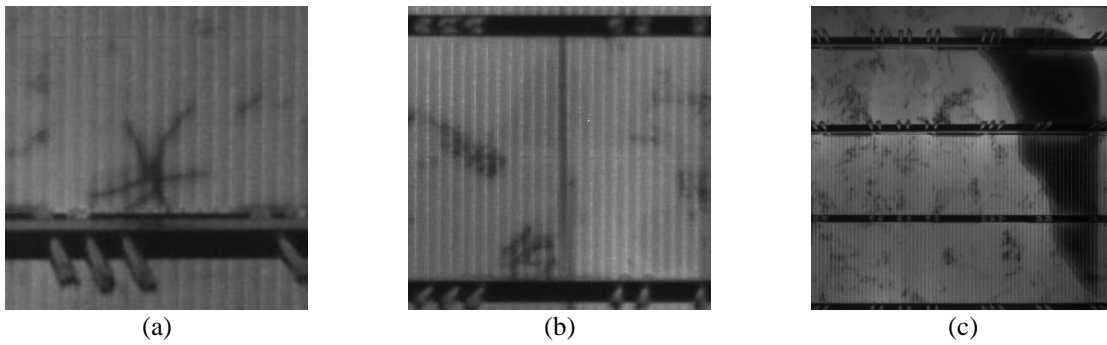


Fig. 3: (a) 160*160 image, (b)224*224 image, (c)448*448 image

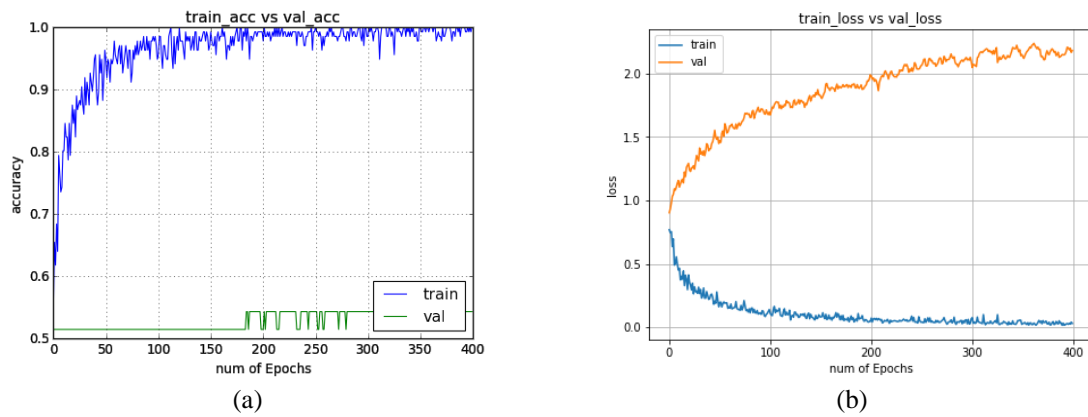


Fig. 4: training result (a)accuracy ,(b)loss

Keywords: solar panel defect detection, deep learning

Acknowledgements

Financial support was granted in part by the Ministry of Science and Technology of Taiwan R.O.C under MOST 108-2221-E-218-006, MOST 108-2622-E-218-005-CC3 and MOST 108-2221-E-218-021.

Control of Flow Instability in Axial-flow Fan with Upstream Obstacle Using Cross-partition Plate

Takeru Shinohara¹⁾, Ryoichi Moriyama²⁾, Risa Yoshie³⁾, Koichi Nishibe⁴⁾, Hiroshi Ohue⁵⁾, and Kotaro Sato⁶⁾

- ¹⁾ Graduate School of Integrative Science and Engineering, Tokyo City University, Japan
E-mail: g1881028@tcu.ac.jp
- ²⁾ Graduate School of Integrative Science and Engineering, Tokyo City University, Japan
E-mail: g1881061@tcu.ac.jp
- ³⁾ Graduate School of Integrative Science and Engineering, Tokyo City University, Japan
E-mail: g1981051@tcu.ac.jp
- ⁴⁾ Department of Mechanical Engineering, Tokyo City University, Japan
E-mail: knishibe@tcu.ac.jp
- ⁵⁾ Department of Mechanical Engineering, Tokyo City University, Japan
E-mail: hohue@tcu.ac.jp
- ⁶⁾ Department of Mechanical System Engineering, Kogakuin University, Japan
E-mail: at12164@ns.kogakuin.ac.jp

Abstract

In present study, we propose to install a cross-partition plate at the space between upstream obstacle and the fan inlet as one of method of improving fan performance and attenuating pressure fluctuation induced by the flow instability in axial-flow fan with upstream obstacle. Installing the cross-partition plate at the space between upstream obstacle and the fan inlet is effective to control the flow instability and improve the fan performance.

Axial-flow fans have been applied to versatile application including cooling heat element and ventilation. In addition, the axial-flow fans are integrated in compact electronic devices such as PC for cooling heated substrates, because they are comprised of simpler parts and can be more easily downsized than other flow-type of rotating machinery. To date, several researchers have reported its performance degradation and generating a flow instability with pressure fluctuation in above-mentioned usage situation that there are many obstacles at upstream or downstream of the axial-flow fan ^[1-3]. However, many issues to be solved on mechanism of the performance degradation and generation of flow instability are remained. Furthermore, a specific method of recovering the fan

performance and controlling the flow instability have not been established.

In present study, we propose to install a cross-partition plate at the space between upstream obstacle and the fan inlet as one of method of improving fan performance and attenuating pressure fluctuation induced by the flow instability in axial-flow fan with upstream obstacle. Mainly, we investigated the effect of the length of cross-partition plate on the performance curve and amplitude of the pressure fluctuations by conducting both experiments and computational fluid dynamics (CFD). This paper indicates results obtained from CFD and discusses the effectiveness of the presence/length of cross-partition plate on the control of the flow instability.

Figure 1 shows the configuration of test fan/cross-

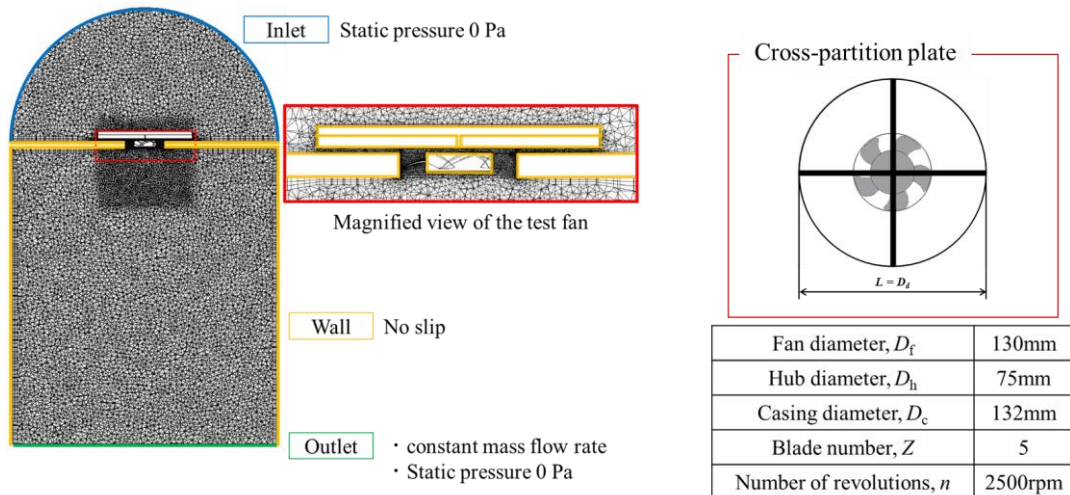


Fig.1 Configuration of test fan/cross-partition plate and typical mesh with boundary condition ($L = D_c$)

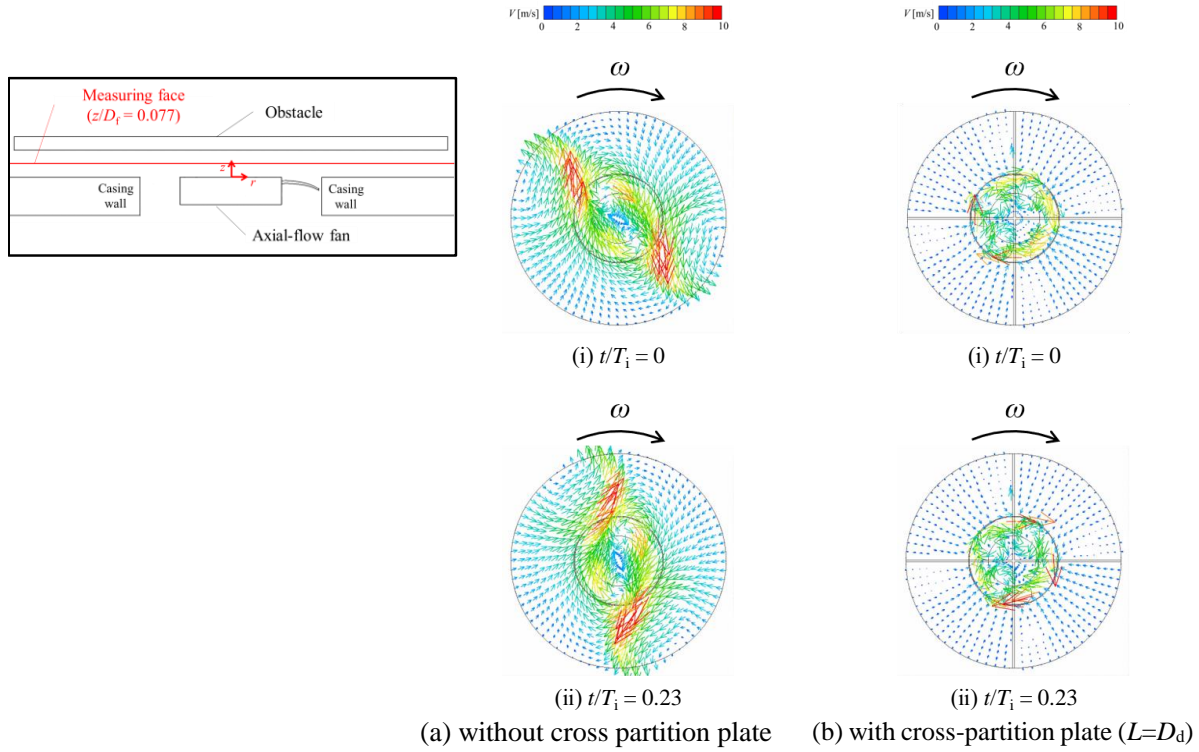


Fig. 2 Example of instantaneous velocity vectors at low flow rate ($\Phi = 0.049$) from CFD ($G = 20\text{mm}$ and $z/D_f = 0.077$)

partition plate and typical mesh with boundary condition for CFD in case of the gap between upstream disk-shaped obstacle and the fan inlet, G , equals 20 mm and the length of cross-partition plate is same as the obstacle diameter ($L = D_d$). The height of cross-partition plate, H , is 14mm. CFD conducted using thermo-fluid simulation software SC/Tetra (MSC Software Corporation) with assuming three-dimensional viscous flow. The governing equation and turbulence model are Reynolds-averaged Navier–Stokes equation and standard $k-\varepsilon$ model, respectively. Boundary conditions were applied as shown in accordance with previous our group study [1, 3]. In CFD calculation, rotating speed of the axial-flow fan was set 2500 rpm constant and number of mesh is approximately 6,000,000. Note that the miscellaneous parts of the axial-flow fan (e.g. struts) were ignored to reduce number of mesh and total calculating time.

Figure 2(a) and 2(b) shows example of instantaneous velocity vectors at low flow rate ($\Phi = 0.049$) from CFD ($G = 20\text{mm}$ and $z/D_f = 0.077$) with and without cross-partition plate ($L = D_d$), respectively. The flow coefficient Φ is calculated from the following formula.

$$\Phi = \frac{Q}{\frac{1}{4}\pi U_{\theta T} (D_f^2 - D_h^2)} \quad (1)$$

Where Q is the flow rate, $U_{\theta T} (=4\pi n D_f / 60)$ is a blade tip circumferential-velocity.

Panels (i) and (ii) show dimensionless time based on propagation period of flow instability of without

cross partition plate, T_i , equal 0 and 0.23, respectively. From panel 2(a)(i) and 2(a)(ii), a counterclockwise vortex pair is observed in outer region of the fan diameter and it propagates circumferentially in same direction of fan rotating. In contrast, in panel 2(b)(i) and 2(b)(ii), the counter-clockwise vortex pair is not seen clearly. In addition, we clarify that pressure difference between inlet and outlet boundaries of the axial-flow fan under same flow rate with the cross-partition plate (Fig. 2(b)) is higher than that without it (Fig. 2 (a)). Furthermore, we also demonstrated these CFD results in the experiment.

These results prove that installing the cross-partition plate at the space between upstream obstacle and the fan inlet is effective to control the flow instability and improve the fan performance.

References:

- [1] Takahashi, M., et.al., “Influence of Obstacles on Flow Characteristics of Axial Flow Fan”, *Journal of Turbomachinery Society of Japan*, **43-6**, 336-347 (2015)
- [2] Kawaguchi, K., et.al., “Flow around Fan Blade and Pressure Fluctuation on Blade Surface of Small Axial Fan with Obstacle near Inlet”, *Journal of Turbomachinery Society of Japan*, **41-12**, 19-29 (2013)
- [3] Nakamura, S., et.al., “Influence of an Upstream Obstacle on the Flow Characteristics of Axial-flow Fans”, *FEDSM2014*, **FEDSM2014-21251** (2014)

Influence of Number of Partition Plates on Performance of Axial-flow Fan with Upstream Obstacle

**Risa Yoshie¹⁾, Takeru Shinohara²⁾, Ryoichi Moriyama³⁾, Koichi Nishibe⁴⁾,
Hiroshi Ohue⁵⁾, and Kotaro Sato⁶⁾**

¹⁾Graduate School of Integrative Science and Engineering, Tokyo City University, Japan
E-mail: g1981051@tcu.ac.jp

²⁾ Graduate School of Integrative Science and Engineering, Tokyo City University, Japan
E-mail: g1881028@tcu.ac.jp

³⁾ Graduate School of Integrative Science and Engineering, Tokyo City University, Japan
E-mail: g1881061@tcu.ac.jp

⁴⁾ Department of Mechanical Engineering, Tokyo City University, Japan
E-mail: knishibe@tcu.ac.jp

⁵⁾ Department of Mechanical Engineering, Tokyo City University, Japan
E-mail: hohue@tcu.ac.jp

⁶⁾ Department of Mechanical System Engineering, Kogakuin University, Japan
E-mail: at12164@ns.kogakuin.ac.jp

Abstract

This paper investigates that influence of the number of the partition plates on improving performance and attenuating flow instability of the axial-flow fans with upstream obstacles by means of computational fluids dynamics (CFD).

Actual usage environment of axial-flow fans is drastically different from an ideal one such as a performance test prior to shipment. Especially, for cooling of heat elements inside of an electronic device, the axial-flow fans are installed inside it. Thus, the axial-flow fans operate with upstream and/or downstream obstacles such as housings and electronic substrates. In addition, the usage environment of axial-flow fans is increasingly severe because those electronic devices have been highly miniaturized in recent years. To date, it has been reported that a performance degradation and generation of flow instability with pressure fluctuation at a low flow rate region in the axial-flow fans with upstream obstacle [1-3], and experimental and numerical studies have begun to improve the performance and control of the flow

instability. To solve this issue, Shinohara et. al. [3] proposed to install a cross-partition plate at the space between upstream obstacle, and succeeds to improve the performance and control the flow instability. However, an optimal design of the cross-partition plate has not been discussed enough for practical use.

As a first step to establish its optimal design, this paper investigates that influence of the number of the partition plates, N , under the constant length of partition plates (same as diameter of disk-shaped obstacle) and the gap between upstream disk-shaped obstacle and the fan inlet ($G = 20\text{mm}$) on improving performance and attenuating flow instability of the axial-flow fans with an upstream obstacle by means of computational fluids dynamics (CFD).

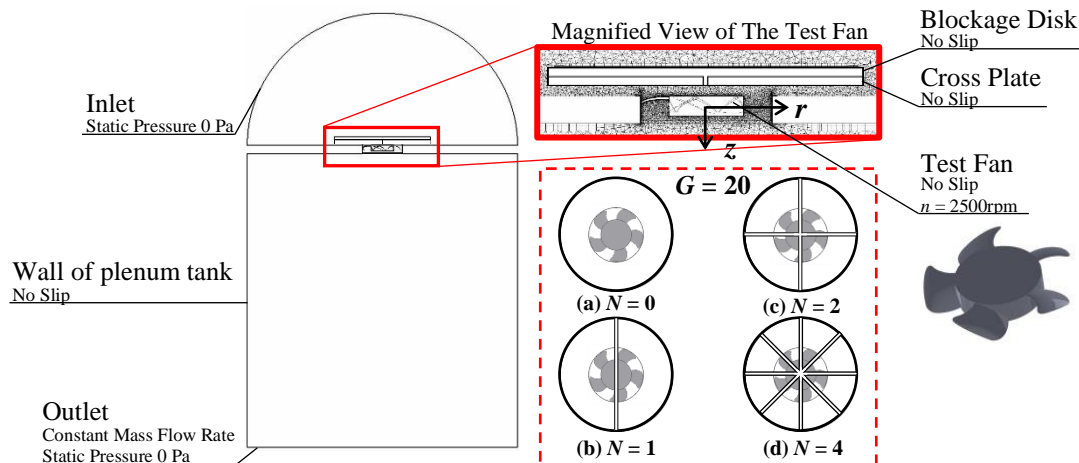


Fig. 1. Calculating domain and boundary condition with the configuration of partition plates.

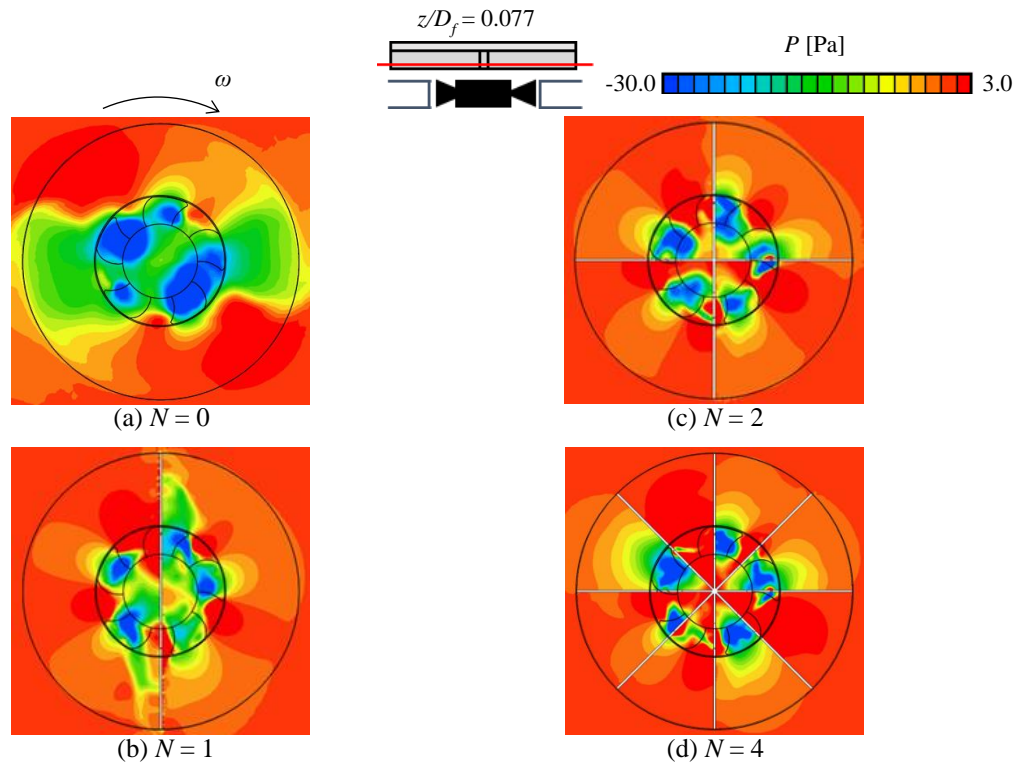


Fig. 2. Example of instantaneous pressure distributions at low flow rate ($\Phi = 0.005$, $G = 20\text{mm}$, $z/D_f = 0.077$)

Figure 1 shows calculating domain and boundary condition, and panels (a)-(d) show the configuration of partition plates for $N = 0$ (no partition plate, with disk-shaped obstacle only), 1, 2 and 4, respectively. CFD is conducted using a commercial simulation code SC/Tetra (MSC Software Corporation) and the flow field is assumed unsteady three-dimensional viscous flow. The governing equation, turbulence model, and boundary condition are same as work of Shinohara et. al. [3]. Rotating speed of the test fan was fixed 2,500 rpm constant and total number of mesh is approximately 6,000,000. Geometry of the miscellaneous parts of the test fan was simplified to save the calculation cost.

Figure 2 shows instantaneous static pressure distributions at the section ($z/D_f = 0.077$) and low flow rate (dimensionless flowrate, $\Phi = Q/\pi U_{T\theta}(D_f^2 - D_h^2) = 0.05$, where, Q is mass flow rate, $U_{T\theta}$ is the blade tip circumferential velocity of the test fan, D_f is the diameter of the test fan, and D_h is the diameter of the hub). Panels (a)-(d) show the results in case of $N = 0$, 1, 2 and 4, respectively. In Fig. 2(a), in addition to low pressure (blue color) regions correspond to position of suction side of blade are observed, flow instability is generated with a pair of low pressure (green color) region, namely number of cell structure equals 2, in outer region of the fan diameter. Furthermore, from the movie observation, the pair of low-pressure region propagates circumferentially in same as the fan rotational direction. On the other hand, in Figs. 2(b)-2(d), although the pair of low-pressure region shown in Fig. 2(a) is not seen, it is observed that the low-

pressure regions generated on suction surface, and they interfere in the partition plates.

Regarding the fan performance, we also conducted CFD and clarify that the pressure difference between inlet and outlet boundaries of the test fan with the upstream obstacle under $\Phi = 0.05$ for $N = 1, 2$ and 4 are higher than that without the partition plate ($N = 0$) but less than that without the obstacle. We assume the reason why the pressure difference is recovered by installing partition plates is that a pre-swirl flow generated at space between fan and obstacle is attenuated by installing partition plates. Accordingly, the difference of angular momentum is increased.

Acknowledgement

I am grateful to M. Shimizu, S. Nakano, and S. Nishiyama – students of Tokyo City University – for their assistance with data processing.

References:

- [1] Takahashi, M., et. al., “Influence of Obstacles on Flow Characteristics of Axial Flow Fan”, *Journal of Turbomachinery Society of Japan*, **43-6**, 336-347 (2015)
- [2] Kawaguchi, K., et. al., “Flow around Fan Blade and Pressure Fluctuation on Blade Surface of Small Axial Fan with Obstacle near Inlet”, *Journal of Turbomachinery Society of Japan*, **41-12**, 19-29 (2013)
- [3] Shinohara, T., et. al., “Influence of Obstacles on Performance Characteristics of Axial Flow Fan”, *the 81th TSJ plenary meeting* (2019)

Numerical Investigation on Unsteady Characteristics of Vortex Tube

Shunsuke Kawamura¹⁾, Ryoichi Moriyama²⁾, Takeru Shinohara³⁾, Koichi Nishibe⁴⁾, and Hiroshi Ohue⁵⁾

¹⁾Graduate School of Integrative Science and Engineering, Tokyo City University, Japan

E-mail: g1981011@tcu.ac.jp

²⁾ Graduate School of Integrative Science and Engineering, Tokyo City University, Japan

E-mail: g1881061@tcu.ac.jp

³⁾ Graduate School of Integrative Science and Engineering, Tokyo City University, Japan

E-mail: g1881028@tcu.ac.jp

⁴⁾ Department of Mechanical Engineering, Tokyo City University, Japan

E-mail: knishibe@tcu.ac.jp

⁵⁾ Department of Mechanical Engineering, Tokyo City University, Japan

E-mail: hohue@tcu.ac.jp

Abstract

We investigated the influence of unsteady flow characteristics such as a vortex periodical oscillation generated in the swirling flows inside of the vortex tube on its performance by conducting a three-dimensional unsteady flow simulation. As the obtained results, we also observe the vortex periodical oscillation similar to the previous study, and discuss the possibility to increase its performance by controlling the amplitude and frequency of vortex periodical oscillation.

A vortex tube is used various products such as a cutting heat removal, molten solder quenching and air-conditioned clothes. Because it has a simpler mechanical structure, no moving parts inside it, than other heat exchangers and needs no refrigerant. The vortex tube separates a compressed air into hot and cold streams simultaneously by the energy separation effect induced by interfering of swirl flows inside the tube. To date, many experimental and numerical studies have been conducted, and they reported the mechanisms of the temperature separation^[1-5], and the

optimization of its geometry to improve the temperature separation efficiency^[1-4]. Recently, Zhang, et al.^[3-4] conducted unsteady calculations using the computational fluid dynamics (CFD) and discussed the relation between the mechanism of the energy transferring and a vortex periodical oscillation in axial-direction of the tube. However, there are still unclear points on the details of relation between unsteady flow characteristics and the energy transferring.

To elucidate those unclear points, we investigated

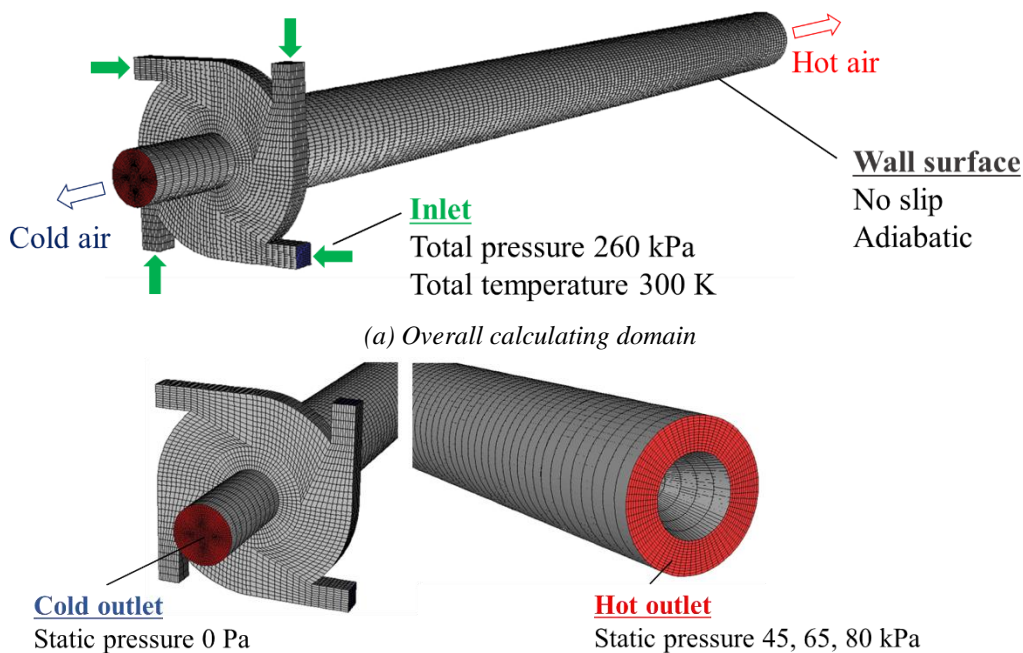


Fig. 1 Typical grids and boundary conditions for CFD.

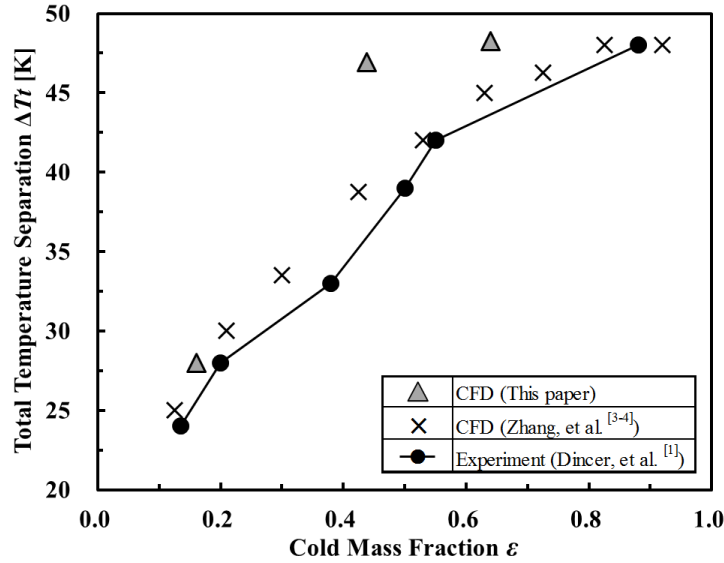


Fig. 2 Relation between total temperature separation and cold mass fraction from CFD.

the influence of unsteady flow characteristics of the swirling flows in the vortex tube on the performance by conducting an unsteady simulation using CFD. As the obtained results, we also observe the vortex periodical oscillation similar to the previous study and discuss the possibility to increase its performance by controlling the amplitude and frequency of vortex periodical oscillation.

Figure 1 shows the typical grids and boundary conditions for CFD. Panels 1(a) and 1(b) show the overall and magnified view around cold and hot outlet, respectively. CFD was conducted using the commercial simulation code ANSYS Fluent 19.1 [6] assuming a three-dimensional compressible viscous flow. The Reynolds-averaged continuity, Navier–Stokes and energy equations with Reynolds stress model (Linear pressure-strain model) and standard wall function [6] are applied as governing equations and the wall treatment in accordance with the work of Zhang, et al. [3-4], respectively. For boundary conditions, Regarding the boundary conditions, constant total pressure with room temperature and atmospheric pressure was set to the four inlet nozzles, and cold outlet, respectively. Instead of installing a control valve near the hot exit, static pressure differences (45,65, and 80 kPa) were set to the hot exit. All of the walls were no-slip and adiabatic condition. Total number of the grids is approximately 250,000 points. To reduce the calculation cost, Non-iterative time-advancement (NITA) scheme which sets number of calculation loops required for the convergence adequately was applied.

Figure 2 shows the relation between total temperature separation, ΔT_t (the difference between cold and hot outlet), and cold mass fraction ϵ ($= m_c/m_{in}$, where, m_c and m_{in} are cold mass flow rate and inlet mass flow rate, respectively) obtained from CFD. ΔT_t and ϵ are the time- and spatial-averaged values. Filled plots denote present CFD results. For reference, the

experimental and CFD results of Dincer, et al. [1] and Zhang, et al. [3-4] also plotted as a circle and cross mark, respectively. The present CFD result indicates ΔT_t increases with increasing ϵ , and it is qualitatively consistent with those previous works. In addition, we also investigated the time variation of the velocity and pressure fields and observed the vortex periodical oscillation in axial-direction of the tube similar to the work of Zhang [3-4]. From these results, our calculation approach is validated.

In this study, we focus the unsteady characteristics of the vortex periodical oscillation. By changing the inlet nozzle pressure with time, the influence of the amplitude and frequency of the vortex periodical oscillation on its performance is discussed.

References:

- [1] Dincer, et al., “Experimental investigation of the performance of a Ranque–Hilsch vortex tube with regard to a plug located at the hot outlet”, *Heat Mass Transfer*, Vol. 44, 367–373 (2008).
- [2] Baghdad, et al., “Numerical study of energy separation in a vortex tube with different RANS models”, *International Journal of Thermal Sciences*, Vol. 50, 2377-2385 (2011).
- [3] Bo Zhang, et al., “Analysis on the fluid flow in vortex tube with vortex periodical oscillation characteristics”, *International Journal Heat and Mass Transfer* Vol. 103, 1166–1175 (2016).
- [4] Bo Zhang, et al., “Analysis of the unsteady heat and mass transfer processes in a Ranque–Hilsch vortex tube: Tube optimization criteria”, *International Journal Heat and Mass Transfer*, Vol. 127,68-79 (2018).
- [5] Mitsuru Kurosaka, Acoustic streaming in swirling flow and the Ranque–Hilsch (vortex-tube) effect *J Fluid Mech*”, Vol. 124, 139-172 (1982).
- [6] ANSYS Fluent–Theory Guide, Release 19.0, ANSYS, Inc., Canonsburg, PA (2018).

Study on improvement of water absorption effect in sipes of studless tire

Hiroto Uchiyama¹⁾, Yukio Nakajima^{2)*}

¹⁾Department of Mechanical Engineering, Graduate School of Engineering, Kogakuin University, Tokyo, Japan
E-mail: am18015@ns.kogakuin.ac.jp

²⁾Department of Mechanical Engineering, Graduate School of Engineering, Kogakuin University, Tokyo, Japan
E-mail: y-nakaji@cc.kogakuin.ac.jp

Abstract

A winter tire with studs had superior braking performance on ice and snow, but it caused the dust pollution by ploughing road if it is not covered by snow or ice. After studded tires were prohibited using in Japan from 1990, winter tires without studs but with many sipes called studless tire was developed in Japan. Sedimented dust decreased as increasing the equipping rate of studless tires. Meanwhile, the traffic accident in winter increased after the introduction of studless tires, because the friction coefficient of ice extremely reduces by the reason that studless tire polishes ice at the intresection. Hence, the increase of friction coefficient between tire and ice is the important subject in the tire industry.

1. Mechanism of friction on ice and objective of the research

The coefficient between tire and ice can be increased by increasing the contact area between tire and ice and by increasing the ploughing effect. (Fig.1) The former goal can be achieved by sipes (narrow grooves in tread) to remove water between tire and ice, and by increasing tread stiffness. The latter goal can be achieved by increasing sipes. In the patent survey, we found that the number of patents on removing water is rare. So the objective of the research is to study the ways to remove water between tire and ice.

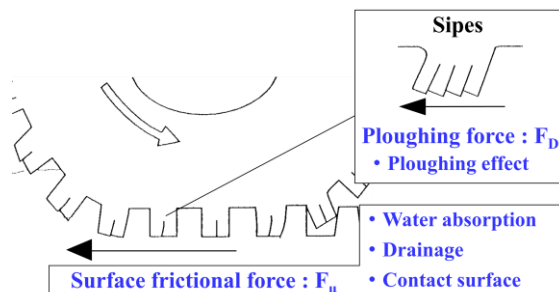


Fig.1. Force that works when driving on snow and ice

2. Contact angle between rubber and ice

The water absorbency is explained by the contact angle θ between water and rubber. If the relation of $\theta < 90^\circ$ is satisfied, the water will be absorbed by sipes. Fig.2 shows the measurement of contact angle between rubber of studless tire and water. Because the measured contact angle is in the range of 100 to 120°, the water absorbency may not be expected by the sipes of studless tire. But we found that the contact angle between rubber and water is less than 90°, if water is partly remained on rubber, as shown in Table.2. Furthermore, if the surface roughness is changed, the contact angle can be changed. So the objective of the research is to find the ways to absorb

water by changing surface roughness.

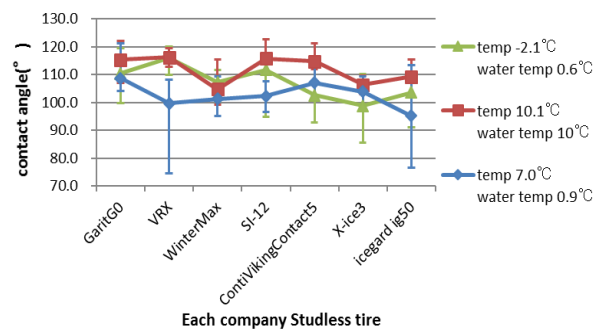


Fig.2. Contact angle between rubber of studless tire and water

Table 1. Contact angle between rubber of studless tire and water, when water is remained on rubber

	Surface condition	Picture to measure contact angle	Contact angle
Smooth			44.4°
Rough			3.6°

3. Water absorption experiment using a sipe with fine grooves

Silicone rubber is used for water absorption experiments. This is because it has high visibility and has the same contact angle as the tire. As shown in Fig.3, molding silicon rubber into a mold that has been finely processed with a laser processing machine, the water surface was moistened as shown in Fig.4. Silicon rubber then a water absorption experiment was conducted with the sipe rubber facing each other as shown in Fig.5. State of the water absorption experiment and the water absorption process of silicon rubber are shown in Fig.6 and Fig.7. From the results of the water absorption experiment, the graph

showing the relationship between the water absorption area and the water retention rate on the surface is shown in Fig.8. The graphs showing the multiple regression analysis and the contribution ratio of each parameter are shown in Fig.9 and Fig.10. These graphs show that the water retention rate can be controlled by the groove width and groove depth,

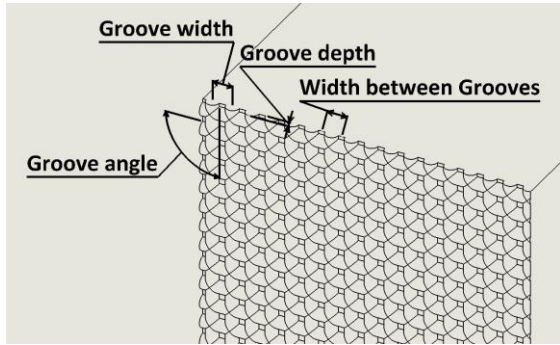


Fig.3. Silicon rubber surface

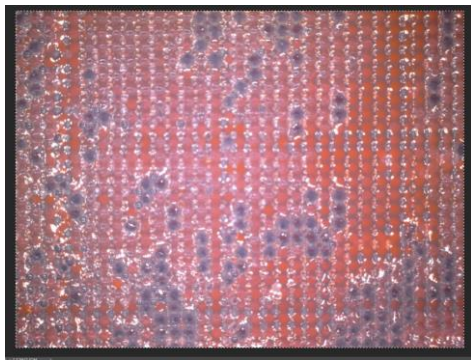


Fig.4. Moistened silicon rubber surface

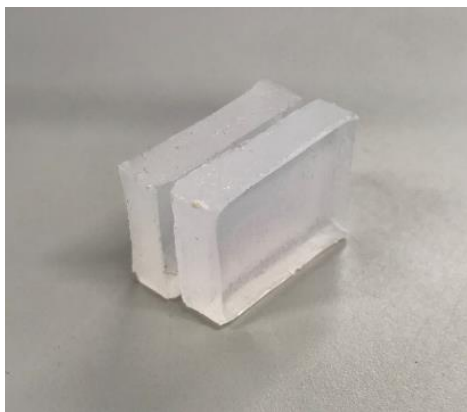


Fig.5. Silicon rubber facing each other

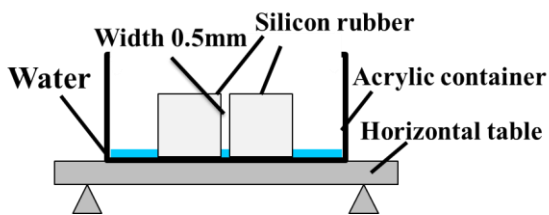


Fig.6. State of Water absorption experiment

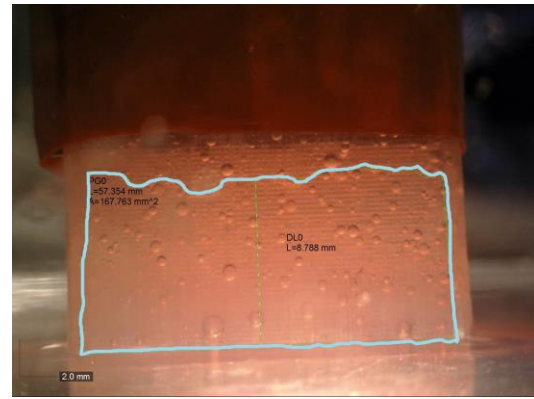


Fig.7. Water absorption process of silicon rubber

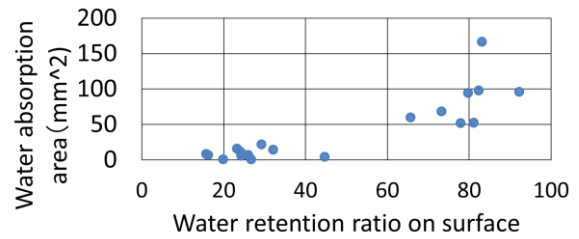


Fig.8. Relationship between water absorption area and water retention ratio on surface

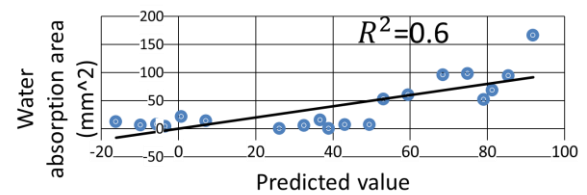


Fig.9. Multiple regression analysis

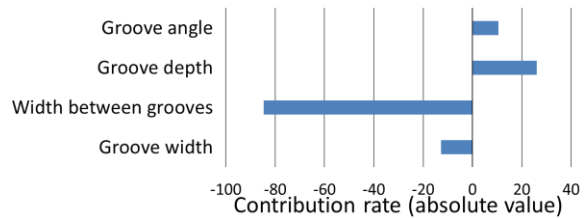


Fig.10. Contribution ratio of four parameters

4. Conclusion

Increasing water absorption in a sipe by adding microscopic surface roughness, the friction on ice may be improved by this new sipe technology.

Development of non-deteriorating lithium-sulfur battery

Kazuki Machida¹⁾, Yusuke Ushioda¹⁾, Tatsuya Kawamura¹⁾, Hibiki Miyauchi¹⁾, Kohei Inaba¹⁾, Yuki Ishino¹⁾, Keitaro Takahashi¹⁾, Masayoshi Watanabe²⁾, Shiro Seki¹⁾

¹⁾Department of Environmental Chemistry and Chemical Engineering, School of Engineering, Kogakuin University, Tokyo, Japan

²⁾Department of Chemistry and Biotechnology, Yokohama National University, 79-5 Tokiwadai, Hodogaya-ku, Yokohama, Kanagawa 240-8501, Japan

¹⁾E-mail: s316068@ns.kogakuin.ac.jp

Introduction

Renewable energy is attracted attention for realization of low-carbon society, and the large-capacity batteries receive strong demands for various usage targets. Energy density of lithium-ion batteries are limited by material properties, such as electrodes and electrolytes. Therefore, the realization of lithium-sulfur (Li-S) batteries, which are one of the next-generation high-performance innovative battery systems, is expected. In general, lithium metal is used as the negative electrode. On the other hand, elemental sulfur (S) is also used as the positive electrode, and it has high theoretical reversible capacity of 1,672 mAhg⁻¹. In addition, the electrode can be prepared at low cost owing to their resource performances. However, effect of Li metal negative electrode is unclear due to their chemical properties with charge/discharge. In this study, we suggest Li-doped negative electrode for suppressing the Li-dendrite. Then, we obtained Li₄Ti₅O₁₂ (LTO) electrode as stable negative electrode, which is strain-free intercalation material, and high reversible characteristics of battery system are expected.

Experimental

To applying LTO for Li-S batteries, electrochemical doping of Li into LTO is required owing to their lack of carrier ion into LTO. Therefore, [Li] electrolyte |LTO] cells were assembled by using disassemble cell, which can be taken out cell

materials without short circuit. After takeoff of Li-doping LTO, lithium (Li-doped) -sulfur battery used SPAN as sulfur positive electrode ([LTO|[Li(SL)₂]TFSA|SPAN] cell) was fabricated. (SPAN:developed non-degraded S positive electrode). Charge / discharge performance of prepared cells were evaluated.

Result and discussion

Fig.1 shows the charge / discharge profiles of prepared cell at 303K. Although operating voltage and capacity are relatively low, reversible charge / discharge were observed. There was no significant capacity fade with charge/discharge, and it suggests the possibility of realizing a non-deteriorating battery.

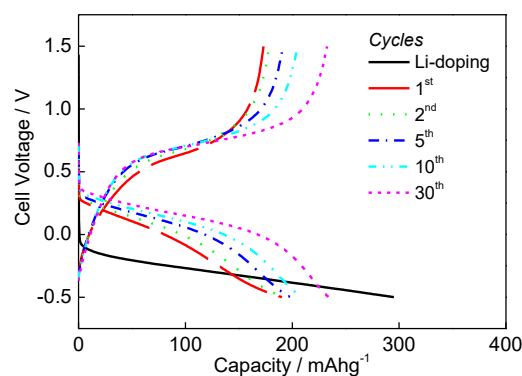


Fig.1 Charge-discharge profile
[LTO] [Li (SL)₂] TFSA|SPAN] cell.

Design of Integrated Converter with Energy Multi-directional Transmissions for Photovoltaic Source Applications

Tsung-His Li, Yu-Hsiang Chen, and Te-Chun Hung

Department of Electrical Engineering, Southern Taiwan University of Science and Technology, Tainan City, Taiwan

E-mail: tchung@stust.edu.tw

Abstract

This paper proposes an integrated converter with energy multi-directional transmissions for photovoltaic source applications as shown in Fig. 1. Since the photovoltaic source is an unstable power supply, so the storage device and the photovoltaic source are usually applied together to support the energy. Therefore, this paper proposes an integrated converter, which can be applied in the photovoltaic source and the storage device at the same time. There are three energy directional transmissions in the proposed circuit. The first, the PV source supplies to DC Bus and the storage device B_1 , when the input voltage is insufficient, the storage device B_1 will support the energy to DC Bus. When there is residual energy in DC Bus, the proposed circuit can also transfer the energy to storage device B_1 . In addition, the feedback mechanism is applied in this paper, and detecting the voltage signal of V_{in} , V_{bus} , and V_{bat} by the feedback system can control the duty cycle of each switches to achieve a stable output voltage. Finally, to validate the feasibility of this proposed circuit, this circuit has been tested in the simulation software under some scenarios. After the simulated tests, the proposed circuit can be referred for photovoltaic system applications.

Keywords: Integrated converter, energy multi-directional transmissions, and photovoltaic source applications.

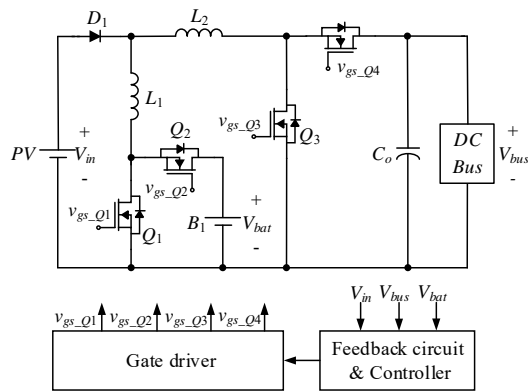


Fig. 1. The diagram of the proposed circuit.

Circuit architecture

The integrated circuit consists of the PV source, the input diode D_1 , the input inductors L_1 , L_2 , power transistors Q_1 – Q_4 , the storage device B_1 , and the output capacitor C_o . There are three operation mode in this proposed circuit architecture, the first mode is multi-directional boost mode, the PV source is used as the input voltage V_{in} , D_1 can prevent the current to flow backward, and the energy is stored in L_1 by Q_1 and Q_2 , the energy is released to storage device B_1 during the next operation state, and controlling the duty cycle of Q_1 and Q_2 stores the energy to L_2 , when the next operation state, the energy releases to DC Bus. The second mode is boost-supporting of the storage device mode. When PV is insufficient to be replaced by the storage device B_1 as power supply, the energy is stored in L_1 and L_2 by Q_2 , Q_3 , and Q_4 , and during next operation state the energy is released to DC Bus. The third mode is buck mode. The residual energy from DC Bus V_{bus} can be transferred to L_1 and L_2 by p Q_2 , Q_3 , and Q_4 , and during next operation state, the energy from L_1 and L_2 will be

transferred to the storage device B_1 .

Experimental result

In order to verify the feasibility of the proposed circuit, the behavior of the proposed circuit is test through the computer simulation software. The first, multi-directional boost mode is simulated and the waveform diagram is shown in Fig. 2, when the input voltage V_{in} is 100 V, the duty cycles of Q_1 and Q_3 are 33% and 50% respectively, the voltage of the storage device V_{bat} can be charged to 150 V, and the voltage of the DC Bus V_{bus} is 200 V.

Then, boost-supporting of the storage device mode is verified by the software and the waveform diagram is shown in Fig. 3. When the voltage of storage device V_{bat} is 150 V, Q_1 always turns on and the duty cycle of Q_3 is 25%, the voltage of DC Bus V_{bus} can be ranged to 200 V.

The last mode is buck mode, the test waveform is shown in Fig. 4. The voltage of DC Bus V_{bus} is 200 V, Q_2 always turns on and the duty cycle of Q_4 is 75%, the voltage of B_1 V_{bat} can be charged to 150 V.

Through the above test data, these three modes of operation can be proved, and the voltage of each device can meet the design of the proposed circuit in this paper.

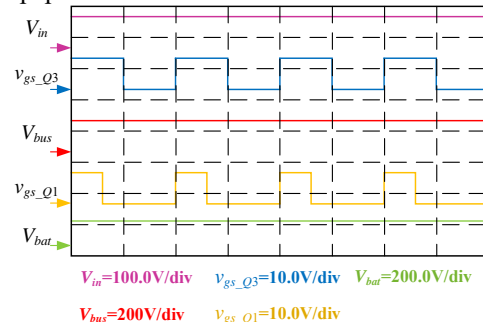


Fig. 2 The waveform diagram of multi-boost mode

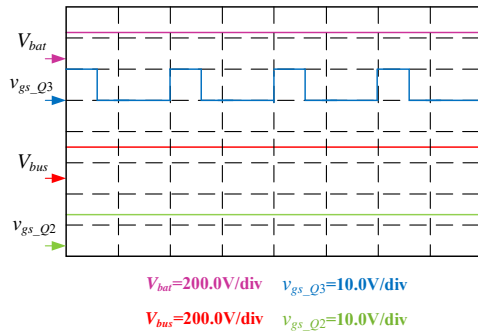


Fig. 3 The waveform diagram of boost-supporting of the storage device mode

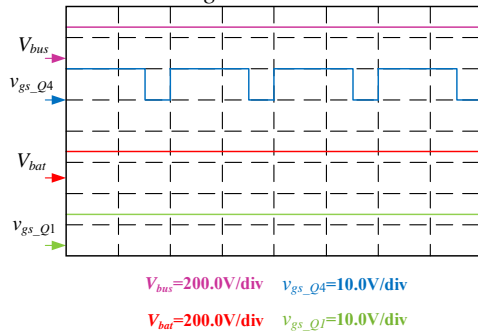


Fig. 4 The waveform diagram of buck mode

Conclusion

This paper has proposed an integrated converter, applying the judgment of the input voltage switches the circuit operation mode; the proposed circuit cannot only improve the cost and size of the circuit, but also achieve the energy multi-directional transmissions. Through the simulated waveform can prove the proposed circuit can achieve stable voltage with energy multi-directional transferring capability. Since this proposed circuit is integrated architecture application, which is provided with the advantages of cost, circuit size and reliability. Therefore, the proposed circuit contributes to the development of the renewable energy industry.

References:

- [1] F. Akar , Y. Tavlasoglu, E. Ugur, B. Vural, and I. Aksoy, "A Bidirectional Nonisolated Multi-Input DC–DC Converter for Hybrid Energy Storage Systems in Electric Vehicles," *IEEE Transactions on Vehicular Technology*, vol. 65, No. 10, pp. 7944-7955, Oct. 2015.

Development of the residual ammonia removing system in hydrogen generation from ammonia

Kana Hatori¹⁾ and Takashi Saika¹⁾

¹⁾Mechanical Engineering, Graduate School of Engineering, Kogakuin University, Tokyo, Japan
E-mail: am18053@ns.kogakuin.ac.jp

Abstract

In recent years, global warming has become one of the biggest problems in the world. The main reason is increasing the greenhouse gasses. Hydrogen is expected to reduce the amount of greenhouse gasses included carbon dioxide. Hydrogen used as energy source of fuel cell does not emit greenhouse gasses because of no carbon atoms. Whereas, it has problems such as storage and transportation. Thereby Ammonia is also anticipated as the energy source recently and we constructed the hydrogen generation system with ammonia as the hydrogen carrier. When ammonia is thermally decomposed, the low concentration of ammonia remains. However, it has been found out that the low concentration of ammonia causes decreasing the efficiency of fuel cell. Therefore, in this study, we will develop the device to remove remained ammonia in decomposition air.

1. Introduction

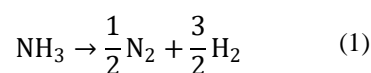
In recent years, the environmental problems including global warming are concerned in the whole world. The mainly cause is the increasing the greenhouse gasses, we have to solve these problems immediately.

Hydrogen is lately attracted to considerable attention as the clean energy. When hydrogen is used as the energy source, it generates just water and heat. On the other hand, it needs energy to liquefy to transport and store. We focus on ammonia and consider the hydrogen generation system taken off ammonia. When ammonia decomposes with heat, the little amount of ammonia remains in the decomposition air. It has been found out that the residual ammonia concentration of more 0.1 ppm in the decomposition air causes decreasing in output of fuel cell by the catalyst electrode poisons. In this research object is to remove the low concentration ammonia.

2. Ammonia characteristic

Ammonia is composed of hydrogen and nitrogen and the colorless gas with the pungent smell. It is easier to transport and store than hydrogen. As the ammonia liquefies under the conditions at 0.84 MPa at a temperature of 20°C, it can be easier to transport and store than hydrogen. Hydrogen liquefies at -253°C or high pressure. Since NH₃ has a hydrogen content of 17.8 wt% and is equivalent to or higher than propane and ethanol, which are carbon compounds containing other hydrogen, a large amount of hydrogen can be extracted from ammonia. By contrast, it is dangerous to handle because of poisonous.

3. The hydrogen supply system from ammonia



Thermal decomposition of ammonia with catalyst is shown this chemical formula.

The hydrogen supply system made from ammonia is shown as Fig. 1. To produce hydrogen from ammonia as Fig. 1, ammonia is needed to heat with the catalyst (metal catalyst of ruthenium and base metals Ni or Fe) at the appropriate temperature of 700 to 800°C. On the other hand, it has found out that 300 ppm ammonia remains in the decomposition air, the dissociated gas is supplied to the fuel cell after removing the low concentration ammonia.

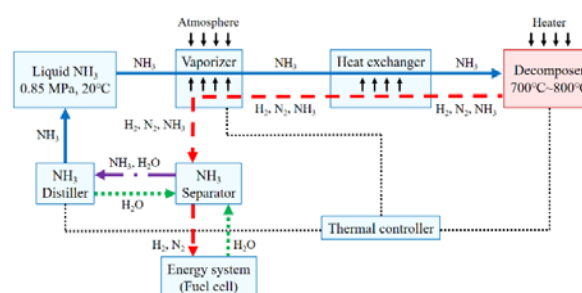


Fig. 1 The hydrogen supply system from ammonia

4. Ammonia removal experiment and consideration

The experiment device is equipped with the diffuser tube. This tube plays the role to makes the ammonia in the experimental gas easier to melt in the water.



Fig.2 The experiment device

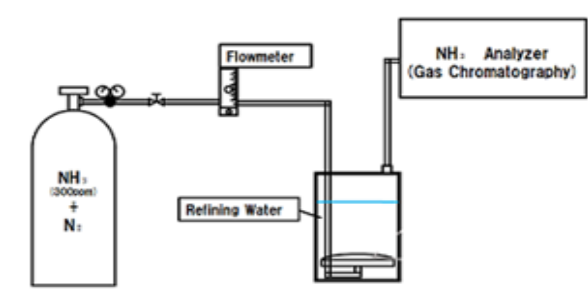


Fig. 3 The experimence oerview

In the previous research, the residual concentration rate was 300 ppm when ammonia decomposed at 800°C. The nitrogen gas that used on this research contains 300 ppm ammonia^[1]

The amount of ammonia is 0.0048 L/min in the experiment gas with the flow rate at 16 L/min. It assumes that ammonia of 0.0018 mol remains in only water during 8 minutes 16 seconds to detect ammonia. Therefore, the neutralization reaction experiment was conducted with the same amount of acid substance (0.0018 mol).

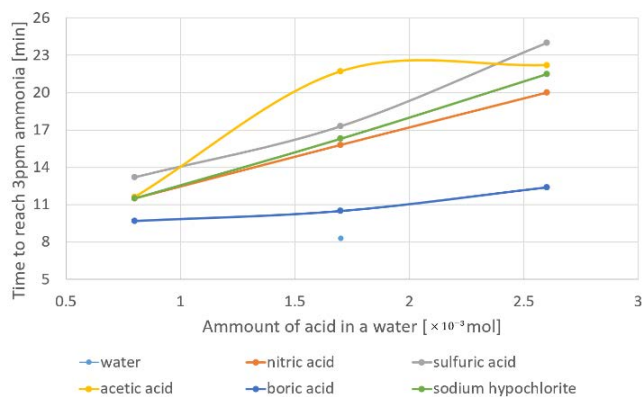


Fig. 4 Time to detect 3ppm ammonia

The time to detect ammonia with acids extends compared to the water. These extends approximately twice experiment with only water. As sulfuric acid and boric acid which are strong acid completely ionize to water, ammonia ion reacts with each negative ion in the solvent. It presumed that it is connected to extend the time to detect ammonia.

The result with boric acid is shorter than other acid. It assumes that the amount of boric acid input doesn't completely ionize.

5. Conclusion

In this experience it is found out that the strength of acid effects the extending the removal ammonia time. The most effective acid to ammonia is sulfuric. The further experiment will be conducted with dry adsorbent. We are going to make the compact and light device such as a cart vehicle with the mixture acid water and dry adsorbent based on those experiment.

References:

- [1] Takashi Saika, Tetsuo Nohara, Yuji Aoki, Hiroshi Mitsui, Yosuke Saito, Masato Iwami, International Journal of Energy for a Clean Environment, **10**(1-4), 1-13 (2009).

Optical Characterization under Different Annealing Temperature by Sputter System Grow Ga₂O₃ Film Hon Kuan* and Sheng-Hsiung Chang

Department of Electro-Optical Engineering, Southern Taiwan University of Science and Technology, Taiwan

*Corresponding author e-mail: hkuan@stust.edu.tw

Abstract

In this study, Ga₂O₃ thin film were prepared on sapphire substrates by RF magnetron Sputter system. and we observed the Ga₂O₃ thin film layers characteristics of emission by Photoluminescence measurement.

At first, Ga₂O₃ thin film grow on sapphire substrates, we have three layer of thickness, 100nm, 200nm and 300nm, respectively. And then, in the annealing procedure in oxygen gas and different process temperature(400°C~ 800°C). At the analytical profile of X-ray Diffraction, we can found that the peak an increase, and the FWHM is narrowed gradually as Figure 1. It's meant that the quality of these thin film are better. The results of Photoluminescence indicated that emission wavelength are location at 400nm, 480nm and 620nm as Figure 2. And the intensity of emission peaks are increasing with the thickness. But after annealing program, peaks intensity are decreased with annealing temperature increase, especially in the oxygen environment. This is further proof that the main factor emission light of Ga₂O₃ thin film is come from own defect.

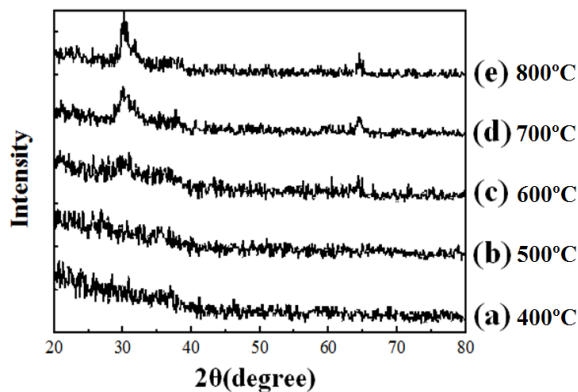


Fig.1 Gallium oxide films of different annealing temperature XRD spectrum

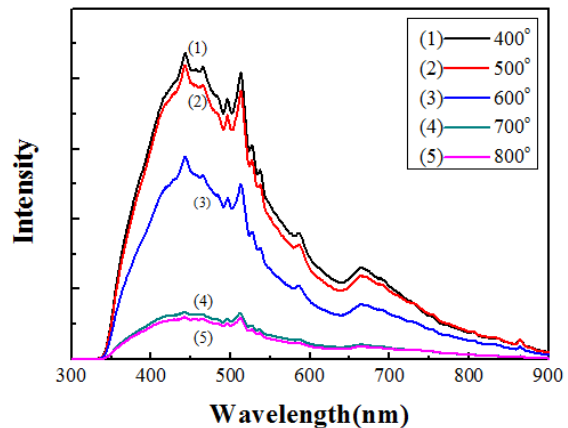


Fig.2 . Gallium oxide films of different annealing temperature Photoluminescence

References:

- [1] 马海林, 苏庆, 兰伟, 刘雪芹兰州大学物理学院, 甘肃兰州, 氧流量对热蒸发 CVD 法生长 β -Ga₂O₃ 纳米材料的结构及发光特性的影响(<http://www.paper.edu.cn>).
- [2] 郭豐榮。鋁銻氧化物光電特性之研究, 南臺科技大學光電工程研究所, 碩士論文(2011)。
- [3] 賴鈞偉。矽基及氮化鎵發光二極體材料之研究, 南臺科技大學光電工程研究所, 碩士論文(2014)。
- [4] 張世育。矽量子點鑲嵌在氮化矽薄膜之合成與光學性質研究, 中華大學電機所光電組, 碩士論文(1996)
- [5] RUI SUN, GUI-GEN WANG, HUA-YU ZHANG, JIE-CAI HAN, XIN-ZHONG WANG, LIN CUI, XU-PING KUANG, CAN ZHU, LEI JIN, ELSEVIER. JOURNAL OF ALLOYS AND COMPOUNDS 580(2013) 517-521.
- [6] J. B. VARLEY, J. R. WEBER, A. JANOTTI, AND C. G. VAN DE WALLE APPLIED PHYSICS LETTERS 97, 142106 (2010).

GaAs-Based p-i-n Band-Pass Near-Infrared Photodetector Grown by Metal-Organic Chemical Vapor Deposition

Y. X. Xu, C. K. Wang, and Y. Z. Chiou

Department of Electronic Engineering, Southern Taiwan University of Science and Technology, Tainan, Taiwan
E-mail: ckwang@stust.edu.tw

Abstract

In this study, GaAs-based p-i-n band-pass near-infrared photodetectors (PDs) grown by metal-organic chemical vapor deposition (MOCVD) were fabricated and investigated. It was found that the photo current of band-pass PDs was higher than that of original PD. And, it can be obviously observed from the spectral responsivity that the band-pass characteristics of PD can be efficiently achieved by inserting a p-type $\text{Al}_{0.1}\text{Ga}_{0.9}\text{As}$ absorbed layer.

It is well known that near-infrared optical device demand has grown significantly in recent years. Its scope of applications includes safety monitoring [1], biometric systems [2], digital medical [3], and vehicle application [4]. The near-infrared PDs usually use the GaAs-based material, which has high mobility, high electron saturation velocity, and direct bandgap feature. Moreover, the p-i-n structure PD has a less dark current level compared to the metal-semiconductor-metal (MSM) PD. In previous studies, the p-i-n GaAs-based PDs have already been discussed for a long time [5-7]. However, the discussion of band-pass type GaAs-based PDs is still absent, especially using the semiconductor film to be the filter.

In this study, the band-pass GaAs-based PDs grown on GaAs substrate by MOCVD were fabricated and investigated. The original PD consists of a 0.5- μm -thick GaAs buffer layer, a 2- μm -thick n-type GaAs layer, a 3- μm -thick un-doped GaAs layer, and a 50-nm-thick p-type GaAs layer. Furthermore, the fabrication of band-pass PD was based on the processing of original PD, but we inserted p-type $\text{Al}_{0.1}\text{Ga}_{0.9}\text{As}$ absorbed layer between 3- μm -thick un-doped GaAs layer and 50-nm-thick p-type GaAs layer as the "filter layer". After processing, the fabricated PDs were all mounted onto the TO-39 metal can packages.

Figure 1 shows the dark current of these two devices. It was found that the dark currents of the original and band-pass PDs were 4.32×10^{-11} and 1.02×10^{-6} A at -5 V, respectively. Figure 2 shows the photo current of these two devices. It can be seen that the photo current of band-pass PDs was higher than that of original PD. Furthermore, the photo to dark current ratios (PDCR) of the original PD and the band-pass PD at -5 V were 2.26×10^4 and 1.23×10^1 , respectively.

Then, the spectral responsivity measurements by a HORIBA/JOBIN YVON/SPEX TRIAX 320 system were performed with a 150 W halogen lamp light source and a standard synchronous detection scheme. Figure 3 shows the responses of the original and band-pass PD. It can be obviously observed from the

spectral responsivity that the band-pass characteristics of PD can be efficiently achieved by inserting the "filter layer", which has a very narrow full-width half maximum (FWHM) of 79 nm. Moreover, the highest responsivities of the original and band-pass PD are 0.159 (at 866 nm) and 0.397 (at 850 nm) A/W, respectively. And, the highest external quantum efficiency (EQE) of band-pass PD was 58.01%, which was higher than that of the original PD of 22.76%.

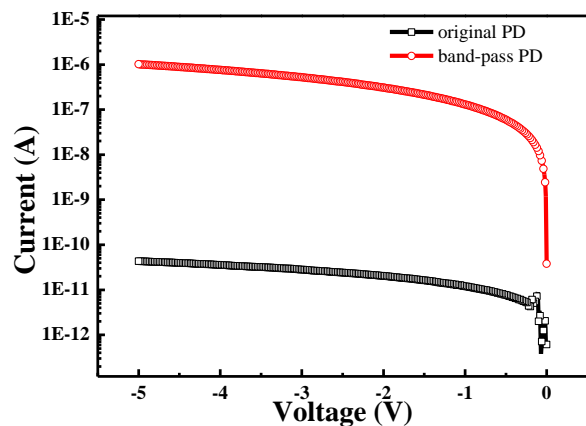


Fig. 1 The dark current of the photodiode

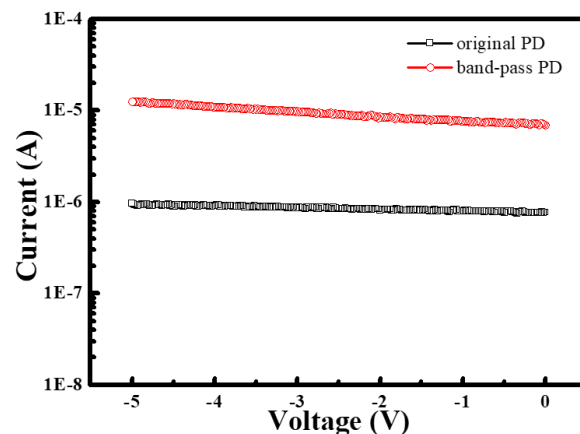


Fig. 2 The photo current of the photodiode

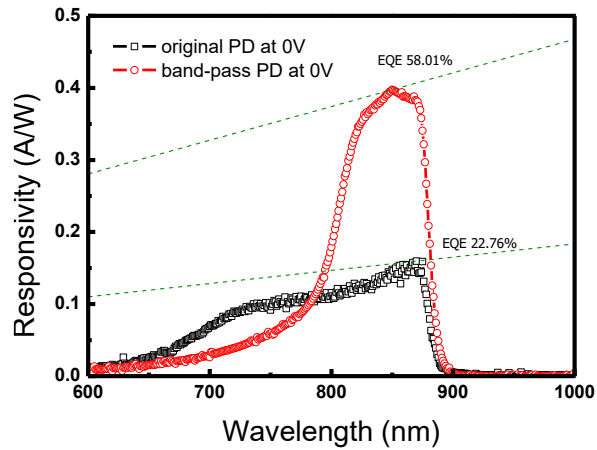


Fig. 3 The responsivity of the photodiode

References:

- [1] Jonsson P, Casselgren J, and Thornberg B, *IEEE Sens. J.*, 3, 1641–1656 (2015).
- [2] S. Crihalmeanu and A. Ross, *Pattern Recognition. Lett*, 33, 1860–1869 (2012).
- [3] Kiening KL, Unterberg AW, Bardt TF, Schneider GH, Lanksch WR, *JNeurosurg*, 85, 751-757 (1996).
- [4] M. Fukuzawa, H. Hama, N. Nakamori, and M. Yamada, *Proceedings of 11th International Conference on Computer and Information Technology*, 516-520 (2008).
- [5] Meng-Chyi Wu, Yun-Hsun Huang, and Chong-Long Ho, *IEEE Electron Device Lett*, 9, 797-799 (2007).
- [6] B. Bouabdallah, Y. Bourezig, and B. Benichou, *Microelectron. Reliab*, 3, 447-453 (2010).
- [7] Yi-Jen Chiu, Siegfried B. Fleischer, and John E. Bowers, *IEEE Photonics Technol. Lett*, 7, 1012-1014 (1998).

GaN-based Solar Devices featuring Mn-related Intermediate Band Absorption

Kuan-Ting Chen ²⁾, Feng-Wu Lin ¹⁾, Po-Cheng Chen ²⁾, Jinn-Kong Sheu ²⁾, and Ming-Lun Lee ^{1)*}

¹⁾Department of Electro-Optics Engineering, Southern Taiwan University of Science and Technology, Taiwan
E-mail: minglun@stust.edu.tw

²⁾Department of Photonics, National Cheng Kung University, Tainan 70101, Taiwan

Abstract

In this work, we investigate the characteristics of GaN-based solar cells with manganese(Mn)-doped GaN/AlGaIn absorption layers. The Mn-doped devices exhibit a higher conversion efficiency compared to the devices without Mn doping in the absorption layer. This increase in conversion efficiency is attributed to the fact that the Mn-related energy states cause below bandgap photon absorption and thereby contribute an additional photocurrent. According to the electroluminescence spectra and the spectral responses obtained from the Mn-doped devices, it is shown that the Mn-related energy states form a partially filled intermediate band (IB) within the bandgap of the Al_xGa_{1-x}N layer.

The concept of intermediate band solar cells (IBSCs) has been proposed to improve the efficiency of solar cells [1-2]. In this study, we demonstrate that GaN solar cells with Mn-doped GaN/AlGaIn absorption layers exhibit up-conversion property through the Mn-related IB in the forbidden bandgap. GaN-based solar cells with Mn-doped GaN/AlGaIn absorption layers grown by MOCVD were presented. Fig. 1 showed the structures of samples used in this study.

To clarify whether the IB-related transitions exist in the fabricated devices or not, a series of optical characterizations, including spectral response and electroluminescence, were conducted. In addition, solar parameters were also obtained from the photovoltaic cells, as shown in Table I. Although the Mn-doped devices exhibited a relative lower open-circuit (V_{oc}), the photocurrent density and hence the conversion efficiency were markedly higher than those of reference devices (i.e., without Mn doping in the absorption layer). This increase in photocurrent was attributed to the fact that IB-related transitions resulted in the below bandgap absorption, that is, the up-conversion phenomenon. As shown in Fig. 2(a), a typical EL spectrum taken from the Mn-doped devices under forward bias (at 100 mA) could indirectly evidence this contention. In other words, a broad band peaked at 620 nm, and a long-wavelength shoulder peak at 850 nm could be tentatively attributed to the electron transitions involving Mn-related states within the bandgap of the GaN absorption layer. Fig. 2(b) displays a schematically band diagram of GaN with IB resulting from Mn doping. Spectral responses taken from the Mn-doped devices showed the below band absorption, while the reference devices do not exhibit the below band absorption, shown in Fig. 2(c)

In light of the EL and response spectra, the 620 nm-centered emission band was attributed to the transition between the Mn-related IB and the CB. The 850 nm-centered emission band was attributed to the transition between the Mn-related IB and the VB.

In summary, the preliminary results of this study demonstrated the feasibility of Mn-doped GaN-based materials as absorption layers applied to IBSC. The EL spectrum and spectral response have preliminarily evidenced the presence of Mn-related IB in the Mn doped Al_xGa_{1-x}N layers. Under AM1.5G solar simulator, a prominent increase in the photocurrent density and hence an enhancement of power conversion efficiency was obtained from the GaN/AlGaIn solar cells with with absorption layer.

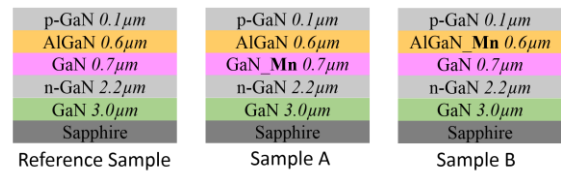


Fig. 1 Schematic layer structures used in this study.

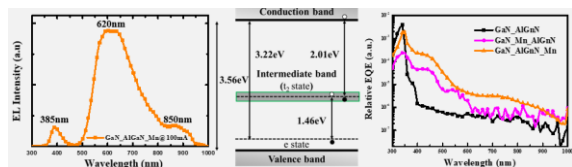


Fig. 2. (a) typical EL spectrum of the sample A ;(b)schematic band diagram of GaN with IB; and(c)typical spectral responses taken from the fabricated solar cells.

Table I. Typical V_{oc} , J_{sc} , FF, and conversion efficiency of the fabricated solar cells measured under one-sun AM1.5G standard testing condition.

Device	V_{oc} (V)	J_{sc} (mA/cm ²)	FF (%)	η (%)
GaN/AlGaIn	2.26	0.0018	74.148	0.00372
GaN _{Mn} /AlGaIn	2.20	0.0054	40.477	0.00523
GaN/AlGaIn _{Mn}	1.92	0.0378	36.351	0.02663

References:

- [1] A. Luque, "Increasing the Efficiency of Ideal Solar Cells by Photon Induced Transitions at Intermediate Levels", Phys. Rev. Lett, Vol. 78, pp 5014-5017, 1997.
- [2] A. Martí, "Production of Photocurrent due to Intermediate-to-Conduction-Band Transitions A Demonstration of a Key Operating Principle of the Intermediate-Band Solar Cell", Phys. Rev. Lett, Vol.97, pp 247701, 2006.

LED miniaturization for monolithic μ -LED using ICP etching

Shoma Takeda¹⁾, Tomohiro Yanaguchi¹⁾, Takeyoshi Onuma¹⁾, and Tohru Honda¹⁾

¹⁾ Department of Electronic Engineering and Electronics, Kogakuin University, Japan
E-mail:cm19031@ns.kogakuin.ac.jp

Abstract

LED miniaturization to fabricate of monolithic μ -LED arrays was demonstrated by etching the LED wafer using the inductively-coupled-plasma (ICP) etching method. The ICP etching was conducted using chlorine, boron trichloride, and argon gases with a mixture ratio of 9:1:2. Surface SEM and cathodoluminescence (CL) mapping images confirmed that the etching depth was enough to isolate the whole LED structure.

Introduction The GaN based light-emitting-diodes (LEDs) have already been employed in various applications such as solid-state lighting and backlight unit of liquid-crystal-display (LCD) due to their characteristics such as long life-time, high-luminous-efficiency, high-contrast, and high-response-time [1]. The LED based display leads reduction of power consumption by eliminating the polarizing plate in LCD, and it is used as large size displays in outdoor since LED has better luminous efficiency than the organic light-emitting-diode (OLED). Realization of LED based display is a challenging issue, but huge expansion of LED market is expected since it has potential for applications such as wearable watches, mobile phones, smart glass, and virtual-reality devices [2]. One of the technical issues is to miniaturize LED size down to micrometer-scale (μ -LED) to develop high-definition display [3]. The inductively-coupled-plasma (ICP) etching method has already been widely used to fabricate GaN based LEDs and laser diodes due to its relatively high etching rate, highly anisotropic profile, and less etching damage compared to the other dry etching methods [4].

In this study, miniaturization of LED and fabrication of monolithic μ -LED arrays are demonstrated by etching the LED wafer using the ICP etching method.

Experiment The LED wafers consist of p-GaN (100 nm) / GaInN MQWs (total thickness of 100 nm) / n-GaN (1 μ m) / i-GaN (2.5 μ m). The structures were grown on *c*-plane sapphire substrates by MOVPE. A 200-nm-thick nickel film was deposited on the LED wafer using the electron-beam evaporation. It was then patterned by photolithography followed by wet etching using nitric acid. The ICP etching was conducted using chlorine, boron trichloride, and argon gases with a mixture ratio of 9:1:2 and total flow rate of 30 sccm for 3 min. The ICP and RF power were set to 300 and 200 W, respectively. The etched LED wafers were characterized by spatially-resolved cathodoluminescence (CL) equipped with a scanning electron microscope (SEM) and stylus profiler measurements.

Results and Discussion Surface SEM and CL mapping images of etched LED wafer are shown in

Figs. 1(a) and 1(b), respectively. Duration of 3 min. reached an etching depth of 2.79 μ m. Removal of by-product and subsequent flat etching surface was implemented effectively by using the chlorine, boron trichloride, and argon gas mixture, resulting in a relatively high etching rate of 0.93 μ m/min by changing in etching gases ratio. This led us to stop the etching uniformly at the i-GaN layer. Indeed, CL with a wavelength of 457 nm was only observed on the mesa structures of LED array. The measurements confirm the etching depth is enough to isolate the whole LED structure. Present results ensure further miniaturization of LED size.

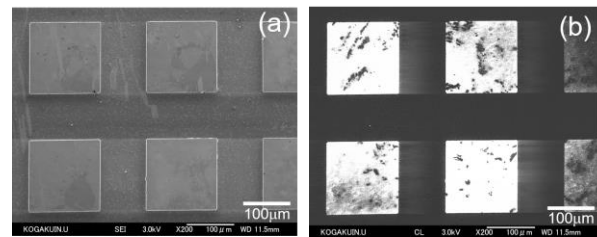


Fig. 1. (a) Surface SEM and (b) CL mapping images of etched LED.

Acknowledgement

The authors would like to thank Dr. T. Takahashi and Dr. M. Shimizu of National Institute of Advanced Industrial Science and Technology for the LED furnishing. This work is supported in part by Takahashi Industrial and Economic research Foundation.

Reference

- [1] Z. J. Liu *et al.*, IEEE Photonic. Tech. Lett. **25**, 13 (2013).
- [2] T. Wu *et al.*, Applied Sciences **8**, 9 (2018)
- [3] H.-Y. Lin *et al.*, Photonic Research **5**, 411 (2017).
- [4] R. J. Shul *et al.*, Appl. Phys. Lett. **69**, 1119 (1996).

Structural characterization of epitaxial GaInN films by X-ray diffraction

Hiroki Hirukawa, Ryosuke Yoshida, Tomohiro Yamaguchi, Takeyoshi Onuma, and Tohru Honda

¹⁾Department of Electronic Engineering and Electronics, Graduate School of Engineering, Kogakuin University, Japan

E-mail: cm19039@ns.kogakuin.ac.jp

Optical wireless power transmission (OWPT) is an innovative technology to supply electricity with a simple set up including light source and photovoltaic receiver such as a solar cell^[1]. GaInN-based blue laser diode (LD) and light-emitting diode (LED) are promising candidates for light sources in the OWPT system since the blue light contributes to increase an output open-circuit voltage. To suppress a Stokes-loss in the system, GaInN-based photovoltaic receiver is suitable to receive the blue light. GaInN is an alloy semiconductor of InN and GaN with bandgap energy of about 0.7 and 3.4 eV, respectively. Accordingly, bandgap energy of GaInN alloy can be controlled between 0.7 and 3.4 eV by tuning the In composition. It has been reported that GaInN with In composition of 20% is suitable for the photovoltaic receiver with high absorption sensitivity in blue light^[2].

GaInN films have typically been grown on GaN/sapphire templates because of the unavailability of bulk GaInN substrates in the market. However, the hetero-epitaxial growth of GaInN on the GaN template causes the plenty of crystal defects due to the lattice mismatch between GaInN and GaN, although the GaInN film thicker than the critical thickness is essential to sufficiently absorb the blue light in OWPT system.

In this study, GaInN films with a thickness of 0.4 μm , which is beyond the critical thickness, were epitaxially grown on GaN/sapphire templates by radio-frequency plasma-assisted molecular beam epitaxy (RF-MBE). The structural characterization including crystal defects of GaInN films was performed using X-ray diffraction (XRD) measurements.

GaInN films were grown on GaN/sapphire templates at different temperatures between 520 and 720°C by RF-MBE. The samples were evaluated by XRD reciprocal space mapping (RSM) measurements to calculate the In composition and relaxation ratio from the GaInN diffraction peak position^[3]. The samples were also evaluated by symmetric X-ray rocking curve (XRC) measurements to calculate the screw type threading dislocation density (screw TDD), which is one of crystal defects, from the full width of half maximum (FWHM) values of the diffraction peaks^[4].

Figure 1 shows the relaxation ratio and In composition as a function of growth temperature. As can be seen in Fig. 1, GaInN films with In compositions of about 25% were obtained at the growth temperatures between 520 and 700°C. The In

composition was decreased at the growth temperatures above 700°C. This is due to desorption of nitrogen at high temperatures. Correspondingly, the relaxation ratio of GaInN decreased increasing growth temperatures.

Figure 2a shows Williamson-Hall plot obtained from the FWHM values of the diffraction peaks corresponding to (000*l*) planes with $l = 2, 4$ and 6. The slope of the fitted straight line in each sample corresponds to the tilt value α . The correlation between screw TDD ρ_s and tilt value α is given by

$$\rho_s = \frac{\alpha^2}{4.35b^2} \quad (1)$$

where $|b|$ is the magnitude of the Burgers vector corresponds to the lattice constant of GaInN in c axis.

Figure 2b shows the screw TDD as a function of growth temperature. As can be seen in Fig. 2b, the screw TDD decreased with increasing the growth temperatures up to 720°C. The screw TDD with $3.0 \times 10^9 / \text{cm}^2$ was estimated in GaInN films grown at 720°C.

These indicate that XRD is a powerful tool to evaluate structural characterization of epitaxial GaInN films. In order to fabricate GaInN-based OWPT photovoltaic receiver, more than one order of magnitude reduction of the screw TDD in GaInN films is necessary.

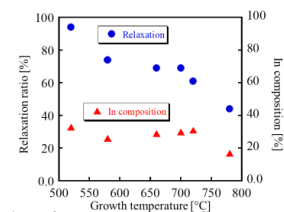


Fig. 1. Relaxation ratio and In composition as function of growth temperature.

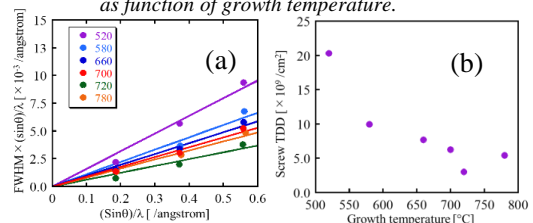


Fig. 2. (a) Williamson-Hall plot obtained from symmetric XRC. (b) Screw TDD as function growth temperature.

References:

- [1] Y. Katsuta and T. Miyamoto, *Jpn. J. Appl. Phys.*, **57**, 08PD01 (2018).
- [2] S. Valdueza-Felip *et al.*, *Sol. Energy Mater. Sol. Cells*, **160**, 355 (2017).
- [3] S. Pereira *et al.*, *Appl. Phys. Lett.*, **80**, 3913 (2002).
- [4] T. Metzger *et al.*, *Phys. Stat. Sol. (A)* **176** (1999) 391.

Ultraviolet–visible absorption and photocatalytic properties of TiO₂ thin film on titanium substrate via ultrasonic mechanical coating process

Jian-Yu Chen^{†,1)}, Jin-Fu Chen,²⁾ and Chang-Ning Huang^{*,1)}

¹⁾Department of Chemical and Materials Engineering, Southern Taiwan University of Science and Technology, Tainan, Taiwan

E-mail: ma840104@stust.edu.tw

²⁾ Metal Industries Research & Development Centre, Kaohsiung, Taiwan

E-mail: huck2000@ms47.hinet.net

*Corresponding author's e-mail: cnhuang@stust.edu.tw

Abstract

In this study, the TiO₂ thin film was synthesized on titanium substrate by ultrasonic mechanical coating. Such thin film has extraordinary absorption on visible spectrum, and photocatalytic properties under Xenon lamp irradiation. It is about 3.5 μm thickness from the cross-sectional image of the SEM. The XRD illustrated the peaks from rutile or anatase, which depend on the phase of initial powders, and titanium substrate. The Raman shows the broadening peaks of rutile or anatase-type vibration modes. In addition, the extra multiple tiny unknown signals were observed in Raman spectra. This research shed light on a new low cost, short reaction time and high performance coating technique for photocatalytic and photoelectrochemical applications.

Photocatalytic activities of TiO₂ is always a crucial issue for scientific communities. However, it has some drawbacks because of the large band gap (3.0–3.2 eV), which allows light absorption only in the UV region (only 5% of solar spectrum). Black TiO₂ was usually obtained via hydrogenation at high pressure and high temperature. Modified TiO₂ (black TiO₂) nanoparticles (NPs) produced by different methods showed enhanced visible light absorption than ordinary white TiO₂ NPs. This research focused on the new synthetic route of TiO₂ thin film via ultrasonic mechanical coating technique. Commercial Ti was chosen as the substrate material and TiO₂ powders of anatase and rutile phases with average powder size around 44 μm (325 mesh) were used in the ultrasonic mechanical coating process. Such TiO₂ powders were being mixed with ethanol to form a suspension solution, and then spread onto the substrates. The vibration generator was powered by a piezoelectric motor and high-amplitude oscillations of the resonator was applied under a fixed vibration frequency of 20 kHz and vibration amplitude of 45, 60 and 80 μm, resulting in an acceleration of the stainless steel balls (1~3mm in diameter) to initiate their chaotic motion inside the chamber. The bombardment of the stainless steel balls produced strong impacts on the substrate surface. The TiO₂ powders around 44 μm in diameter would be broken to smaller sizes and inserted into the substrates during the ultrasonic mechanical coating process. The coating treatments caused by the impact of stainless balls were conducted 30 sec for a cycle. Each sample was being undergone four cycles, i.e. 2 min of coating treatment. The single phase TiO₂ thin film of anatase or rutile can be produced by the ultrasonic coating technique via the identification of XRD measurements. The SEM illustrated the average grain

size is around 50~100nm and some cracks were formed during bombardment process.

Photocatalytic experiments were carried out using a Pyrex reaction cell. An Xenon lamp 40 W, fixed in the middle of the quartz cell, was used as a light source. During the experiments of photodegradation of methyl orange by UV irradiation in the presence of TiO₂ thin film, the initial concentration of methyl orange was prepared around 1ppm. The significant photodegradation of methyl orange can be observed from TiO₂ thin film on titanium substrate. From the results, the rutile TiO₂ thin film on Ti substrate has the best efficiency of photodegradation. The ultraviolet–visible absorption spectra were obtained by the diffuse reflectance spectra measurements that showed enhanced absorption in the visible range of 400-700 nm. This results was accord with our photocatalytic experiments under visible light and also the literature about black titania. The broadening peaks of rutile or anatase-type vibration modes with extra multiple tiny unknown signals were observed in Raman spectra. Such broadening peaks and tiny unknown signals could be attributed to the bombardment and amorphization effects.

References:

- [1] Sergey Komarov, Sang Son, Naohito Hayashi, Sergey Kaloshkin, Oleg Abramov, Eiki Kasai, *Development of a novel method for mechanical plating using ultrasonic vibrations*, Surface & Coatings Technology, **201**, 6999-7006 (2007).
- [2] Sergey Romankov, Sergey Komarov, Naohito Hayashi, Shunkichi Ueno, Sergey Kaloshkin, Eiki Kasai, *Effect of temperature on deposition of LaPO₄ coatings produced by ultrasonic-based*

coating process on steel substrates, Surface & Coatings Technology, **202**, 4285-4290 (2008).

- [3] Chenyao Fan, Chao Chen, Jia Wang, Xinxin Fu, Zhimin Ren, Guodong Qian and Zhiyu Wang, *Black Hydroxylated Titanium Dioxide Prepared via Ultrasonication with Enhanced Photocatalytic Activity*, Sci. Rep. **5**, 11712-11721 (2015).

Wettability of Sodium Halide Solutions on Hydrophobic Surfaces

Ibuki SHIBAGAKI¹⁾, Naoya YOSHIDA²⁾, and Toshinori OKURA²⁾

¹⁾ Department of Applied Chemistry and Chemical Engineering, Graduate School of Engineering, Kogakuin University, Tokyo, Japan

²⁾ Department of Applied Chemistry, School of Advanced Engineering, Kogakuin University, Tokyo, Japan
E-mail : nyoshida@cc.kogakuin.ac.jp

Abstract

Dynamic wettability, *e.g.* sliding angle, is affected by complicated factors such as tiny roughness and chemical heterogeneity, changes in interface molecular structure. It is considered that sliding angle against solution is possibly affected by changes in solid-liquid interface structure by adsorption of solute. In this study, we fabricated decyltrimethoxysilane (DTMS) self-assembled monolayers and DTMS / 3 - aminopropyltriethoxysilane (APS) mixed self-assembled monolayers on Si wafers, and evaluated wettability against sodium halide solutions. As a result, contact angles on both surfaces showed the similar values, however, sliding angles showed different values between DTMS and DTMS-APS. On DTMS-APS, halide anions were detected by XPS spectra after alternate soaking. Thus, it is considered that adsorption of anion affect sliding angle.

1. Introduction

Wettability is one of the important surface properties in many fields. Contact angle is determined by surface energy and roughness. Sliding angle is affected other factors, and expressed by Furmidge equation^[1]

$$\sin \alpha = \frac{w\gamma_{LV}(\cos \theta_{rec} - \cos \theta_{ad})}{mg}$$

where α is inclined angle, m is weight of droplet, g is gravity acceleration, w is width of droplet, γ_{LV} is surface tension of liquid, θ_{rec} and θ_{ad} are receding and advancing contact angle respectively. Contact angle hysteresis, that is $(\cos \theta_{rec} - \cos \theta_{ad})$, is affected by complicated factors, such as chemical and physical inhomogeneity. In the case of solution, changes in solid-liquid interface structure by adsorption of solute may affect sliding angle. In this study, we measured wettability of sodium halide solutions on decyltrimethoxysilane (DTMS) and DTMS-3-aminopropyltriethoxysilane (APS) self-assembled monolayers, and evaluated the effects of solute on sliding angle.

2. Experimental

Si wafer was cleaned by UV-Ozone treatment, and immersed into the solution of DTMS or DTMS-APS for 3 days. The sample was rinsed by isopropyl alcohol (the case of immersed in DTMS-APS solution), dichloromethane, acetone, and deionized water, successively, and dried at 100°C for 60 min.

Wettability of water and NaX aq. ($X = \text{Cl}, \text{Br}, \text{I}$) on obtained samples were. Contact angle was measured by sessile drop method and with a droplet of 3 μL . For sliding angle, a droplet size was 30 μL . All contact angles and sliding angles were obtained as an average of 5 and 3 measurements respectively. Adsorption of solutes was tried to be detected by alternate soaking method. Fig. 1 shows schematic illustration of alternate soaking method, and its procedure was as follows : 1) the samples were soaked in 0.2 M NaX aq. for 30 s, 2) rinsed by deionized water, 3) soaked in 0.2 M AgNO_3 aq. for 30 s, 4) rinsed by deionized water again. These processes were repeated 10 cycles. The samples before / after alternate soaking were characterized by X-ray photoelectron spectroscopy.

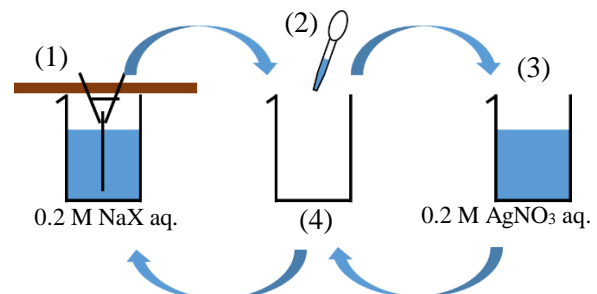


Fig. 1 Schematic illustration of alternate soaking method

3. Results & Discussion

Fig. 2 shows difference between wettabilities of water and sodium halide solutions. Contact angles against each solution were almost similar values. Sliding angles against sodium halide solutions on DTMS were higher, however, those on DTMS-APS showed smaller values.

Fig. 3 shows XPS spectra of DTMS and DTMS-APS before / after alternate soaking. Spectra of DTMS after alternate soaking did not show any peaks of silver, chlorine, bromine, iodine, however, those of DTMS-APS show silver and each halides peaks, that is, silver halide was deposited on DTMS-APS by alternate soaking process. Thus it is thought that adsorption of ion may affect sliding angle on surface that have polar groups.

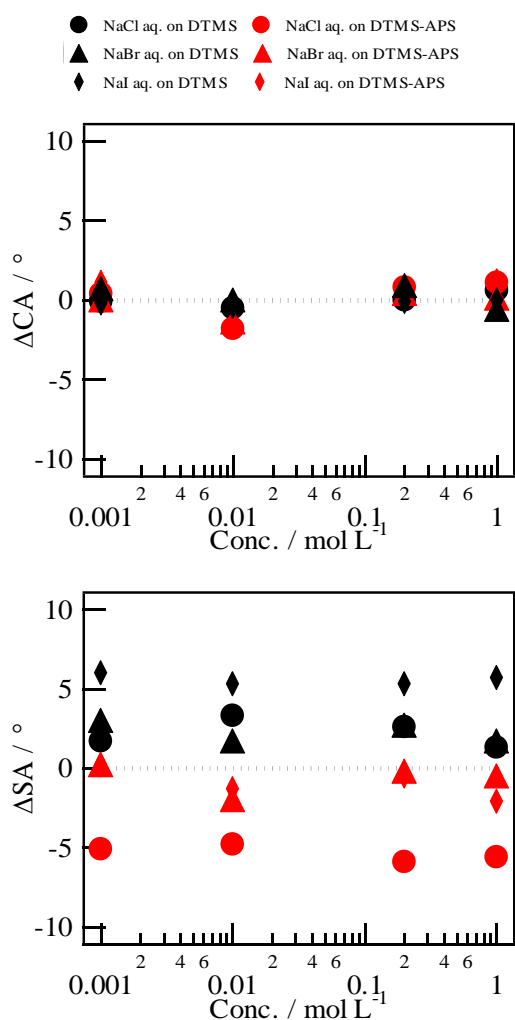


Fig. 2 Difference of wettabilities between water and sodium halide solutions ; (upper) contact angle, (lower) sliding angle

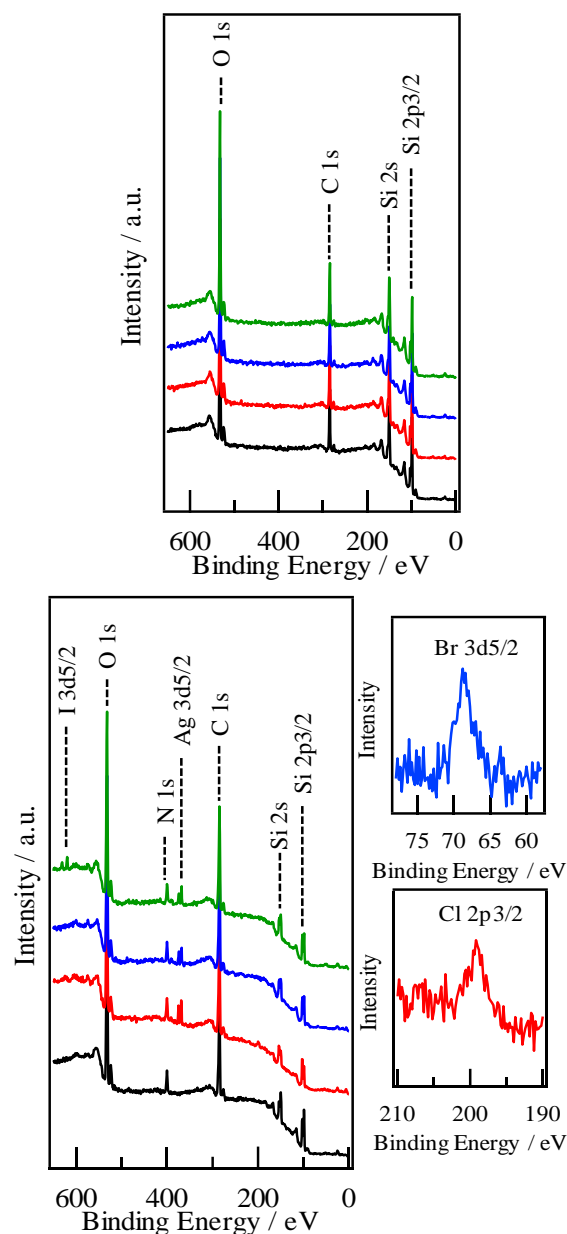


Fig. 3 XPS spectra of DTMS (upper) and DTMS-APS (lower) before / after alternate soaking : before alternate soaking (black line), after alternate soaking in 0.2 M NaCl aq. and 0.2 M AgNO₃ (red line), 0.2 M NaBr aq. and 0.2 M AgNO₃ (blue line), and 0.2 M NaI aq. and 0.2 M AgNO₃ (green line)

Reference

- [1] C. G. L. Furnidge, *J. Colloid Sci.*, **17**, 309 (1962)

Microstructural analysis using TEM in GaInN film grown by RF-MBE

S. Ohno¹, H. Hirukawa¹, R. Yoshida¹, T. Yamaguchi¹, T. Kiguchi², H. Hashimoto¹,
T. Onuma¹, and T. Honda¹

1) Department of Electrical Engineering and Electronics, Graduate School of Engineering, Kogakuin University,
Tokyo, Japan

E-mail: cm19008@ns.kogakuin.ac.jp

2) Institute for Materials Research, Tohoku University, Miyagi, Japan

Abstract

Microstructural analysis using transmission electron microscopy (TEM) was carried out in the GaInN film grown on a (0001)GaN/ α -Al₂O₃ template by radio-frequency plasma-assisted molecular beam epitaxy (RF-MBE). The compositional pulling was observed in the GaInN film. Some voids were also observed in the GaInN film. The microstructure around these voids is discussed.

GaInN is the material applying to visible light emitters of light emitting diode (LED) and laser diode (LD) [1]. This material is also expected to be applied in the photovoltaic receiver responding to visible wavelength range. However, the fabrication of these devices with high-In-content Ga_{1-x}In_xN ($x > 0.15$) has still been a challenging topic. GaInN films are widely grown on GaN. Since there is a large lattice mismatch between GaInN and GaN, lots of crystal defects, such as dislocation, are generated in the film with a thickness beyond critical thickness [2]. Compositional pulling, where In atoms are swept out from GaInN film, also occurs to reduce the residual strain of GaInN grown on GaN. Owing to this compositional pulling effect, the In composition of GaInN becomes lower near the interface between GaInN and GaN [3-4].

In this paper, microstructural analysis, including crystal defects and In fluctuation, using transmission electron microscopy (TEM) was carried out in the GaInN film with a thickness beyond critical thickness grown by radio-frequency plasma-assisted molecular beam epitaxy (RF-MBE).

A GaInN film with a thickness of approximately 400 nm was grown at the thermocouple temperature of 780°C on a (0001)GaN/ α -Al₂O₃ template by RF-MBE. The averaged In composition and relaxation ratio of this film were confirmed to be approximately 17% and 44%, respectively, using X-ray diffraction (XRD) measurement. This film was characterized by TEM and scanning TEM (STEM) for the observations of crystal defects and In fluctuation of GaInN, respectively. The acceleration voltage of 200 kV was used in these measurements. The lamella was manufactured with a focused ion beam (FIB).

Figure 1(a) shows a STEM high angle annular dark field (STEM-HAADF) image. Figure 1(b) shows a line profile of atomic composition along [0001] direction at the area of Fig. 1(a) using STEM energy dispersive X-ray spectrometry (STEM-EDX). In and Ga composition increases and decreased from the interface of GaInN/GaN to the surface of GaInN, respectively. Thus, compositional pulling was also

observed in this film. Figures 1(c) and 1(d) show bright field (BF) images with $\vec{g} = [0008]$ and $\vec{g} = [30\bar{3}0]$ condition, respectively. Some voids were observed in these images. Most of voids were formed in the GaInN area on the screw dislocation in the GaN underlayer. The voids were decorated with edge dislocations, as shown in Fig. 1(d). The formation mechanisms of voids and the edge dislocations around voids will be discussed.

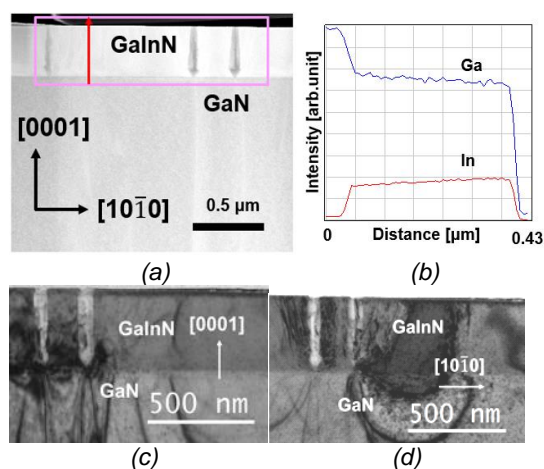


Fig. 1 (a)STEM-HAADF image, (b)Line profile using STEM-EDX along [0001] of composition and TEM images using (c) $\vec{g} = [0008]$ BF, (d) $\vec{g} = [30\bar{3}0]$ BF of GaInN grown at the thermocouple temperature of 780°C.

References:

- [1] Zuzanna Liliental-Weber, Jpn. J. Appl. Phys. **53**, 100205 (2014).
- [2] S.Srinivasan *et al.*, Appl. Phys. Lett. **83**, 5187 (2003).
- [3] K. Hiramatsu *et al.*, MRS Internet J. Nitride Semicond. Res. **2** (1997).
- [4] C. Bazioti *et al.*, J. Appl. Phys. **118**, 155301 (2015).

Nano-micelles incorporated with quantum dots for anti-cancer drug therapy

Yiu-Juan Lin¹⁾, Kun-Bau Huang²⁾, Yu-Chun Wu³⁾, Pragma Rani⁴⁾, Hong-Ru Lin^{*2)}

¹⁾Department of Nursing, Chung Hwa University of Medical Technology, Tainan 717, Taiwan

²⁾Department of Chemical and Materials Engineering, Southern Taiwan University of Science and Technology, Tainan 710, Taiwan

³⁾National Laboratory Animal Center, National Applied Research Laboratories, Tainan 741, Taiwan

⁴⁾Department of Metallurgical and Materials Engineering, Indian Institute of Technology Roorkee, Roorkee, Uttarakhand-247667, India
E-mail: hrlin@stust.edu.tw

Abstract

The main objective of this study is to prepare Pluronic-Chitosan nano-micelles for QDs encapsulation and to develop tumor-targeting drug delivery system for cancer therapy with combination of quantum dots technology and anti-cancer drug therapy.

Two kinds of QDs were used in this study for comparison, one is water-dispersed ZnO QD which was prepared by chemical sedimentation method and the other is water-soluble CdTe QD which was obtained from local supplier. Pluronic nano-micelles containing QDs and anti-cancer drug (doxorubicin hydrochloride, Dox) were prepared according to the method developed previously by our laboratory [1, 2]. Folic acid was used as a target agent for receptor-specific delivery purpose and it was conjugated with chitosan. Then, the surface of Pluronic micelles containing QDs and anti-cancer drug were modified by folate-conjugated chitosan to obtain anti-cancer drug-loaded QD-Pluronic-chitosan-folate nano-carriers.

In vitro drug release studies were conducted in PBS solution at 37 °C to compare before and after the modification of micelle surface as well as the modification concentration. Fig. 5 shows the drug releasing experiment result, in which the top most curve denotes the micelle without modification and down in sequence are the curves with increasing surface modification; Fig. 1(a) shows that the cumulative release amount of drug from the micelle without modification, after 2 days, reaches 65% while the micelle after modification reaches only 20% and after 3 days the drug loaded in micelle without surface modification was released up to 75%. The cumulative release amount observed for micelle modified by Fc-Chi of different proportions was between 55-65% after 6 days; during 7-14 days, the cumulative release amount was gradual and after 14 days, the cumulative release amount reached 70-85%. Next, comparing the release behavior of nano-micelle of ZnO and CdTe QDs after loading with Dox; Fig. 1(b) shows the experiment result, and it can be seen that the release curves are similar, from this we can deduce that the change in the core QDs doesn't influence the drug release.

In order to test the cytotoxic effect of drug loaded QDs-Plu-Fc-Chi prepared in this experiment against

cancer cell MCF-7, we dissolve QDs-Plu-Fc-Chi in the PBS solution and the culture medium containing 105 cancer cells for preculture. After that the absorbance is analyzed by ELISA and the cell viability is calculated by comparing with the control. Fig. 2(a) shows the plot of anti-cancer drug Doxorubicin loaded QDs with fixed concentration versus the action time; on the 1st day, the observed cell viability of pure Doxorubicin is 86% but the cell viability of ZnO-Plu-Fc-Chi and CdTe-Plu-Fc-Chi decreased to 39% and 41% respectively; coming to the last day i.e. the 3rd day, the cell viability of pure Doxorubicin decreased to 36% and that of ZnO-Plu-Fc-Chi and CdTe-Plu-Fc-Chi to 16%. The result clearly indicates that the nano-micelle after surface modification by chitosan becomes more specific to the cancer cells due to presence of folic acid and increases the adhesive strength of nano-micelle to cell through electrostatic interactions, which in turn improves its cytotoxic effect. The expression of folate receptors in normal tissues is very low while it is very high in the case of several human cancers cells. Folic acid or its conjugates combine with folate receptor situated at the surface of cancer cells and are internalized to intracellular compartments to form endosomes. As the conjugation between folate receptor and folate conjugates separates in acid environment (pH = 5.0~5.5), folate receptors return back to the cell surface after dissociation and folate conjugates are degraded by lysosome or released into the cytosol.

Next, the cytotoxic effect is observed on the variation of drug concentration with culture time fixed to 1 day and Fig. 2(b) shows the experiment result. When the concentration is 10 µg/ml, the cell viability of pure drug Doxorubicin is 86% while the cell viability of ZnO-Plu-Fc-Chi and CdTe-Plu-Fc-Chi is 38% and 35% respectively; when the concentration is 20 µg/ml, the cell viability of pure drug Doxorubicin is 78% while the cell viability of ZnO-Plu-Fc-Chi and CdTe-Plu-Fc-Chi is 28%; when

the concentration increased to 30 $\mu\text{g/ml}$, the cell viability of pure drug Doxorubicin, ZnO-Plu-Fc-Chi and CdTe-Plu-Fc-Chi decreased to 74%, 25% and 25% respectively. After observation, it was found that with increase in the drug concentration the cell viability decreases, but when the concentration increases to 30 $\mu\text{g/ml}$, the cell viability decrease range is not obvious. It is mentioned in the Preface that the cadmium compound QDs are easy to ionize in heavy metal ion as Cd^{2+} which makes it more toxic to cells, however, after the actual comparison, the cell viability of ZnO-Plu-Fc-Chi and CdTe-Plu-Fc-Chi has negligible difference. It is speculated that the degree of ionization of CdTe QDs into Cd^{2+} decreases greatly after being encapsulated by Pluronic, so the cell viability increases markedly, close to ZnO-Plu-Fc-Chi with low toxicity.

This experiment proves that the nano-micelle prepared in this experiment has good specificity to the cancer cell, able to increase the cytotoxic effect of drugs and reduces the side effects while improving the therapeutic effect.

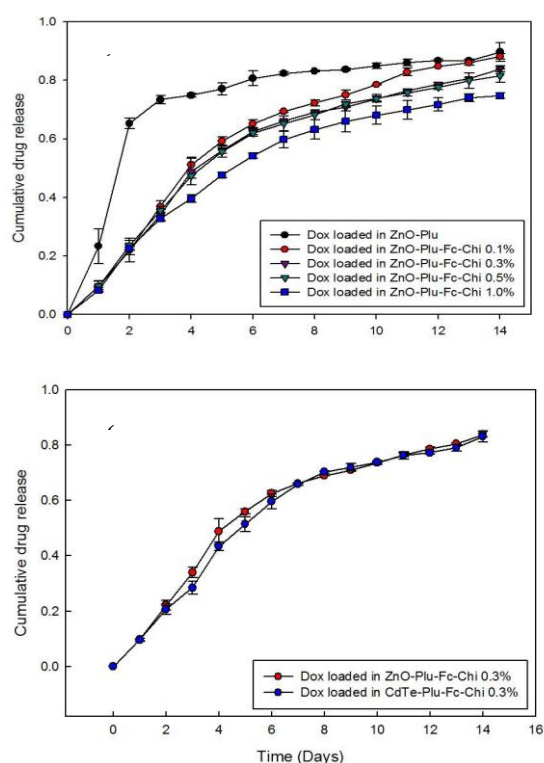


Fig. 1 Drug release versus time profiles of (a) Dox-loaded ZnO nano-micelles and (b) Dox-loaded ZnO and CdTe nano-micelles in PBS solution.

References:

- [1] Lin, H. R.; Chang, P. C. *J. Biomed. Mater. Res. B* 2013, 101B, 689–699.
 [2] Lin, H. R.; Li, Y. S.; Lin, Y. J. *Colloid Polym. Sci.* 2016, 294, 1209–1216.

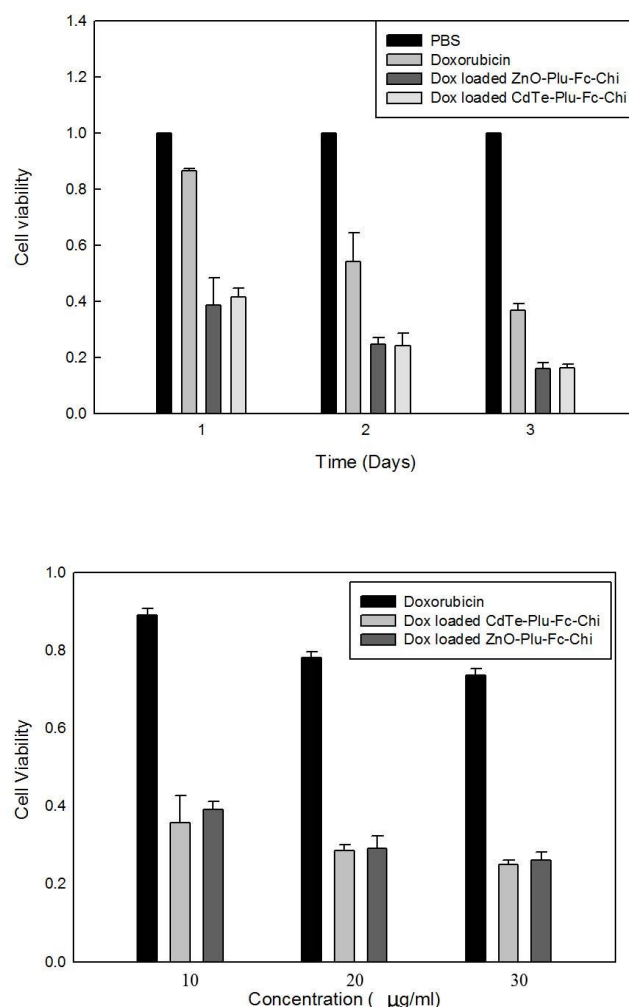


Fig. 2 (a) Cell viability of Dox loaded ZnO-Plu-Fc-Chi and Dox loaded CdTe-Plu-Fc-Chi nano-micelles in different time (n=12); (b) Cell viability of drugs in different concentrations after 1 day (n=12).

Proposal of sulfolane-based gel polymer electrolyte for Li-S batteries

Hibiki Miyuchi, Keitaro Takahashi, Yuki Ishino, Kohei Inaba, Yusuke Ushioda, Tatsuya Kawamura, Kazuki Machida, and Shiro Seki

Department of Environmental Chemistry and Chemical Engineering, Kogakuin University, Tokyo, Japan
E-mail: s316075@ns.kogakuin.ac.jp

Abstract

Lithium-ion batteries have the advantage of high capacity and long cycle life. Performance improvements are required for environmental problems, and therefore, practical application of Lithium-Sulfur (Li-S) batteries is strongly expected. Li-S batteries are used elemental sulfur (S) as positive electrode material and have high theoretical capacity ($1,672 \text{ mAhg}^{-1}$). Chemical reactions between S and Li^+ are multistep reactions, Li_2S_n (lithium-polysulfide: $2 \leq n \leq 8$) are generated and it can dissolve into electrolyte solution, which is main factor of degradation of Li-S batteries. Therefore, in this study, we focus on sulfolane solvent with low solubility of Li_2S_n ^[1] and prepared gel polymer electrolyte (GPE), and evaluated thermal stability and temperature dependence of ionic conductivity with Li salt and polymer composition changes.

Experiments

In this study, we used sulfolane (SL, electrolyte solvent), $\text{LiN}(\text{SO}_2\text{CF}_3)_2$ (LiTFSA, Li salt), and polyether based polymer (host polymer) as electrolyte materials. As preparation of electrolyte solution, SL and LiTFSA were mixed at each molar ratio SL : LiTFSA = $x:1$ ($x=1, 1.5, \text{ and } 2$, respectively). Next, as preparation of GPE, electrolyte solutions and polymer (P(EO/PO)) were mixed at each weight ratio electrolyte solution : polymer = $y : (10 - y)$ ($y = 7, 8, \text{ and } 9$, respectively), and then added DMPA as photo initiator. After that, radical polymerized by UV irradiation. Prepared samples were defined as follows: $(x),y\text{EI}+(10-y)\text{Po}$. Thermal stability and ionic conductivity of prepared samples were measured by TG-DTA (Thermal gravimetric-differential thermal analyzer) and AC impedance method.

Results & Discussion

Fig.1 shows the TG curves of prepared samples. All TG curves exhibited 3 steps weight reduction without neat SL, samples might be evaporated or decomposed in this order: SL, polymer, LiTFSA. From the first step weight reduction, thermal stability of GPE was improved with increase of Li salt concentration. Also, in the case of same electrolyte solution, thermal stability was improved with decrease of polymer composition. Therefore, Li^+ should be coordinated with not only SL but also ether oxygen polymer.

Fig.2 shows temperature dependence of ionic conductivity of prepared GPE samples. All samples

exhibited non-Arrhenius type curves as well as polymer electrolyte and higher σ than polymer electrolyte (black circle) at all measured temperature. From results, σ increased with SL composition. On the other hand, there was different trend of curve by changing of polymer composition. Especially, lowest polymer composition samples indicated high σ at low temperature. Therefore, changes of ionic transport mechanism by temperature and polymer composition were suggested.

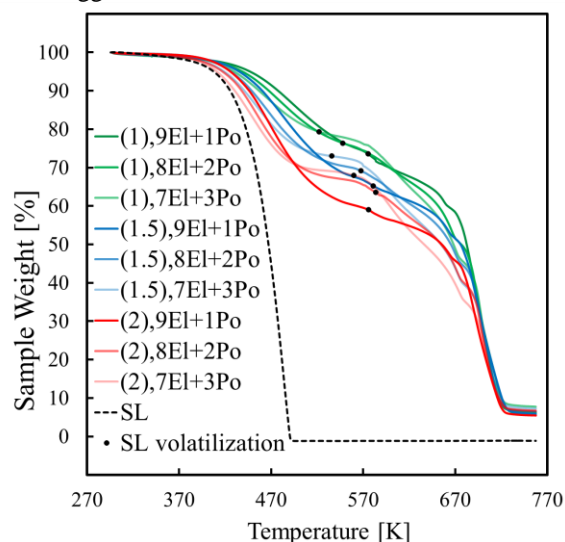


Fig. 1. TG curves of GPE.

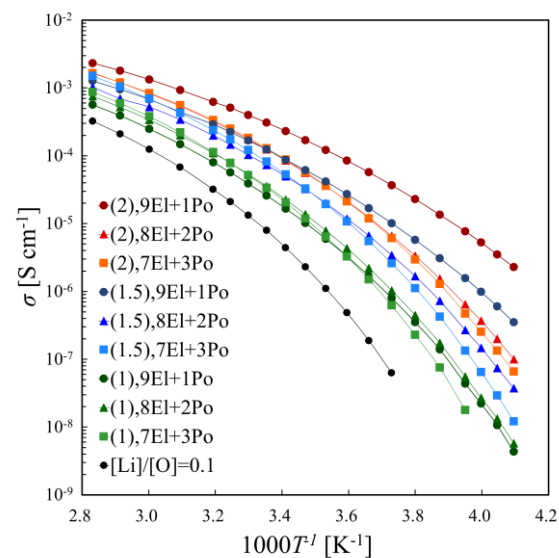


Fig.2. Ionic conductivity of GPE.

References

- [1] A. Nakanishi et al., *J. Phys. Chem. C*, **123**, 14229-14238 (2019).

Proposal and evaluation of physicochemical property for sodium conductive new solid electrolyte

Yuji Yokomaku, Koji Hiraoka, Masaki Kato, Kohei Inaba, Hibiki Miyauchi, Shiro Seki

Department of Environmental Chemistry and Chemical Engineering, School of Advanced Engineering,
Kogakuin University, Tokyo, Japan
E-mail: s316085@ns.kogakuin.ac.jp

Abstract

Conventional sodium-sulfur battery is consisted of sodium metal as anode, sulfur as cathode and β -Al₂O₃ as electrolyte, respectively, and it is widely turned to practical use as electric energy storage devices because of their high abundance resource. On the other hand, this system has serious problems as fire risk because sodium metal and sulfur are used at high temperature and liquid state. In this study, gel polymer electrolyte, which is consisted of sulfolane (SL) based liquid electrolyte, was prepared and physicochemical and electrochemical properties were evaluated. Obtained gel electrolyte exhibited high ionic conductivity and formability with electrodes, and suggested the possibility of room temperature operating sodium sulfur battery. In particular, optimized electrolyte ((6SL)8EL+2Po composition) exhibited quite high ionic conductivity (8.0×10^{-4} S/cm) at 303 K. Therefore, this electrolyte is expected to suitable electrolyte material for sodium sulfur battery operating at low temperature.

Introduction

In general, sodium-sulfur battery operates by redox reaction of sodium and sulfur during charge and discharge. This battery system is obtained β -Al₂O₃ as electrolyte, sodium metal as anode and sulfur as cathode. The sodium-sulfur battery has been applied as the large-scale storage system because it has 786 Wh/kg of weight energy density and 4,500 cycles. On the other hand, this system has serious problems as fire risk owing to their chemical safety of sodium metal and sulfur at high-temperature and liquid state. To solve these problems, we propose low temperature operated sodium-sulfur battery using organic gel electrolyte with polyether-based host polymer and sulfolane (SL)-based electrolyte solution. Herein, thermal stability and ionic conductivity of proposed sodium conductive gel polymer electrolyte were evaluated.

Experimental

Liquid electrolytes were prepared by mixing of SL and NaTFSA using shading bottle in Ar-filled glove box. The molar ratio were changed to x SL:NaTFSA ($x=2,3,4,5$ and 6 , respectively). These liquid electrolytes and polyether-based macromonomer (P(EO/PO), polyether) were mixed with changing weight ratio as followed formula, y liquid electrolytes:(10- y)Polymer ($y=7$ and 8). After added DMPA as photo-initiator, gel polymer electrolyte was fabricated by photo-polymerization by UV irradiation. Prepared samples were defined as $(xSL)_yEl+(10-y)Po$. Thermophysical properties of fabricated gel polymer electrolytes were evaluated by thermogravimetric analysis (TG, Thermo plus EVO2, Rigaku Co., Japan). In addition, ionic conductivities were measured by electrochemical impedance method (VSP, Bio-Logic Co., France).

Result and Discussion

Figure 1 shows appearance of polyether/SL composite gel polymer electrolyte. Prepared gel polymer electrolyte shows high flexibility at room temperature. Therefore, polymer matrix would be played role as skeleton and maintaining phase to SL liquid electrolyte. Figure 2 shows TG curves of polyether/SL sample. The thermal stability of polyether/SL gel tended to decrease with SL composition due to the increasing of free SL in the polymer matrix. The sample weight didn't change below 373 K, polyether/SL gel is expected as solid electrolyte for new-type sodium-sulfur battery operated below 373 K. Figure 3 shows temperature dependence of ionic conductivity for polyether/SL gel electrolytes. Ionic conductivity increased with addition of SL because of their decreasing viscosity in the liquid electrolyte. In the case of constant composition of SL, lower polymer composition (2Po) samples showed high ionic conductivity. Increasing of ionic conductivity were attributed to the ratio of SL which contribute to mainly ionic conduction.



Fig. 1. Appearance of polyether/SL gel electrolyte.

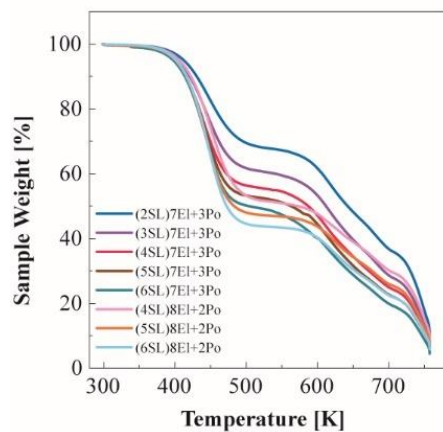


Fig. 2. TG curves of polyether/SL gel electrolyte.

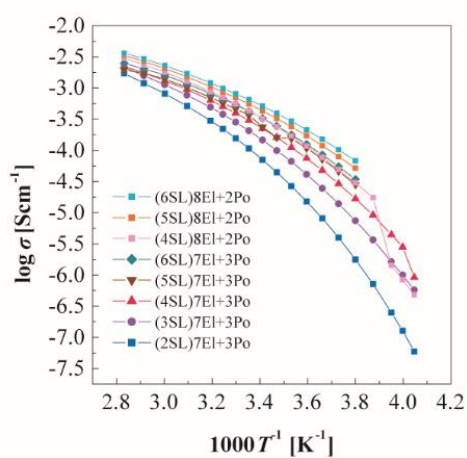


Fig. 3. Temperature dependence of ionic conductivity for polyether/SL gel electrolyte.

References:

- [1] N. Yabuuchi, *et.al.*, *Chem. Rev.*, **114**, 11636 (2014).